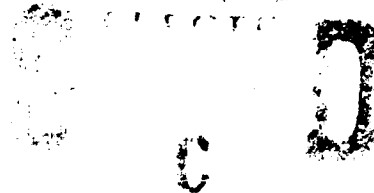


AD-A242 666



The Pennsylvania State University  
APPLIED RESEARCH LABORATORY  
P.O. Box 30  
State College, PA 16804

DTIC



DEVELOPMENT AND EVALUATION OF LASER  
DOPPLER TECHNIQUES FOR MEASUREMENTS OF  
FLEXURAL AND LONGITUDINAL STRUCTURAL INTENSITY

by

Timothy E. McDevitt

Technical Report No. TR 91-013  
October 1991

L.R. Hettche, Director  
Applied Research Laboratory

Approved for public release; distribution unlimited

01 1104 105

91-15026



# REPORT DOCUMENTATION PAGE

Form Approved  
OMB No. 0704-0183

Public reporting burden for this collection of information is estimated to average 1 hour per response, including the time for reviewing instructions, searching existing data sources, gathering and maintaining the data needed, and completing and reviewing the collection of information. Send comments regarding this burden estimate or any other aspect of this collection of information, including suggestions for reducing this burden, to Washington Headquarters Services, Directorate for Information Operations and Reports, 1215 Jefferson Davis Highway, Suite 1204, Arlington, VA 22202-4302, and to the Office of Management and Budget, Paperwork Reduction Project (0704-0183), Washington, DC 20503.

1. AGENCY USE ONLY (Leave blank)		2. REPORT DATE May 1991		3. REPORT TYPE AND DATES COVERED	
4. TITLE AND SUBTITLE Development and Evaluation of Laser Doppler Techniques for Measurements of Flexural and Longitudinal Structural Intensity				5. FUNDING NUMBERS	
6. AUTHOR(S) Timothy E. McDevitt					
7. PERFORMING ORGANIZATION NAME(S) AND ADDRESS(ES) The Pennsylvania State University Applied Research Laboratory P.O. Box 30 State College, PA 16804				8. PERFORMING ORGANIZATION REPORT NUMBER  TR 91-013	
9. SPONSORING / MONITORING AGENCY NAME(S) AND ADDRESS(ES)				10. SPONSORING / MONITORING AGENCY REPORT NUMBER	
11. SUPPLEMENTARY NOTES					
12a. DISTRIBUTION / AVAILABILITY STATEMENT				12b. DISTRIBUTION CODE	
13. ABSTRACT (Maximum 200 words) Based on the hypothesis that both flexural and longitudinal vibrational energy flow can be measured non-intrusively by an optical technique which can be extended to broadband vibrations, a two-channel laser vibrometer system is developed and evaluated for cross-spectral power flow measurements. The cross-spectral power flow results from tests on small resonant beams and rods are verified by comparison with one-dimensional energetics and standing wave power flow results (obtained with a single scanning laser beam of the two-channel vibrometer). Among the contributions of the thesis are: development and validation of the laser technique for measuring flexural power flow in reverberant fields; introduction of a procedure to maximize phase accuracy which eliminates phase bias error and coherent noise error; an investigation into the differential Doppler method for measuring longitudinal power flow including an analytical model of the effects of bending on the longitudinal power flow measurements; studies of the optical parameters which dictate the performance of the reference beam method and differential Doppler method; and a quantification of how physical and measurement parameters affect the accuracy of this non-intrusive two-point vibrational power flow measurement. Also included are literature surveys covering the measurement of vibration intensity and the uses of laser vibrometry, and a section covering fundamental principles of both the reference beam and differential Doppler method.					
14. SUBJECT TERMS laser doppler, structural intensities, flexure, longitudinal vibration, energy flow, laser vibrometer, cross spectral power flow, beams, rods				15. NUMBER OF PAGES 256	
				16. PRICE CODE	
17. SECURITY CLASSIFICATION OF REPORT Unclassified	18. SECURITY CLASSIFICATION OF THIS PAGE Unclassified	19. SECURITY CLASSIFICATION OF ABSTRACT Unclassified	20. LIMITATION OF ABSTRACT		

## ABSTRACT

Based on the hypothesis that both flexural and longitudinal vibrational energy flow can be measured non-intrusively by an optical technique which can be extended to broadband vibrations, a two-channel laser vibrometer system is developed and evaluated for cross-spectral power flow measurements. The cross-spectral power flow results from tests on small resonant beams and rods are verified by comparison with one-dimensional energetics and standing wave power flow results (obtained with a single scanning laser beam of the two-channel vibrometer). Among the contributions of the thesis are: development and validation of the laser technique for measuring flexural power flow in reverberant fields; introduction of a procedure to maximize phase accuracy which eliminates phase bias error and coherent noise error; an investigation into the differential Doppler method for measuring longitudinal power flow including an analytical model of the effects of bending on the longitudinal power flow measurements; studies of the optical parameters which dictate the performance of the reference beam method and differential Doppler method; and a quantification of how physical and measurement parameters affect the accuracy of this non-intrusive two-point vibrational power flow measurement. Also included are literature surveys covering the measurement of vibration intensity and the uses of laser vibrometry, and a section covering fundamental principles of both the reference beam and differential Doppler method.

Accession For  
A-1

## TABLE OF CONTENTS

LIST OF FIGURES . . . . .	vii
LIST OF TABLES . . . . .	xi
NOMENCLATURE . . . . .	xii
ACKNOWLEDGEMENTS . . . . .	xvii
INTRODUCTION . . . . .	1
Chapter I. LITERATURE SURVEY OF STRUCTURAL INTENSITY AND ITS MEASUREMENTS . . . . .	7
Chapter II. LASER VIBROMETRY . . . . .	53
BACKGROUND AND USES TO DATE . . . . .	53
POTENTIAL OF LASER VIBROMETRY AS A STRUCTURAL INTENSITY TECHNIQUE . . . . .	55
THE TWO-CHANNEL LASER DOPPLER VIBROMETER SYSTEM . . . . .	58
SETUP OF THE TCV SYSTEM . . . . .	59
FUNDAMENTALS OF OPERATION . . . . .	65
The Reference Beam Technique . . . . .	66
The Differential Doppler Technique . . . . .	71
LASER VIBROMETER SIGNAL PROCESSING . . . . .	75
LASER VIBROMETER NOISE SOURCES . . . . .	81
Characteristics of Laser Speckle . . . . .	81
Speckle Noise Due to Normal Motion . . . . .	83
Speckle Noise Due to Transverse Motion . . . . .	84
Doppler Broadening . . . . .	86
Miscellaneous Noise Sources . . . . .	90
POSSIBLE EFFECTS OF LASER VIBROMETER NOISE SOURCES ON STRUCTURAL INTENSITY MEASUREMENTS . . . . .	93
Chapter III. FLEXURAL INTENSITY MEASUREMENTS USING THE TCV SYSTEM . . . . .	98
FORMULATION OF THE APPROACH . . . . .	98
EXPERIMENTAL SETUP AND PROCEDURE . . . . .	105
RESULTS OF FLEXURAL INTENSITY TESTS . . . . .	110
CONCLUSIONS . . . . .	116

Chapter IV. CHARACTERISTICS CONTROLLING THE SIGNAL-TO-NOISE RATIO IN THE REFERENCE BEAM METHOD . . . . .	117
INTRODUCTION . . . . .	117
CARRIER-TO-NOISE RATIO AND PLL PERFORMANCE AS APPLIED TO THE REFERENCE BEAM METHOD . . . . .	118
SIGNAL-TO-NOISE RATIOS OF THE VELOCITY SIGNALS IN THE REFERENCE BEAM METHOD . . . . .	132
SIGNAL RELATED PLL CHARACTERISTICS . . . . .	135
Chapter V. SOURCES OF ERROR IN FLEXURAL INTENSITY MEASUREMENTS DUE TO TCV SYSTEM CHARACTERISTICS . . . . .	147
INTRODUCTION . . . . .	147
RANDOM ERROR IN TCV FLEXURAL INTENSITY MEASUREMENTS . . . . .	148
COHERENT NOISE . . . . .	153
REMOVAL OF COHERENT NOISE AND PHASE BIAS EFFECTS . . . . .	156
EFFECTS OF VIBRATION OF THE OPTICS . . . . .	162
OPTIMIZATION OF TCV SYSTEM DESIGN FOR MAXIMUM ACCURACY . . . . .	163
Chapter VI. LONGITUDINAL INTENSITY MEASUREMENTS USING THE TCV SYSTEM . . . . .	166
INTRODUCTION . . . . .	166
FORMULATION OF THE APPROACH . . . . .	167
EXPERIMENTAL SETUP AND PROCEDURE . . . . .	173
RESULTS OF LONGITUDINAL INTENSITY TESTS . . . . .	176
ANALYSIS OF LONGITUDINAL POWER FLOW RESULTS . . . . .	186
CONCLUSIONS . . . . .	203
Chapter VII. CHARACTERISTICS CONTROLLING THE SIGNAL-TO-NOISE RATIO IN THE DIFFERENTIAL DOPPLER METHOD . . . . .	205
INTRODUCTION . . . . .	205
CARRIER-TO-NOISE RATIO AND PLL PERFORMANCE AS APPLIED TO THE DIFFERENTIAL DOPPLER METHOD . . . . .	206
SIGNAL-TO-NOISE RATIOS OF THE VELOCITY SIGNALS IN THE DIFFERENTIAL DOPPLER METHOD . . . . .	217
Chapter VIII. SOURCES OF ERROR IN LONGITUDINAL INTENSITY MEASUREMENTS DUE TO TCV SYSTEM CHARACTERISTICS . . . . .	220
INTRODUCTION . . . . .	220
RANDOM ERROR IN TCV LONGITUDINAL INTENSITY MEASUREMENTS . . . . .	220
Chapter IX. SPECKLE DYNAMICS AND SIGNAL DETECTION IN THE REFERENCE BEAM AND DIFFERENTIAL DOPPLER MODES . . . . .	225
INTRODUCTION . . . . .	225
SPECKLE DYNAMICS IN THE REFERENCE BEAM MODE . . . . .	226
SPECKLE DYNAMICS IN THE DIFFERENTIAL DOPPLER MODE . . . . .	228
CONCLUSIONS . . . . .	232

Chapter X. CONCLUSIONS AND RECOMMENDATIONS FOR FURTHER STUDY . .	234
BIBLIOGRAPHY . . . . .	237
Appendix A. DERIVATION OF CROSS-SPECTRAL EXPRESSIONS FOR POWER FLOW . . . . .	243
LONGITUDINAL POWER FLOW . . . . .	243
FLEXURAL POWER FLOW . . . . .	245
FINITE DIFFERENCE APPROXIMATION . . . . .	247
Appendix B. PHASE ANGLE BETWEEN TWO POINTS SEPARATED BY $\Delta x$ ON A RESONANT BEAM (AND ROD) WITH WAVENUMBER $k$ AND MIDPOINT OVER THE ANTINODE . . . . .	250
FLEXURAL CASE . . . . .	251
LONGITUDINAL CASE . . . . .	252
Appendix C. RELATIONSHIP BETWEEN THE CROSS-SPECTRUM AND THE COMPLEX FORMS OF TWO SINUSOIDAL SIGNALS . . .	255

## LIST OF FIGURES

<u>Figure</u>	<u>Page</u>
1.1      Directions of Displacements, Slopes, Forces and Moments	8
1.2      The Biaxial Accelerometer . . . . .	13
1.3      Transducer Array for General 1-D Flexural Wave Case . .	18
1.4      Transducer Array for General 2-D Flexural Wave Case . .	21
1.5      Accelerometer Configurations for Measuring Longitudinal and Angular Accelerations . . . . .	24
1.6      The Vibration Intensity Transducer . . . . .	25
1.7      Effect of Sensor Mass on Response of Various Types of Panels . . . . .	38
1.8      Accelerometer Array Used for Flexural Waves in Slender Cylinders . . . . .	52
2.1      Schematic of a Single Vibrometer Unit Arranged for Surface-Normal Vibration Measurements . . . . .	60
2.2      Layout of the Scanning Dual Laser Vibrometer System . .	62
2.3      Schematic of a Single Vibrometer Unit Arranged for In-Plane Vibration Measurements . . . . .	64
2.4      Michelson Interferometer . . . . .	67
2.5      Illumination of Surface for In-Plane Sensitivity . . . .	73
2.6      Block Diagram of a Phase-Locked Loop . . . . .	77
2.7      Phase Mismatch Between PLL Units . . . . .	80
2.8      The Influence of Noise Correlation in the Measured Cross-Spectrum . . . . .	94
3.1      Mechanical and Optical Setup for Flexural Intensity Measurements . . . . .	106
3.2      Comparison of Flexural Power Flow Results for $n = 10$ , $\eta = 0.013$ , $f = 2520$ Hz . . . . .	111

3.3	Comparison of Flexural Power Flow Results for $n = 12$ , $\eta = 0.012$ , $f = 3712$ Hz . . . . .	113
3.4	Comparison of Flexural Power Flow Results for $n = 8$ , $\eta = 0.003$ , $f = 5650$ Hz . . . . .	115
4.1	Comparison of Downmixed Photodetector Spectra With and Without Light to Photodetector . . . . .	121
4.2	Comparison of Downmixed Photodetector Spectra at Two Different Levels of Total Laser Power . . . . .	123
4.3	Comparison of Downmixed Photodetector Spectra at Two Nearby Points on a Stationary Object . . . . .	126
4.4	Comparison of Velocity Spectra for Different CNR Values With Signal at 4 kHz . . . . .	129
4.5	Comparison of Velocity Spectra for Different CNR Values With Signal at 400 Hz . . . . .	130
4.6	Noise Floors of the Two PLL Processors at Approximately 51 dB CNR . . . . .	133
4.7	Noise Floor at Approximately 51 dB CNR for PLL Unit 1 (Signals Corresponding to Acceleration Amplitudes in $g$ Are Also Shown) . . . . .	136
4.8	Noise Floor at Approximately 51 dB CNR for PLL Unit 2 (Signals Corresponding to Acceleration Amplitudes in $g$ Are Also Shown) . . . . .	137
4.9	Sensitivity Curves for PLL Unit 1 at High Frequencies Versus Frequency Deviation . . . . .	139
4.10	Sensitivity Curves for PLL Unit 2 at High Frequencies Versus Frequency Deviation . . . . .	140
4.11	Sensitivity Curves for PLL Unit 1 at Low Frequencies Versus Frequency Deviation . . . . .	141
4.12	Sensitivity Curves for PLL Unit 2 at Low Frequencies Versus Frequency Deviation . . . . .	142
4.13	Sensitivity Versus Amplitude for PLL Unit 1 . . . . .	144
4.14	Sensitivity Versus Amplitude for PLL Unit 2 . . . . .	145
5.1	Coherence of Noise Between TCV Channels in the Reference Beam Mode . . . . .	157



5.2	Illustration of the Effects of Coherent Noise on the Measured Cross-Spectrum . . . . .	158
5.3	Illustration of the Effects of Coherent Noise, Phase Bias, and Photodetector Switching on the Measured Cross-Spectrum . . . . .	160
6.1	Mechanical and Optical Setup for Longitudinal Intensity Measurements . . . . .	175
6.2	Comparison of Longitudinal Power Flow Results for $n = 3$ , $\eta = 0.04$ , $f = 13.3$ kHz . . . . .	178
6.3	Illustration of the Effects of the Bending-Induced Longitudinal Motion . . . . .	180
6.4	Bending-Induced Longitudinal Component of Motion . . . . .	182
6.5	Comparison of Longitudinal Power Flow Experimental Results and Theoretical Results ( $\Delta x = 15.24$ cm, $\theta_L = -1.86$ radians) . . . . .	196
6.6	Comparison of Longitudinal Power Flow Experimental and Theoretical Results ( $\Delta x = 15.24$ cm, $\theta_L = 0.0$ radians) . . . . .	197
6.7	Comparison of Longitudinal Power Flow Experimental and Theoretical Results ( $\Delta x = \lambda_B$ , $\theta_L = 0.0$ radians) . . . . .	198
6.8	Comparison of Longitudinal Power Flow Experimental and Theoretical Results (Shifted Antinodes) ( $\Delta x = \lambda_B$ , $\theta_L = 0.0$ radians) . . . . .	199
6.9	Comparison of Longitudinal Power Flow Experimental and Theoretical Results ( $\Delta x = \lambda_B$ , $\theta_L = -1.86$ radians) . . . . .	200
7.1	Comparison of Downmixed Photodetector Spectra With and Without Light to Photodetector for the Differential Doppler Mode . . . . .	208
7.2	Comparison of Downmixed Photodetector Spectra at Two Nearby Points on a Stationary Object for the Differential Doppler Mode . . . . .	210
7.3	Comparison of Velocity Noise Floors for Different CNR Values for the Differential Doppler Mode . . . . .	212

7.4	Comparison of Velocity Noise Floors for Two Different CNR Values for the Differential Doppler Mode at Low Frequencies . . . . .	215
7.5	Comparison of Velocity Noise Floors for the Two PLL Units at a CNR of 60 dB in the Differential Doppler Mode . . . . .	216
7.6	Noise Floor at a CNR of 60 dB for PLL Unit 1 and Signals Corresponding to Acceleration Amplitudes in g for $\theta/2$ of 5.9° in the Differential Doppler Mode . . . . .	218
7.7	Noise Floor at a CNR of 60 dB for PLL Unit 2 and Signals Corresponding to Acceleration Amplitudes in g for $\theta/2$ of 5.9° in the Differential Doppler Mode . . . . .	219
9.1	Effect of an Aperture on the Noise Floor in the Differential Doppler Mode in the Presence of Appreciable Bending . . . . .	231

## LIST OF TABLES

<u>Table</u>	<u>Page</u>
4.1 Comparison of CNR Values for Various Amounts of Total Laser Power in the Reference Beam Mode . . . . .	124
5.1 Influence of CNR on the Number of Samples Required for 10% Random Error in Power Flow Measurement With the Reference Beam Mode . . . . .	151
5.2 Influence of Power Flow on the Number of Samples Required for 10% Random Error in Power Flow Measurement With the Reference Beam Mode . . . . .	152
7.1 Comparison of CNR Values for Various Amounts of Total Laser Power in the Differential Doppler Mode . . . . .	209
8.1 Influence of CNR on the Number of Samples Required for 10% Random Error in Power Flow Measurement With the Differential Doppler Mode . . . . .	222
8.2 Influence of Power Flow on the Number of Samples Required for 10% Random Error in Power Flow Measurement With the Differential Doppler Mode . . . . .	223
8.3 Influence of Lens Focal Length on the Number of Samples Required for 10% Random Error in Power Flow Measurement With the Differential Doppler Mode . . . . .	224

## NOMENCLATURE

a	Acceleration
A	Amplitude
A'	Reflected Amplitude
b	Bandwidth
B	Bending Rigidity
cm	Centimeter
CNR	Carrier-to-Noise Ratio
d	Diameter of Laser Spot
dB	Decibels
e	Electron Charge
E	Total Energy (Kinetic Plus Potential)
f	Frequency (cycles per second)
f.l.	Focal Length of Lens
F	Force
F(s)	Laplace Transform of PLL Loop Filter Function
FFT	Fast Fourier Transform
FM	Frequency Modulated (or Modulation)
g	Acceleration Due to Gravity ( $9.81 \text{ m/s}^2$ )
G	Shear Modulus
$G_{xx}(\omega)$	One-sided Autospectrum of Signal $x(t)$
$G_{xy}(\omega)$	One-sided Cross-Spectrum of Signals $x(t)$ and $y(t)$
h	Thickness
$H_{TOT}$	Accelerometer Frequency Response Function
Hz	Hertz (Cycles per Second)

i	$\sqrt{-1}$
I	Moment of Inertia
$I_L$	Light Intensity
Im	Imaginary Part of a Quantity
j	Summation Index
k	Wavenumber
kHz	Kilohertz
K	PLL Sensitivity
$K_1$	Sensitivity of PLL Unit One
$K_2$	Sensitivity of PLL Unit Two
$K_d$	Gain of PLL Phase Detector
$K_0$	Gain of PLL VCO
L	Length
m	Mass, Meter, Heterodyne Efficiency
m'	Mass per Unit Length
mm	Millimeter
m(t)	Noise Signal in Channel 1
mW	Milliwatt
$M_x$	Bending Moment in x Direction
$M_{xy}$	Twisting Moment
MHz	Megahertz
n	Mode Number
n(t)	Noise Signal in Channel 2
$n_d$	Number of Spectral Averages
p(A)	Probability Density Function of Amplitude A

P	Structural Power Flow (Structural Intensity • Cross-Sectional Area)
$P_{SN}$	Electrical Power Due to Shot Noise
$P_E$	Electrical Power
$P_L$	Light Power
PLL	Phase-locked Loop Processor
Q	Shear Force
r	Radius
re	With Reference to the Indicated Voltage Level
R	Reflection Coefficient
Re	Real Part of a Quantity
RMS	Root Mean Square Value
$R_{xy}(\tau)$	Cross Correlation
s	Spectral Sensitivity of Photodetector
S	Cross-Sectional Area
SNR	Signal-to-Noise Ratio
$S_{xy}(\omega)$	Cross-Spectral Density of Signals $x(t)$ and $y(t)$
t	time
T	Torsional Stiffness
$u(t)$	True Signal in Channel 1
v	Velocity
$v(t)$	True Signal in Channel 2
V	Voltage
$V_{AN}$	Vibrometer Voltage Reading at Antinode
$V_N$	Vibrometer Voltage Reading at Node
VCO	Voltage-Controlled Oscillator
x	Axial Position

$x(t)$	Measured Signal in Channel 1
$y(t)$	Measured Signal in Channel 2
$Y$	Young's Modulus
$Z$	Complex Structural Impedance
$\beta$	Angle Between Velocity Vector and Sensitivity Vector
$\gamma^2$	Ordinary Coherence
$\gamma_{xy}$	Shear Strain
$\delta(\omega)$	Phase Mismatch (As a Function of $\omega$ )
$\Delta$	Change or Difference in a Quantity, also Transducer Spacing
$\nabla^2$	Two-Dimensional Laplace Operator
$\epsilon$	Strain
$\epsilon_r$	Normalized Random Error
$\epsilon_b$	Normalized Bias Error
$\eta$	Loss Factor, or Quantum Efficiency
$\theta_x$	Slope of Surface in x direction
$\theta/2$	Lens Half-Angle
$\lambda$	Wavelength
$\nu$	Poisson's Ratio
$\xi$	Displacement
$\xi_{AN}$	Displacement at Antinode
$\xi_N$	Displacement at Node
$\pi$	3.14159...
$\Pi$	Structural Power Flow
$\Pi_E$	Structural Power Flow Obtained by Energetics Method
$\Pi_{SW}$	Structural Power Flow Obtained by Standing Wave Method
$\Pi_{2P}$	Structural Power Flow Obtained by Cross-Spectral Method

$\rho$	Mass Density
$\sigma$	Normal Stress
$\sigma_0$	Speckle Size
$\tau_{sy}$	Shear Stress
$\phi, \psi$	Phase Angles or Phase Angle Differences
$\omega$	Circular Frequency (radians per second)
$\Omega$	Electrical Resistance

#### DENOTATIONS

*	Denotes the Conjugate of a Complex Quantity such as $\bar{Z}^*$
$\sim$	Denotes a Complex Quantity such as $\bar{Z}$
$\cdot$	Denotes First Derivative of a Quantity with Respect to Time such as $\dot{\xi}$
$\ddot{\phantom{x}}$	Denotes Second Derivative of a Quantity with Respect to Time such as $\ddot{\xi}$
$\langle \rangle_t$	Denotes Time Average of a Quantity
$\langle \rangle_x$	Denotes Spatial Average of a Quantity
$  $	Denotes Magnitude of a Complex Quantity such as $ Z $
$\exp(x)$	Denotes $e^x$



## INTRODUCTION

The flow of vibration energy through a structure can occur in several forms including flexural waves, longitudinal waves, and shear waves. Introduced by Noiseux in 1970, the structural intensity method is a technique which allows one to determine experimentally how this vibration energy is transmitted or dissipated throughout a structure. Most of the focus has been on the flow of energy due to flexural waves, since these are typically dominant from a sound radiation standpoint. However, the technique is equally applicable to longitudinal waves. Cremer, Heckl and Ungar (1973) have illustrated how flexural and longitudinal energy can interact at structural joints which makes longitudinal intensity an important value from an energy balance standpoint.

The measurement of vibrational "power flow" or structural intensity can be accomplished in the flexural farfield by the use of two closely spaced transducers and a finite difference approximation. (NOTE: The use of the term "power flow" is widespread in the structural intensity field despite its inaccuracy. It is actually an energy flux or simply a power measurement. "Power flow" may be used in this thesis where it is more correctly a "power" which is measured.) Two accelerometers have been used in the past to accomplish this task. Unfortunately, accelerometers can alter the dynamic behavior of the vibrating structure. Additionally accelerometers cannot easily probe a surface for the purpose of mapping the structural energy flow paths.

These and other related considerations have hindered the practical implementation of structural intensity measurements to date.

Consequently, there is a need for a technique which can measure the real-time structural response simultaneously at two closely spaced points without mass-loading the structure and without requiring the repeated bonding of transducers to the surface. This thesis details the development and evaluation of a two-channel laser Doppler vibrometer system (TCV system) as a structural intensity probe. This device focuses laser light to two spots on a vibrating surface and, by the use of the Doppler shift in the backscattered light, determines the direction and magnitude of the energy flow-rate by signal processing methods which have been used for accelerometers. Theoretically, the instrument can be used to quickly scan a surface to map out the structural intensity due to surface-normal as well as in-plane waves so that the energy flow due to three wave types (flexural, longitudinal, and shear) can be monitored with the same instrument.

The basic concepts of structural intensity and a review of the various methods which have been used to measure structural intensity to date are discussed in Chapter I. This is a detailed literature survey which includes references to many of the problems with the current intensity measurement techniques.

Chapter II reviews the uses of laser Doppler vibrometry to date, and presents a description of the TCV system constructed at the Applied Research Laboratory at The Pennsylvania State University. Additionally, it details the fundamental principles of vibrometry in the reference beam mode (which is used for detection of surface-normal vibration) and

vibrometry in the differential Doppler mode (which is used for detection of in-plane vibration). Also discussed are noise sources in laser vibrometry and related electro-optic parameters which can effect structural intensity measurements when the TCV system is used. This discussion is relatively brief and is meant to serve as a background to the discussions related to intensity measurements.

The balance of the text is split into two major parts. The first pertains to the measurement of flexural intensity using the TCV system in the reference beam mode, while the second pertains to the measurement of longitudinal intensity using the TCV system in the differential Doppler mode.

Chapter III formulates the cross-spectral (two-point) flexural intensity equation in terms of the TCV system output from basic vibrometer principles. It also presents two alternate equations for flexural intensity which are only applicable in a special case and which are only used in this work for validation of the much more versatile cross-spectral technique. The chapter then describes the experimental setup and test procedure used for validation of the TCV cross-spectral technique and presents the experimentally obtained flexural intensity by way of the three approaches.

The remaining chapters on flexural intensity focus chiefly on the optical and electronic aspects of the TCV system in the reference beam mode. These aspects can greatly influence the measurement accuracy of the system in practical situations and hence they form the evaluation portion of the thesis for flexural intensity. Chapter IV primarily describes the electro-optical parameters which ultimately determine the

vibrometer channel signal-to-noise ratio. This is an important quantity in intensity measurements as it determines intensity random error. Chapter V details and analyzes the influence of three potential sources of intensity error due to TCV system characteristics when in the reference beam mode. These sources include random error, bias error (particularly phase bias error), and coherent noise. Phase bias and coherent noise error are addressed at the same time since their deleterious effects can be removed simultaneously by a technique described in the chapter.

Chapter VI introduces the topic of longitudinal intensity. In a manner similar to Chapter III, it derives the cross-spectral longitudinal intensity and the two alternate longitudinal intensity equations in terms of the TCV output. It also presents the longitudinal intensity test results and a discussion.

Chapter VII then describes the parameters which influence the signal-to-noise ratio in the differential Doppler technique. The differential Doppler technique appears to be rarely used in vibrometry, compared to the reference beam technique and there is little theory available on the differential Doppler technique. Therefore the influence of some parameters on the signal-to-noise ratio is obtained experimentally. Ultimately the chapter predicts vibrometer signal-to-noise ratios as a function of both the optical conditions and the amount of in-plane motion. This lays the foundation for longitudinal intensity random error predictions.

Chapter VIII presents predictions of random error as a function of various optical conditions and longitudinal intensity. As explained in the chapter, coherent noise is not a source of error in the differential Doppler technique and so is not addressed. Phase bias error is not addressed in this chapter since it is removed in the same fashion as it is in flexural intensity measurements.

Chapter IX includes results of studies conducted on vibrometer signal stability and speckle effects in combined flexural and longitudinal fields.

Finally, Appendices A through C include mathematical derivations which support points made in the text.

There are several original contributions of this thesis. First is the development and implementation of an optical system which can accurately measure flexural power flow by the cross-spectral method. Flexural power flow can be measured by a single vibrometer if phase information (from a shaker or an accelerometer) is available. But in practical usage this approach either adds an extra source (the shaker) or at least relies on an accelerometer (which can cause inaccuracies due to phase errors or mass loading as explained in the thesis). This thesis presents the first reliable truly "non-intrusive" optical vibrational power flow measurement system which is inherently amenable to random vibration measurements where the sources of the power or their locations are unknown.

A second original contribution is that the thesis ties the two fields of structural intensity and laser vibrometry together by relating the various optical parameters in vibrometry to random errors in

intensity measurements. This is useful in practical conditions outside the laboratory. Photodetector switching (although a carry-over from conventional intensity techniques) is introduced for the first time as an optical technique to optimize phase accuracy. Coherent noise and its removal by photodetector switching is also a new consideration for phase accuracy in two-channel optical systems which use a single laser.

To the author's knowledge, the use of the differential Doppler method for vibration work is rare and its use in longitudinal intensity measurement is entirely new. The sections on optical noise random error and laser speckle in the differential Doppler method are also original contributions.

## Chapter I

### LITERATURE SURVEY OF STRUCTURAL INTENSITY AND ITS MEASUREMENTS

The measurement of structural intensity was first introduced by Noiseux in 1970. Recognizing the need for a technique to trace vibration propagation more simply than correlation techniques, he developed an approach for measuring the flow of power due to flexural waves. This approach was limited to the assumptions of negligible material damping (real Young's modulus) and negligible rotational inertia and shear deformation (classical plate theory).

The instantaneous intensity (power per unit width) can be defined in some direction  $x$  as:

$$\Pi_x = Q_x \dot{\xi} + M_x \dot{\theta}_x + M_{xy} \dot{\theta}_y \quad (1.1)$$

Where  $Q_x$  is the shear force in the  $x$ -direction,  $M_x$  is the  $x$ -directed bending moment,  $M_{xy}$  is the twisting moment,  $\dot{\xi}$  is the normal velocity and  $\dot{\theta}_x$  and  $\dot{\theta}_y$  are the time rate of change of slope in the  $x$  and  $y$  directions as shown in Figure 1.1.

Typically one is interested in the time-average intensity:

$$\Pi_x = \langle Q_x \dot{\xi} \rangle_t + \langle M_x \dot{\theta}_x \rangle_t + \langle M_{xy} \dot{\theta}_y \rangle_t \quad (1.2)$$

which Noiseux separated into a shear force component and a moment component so that:

$$\Pi_x = \Pi_{xf} + \Pi_{xm} \quad (1.3)$$

In any case, a knowledge of the internal shear and bending moments is required. However, they can be related to the normal displacement,  $\xi$ , from elasticity theory by:

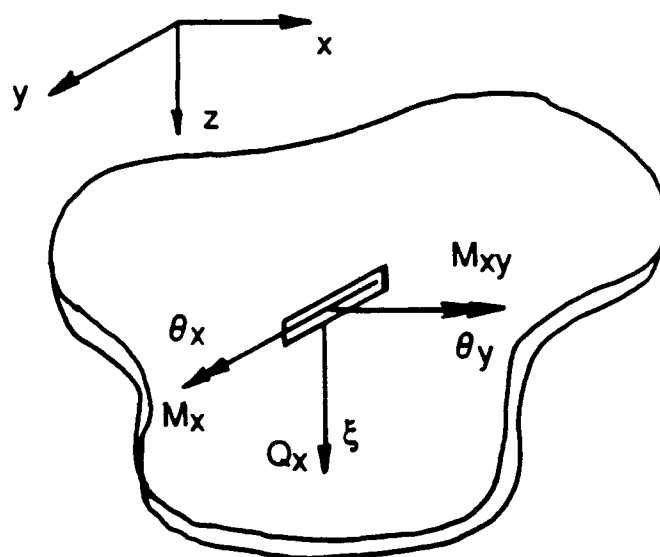


Figure 1.1 Directions of Displacements, Slopes, Forces and Moments (Source: Noiseux 1970)



$$M_x = -B \left( \frac{\partial^2 \xi}{\partial x^2} + \nu \frac{\partial^2 \xi}{\partial y^2} \right) \quad (1.4)$$

$$M_{xy} = M_{yx} = B(1-\nu) \frac{\partial^2 \xi}{\partial x \partial y} \quad (1.5)$$

$$Q_x = -B \frac{\partial}{\partial x} \left( \frac{\partial^2 \xi}{\partial x^2} + \frac{\partial^2 \xi}{\partial y^2} \right) \quad (1.6)$$

where

$$B = \frac{YI}{1 - \nu^2}$$

and Y is Young's modulus,  $\nu$  is Poisson's ratio and I is the moment of inertia per unit width in the x-direction. Consequently, knowledge of the material properties, geometry, and spatial and temporal derivatives of the displacement at a point on the plate will provide the magnitude of flexural power flow in the x direction. By switching subscripts x and y in the preceding equations the intensity in the y direction can be evaluated. The resultant intensity at the point is then the vector sum of  $\Pi_x$  and  $\Pi_y$ .

For a beam uniform in the x direction,  $\frac{\partial}{\partial y} = 0$  and the twisting moment,  $M_{xy}$  is zero so that the intensity becomes:

$$\Pi_x = \langle \dot{Q}_x \xi \rangle_t + \langle \dot{M}_x \theta_x \rangle_t \quad (1.7)$$

where now  $Q_x$  and  $M_x$  are reduced to:

$$Q_x = -B \frac{\partial^3 \xi}{\partial x^3} \quad (1.8)$$

$$M_x = -B \frac{\partial^2 \xi}{\partial x^2} \quad (1.9)$$

and  $B = YI$  since Poisson's ratio no longer plays a role.

For the plate, however, an exact measurement of the intensity at any point requires that all of the parameters in Equation 1.2 be evaluated. This is an extremely difficult procedure. Noiseux, in order to make the measurement of intensity more feasible, noted two things. First, he noted that the shear component  $\langle Q_x \dot{\xi} \rangle_t$ , and total moment component  $[\langle M_x \dot{\theta}_x \rangle_t + \langle M_{xy} \dot{\theta}_y \rangle_t]$  of intensity were equal in the freefield for simple harmonic waves. This permitted the measurement of only one of the quantities, i.e. either  $\Pi_{xf}$  or  $\Pi_{xm}$ .

Second he noted that the total moment component  $\Pi_{xm}$ , could be approximated in special cases by a modified moment component,  $\Pi'_{xm}$ , formulated as:

$$\Pi'_{xm} = \left\langle \frac{(M_x + M_y)}{(1 + \nu)} \dot{\theta}_x \right\rangle_t \approx \Pi_{xm} \quad (1.10)$$

This avoided the necessity of measuring  $M_{xy}$  which, according to Equation 1.5 requires the spatial rate of change in the x direction of the surface slope in the y direction (or vice-versa). Equivalently,  $M_{xy}$  can be written as:

$$M_{xy} = M_{yx} = \left( \frac{2B}{h} \right) \left( 1 - \nu \gamma_{xy} \right) \quad (1.11)$$

where B and  $\nu$  are as defined previously, h is the plate thickness and  $\gamma_{xy}$  is the shear strain which can be expressed as:

$$\gamma_{xy} = \frac{\partial \xi_x}{\partial y} + \frac{\partial \xi_y}{\partial x} \quad (1.12)$$

where  $\xi_x$  and  $\xi_y$  are the x and y displacements of the point. But regardless of the form of  $M_{xy}$ , it does present difficulty in its

measurement and Noiseux developed the approximation in Equation 1.10 to circumvent this for restricted cases.

For example, if the displacement field is such that:

$$\frac{\partial^2 \xi}{\partial x^2} + \frac{\partial^2 \xi}{\partial y^2} = k^2 \xi \quad (1.13)$$

where  $k^4 = \frac{\omega^2 m}{B}$  and  $m$  is the plate surface density and  $\omega$  is the circular frequency then the quantity  $(M_x + M_y)$  is easily measured.

This is because  $(M_x + M_y)$  can be written

$$(M_x + M_y) = -B \left( 1 + \nu \right) \left( \frac{\partial^2 \xi}{\partial x^2} + \frac{\partial^2 \xi}{\partial y^2} \right) \quad (1.14)$$

so that

$$(M_x + M_y) = -B(1 + \nu)k^2 \xi \quad (1.15)$$

and therefore  $\Pi'_{xm}$  would be:

$$\Pi'_{xm} = \left\langle \frac{(M_x + M_y)}{(1 + \nu)} \dot{\theta}_x \right\rangle_t = -Bk^2 \langle \xi \dot{\theta}_x \rangle_t \quad (1.16)$$

This is a quantity which can be measured easily at a single point (as will be described later).

The displacement field in Equation 1.13 occurs for plane harmonic waves in the "freefield" (i.e. in a field not subject to exponential decay of the vibration amplitude which occurs near boundaries for beams and plates).

Summarizing the restrictions on measuring  $\Pi_x$  by way of Equation 1.16:

- (1) The measurement must be made in the freefield so that  $\Pi_{xf} = \Pi_{xm}$  and so that, therefore,  $\Pi_x = \Pi_{xf} + \Pi_{xm} = 2\Pi_{xm}$ . This allows measurement of the moment component only. ( $\Pi_{xf} \neq \Pi_{xm}$  in the nearfield).
- (2) Again, the measurement in the freefield allows the use of  $\Pi'_{xm}$  instead of  $\Pi_{xm}$  since these are shown to be equivalent in this situation and  $\Pi'_{xm}$  is easily measured.

Therefore the measurement of the x-directed intensity in the freefield can be measured as:

$$\Pi_x = 2\Pi'_{xm} = -2Bk^2 \langle \dot{\xi} \theta_x \rangle_t \quad (1.17)$$

and in the y direction as:

$$\Pi_y = -2Bk^2 \langle \dot{\xi} \theta_y \rangle_t \quad (1.18)$$

and the resultant freefield flexural intensity is  $\Pi = \sqrt{\Pi_x^2 + \Pi_y^2}$ .

Noiseux measured the freefield flexural intensity by two accelerometers; one supplied the normal acceleration (and the normal displacement by way of integration) and the other supplied the rotational velocity at the point measured by positioning the accelerometer mounted on its side. The combined "biaxial accelerometer" is shown in Figure 1.2. The angular velocity is provided by:

$$\dot{\theta}_x = \frac{\int a_x dt}{d} \quad (1.19)$$

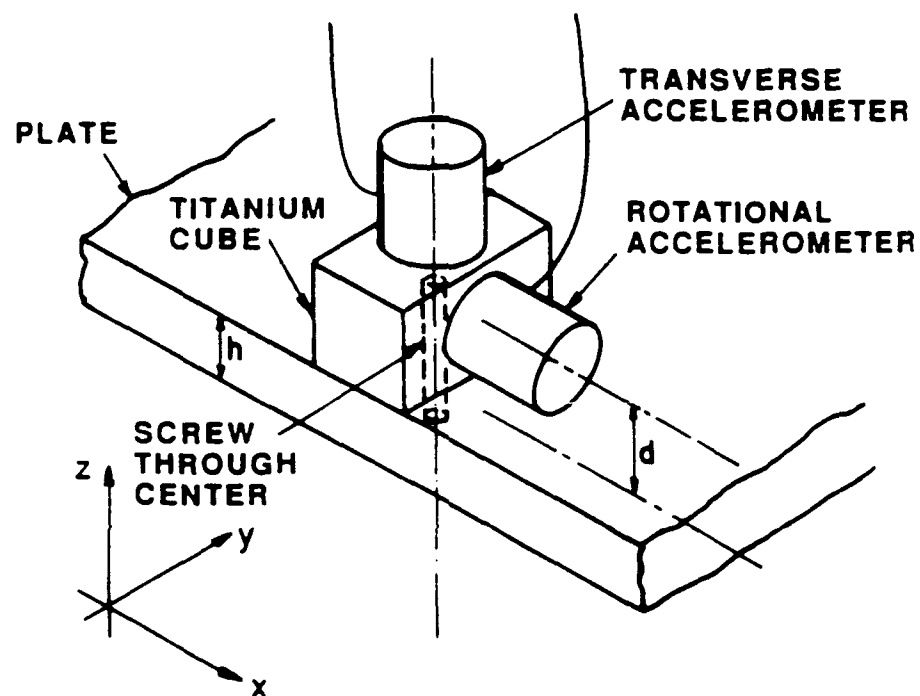


Figure 1.2 The Biaxial Accelerometer (Source: Noiseux 1970)

where  $d$  is the distance between the axis of the linear accelerometer and the neutral plane of the plate and  $a_x$  is the acceleration in the  $x$ -direction.

After illustrating the above approximations in beam and plate freefields and discussing the approximations in nearfields, Noiseux presents experimental results obtained from using the "biaxial accelerometer" for measuring the freefield flexural intensity on an aluminum plate by way of the modified moment component.

The two accelerometers comprising the "biaxial accelerometer" were housed in a cube which was internally threaded so that it could be screwed into the plate through holes made at various measurement locations. The accelerometer channels were phase matched to  $1/2^\circ$ . One third octave band noise was applied to the plate by way of a shaker while the plate was suspended vertically by thin wires.

Turning the rotational accelerometer  $90^\circ$  allowed measurement of  $\Pi'_{ym}$  after measuring  $\Pi'_{xm}$ . Results showed that the intensity vectors pointed away from the source and when the intensities were summed along a line through the plate the total power was shown to be comparable to the power input by the shaker. The intensities at the plate edges, where the freefield assumption does not hold, showed vectors with poor directionality as would be expected.

Two remaining points should be made regarding Noiseux's analysis. First, although he does not directly formulate the case of random excitation, he considers it as equivalent in the limit to many closely spaced sinusoidal components, the total intensity being the sum of the intensities for each of the component frequencies. Second, he

illustrates how for a pure standing wave the intensity is zero. These points are paraphrased below.

In the freefield of a uniform beam, for example, the displacement field is given by (suppressing  $e^{i\omega t}$ , a constant term in the equations):

$$\xi(x, \omega) = [A(\omega)e^{-ikx} + A'(\omega)e^{ikx}] \quad (1.20)$$

where the two terms are right and left travelling waves. Note that since  $k$  is real, material damping is considered negligible so that only end losses are considered. Consequently, the amplitude of the reflected wave, implies a certain reflection coefficient at the end of the

beam,  $R(\omega) = \frac{A'(\omega)}{A(\omega)}$ . The intensities for such a case are:

$$\Pi_{xf} - \Pi_{xm} = -\frac{B}{2} \omega k^3 (|A|^2 - |A'|^2) \quad (1.21)$$

So that if  $R = 1$  then  $\Pi_{xf} - \Pi_{xm} = 0$  for zero material damping. For the case of "j" simultaneous excitation frequencies:

$$\xi(x, \omega) = \sum_j [A_j e^{-ik_j x} + A'_j e^{ik_j x}] \quad (1.22)$$

$$\Pi_{xm} - \Pi_{xf} = -\frac{B}{2} \sum_j \omega_j k_j^3 [|A(\omega_j)|^2 - |A'(\omega_j)|^2] \quad (1.23)$$

After Noiseux's work on structural intensity there was apparently little done in the field until 1976 when Pavic, also addressing flexural vibrations (considering their efficiency in radiating sound), proposed various methods of measuring intensity in a plate by way of using finite difference techniques.

Like Noiseux, Pavic also used simplified bending theory to relate surface motions to internal shear forces and bending moments. He also considered a material with negligible loss factor (real Young's modulus)

and analyzed a flat uniform plate. The finite difference approximation to the various spatial derivatives and the associated transducer configurations and signal processing procedures for both nearfield and farfield measurements are the primary contribution of the work.

In an expanded form of what was previously laid out by Noiseux (in Equations 1.2 through 1.6) Pavic related the instantaneous intensity to the surface normal displacement  $\xi$  by:

$$\begin{aligned} \Pi_x(x, z, t) = B \left[ \frac{\partial}{\partial x} (\nabla^2 \xi) \frac{\partial \xi}{\partial t} - \left( \frac{\partial^2 \xi}{\partial x^2} + \nu \frac{\partial^2 \xi}{\partial z^2} \right) \frac{\partial^2 \xi}{\partial x \partial t} \right. \\ \left. - (1 - \nu) \frac{\partial^2 \xi}{\partial x \partial z} \frac{\partial^2 \xi}{\partial z \partial t} \right] \end{aligned} \quad (1.24)$$

where B is the plate bending rigidity per unit width  $B = \left[ \frac{Yh^3}{12(1 - \nu^2)} \right]$ ,

$\nu$  is Poisson's ratio and  $\nabla^2$  is the two-dimensional Laplace operator. The first term in the brackets represents the shear component, the second term the bending moment component, and the third term the twisting moment component. It is these last two terms which Noiseux set equal to his modified moment component in the flexural farfield and measured at a single point to obtain the intensity.

For the general case (nearfield or farfield) of one-dimensional flexural wave propagation (e.g: flexural vibration of a beam) Pavic approximated the axially directed time average intensity, using Equation 1.24 and finite difference approximations, as:

$$\Pi = \left\langle \frac{B}{\Delta^3} \left[ \dot{\xi}_2(4\xi_3 - \xi_4) - \dot{\xi}_1\xi_3 \right] \right\rangle_t \quad (1.25)$$



The finite difference approximations to the spatial derivatives are:

$$\begin{aligned}\xi &\approx \frac{1}{2} (\xi_2 + \xi_3) \cdot \frac{\partial \xi}{\partial x} \approx \frac{1}{\Delta} (\xi_2 - \xi_3) \\ \frac{\partial^2 \xi}{\partial x^2} &\approx \frac{1}{2\Delta^2} (\xi_1 - \xi_2 - \xi_3 + \xi_4) \\ \frac{\partial^3 \xi}{\partial x^3} &\approx \frac{1}{\Delta^3} (\xi_1 - 3\xi_2 + 3\xi_3 - \xi_4)\end{aligned}\tag{1.26}$$

Here,  $\Delta$  is the transducer spacing,  $\xi_n$  is the deflection at point  $n$ ,  $\dot{\xi}_n$  is the velocity at point  $n$  in the transducer array shown in Figure 1.3 and it is the intensity at point  $x_0$  which is being measured. Of course the spacing  $\Delta$  must be close enough for the finite difference approximations to be accurate. (This paper does not address the choice of  $\Delta$  but Redman-White (1983) makes recommendations as noted later in this review.) The analogue circuit diagram for processing the signals as required by Equation 1.25 was also detailed in his paper.

For the special case of sinusoidal one-dimensional waves where both right and left travelling propagating waves and right and left nearfields exist (for a finite undamped beam), Pavic showed that the expression for  $\xi(t)$  yields an expression for the average intensity which has a component due to the nearfield effects. However, this component was evaluated to be typically an order of magnitude smaller than the propagating wave components if the number of wavelengths along the beam is at least one. Consequently he concluded that the nearfield contribution can be neglected as a component of the measured power flow if the beam contains at least one wavelength.

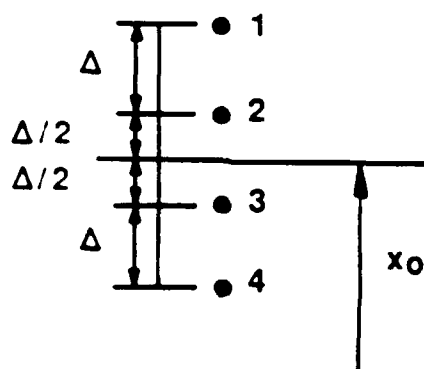


Figure 1.3 Transducer Array for General 1-D Flexural Wave Case (Source: Pavic 1976)

Neglecting the nearfield component of intensity, he showed that the expression for intensity becomes:

$$\Pi_s \approx \frac{(Bm)^{1/2}}{\pi \Delta f} \langle \dot{\xi}_1 \dot{\xi}_2 \rangle_t \quad (1.27)$$

where subscript "s" represents sinusoidal motion,  $\Delta$  is the transducer spacing,  $f$  is frequency,  $m$  is the mass per unit area,  $\dot{\xi}_1$  is the acceleration at location 1 and  $\dot{\xi}_2$  is the velocity at location 2. Therefore only two transducers on a beam are necessary for intensity measurements under this condition.

For other than single sinusoidal waves such as a composite wave consisting of  $j$  frequency components Pavic derived:

$$\Pi = B \sum_j 2\pi f_j k_j^3 (A_{+j}^2 - A_{-j}^2) = \sum_j (\Pi_j) \quad (1.28)$$

which states that the total intensity is simply the arithmetic sum of the intensities contributed by the individual frequency components. This is directly analogous to Noiseux's expression in Equation 1.23.

For narrowband noise with a center frequency of  $f_0$  he obtained:

$$\Pi = \left[ \frac{(Bm)^{1/2}}{2\pi f_0 \Delta} \right] \langle \dot{\xi}_1 [(2\pi f_0)^2 \xi_2 - \ddot{\xi}_2] \rangle_t \quad (1.29)$$

(The positive direction defined from 2 towards 1). And for broadband noise Pavic suggested a similar approach as for narrowband noise but with the use of successive bandpass filtering. Finally, for one-dimensional progressive flexural waves, Pavic showed that the total intensity in the freefield can be approximated (by way of a finite difference approximation) in terms of Fourier transforms of the velocities at two closely spaced points, separated by a distance  $\Delta$  as:

$$\Pi \approx \frac{4(Bm)^{1/2}}{T} \int_0^\infty \text{Im} \left[ \frac{\bar{\xi}_1^*(f) \bar{\xi}_2(f)}{\Delta} \right] df \quad (1.30)$$

where  $T$  = averaging interval,  $\xi_n$  is the Fourier transform of the velocity at point  $N$  and the asterisk represents a complex conjugate and  $B$ , and  $m$  are as defined previously.

Pavic's treatment of two-dimensional waves is less extensive; he proposed an array of eight transducers for the general case as shown in Figure 1.4 and developed the corresponding finite difference approximations to Equation 1.24. The analog circuit diagram to perform signal processing appropriate to Equation 1.24 is schematized. Pavic's paper does not mention experimental results for either the beam or the plate.

In 1980, Goyder and White published three consecutive papers using the concept of power flow in the theoretical evaluation of the ability of foundations and isolators to minimize the flow of power from a point source to a structure and thus minimize the power available for subsequent sound radiation. Although they did not address measurement techniques, the paper derived relationships for power flow in simple structures (rods, beams, and plates) of infinite extent which include negligible and moderate damping, as well as relationships for power flow in infinite beam-stiffened plates. Power flow expressions were also developed for single and two stage isolation systems.

Also in 1980, Verheij advocated the usefulness of frequency domain processing as opposed to time domain processing. This approach offers the advantage of channel switching techniques for the elimination of

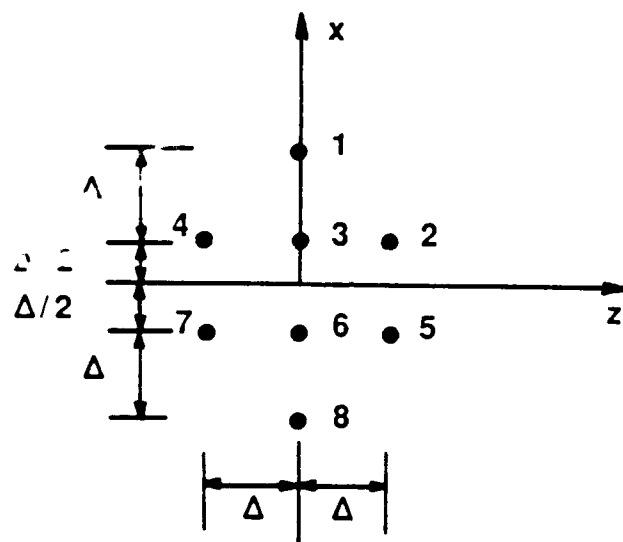


Figure 1.4 Transducer Array for General 2-D Flexural Wave Case (Source: Pavic 1976)

errors caused by phase mismatch (Chung 1978). But its chief advantage is in that an FFT analyzer can be used to process the signals.

For bending waves in a beam he shows that in the farfield, using a finite difference approximation where  $\Delta$  is the distance between two accelerometers, the total power due to flexural wave motion is:

$$\Pi = \frac{2(Bm)^{1/2}}{\Delta} \int_0^{\infty} \frac{\text{Im } G(a_2, a_1, f)}{\omega^2} df \quad (1.31)$$

where  $G(a_2, a_1, f)$  is the one-sided cross-spectral density function between the two accelerometers and Im refers to the imaginary part. This is similar to the expression in Equation 1.30 from Pavic, but is in terms of accelerations rather than velocities.

For nearfields in beams, where Pavic proposed a finite difference approach using four closely spaced accelerometers (separated by distance  $\Delta$ ), Verheij developed the associated cross-spectral equivalence for the total power based on Equation 1.25. This consists of three components of integrated cross-spectra similar to Equation 1.31.

For longitudinal and torsional waves, when using closely spaced accelerometers, the power expressions in terms of cross-spectra become as follows. For longitudinal power flow:

$$\Pi = \frac{-SY}{\Delta} \int_0^{\infty} \frac{\text{Im } G(a_1, a_2, f)}{\omega^3} df \quad (1.32)$$

and for torsional power flow:

$$\Pi = \frac{-T}{\Delta} \int_0^{\infty} \frac{\text{Im } G(a_1, a_2, f)}{\omega^3} df \quad (1.33)$$

where  $S$  is the cross-sectional area,  $Y$  the Young's modulus,  $T$  the torsional stiffness,  $a_{1,2}$  are linear or angular accelerations (as appropriate) and  $\Pi$  is the longitudinal or torsional power flow at the measurement locations as shown in Figure 1.5.

For each of the two measurement locations in Figure 1.5 there are two accelerometers and the input at the location involves a summation of the signals. Verheij recommended summing the two signals at each location in the time domain and continuing the remainder of the processing in the frequency domain. This averaging of two signals for each input then requires that the previous equations be altered; the longitudinal power equation must be divided by four and the torsional power equation must be divided by  $D^2$ .

Rasmussen in 1983 reported measurements of the intensity of flexural plane waves in a plate. He used Noiseux's method of measuring the "modified moment" which for plane waves in a freefield is equal to one half the total intensity. The appropriate expression for the total power per unit width (the intensity) is:

$$\Pi = \left\langle \frac{2\sqrt{Bm}}{\omega} \dot{\theta}_x \ddot{\xi} \right\rangle_t \quad (1.34)$$

where  $\theta_x$  is the x-directed angular velocity and  $\xi$  is the acceleration at the measuring point. This "vibration intensity transducer" was constructed as shown in Figure 1.6.

The acceleration at the measuring point was approximated as:

$$\ddot{\xi} \approx \frac{1}{2} (\ddot{\xi}_1 + \ddot{\xi}_2) \quad (1.35)$$

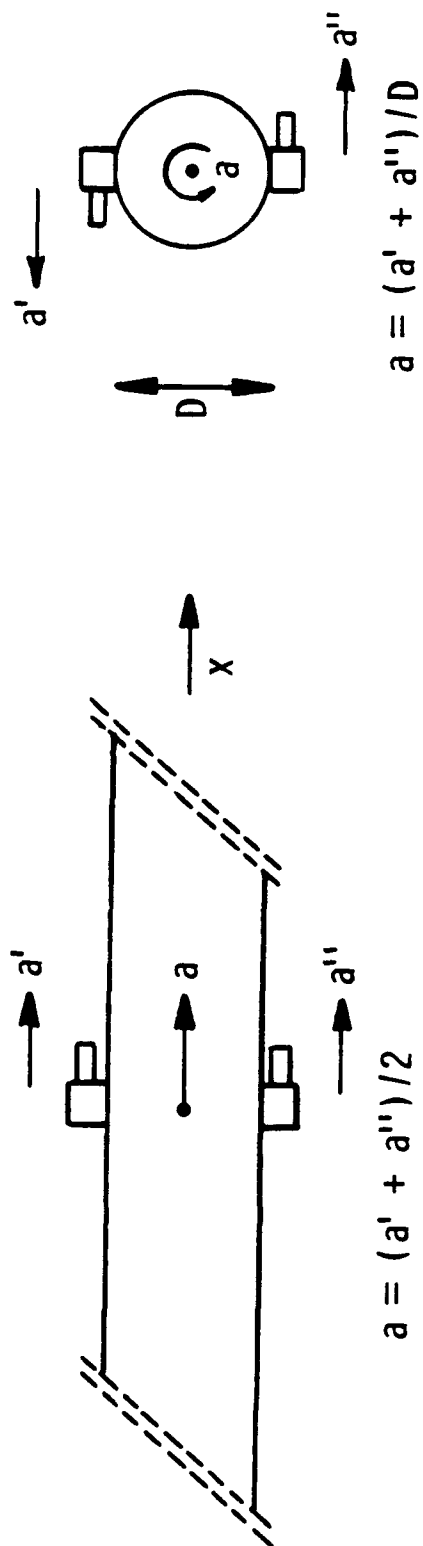


Figure 1.5 Accelerometer Configurations for Measuring Longitudinal and Angular Accelerations (Source: Verheij 1980)



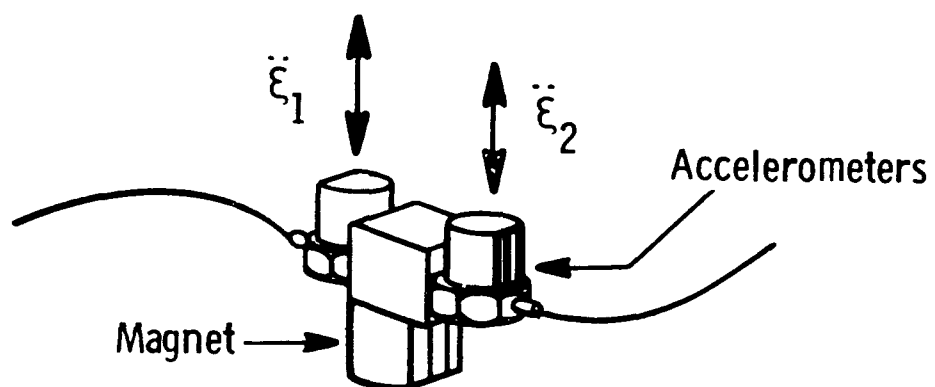


Figure 1.6 The Vibration Intensity Transducer  
(Source: Rasmussen 1983)

and the angular velocity was approximated as

$$\dot{\theta}_x \approx \left( \frac{\ddot{\xi}_2 - \ddot{\xi}_1}{\Delta r} \right) dt \quad (1.36)$$

so that the approximation for the intensity was

$$\Pi \approx \frac{2\sqrt{Bm}}{\omega} \left\langle \frac{1}{2} (\ddot{\xi}_1 + \ddot{\xi}_2) \frac{(\ddot{\xi}_1 - \ddot{\xi}_2)}{\Delta r} dt \right\rangle_t \quad (1.37)$$

where  $\Delta r$  was the distance between accelerometers.

Using this transducer, intensity measurements were made on an iron plate excited by a shaker and damped at two points by viscous dampers. At each excitation case (single frequency) there were three power levels recorded. The first was the power delivered by the vibration exciter found by simultaneously measuring the exciter force and drive point acceleration. This provided the input power  $\Pi_{\text{input}} = \left( \frac{a}{2\pi f} \cdot F \sin \phi \right)$  where  $\phi$  was the phase angle between the force and acceleration. The second power level was measured by integrating the intensity at a number of points around the source. The third power level was the power absorbed by the viscous dampers as measured by integration of intensity around these two points. The three levels agreed very closely (typically within 3% of one another) for the set of single frequencies tested. Furthermore the directionality of the intensity vectors provided verification; the vectors typically pointed away from the source and toward the two viscous dampers.

Rasmussen noted that the accuracy of the vibration intensity method, in the high frequency range, is determined primarily by the mass, the mounting resonance frequency, and by the mounting base area of

the transducer; the mass must be small to prevent mass loading, and the first resonance of the mounting base area should cover less than one quarter of the bending wavelength. The low frequency limit was due to the requirement to be in the freefield, which for long flexural wavelengths precluded any legitimate testing area on the plate.

Also in 1983, Redman-White published a paper dealing with the experimental measurement of flexural intensity. He evaluated two accelerometer techniques for measuring the power flow in the farfields of uniform beams and a four linear accelerometer array technique for measuring the power flow in the farfield of uniform plates.

First Redman-White illustrated that for one-dimensional waves, a two-degree of freedom accelerometer which is sensitive to linear acceleration as well as rotation at a point can serve to measure a signal proportional to the shear force component of power flow and hence (in the farfield) total flow. However, he cited problems with this technique and continues by discussing the two linear accelerometer finite difference technique.

The possible sources of error in this technique, according to Redman-White, include: nearfield errors, finite difference errors, bandwidth limitations, and instrumentation errors. Nearfield error, which arises due to measuring only one power component (and assuming the other component is equal) in the nearfield, can be shown to be  $\pm 20\%$  if measurements are made as close as  $\lambda/10$  from discontinuities. He suggested avoiding measurements within  $\lambda/2$  of discontinuities in the structure.

The error associated with the finite difference approximation to the spatial derivatives in the intensity equations leads to an underestimation of the actual power by the following relationship:

$$\Pi_{\text{Actual}} = \Pi_{\text{Measured}} \cdot \frac{k\Delta}{\sin(k\Delta)} \quad (1.38)$$

where  $k$  is the wavenumber and  $\Delta$  is the accelerometer separation. This implies that  $\Delta$  should be kept small but this correction can be applied to the data, especially for pure tone excitation. (Redman-White suggests keeping  $\Delta$  between  $0.15\lambda$  and  $0.20\lambda$ ).

Bandwidth limitations refer to errors in using the equations, derived for single frequency excitation, for finite bandwidth excitation such as the error due to the variation of  $k\Delta$  with frequency. Redman-White noted that a bandwidth ratio ( $\delta f/f_0$ ) of 0.3 in the autospectrum of the wave motion yields a measurement error of 3%. He notes, however, that intensity patterns can change very rapidly with frequency.

Instrumentation errors include those associated with channel phase errors (phase mismatch), with transducer placement accuracy, and errors in the quadrature function (which he uses on one of the acceleration signals to obtain the expression for the total power flow) for the one accelerometer signal. The most important error, which is the "main limitation of any intensity measurement system," is system phase tolerances. A standing wave will have an erroneous power flow component if a phase mismatch is present between the channels. This will have a value:

$$\Pi_{\text{error}} = \frac{YIk^2\omega B^2}{2\Delta} (\sin \phi [\cos(k\Delta) - \cos(2kx - k\Delta)]) \quad (1.39)$$

where  $\phi$  is the phase mismatch. In order to minimize this error he suggested using as large a value of  $\Delta$  as practical. For single frequency excitation, the error due to a large value of  $\Delta$  can be corrected according to equation 1.38 but a large value of  $\Delta$  causes the details of the intensity to be lost.

He also discussed effects of phase errors in the quadrature operation (which is required by his time-domain approach to obtaining the power flow). Most of these same errors are applicable for two-dimensional measurements. There is, however, an additional error due to the angle which the wavefront makes with the axis of the accelerometers - a trace wavenumber effect when four accelerometers are used simultaneously to determine the vector. Redman-White plotted the percent error in the power flow versus incident wave direction for various accelerometer spacings. This is applicable to the accelerometer measurement technique where simultaneous measurements of the intensity components in two orthogonal directions are obtained by placing the accelerometers symmetrically at a distance of  $\Delta/2$  from the measurement point.

Beyond the points listed above Redman-White also cautioned that the method of mounting accelerometers can adversely effect phase tolerances. Additionally he emphasized the importance of dynamic range capability in error reduction; with typical instrumentation, a standing-to-propagating wave ratio of 20:1 will probably yield meaningless power flow measurements.

Researchers at the Naval Research Laboratory, published a paper illustrating a non-contact technique for the measurement of structureborne intensity in plates (Williams, Dardy, and Fink 1985). The object of this approach was to measure structural intensity without the use of accelerometers since these transducers can lead to problems due to their transverse sensitivity, their weight and rotational inertia, and due to the necessity of phase and amplitude matching of two accelerometers for intensity purposes.

This technique, called SIMAP (structural intensity from the masurement of acoustic pressure) uses a single hydrophone/microphone to measure the pressure over a plane located as close as possible to the vibrating plate. Using principles of nearfield acoustical holography, the normal surface velocity on the plate is extracted from the pressure measurement. Normal acoustic intensity at the plate surface is available from SIMAP measurements also.

The measurement process involved scanning a hydrophone at 1089 points 1.3 cm from a submerged plate surface and recording the pressure amplitude and phase with respect to the vibration generator. Since SIMAP uses input from the "entire" surface, all of the various spatial derivatives in the flexural intensity expression are available and no structural nearfield restrictions are necessary. Spatial derivatives were determined by two techniques. The first was a point-by-point finite difference technique which (similar to Pavic's proposed finite difference approaches) used data local to the point in question to determine the spatial derivatives at the point. The second was a "full-field" technique which evaluated spatial derivatives at a point by a

Fourier transform technique which used the entire measured velocity field and was considered more accurate.

Experimental results showed several interesting points. First, the measured mechanical power radiating from the driver region was typically fifteen percent lower for the finite difference approach versus the full-field Fourier transform approach to finding spatial derivatives (the exact finite difference algorithm used was not specified). Second, the value of this power evaluated from impedance head measurements was in close agreement with that calculated by the Fourier transform approach. And third, although the power radiated into the fluid from the driver region itself was typically only 5% of the total mechanical power input, the power radiated by the entire plate into the fluid was typically 40% of the mechanical power input.

Finally, results showed that structural intensity is a more reliable approach to locating vibration sources than acoustic intensity. Acoustic intensity according to the authors, generated psuedo-sources whereas structural intensity correctly identified the real sources.

A second non-contact approach to measuring flexural structural intensity was published in 1985 by Clark and Tucker. They used real-time holographic interferometry of a vibrating plate by use of a thermoplastic hologram recorder which develops in place. The displacement of the plate could be viewed through the developed hologram of the static object by means of interference fringes. The authors pulsed the illumination in quadrature with the sinusoidal excitation and observed fringes indicative of a travelling wave. (At quadrature with the forcing function a pure standing wave would show zero displacement).

The direction of the intensity vector is perpendicular to the propagating wave fringes and the magnitude of the intensity is determined from the spatial derivatives of the propagating wave displacement field assuming sinusoidal time variation.

Also in 1985, Pavic published two consecutive papers concerning the measurement of vibration with strain gages, preferred over accelerometers for their virtually non-existent mass and thickness and their relatively low price. In the first paper (1985A), Pavic developed strain gage bridge configurations which supply the acceleration (or velocity) at a point by way of finite difference approximations to spatial derivatives. This is done for in-plane and bending vibrations in plates and beams for both nearfield and farfield conditions. (Farfield simplifications of the bridge configurations are made by virtue of the approximation that the vibration in the farfield is dominated by propagating waves which, within the small measurement area, display the properties of plane waves). The number of gages can be large (as many as ten are required for flexural nearfield in plates) but in the farfield the number required are: four for in-plane plate accelerations, two for flexural plate velocities and one for flexural beam velocities.

Pavic (1985B) discussed the error in the first and second order spatial derivatives due to the finite difference approximations. These are a function of the gage spacing, the vibration field (i.e.: frequency, for plane harmonic waves) and the wave propagation angle. Additionally he discussed the errors due to the measurement accuracy of the various strain gage bridge configurations. (The error due to the



finite gage length, for a gage spacing much smaller than the gage length, is insignificant in comparison to the error of the finite difference approximations).

Based on an expression for systematic errors in the strain gage bridge configuration (caused by finite difference and bridge accuracy errors) and based on an expression for statistically independent instrumentation noise, Pavic (1985B) developed expressions for the optimum gage spacing and minimum surface acceleration levels for certain signal-to-noise ratios. These are developed as a function of frequency and wave type (flexural or in-plane). For comparison, an analogous development was made for accelerometers where expressions for optimum mass and acceleration threshold are determined versus frequency for a desired signal-to-noise ratio. These expressions are based on the simple facts that for strain gages a small spacing yields low finite difference and gage bridge errors but a small signal (since the strain gage bridge signals result from strain gage differences). This occurs in a fixed instrumentation noise background. In an analogous fashion the systematic error in accelerometer measurements decreases as its mass but then so does its signal in a fixed noise background.

Pavic (1985B) reported experimental results using the strain gage bridge configurations for deriving acceleration at a point and compared the resulting signals to accelerometer signals. For in-plane accelerations of a plate, a bridge consisting of eight gages was used on each side of the plate to subtract flexural wave signals. The output compared favorably to accelerometer output except at higher frequencies (approaching 4 kHz). Pavic explained that some of this was due to the

transverse sensitivity of the accelerometers (arranged one on each side to subtract flexural effects) which allowed for some of the flexural signal to contaminate the longitudinal results.

For plate flexural accelerations a bridge of ten gages was employed (for nearfield conditions), and for flexural velocities a bridge consisting of two gages for farfield conditions was employed. Good matching between bridge and accelerometer waveforms for four octave bands (500 Hz, 1 kHz, 2 kHz, 4 kHz) were obtained.

Good waveform matching was also obtained with one-dimensional longitudinal and flexural waves in a pipe where combinations of six longitudinally oriented gages were used.

Pavic's development of systematic error in accelerometer measurements, in Appendix II of his second paper (1985B), is of interest. Pavic formulated the total systematic error due to accelerometer resonance and due to mass loading purely in terms of its mass as:

$$\epsilon_b = \underline{H}_{TOT}(f) - 1 \approx \frac{f^2 m^{2/3}}{C^2} - \frac{i 2\pi f m}{\underline{Z}(f)} \quad (1.40)$$

where:

$\underline{H}_{TOT}$  - the accelerometer frequency response function

$f$  - the vibration frequency (Hz)

$C$  - a constant of proportionality relating the accelerometer resonant frequency to the cube root of its mass

$i$  -  $\sqrt{-1}$

$\underline{Z}(f)$  - the complex impedance of the structure at the accelerometer location

$m$  - accelerometer mass

This error is complex since the accelerometer output contains frequency dependent deviations of both amplitude and phase from the true acceleration.

Quinlan, in 1985, wrote an experimental thesis on the use of a four-accelerometer probe in the flexural farfields of beams and plates. Quinlan measured the "modified moment" component and multiplied by two for the total intensity in the farfield (as did Noiseux). As in all the previous work (and work to this date) the analysis applied only to frequencies where the flexural wavelengths were large compared to cross-sectional dimensions so that classical plate theory is assumed (negligible rotational inertia effects and transverse shear deformations).

Quinlan introduced the concepts of potential and kinetic energy density which can be measured using the same apparatus. He also defined, analogous to acoustical power flow, both active and reactive intensity; the active intensity corresponds to the travelling wave intensity and the reactive intensity (ignored by most researchers in intensity measurements) corresponds to the standing wave intensity.

In order to increase the signal-to-noise ratio for his active intensity measurements he used constrained damping layer material on portions of the test structures to make power flow more detectable.

Using basic definitions of power flow, farfield assumptions, finite difference approximations, and cross-spectral definitions he showed that for single frequency excitation (to which he limited the experimental work) the total power can be written as:

$$\Pi_{TX} = \frac{-2\sqrt{Bm}}{\omega^2 \Delta r} \text{Im}(\underline{S}_{21}) + i \frac{\sqrt{Bm}}{\omega^2 \Delta r} (S_{11} - S_{22}) \quad (1.41)$$

where

- B = bending rigidity of the plate
- m = mass per unit area of the plate
- $\omega$  = circular frequency
- $\Delta r$  = accelerometer spacing
- i =  $\sqrt{-1}$

$S_{11}$ ,  $S_{22}$ ,  $\underline{S}_{21}$  = auto and cross-spectra of the two accelerometer signals

The real part of the expression is the active or propagating intensity and the imaginary part is the reactive or non-propagating part of the intensity.

Quinlan did not use simultaneous input of all four accelerometers but rather used each pair separately in Equation 1.41 to determine the magnitude of the intensity vector in each of the two orthogonal directions. The resultant intensity is the vector sum of these two values.

The probe, which housed the four accelerometers, was positioned automatically. Due to the use of four accelerometers, the probe did not have to be rotated to locate the intensity vector direction. Only probe translations, controlled by computer, were necessary.

Probe weight was considered in finding the frequency above which the plate response would be down by at least 3 dB due to mass loading, assuming that the test structure could be modeled as a lumped system at the point of interest and assuming a fairly weak modal response. The influence of sensor mass, under these assumptions is illustrated in

Figure 1.7 reproduced from Quinlan's thesis. Effects of mass loading as a function of spatial location on the plate were not investigated.

The accelerometers were in a single magnet which mounted to the surface. Some consideration was given to mounting as it was known that different mounting techniques could seriously affect accelerometer performance.

Quinlan reviewed errors associated with channel gain and phase mismatch. From Elko's work (Elko 1984) the normalized bias error for the active intensity defined as:

$$\xi_b(\omega) = \frac{\hat{\Pi}(\omega) - \Pi(\omega)}{\Pi(\omega)} \quad (1.42)$$

where  $\hat{\Pi}(\omega)$  is the measured intensity and  $\Pi(\omega)$  is the true intensity, is:

$$\epsilon_b(\omega) \approx |H_0(\omega)| |H_1(\omega)| [1 + \delta(\omega) \cot \phi_{12}(\omega)] - 1 \quad (1.43)$$

where  $|H(\omega)|$  are the moduli of the frequency response functions of the two channels,  $\delta(\omega)$  is the phase mismatch in the two channels, and  $\phi_{12}(\omega)$  is the actual phase difference between the two points on the structure. Consequently the magnitude of the gain in the channels plays a role in the bias error, but for the case where the actual phase difference  $\phi_{12}(\omega)$  is very small the bias error can be very large even for a small phase mismatch. For a fixed separation between the transducers, this occurs at low frequencies.

If it is assumed that the gain in each channel is unity and that channel mismatch is small, Equation 1.43 can be approximated as:

$$\epsilon_b \approx \frac{\sin[\delta(\omega)] \operatorname{Re}[S_{12}(\omega)]}{\operatorname{Im}[S_{12}(\omega)]} \quad (1.44)$$

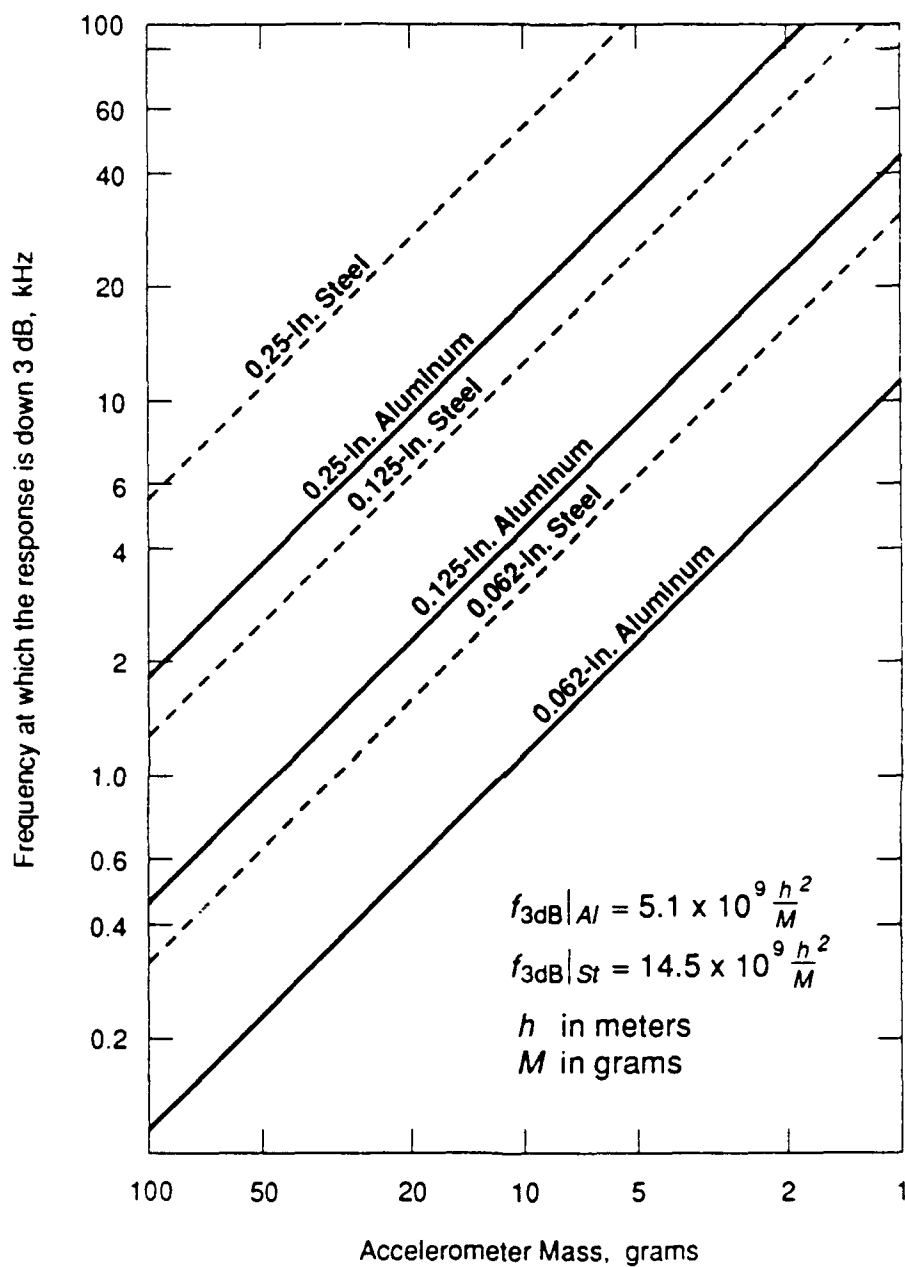


Figure 1.7 Effect of Sensor Mass on Response of Various Types of Panels (Source: Quinlan 1985)

where  $\text{Re}[S_{12}(\omega)]$  and  $\text{Im}[S_{12}(\omega)]$  correspond to the real and imaginary parts of the cross-spectrum between the measuring points. This implies, as noted by Quinlan, that measurements of active power flow in highly reactive fields (strong-standing wave fields) can yield large bias errors even for a small phase mismatch between the channels.

In order to minimize these effects Quinlan calibrated his probe to effectively remove gain and phase mismatch errors. This was done by first determining the gain values of each channel by normalizing the accelerometer sensitivities to the accelerometer sensitivity of the first channel. This provided relative gain values. Second, the phase mismatch for each pair of accelerometers versus frequency was determined. The measured cross-spectrum  $G_{01}'(\omega)$  could then be corrected to obtain the "true" cross-spectrum  $G_{01}(\omega)$  according to the following equation:

$$G_{01}(\omega) = \frac{G_{01}'(\omega)}{|H_0(\omega)| |H_1(\omega)|} e^{-i\phi(\omega)} \quad (1.45)$$

Where :

$|H_0(\omega)|$  is the gain of Channel 0

$|H_1(\omega)|$  is the gain of Channel 1

and  $\phi(\omega)$  is the phase mismatch between the two channels.

This correction was made automatically during the data acquisition process. Transfer functions and phase mismatch data were obtained by setting the intensity probe on a uniformly excited piece of steel plate and taking appropriate spectral quantities.

Qualitatively (with respect to relative vector amplitudes and directions) the active intensity results were generally very good (for example: the system was capable of detecting losses due to the presence

of a patch of damping material as well as effects of a blocking mass). A quantitative check of the data was obtained by comparing the power input by the shaker to the line integral of intensity measured around the shaker. This showed that over the complete frequency range tested (from 300 Hz to 1000 Hz) the power difference ranged from 6.8 dB to 4.4 dB. Quinlan attributed the difference at some frequencies to a problem with phase measurement between acceleration and force data in the impedance head. At high frequencies he attributed the differences possibly to accelerometer cable weight, probe weight, or probe dimensions.

In a report to NASA entitled, "A Study of Methods to Predict and Measure the Transmission of Sound Through the Walls of Lightweight Aircraft", written in 1986, researchers at Purdue University reported on the use of the two accelerometer implementation of structural intensity (Bernhard et al. 1986). Limitations were discussed including those fairly well-known such as farfield limitations, propagating wave-to-standing-wave ratio limitations, probe sensitivity, finite difference limitations, and limitations due to channel gain and phase mismatch. However they also reported that for thin plate applications, the probe inertia significantly affected the power input to the plate and when uncompensated the intensity is not accurately measured. It was also noted that this effect changes with damping.

Finite element modeling using ANSYS finite element software was also used to calculate power flow and compared favorably with power flow measurements in both one- and two-dimensional geometries.

The structural intensity portion of the report was a review of Mickol's thesis (Mickol 1986). Mickol used a boundary value analysis to



investigate the effects of accelerometer mass, rotational inertia and position on the response of a beam and on the power input of a shaker assuming a constant amplitude forcing function. As expected, for beams with low moments of inertia these effects can be significant, especially at natural frequencies.

As stated, Mickol used finite element modeling using ANSYS to predict the intensity vector field. This was done for a flat plate with a point damper and gave good qualitative results when the "moments formulation" was used. He suggested that finite element analysis would be a useful tool for predicting power flow in built-up structures.

The "intensity transducer" he used was a two-accelerometer probe with the accelerometers mounted on the sides of an acrylic spacer. The 0.5-inch probe spacing allowed for a frequency range between 120 Hz (which corresponds to  $\lambda/20$ ) and greater than 2000 Hz (for a  $\lambda/2$  spacing). The intensity results were validated by comparing the power input by the shaker (from a force gage and accelerometer) and the contour integral of the intensity around the shaker. For plate measurements, these compared fairly poorly (with a discrepancy of 20 dB).

For beam measurements, the two power calculations also agreed poorly. However, it was found that the inconsistent mechanical power flow due to the repositioning of the probe with each measurement is what caused the problem. When the probe's effect was considered the agreement was found to be much more favorable.

Mickol used the probe switching technique to null out the effects of channel mismatch. This improved the agreement of the injected and integrated powers by 7 dB in the high frequency range for tests on a

one-inch wide beam. He concludes that power comparisons can be quite favorable if several precautions are taken. These include having some form of compensation for mismatch (like switching), using proper excitation (i.e.: avoiding the shaker from inputting power in a form which cannot be detected by the transducers), and accounting for the probe's inertial properties. Also, as he later noted, the phase mismatch between the force gage and accelerometer used in power injection must be slight compared to the phase difference which actually occurs.

Pavic, in 1987, proposed a novel concept for power flow in structures called "structural surface intensity." The potential advantages of this approach to viewing structural power flow would include a capability to handle structures other than uniform beams and plates (as previous experimental structural intensity work was limited to) and a capability to cover more than simple longitudinal and flexural vibration modes. This technique would be characterized by its insensitivity to the geometry of the structure.

The components of surface intensity are defined such that:

$$\Pi_x^s = - \langle \sigma_x v_x \rangle_t - \langle \tau_{xy} v_y \rangle_t \quad (1.46)$$

and

$$\Pi_y^s = - \langle \sigma_y v_y \rangle_t - \langle \tau_{yx} v_x \rangle_t \quad (1.47)$$

where  $\Pi_x^s$  and  $\Pi_y^s$  are the x and y directed surface intensities,  $\sigma_x$  and  $\sigma_y$  are surface normal stresses  $\tau_{xy}$  and  $\tau_{yx}$  are surface shear stresses,  $v_x$  and  $v_y$  are surface velocities. (The minus sign is chosen to satisfy established conventions on stress orientation so that the positive value for an intensity component indicates that power is flowing in the

positive direction of the coordinate axis). Since stresses cannot be measured directly, Equations 1.46 and 1.47 must be cast in terms of surface strains so that:

$$\Pi_x^s = -G \left[ \frac{2}{(1-\nu)} \cdot \langle (\epsilon_x + \nu \epsilon_y) v_x \rangle_t + \langle \gamma_{xy} v_y \rangle_t \right] \quad (1.48)$$

$$\Pi_y^s = -G \left[ \frac{2}{(1-\nu)} \cdot \langle (\epsilon_y + \nu \epsilon_x) v_y \rangle_t + \langle \gamma_{xy} v_x \rangle_t \right] \quad (1.49)$$

where  $G$  is the material shear modulus and  $\nu$  is Poisson's ratio. In terms of cross-spectra, Equations 1.48 and 1.49 become:

$$I_x^s = 2 G \operatorname{Re} \int_0^\infty \left[ \frac{2}{(1-\nu)} (S \epsilon_x v_x + \nu S \epsilon_y v_x) + S \gamma_{xy} v_y \right] df \quad (1.50)$$

$$I_y^s = 2 G \operatorname{Re} \int_0^\infty \left[ \frac{2}{(1-\nu)} (S \epsilon_y v_y + \nu S \epsilon_x v_y) + S \gamma_{xy} v_x \right] df \quad (1.51)$$

Only the real part of the spectra correspond to the net energy flow. The imaginary part does not have a definite physical meaning; it does not represent the "reactive" power (the difference between the absolute instantaneous and net power flow.)

Measurement of surface intensity requires detection of surface strains and in-plane velocities. Pavic noted that the requisite strains (including the shear strain) can be obtained by a suitable strain gage rosette (three gages positioned at  $0^\circ$ - $45^\circ$ - $90^\circ$ ) and that the in-plane velocities can be obtained by a variety of transducers, although he stated that "normally available non-contact ones would be inadequate for intensity application as these are insensitive to in-plane motion."

Pavic discussed possible limitations on the measurement accuracy of this technique. These would be due to: transducer size, equipment

noise, and signal processing averaging period. In regard to transducer size he addressed the problems associated with using accelerometers to measure in-plane motion and suggested a somewhat complicated procedure using two accelerometers in order to cancel out spurious signals.

He noted that equipment noise would probably be dominated by strain gage noise since the surface strains in structureborne sound are typically low, thus providing a low S/N ratio. He suggested that the lack of correlation in strain gage and accelerometer noise should minimize the effects due to the multiplication-averaging process. Fortunately this technique, according to Pavic, is not sensitive to small phase mismatch in the instrumentation channels since the results are a consequence of independent detection of two different physical quantities (velocity and strain) which are multiplied.

Pavic then addressed the influence of finite sampling time,  $T$ , on measurement accuracy for both deterministic and random stationary processes and proposed guidelines for the duration of  $T$  in both cases.

After presenting some results of surface intensity measurement on an elevator drive mechanism, he concluded that the technique has a well founded physical meaning but requires a more efficient measuring technique than one based on strain gages so that a large number of measurements can be easily taken in order to fully exploit the information contained in each reading.

White and Wilby at Astron Research and Engineering wrote a report in 1987 to NASA regarding noise control in aircraft structures which reviews various means of flexural structural intensity measurement and outlines Astron's use of the two-accelerometer approach for broadband random noise excitation.

In their review of the various methods of measuring structural intensity they first considered the two-accelerometer approach to measuring farfield flexural intensity. They recommended as a general rule a transducer spacing of less than  $\lambda/4$  for valid finite difference approximations but greater than  $\lambda/100$  to allow for enough phase difference to be measured. They also mentioned the possibility of strain gages, referring to Pavic (1985A, 1985B) but noted that these must be placed on both sides of the measurement surface to distinguish between in-plane and bending waves. This is not always possible in aircraft structures.

Also mentioned is the possibility of nearfield acoustical holography (Williams, Dardy, and Fink 1985). As an extension of this, White and Wilby also suggested the possibility of scanning a surface with a single acceleration or velocity transducer (such as a laser vibrometer) and forming the cross-spectrum among pairs of points all across the surface. Proper data processing would provide an intensity vector map. The authors also reviewed optical holography (Clark and Tucker 1985) and finite element modeling as research tools in structural intensity.

For their experimental investigation they excited a ribbed plate with broadband random noise with the intent of measuring intensity. This was freely suspended by a bungee cord. A conservative upper limit of 2000 Hz was set on the frequency of excitation to prevent appreciable mass loading by the accelerometers. The spacing was arranged to maintain a travelling wave phase difference of at least ten degrees but not more than ninety degrees.

Unfortunately, repeated tests of attaching and remounting the accelerometers in the same location showed that there was in some cases a random phase variation of as much as  $8^\circ$  when below 2000 Hz while using beeswax mounting for ease of probe relocation.

Care was taken to allow for the analyzer sampling time to be greater than the structure reverberation so that time-delay bias errors would not adversely influence the results. Damping was applied both to reduce reverberation time as well as to test the ability of the technique to detect the resulting power flow changes. Coherence between the transducers was checked as a means of verifying the reliability of the intensity measurements.

As a result of these tests, White and Wilby concluded that it is possible to measure the structural intensity in a structure driven by broadband random noise (limited in frequency by transducer mass loading and spacing considerations), and that the accelerometer technique could give reliable intensity results as close as  $0.4\lambda$  from a structural discontinuity for flexural wave motion.

Carroll (1987) researched the accuracy of farfield flexural intensity measurements which can be obtained by using two accelerometers. He reported that phase errors of several degrees can exist at low frequencies due to cable induced strain associated with the motion of the cable. To avoid this problem he used annular shear accelerometers which demonstrated a phase accuracy of approximately  $0.1^\circ$ . This amount of phase accuracy provided flexural intensity measurements by the cross-spectral technique which agreed with classical measurement methods to within 1 dB for loss factors greater than 0.006.

The classical methods Carroll referred to include a standing wave technique and an energetics technique. These are non-phase sensitive intensity measurement methods which are applicable to power flow in reverberant beams and rods. These two techniques, which form the basis of verification for the laser Doppler cross-spectral techniques studied in this thesis, are outlined in further detail in the chapters on flexural and longitudinal intensity measurements.

A sampling of more recent work in structural intensity measurements consists of three papers published in NOISE-CON 88 proceedings. Downing and Shepherd from NASA Langley Research Center submitted a paper detailing their use of a five-accelerometer probe to measure power flow in a beam. The intent was to illustrate an accelerometer array which is capable of accurately measuring the structural nearfield power flow in the beam. Central finite differencing of the five equally spaced points occupied by the accelerometers allowed all of the spatial derivatives in the flexural power flow expression to be estimated so that no farfield approximations need to be made. The power flow at the central position was then measured.

Determination of the net power flow was made by measuring the various signal cross-spectra and using the following formulation (according to the paper):

$$\Pi_x = \frac{B}{2\Delta^3\omega^3} (\text{Im}[G_{13} - 2G_{23} + 2G_{43} - G_{53}] + \text{Im}[G_{22} - 2G_{32} + G_{42} - G_{24} + 2G_{34} - G_{44}]) \quad (1.52)$$

where

- $\Pi_x$  - Axial power flow due to bending
- B - Bending stiffness
- $\Delta$  - Accelerometer spacing
- $\omega$  - Circular frequency

(Although  $\text{Im}(G_{22})$  and  $\text{Im}(G_{44})$  are zero since autospectra are real quantities).

Downing and Shepherd tested the apparatus on a "semi-infinite" beam (one end buried in the sand) with a blocking mass clamped to the beam to present a structural nearfield. Broadband noise was applied to one beam end (ranging from 200 Hz to 1000 Hz). Results showed that the five-accelerometer probe was in close agreement with a two-accelerometer probe for the farfield. Close to the blocking mass (2 cm away) however, the two-accelerometer power measurements were lower by 6 dB (as would be expected).

The authors concluded that this five-accelerometer probe yields accurate results of power flow in the nearfield but that this method is much more susceptible to phase errors than the two-accelerometer method. A finite difference error analysis for this array is not given.

Kendig, from Westinghouse Research and Development Center, verified the ability of intensity techniques to detect sources of compressional and in-plane shear waves in bars and plates (Kendig 1988). He first tested what is effectively the two-accelerometer technique for compressional power flow in a rod. Two pairs of accelerometers were mounted tangentially on the rod. The net signal from each pair of diametrically opposed accelerometers (which canceled out opposite components of longitudinal motion due to possible bending in the rod)



was used for input to the two-accelerometer method. The intensity for the compressional wave is measured as:

$$\Pi = \frac{-SY}{2\pi\Delta} \int_{-\infty}^{+\infty} \text{Im}\{G(\bar{u}_1, \bar{u}_2, \omega)\} \frac{d\omega}{\omega^3} \quad (1.53)$$

(Although  $G(\ )$  is typically used to denote the one-sided spectrum which does not exist from  $-\infty$  to 0). In the above equation  $\text{Im}\{G(\bar{u}_1, \bar{u}_2, \omega)\}$  is the imaginary part of the cross-spectrum of  $\bar{u}_1$  and  $\bar{u}_2$ . Also,  $\bar{u}_1$  and  $\bar{u}_2$  are signal pairs of closely spaced, tangentially oriented accelerometers. Additionally  $S$ ,  $Y$ ,  $\Delta$  are the rod cross-sectional area, Young's modulus and accelerometer pair spacing, respectively.

Similarly, Kendig noted that for in-plane intensity in plates the appropriate cross-spectral formulation can be derived from the following intensity expression:

$$\Pi_x = \left\langle \frac{Yh}{(1-\nu^2)} \left[ \frac{\partial \xi_y}{\partial y} + \nu \frac{\partial \xi_x}{\partial x} \right] \dot{\xi}_y + Gh \left[ \frac{\partial \xi_y}{\partial x} + \frac{\partial \xi_x}{\partial y} \right] \dot{\xi}_x \right\rangle_t \quad (1.54)$$

where  $\Pi_x$  is the intensity in the  $x$  direction,  $Y$  and  $G$  are the Young's modulus and shear modulus respectively,  $h$  is the plate thickness,  $\xi_x$  and  $\xi_y$  are the  $x$  and  $y$  displacements and the overdot represents the time derivative. The intensity in the  $y$  direction is formed in an analogous manner. The first component is due to normal stress and the second is due to shear stress.

Laboratory experiments were conducted for both a rod and a plate. In both cases tangentially oriented accelerometers were used and were paired up in the through-thickness direction to remove any signals due to bending. The rod was excited from both ends; one signal was a pure tone, the other was broadband noise. Results showed that the technique

correctly identified the opposing direction of power flow for the pure tone versus the noise.

The plate test was conducted in a similar fashion with two pairs of accelerometers closely spaced relative to a wavelength and oriented to respond primarily to axial motions. Results showed that the power flow directions were also correct when shakers were used on opposite edges with differing excitation frequency content. No quantitative checks on power flow results appear to have been conducted.

Using an application of structural intensity measurements to cylinders, Meyer presented a method to measure flexural waves in slender cylinders (Meyer 1988). (This approach as with the flat plate approaches, neglects rotational inertia and shear deformation). The expressions for the axial ( $x$  directed) and tangential ( $\theta$  directed) flexural intensities (analogous to the flat plate expressions) are:

$$- \Pi_x = \left\langle B \frac{\partial}{\partial x} (\nabla^2 w) \frac{\partial w}{\partial t} \right\rangle_{t \text{ shear}} - \left\langle B \frac{\partial^2 w}{\partial x^2} + \frac{\nu}{r^2} \frac{\partial^2 w}{\partial \theta^2} \frac{\partial^2 w}{\partial x \partial t} \right\rangle_{t \text{ bending}} - \left\langle B(1 - \nu) \frac{1}{r^2} \frac{\partial^2 w}{\partial x \partial \theta} \frac{\partial^2 w}{\partial \theta \partial t} \right\rangle_{t \text{ torsion}} \quad (1.55)$$

$$- \Pi_\theta = \left\langle B \frac{1}{r} \frac{\partial}{\partial \theta} (\nabla^2 w) \frac{\partial w}{\partial t} \right\rangle_{t \text{ shear}} - \left\langle B \left[ \frac{1}{r^2} \frac{\partial^2 w}{\partial \theta^2} + \nu \frac{\partial^2 w}{\partial x^2} \frac{1}{r} \right] \frac{\partial^2 w}{\partial \theta \partial t} \right\rangle_{t \text{ bending}} - \left\langle B(1 - \nu) \frac{1}{r} \frac{\partial^2 w}{\partial \theta \partial x} \frac{\partial^2 w}{\partial x \partial t} \right\rangle_{t \text{ torsion}} \quad (1.56)$$

where

$B$  - bending rigidity

$r$  - radius of cylinder

$x$  - axial direction

$\theta$  - tangential direction

$w$  - radial displacement

$t$  - time

$\nu$  - Poisson's ratio

$\Pi_x, \Pi_\theta$  - intensity

$\langle \rangle_t$  - time average of a quantity

shear, bending, torsion - the various components of intensity.

Using five accelerometers arranged in a "cross" shape with axes in the axial and tangential directions and using finite difference approximations with a displacement field for an infinite cylinder excited by a harmonic force, the following spectral representations for the axial and tangential intensities are derived:

$$\Pi_x = \frac{-B}{2\Delta x \omega^3} \left[ 2k_x^2 + \frac{2k_\theta^2}{r^2} \right] \left[ \text{Im}(S_{21}) - \text{Im}(S_{23}) \right] \quad (1.57)$$

and

$$\begin{aligned} \Pi_\theta = \frac{-B}{r\omega^3\Delta\theta} \left[ \frac{2k_\theta^2}{r^2} + (1 + \nu)k_x^2 \right] \left[ \text{Im}S_{24} \right] \\ \frac{-B}{r\omega^3(\Delta x)} (1 - \nu)k_\theta[S_{22} + S_{11} - 2\text{Re}(S_{21})] \end{aligned} \quad (1.58)$$

where  $k_x$  and  $k_\theta$  are the axial and tangential wavenumbers, and  $S$  with subscripts represent the spectra of acceleration signals as numbered in Figure 1.8 ( $k_x$  and  $k_\theta$  are also obtained by formulations using the appropriate spectra). Meyer also developed the relationship between Pavic's structural surface intensity and intensity of bending waves in cylinders. Using structural surface intensity transducers and the five accelerometer array on a cylinder, tests showed good agreement of the derived relationship in the axial direction.

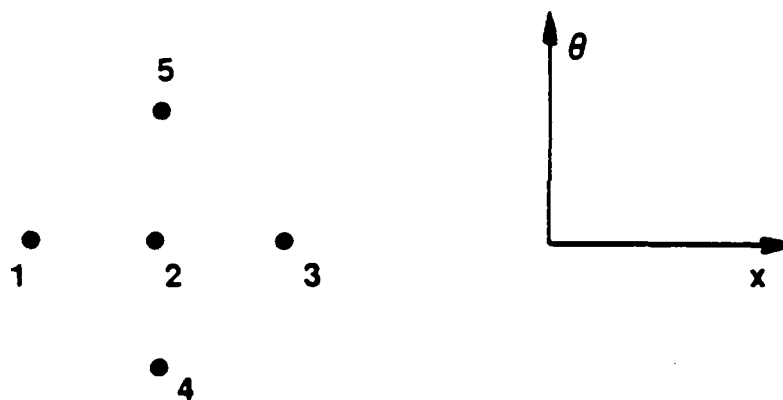


Figure 1.8 Accelerometer Array Used for Flexural Waves  
in Slender Cylinders (Source: Meyer 1988)

## Chapter II

### LASER VIBROMETRY

#### BACKGROUND AND USES TO DATE

The laser vibrometer is potentially an ideal instrument for measuring structural intensity. It focusses laser light to a small spot on the vibrating object and uses the backscattered light to provide the surface velocity in "real time." Consequently the surface is not mass-loaded or locally stiffened as it can be when a conventional transducer is attached.

The advantages of using coherent light to detect surface velocity were recognized early. It was not long after the invention of the laser in the early nineteen sixties that experiments with the first laser vibrometers were conducted (see Massey (1967) for example). This is not surprising since the principles of coherent detection were already well known. What was needed was a source of coherent light to make the technique feasible.

A review of laser vibrometer literature since that time reveals much activity and many applications. Although the laser vibrometer is still not widely used, there have been efforts devoted to making it an affordable, portable device which is not difficult to use (Massey and Carter 1967; Buchave 1975; Halliwell 1979; Pickering, Halliwell, and Wilmshurst 1986). Also on the practical side, papers have been published on conversion of a laser velocimeter to a laser vibrometer (Meynart 1984) and applications of laser vibrometry in engine diagnosis

and in process control (Halliwell, Pullen, and Baker 1983; Halliwell and Eastwood 1984; Eastwood and Halliwell 1985). McDevitt and Stuart (1989) have recently illustrated how the technique can be used for characterization of the dynamic properties of elastomeric materials.

The sensitivity of the laser vibrometer (or heterodyne speckle interferometer as it can also be called) is addressed in a number of references. When the signal is only obscured by shot noise, micro-vibrations down to one nanometer have been reported for frequencies in the MHz range (Willemin and Dandliker 1983). Phase accuracy of  $4^\circ$  has been reported (Dandliker and Willemin 1981), although the authors note that this was essentially limited by the phase accuracy of the network analyzer used. More serious phase accuracy was not pursued. Angstrom order displacement measurements transverse to the laser beam have also been reported (Joyeux and Lowenthal 1971).

Laser vibrometry techniques have been used for detection of gated harmonic surface waves on a steel block (Su 1980; Bouchard and Bogy 1985) where amplitudes down to 5 angstroms have been detected. The scanning capability of a laser vibrometer has been used to its full advantage in a computer controlled laser scanning system which can reconstruct various participating mode shapes from a surface vibrating in a stationary random fashion (Stoffregen 1984).

Applications where the non-contacting nature of the vibrometer is useful have been reported such as in measuring tympanic membrane and auditory organ vibrations (Buunen and Vlaming 1981; Willemin, Khanna, and Dandliker 1987) and rotating flexible disk vibrations (Wlezien, Miu, and Kibens 1984).

Of course laser vibrometry is also amenable to fiber optic applications where a normally optically inaccessible region can be scanned to characterize the vibration response of an object. This is a growing area in vibrometry with an increasing number of techniques being reported (Cockson and Bandyopadhyay 1978; Thierry 1985; Lewin, Kersey, and Jackson 1985; Waters and Mottier 1986).

#### POTENTIAL OF LASER VIBROMETRY AS A STRUCTURAL INTENSITY TECHNIQUE

Practically all of the problems cited in Chapter I concerning errors and limitations of current structural intensity measurement techniques could be circumvented by using a two-channel laser vibrometer probe for these measurements. The vibrometer laser beam has none of the disadvantages of accelerometers. There are no linear or rotational inertia effects and no local stiffening effects to alter the dynamic behavior of the object. There are no mounting effects to distort phase information from the surface. Additionally the vibrometer allows a smaller point from which data are taken on the surface so that the separation distance between two points can be smaller if necessary than is possible using accelerometers.

Probably the biggest advantage to using a two-point laser technique for intensity measurements is the ease with which the intensity can be mapped. The strength of intensity methods lies in their ability to provide a mapping of power flow. Bonding accelerometers or strain gages to the surface and doing this repeatedly to obtain this energy flow map is inconsistent with the power of the

intensity technique. Laser scanning would be a far simpler approach yielding a much quicker mapping of power flow.

The two-channel laser Doppler approach appears to be superior to other possible optical techniques for structural intensity measurements. As compared to real time holography, it is much more sensitive, it does not require a laboratory setup, and combined with the use of a spectrum analyzer the two-channel vibrometer is a real time intensity technique whereas holography is not.

Similarly the two-channel vibrometer would be a much more sensitive technique than a two-probe Fotonic sensor (a white light fiber optic displacement meter) would be. The vibrometer technique also allows for large standoff distances from the vibrating object whereas a Fotonic sensor probe would have to be typically a millimeter from the object surface. This is a disadvantage in studies where there is fluid flow around the object. Additionally, a Fotonic sensor cannot obtain a good signal from a curved surface whereas the vibrometer can.

There are a few disadvantages associated with a two-point laser approach to structural intensity measurement. The most obvious is the expense. Two accelerometers can cost almost two orders of magnitude less than the laser system proposed for these measurements. However, as lasers and laser interferometers continue to gain popularity in industry, the cost of such a system should decrease markedly.

Secondly, any optical interferometer requires vibration isolation since it is not the absolute vibration of the object but rather the object vibration relative to the optics which is measured. This can be



a disadvantage especially in situations where the ambient vibration level is fairly high requiring a vibration isolation system.

Fortunately, however, the vibrometer optics can be designed for long offsets between the optics and the vibrating object. Researchers at ASTRON Research and Engineering for example have successfully used a laser vibrometer at a distance of sixty meters from the object when special collection optics were used. This permits the use of the instrumentation far from the vibration source and greatly facilitates vibration isolation of the optics.

Another disadvantage occurs in studies where object motions transverse to the laser beam are greater than the illuminated spot size. In this case a loss of signal can occur for brief periods which would cause a distortion of the velocity time history depending on the dynamics of the processor. Fortunately, this will not be a problem for the study of flexural waves and it may not be a problem for the study of longitudinal waves as long as the vibration amplitudes are not excessive.

Finally, the laser vibrometer, since it is sensitive to velocity rather than acceleration is not as sensitive as an accelerometer. The background noise in the vibrometer prevents simply using the derivative of the velocity signal for equivalent sensitivity. This situation can make broadband excitation studies difficult if the excitation source provides a flat object acceleration autospectrum since the corresponding velocity autospectrum then falls off as  $1/\omega^2$ . However for single frequency and narrowband analyses (which encompass nearly all of the structural intensity studies to date) this broadband signal fall-off is not a problem.

## THE TWO-CHANNEL LASER DOPPLER VIBROMETER SYSTEM

The two-channel vibrometer (TCV) focuses laser light onto two spots on a vibrating surface and by using the Doppler shift in the backscattered light, yields the real-time surface velocities at these points. Scanning capability allows information to be obtained at points over the whole surface. The unit has the following capabilities: it provides relatively high sensitivity (which is not limited to the laser wavelength), it provides the relative amplitude and phase over the surface even for random motions; it has a high frequency response (theoretically up to the MHz range); it can provide any one of three components of motion for the two points; it is readily adaptable to laser Doppler velocimetry if necessary; it is readily adaptable to fibre optic applications; it can be used on any diffuse surface; it has enough optical power for submerged structure applications; and if desired, it can be converted to a laser speckle interferometer for normal and transverse displacements.

The only limitation of the TCV system as opposed to full-field optical techniques is that it does require scanning and hence cannot provide vibration information simultaneously over the entire surface. However, this is only a limitation in the case of random vibration which is non-stationary. If the random vibration is stationary, scanning the surface provides statistical information which is just as useful and "accurate" as full-field information. Fortunately, most random vibrations of interest are stationary and hence scanning is not a serious limitation.

## SETUP OF THE TCV SYSTEM

Laser Doppler vibrometry is effectively the same as "heterodyne speckle interferometry," except the latter measures displacements and the former, velocities. In an article by Dandliker and Willemin (1981), they illustrate the two different optical setups in heterodyne speckle interferometry which can be used to detect either normal or transverse displacements. These are much the same as the different optical arrangements in laser Doppler vibrometry. There is an optical arrangement for surface-normal vibrations and a second optical arrangement for transverse vibrations. These setups will be described below. (Theory is explained in the next section.)

The setup of a single laser vibrometer unit for detecting surface normal vibrations is shown in Figure 2.1. The laser light is first collimated to allow for an optimum optical signal. The single beam is then split by a beamsplitter which is adjusted to split the beams into a ratio of approximately 99.5 to 0.5. The more powerful beam, the "object" beam or "power" beam, continues through the remaining optics to the beam polarizer which allows for the rotation of the axis of polarization for this beam. It then is focused onto the object by a lens.

The weaker beam, the "reference" beam, is frequency shifted by 40 MHz by a Bragg Cell and then is returned along the optical axis by a "vibrometer adaptor." This reference beam, then, never leaves the optical system.

The object beam, upon backscattering from the target surface, is collected by the lens (dashed line in Figure 2.1) and also is directed

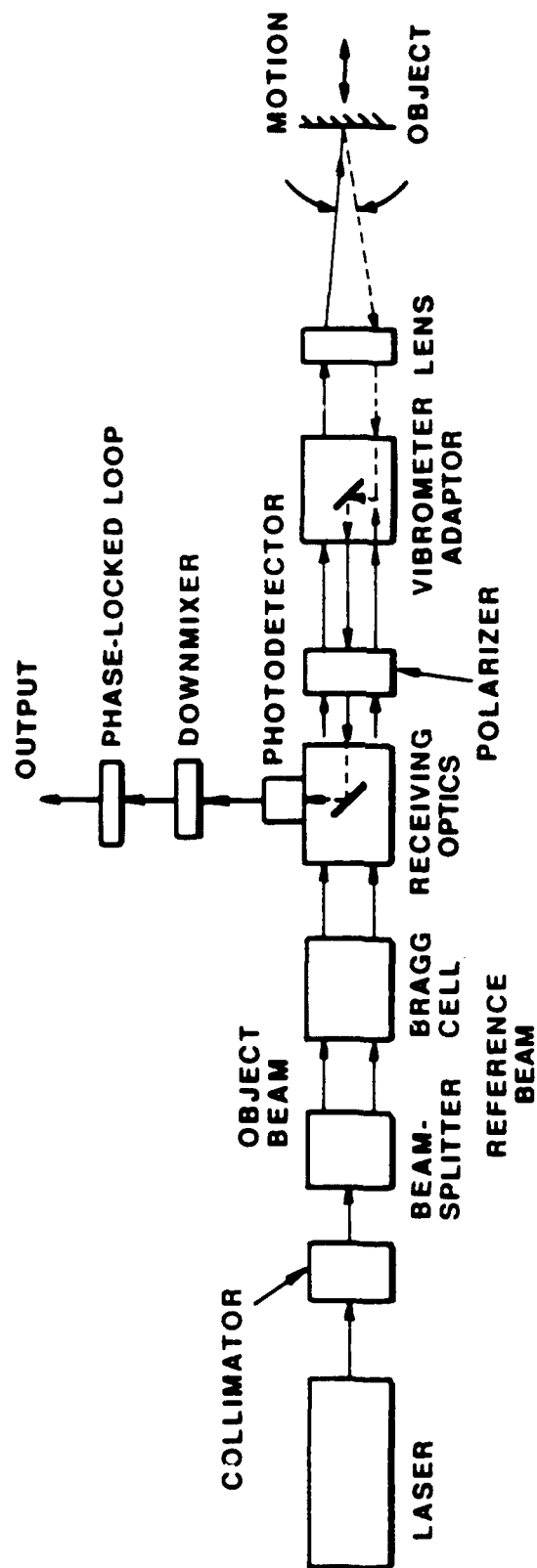


Figure 2.1 Schematic of a Single Vibrometer Unit Arranged for Surface-Normal Vibration Measurements

along the optical axis by the adaptor. The combined object and reference beams are then focused onto the face of a photodetector where they interfere. The electrical output of the photodetector, an FM signal with a carrier of 40 MHz, is then "downmixed" (heterodyne converted) to a more convenient carrier frequency of 50 kHz. This FM signal with a 50 kHz carrier is then demodulated by a phase-locked loop (PLL) to provide a voltage which is proportional to the target normal velocity.

Of course, since the actual system is a "dual" system there are two parallel units of this type which are activated by a single 4-watt argon-ion laser. At the ends of the vibrometers are the scanning mirrors. A schematic appears in Figure 2.2.

The optical components in the system are manufactured commercially. The mixers are commercially manufactured as well. The phase-locked loop processors were designed and assembled at ARL Penn State.

Scanning mirrors for the system are finely adjustable manual control mirrors. Computer controlled motors for beam scanning were not considered justifiable because of the high cost and the fact that the fine positioning offered by computer control would have to be calibrated when shooting through imperfect plexiglass windows and water.

The setup of the laser vibrometer for detecting transverse motions is simpler than that for surface-normal motions and is optically identical to that used for velocimetry. It is illustrated for a single unit in Figure 2.3. Notice that this arrangement uses both beams as

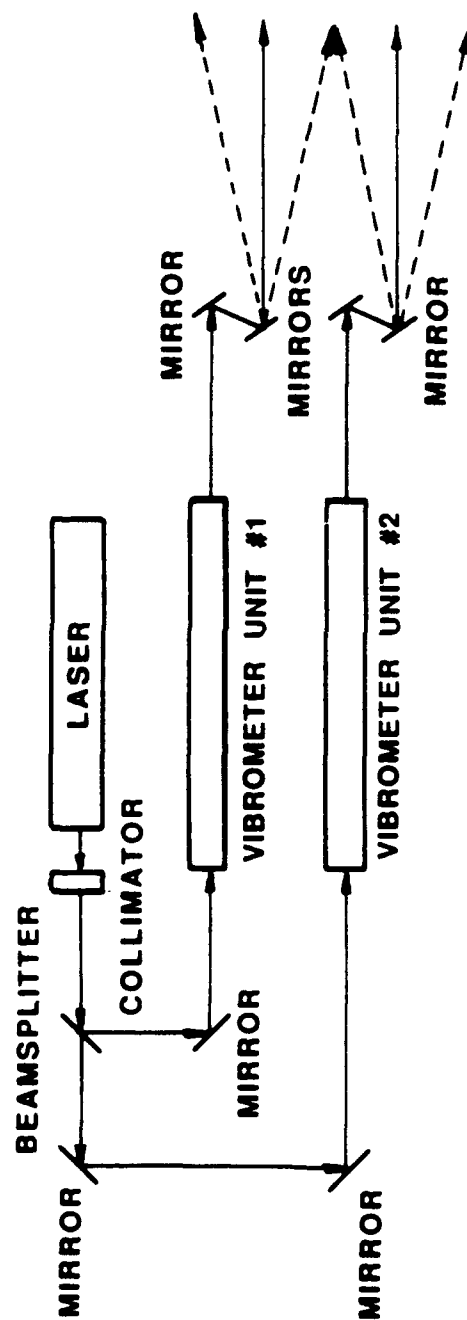


Figure 2.2 Layout of the Scanning Dual Laser Vibrometer System

"object" beams rather than using one object beam and one reference beam. Consequently, it does not require the vibrometer adaptor as does the setup for surface-normal motions.

In the transverse motion arrangement both beams have the same power and so the beamsplitter is adjusted to provide a splitting ratio of 50-50. The polarization rotator, used in the surface-normal optical setup, is not necessary in this setup. The two beams are focused onto the target by the lens. The backscattered light of the combined beams is collected by the same lens and focused onto the face of the photodetector. As in the previous setup, the output from the photodetector is an FM signal with a 40MHz carrier. This is downmixed to a carrier of 50 kHz and demodulated by a PLL to provide a voltage output which is proportional to the target transverse velocity.

The transverse velocity measured by this arrangement is the velocity which is in the same plane as the two converging beams. The two beams can be rotated in order to provide the transverse velocity at a different orientation. Rotational increments of  $45^\circ$  are available. Typically, only the transverse velocities in the horizontal and vertical directions are of interest.

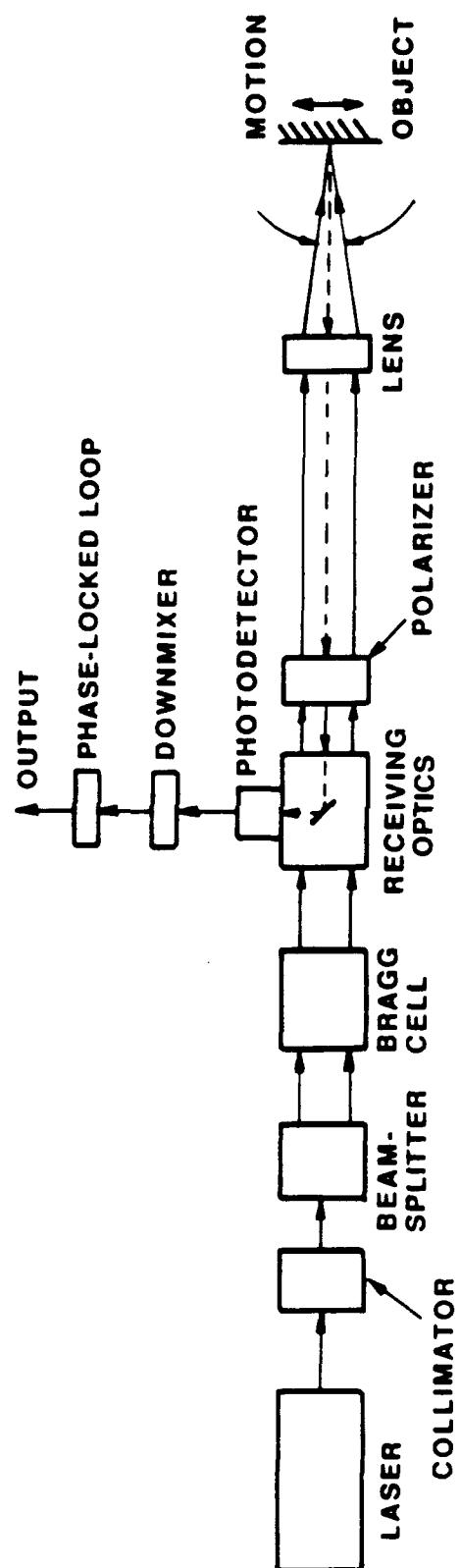


Figure 2.3 Schematic of a Single Vibrometer Unit Arranged for In-Plane Vibration Measurements



## FUNDAMENTALS OF OPERATION

The two optical arrangements referred to above, the surface-normal vibration detection scheme and the in-plane vibration scheme, are referred to as the "reference beam technique" and the "differential Doppler technique," respectively, and in fact are both used in laser Doppler velocimetry. Drain (1980) provides very illuminating explanations of both of these techniques. These explanations are primarily oriented towards velocimetry (fluid velocities) rather than vibrometry (solid vibrations), but the theory is fundamentally the same.

There are two major differences between using these optical techniques for vibrometry rather than velocimetry. First, in vibrometry the laser is focused onto a diffuse solid surface resulting in a large number of "scatterers" whereas in velocimetry there are ordinarily only a few scatterers passing through the focal region or "probe volume" at any time. More specifically, the optical signal backscattered by a diffuse solid surface consists of "laser speckle." This is a randomly spotted pattern caused by the random constructive and destructive interference through space of the backscattered coherent light and is due to the surface roughness. These speckles represent the multiple "scatterers" seen by the photodetector. Ennos (1978) provides useful details on laser speckle and its applications to interferometry.

The second major difference in applying these optical techniques to vibrometry rather than velocimetry is that the optical signal in vibrometry is a continuous signal whereas in velocimetry it consists of individual pedestaled pulses as the light scatterers pass through the probe volume.

The continuous optical signal in vibrometry is best processed by a phase-locked loop (although gated rate meters, spectrum analyzers, and counters have been used) whereas the discontinuous signals in velocimetry are usually processed by counter processors.

Although there are many good references which explain the theory behind the reference beam and differential Doppler techniques (such as Massey 1967; Buchave 1975; Drain 1980) an explanation of the first principles of the two techniques is presented here briefly for the sake of completeness.

#### **The Reference Beam Technique**

This technique, which provides the velocity normal to the surface, is fundamentally a Michelson interferometer setup. This is what will be used to explain the basic principles.

Figure 2.4 shows a Michelson interferometer arrangement. Coherent light emitted from the laser is split by the beamsplitter to form two beam paths. The "reference beam" path travels from the beamsplitter to the mirror, back through the beamsplitter and to the photodetector. The "object beam" path travels from the beamsplitter to the object back to the beamsplitter (by backscatter) and to the photodetector. The two beams interfere at the surface of the photodetector. Depending on their phase difference at the photodetector, they will present a dark or bright image to the detector, thus causing a low or high electrical output from the detector.

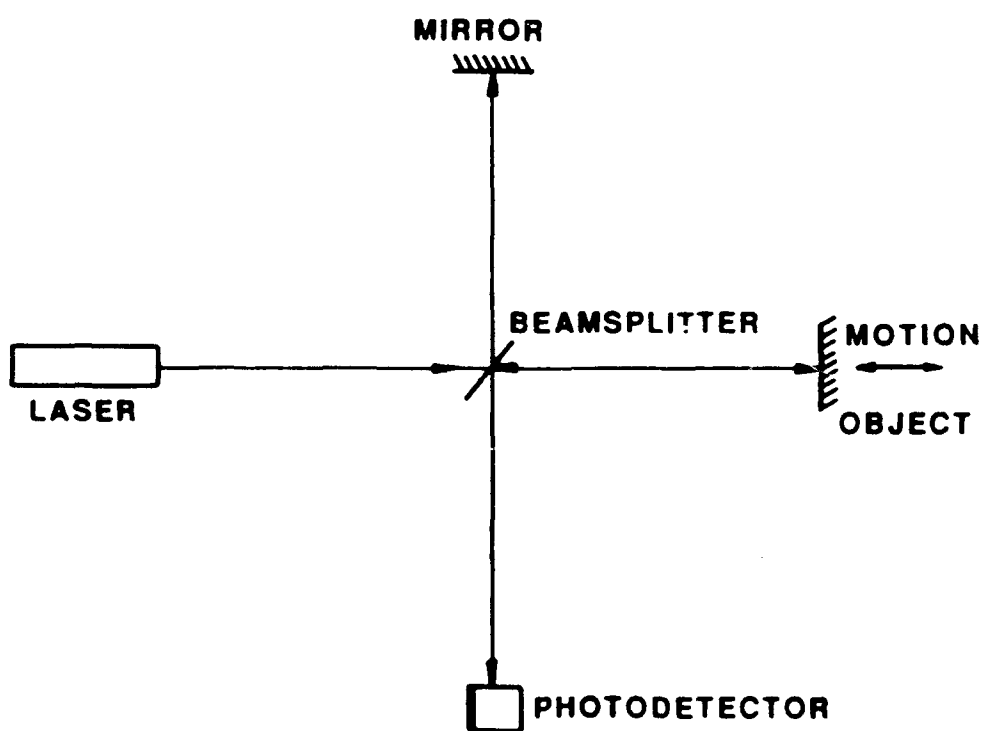


Figure 2.4 Michelson Interferometer

Assuming an initial phase difference of  $\psi$  between the beams when the object is in position D, a displacement of the object of  $\delta$  causes a relative phase difference of:

$$\phi = \frac{2\delta}{\lambda} \pm \psi \quad (2.1)$$

at the face of the photodetector. Taking the time derivative leads to:

$$\frac{d\phi}{dt} = \frac{2}{\lambda} \frac{d\delta}{dt}$$

or

$$f = \frac{2}{\lambda} v \quad (2.2)$$

where  $f$  is the frequency at which the interference fringes are sweeping across the face of the detector and  $v$  is the surface velocity. In this way the frequency of photocurrent issuing from the photodetector is directly proportional to the surface velocity. Actually, it is proportional to surface speed rather than velocity since motion of the object either toward or away from the optics will cause the same frequency; no directionality yet exists in the signal.

In order to impose directionality one of the beams (the reference beam, for example) can be shifted in frequency by some value  $f_s$ . The resulting frequency observed by the photodetector is then:

$$f = f_s \pm \frac{2v}{\lambda} \quad (2.3)$$

At the expense of introducing a carrier frequency of  $f_s$ , directionality is now provided; velocity of the object toward the optics increases the frequency above  $f_s$  while a velocity away from the optics decreases the

frequency below  $f_s$ . The signal from the photodetector is then a frequency modulated signal with a carrier of  $f_s$ . The frequency deviations from the carrier are directly proportional to the surface velocity.

There are some relatively unavoidable phenomena which degrade this signal by way of amplitude modulations (which can be a problem in severe cases) and frequency noise (which limits the resolution of the device).

Amplitude modulations are caused primarily by the laser speckle emanating from a diffuse object. If they are severe they can cause intermittent loss of signal by the processor. Frequency noise is attributable to a number of things: laser speckle, photodetector shot noise, and vibration of the optics to name a few. Noise in laser vibrometry is considered in detail in a later section.

Principles illustrated by way of the Michelson interferometer are easily applied to the actual setup of one vibrometer unit as illustrated in Figure 2.1 except for the following details. These include focusing by the lens, collimation, and polarization rotation as explained below.

Focusing of the object beam allows the vibrometer to be sensitive only within the small depth of field located at the focal distance from the lens. This has an advantage; one can concentrate on what is happening at the focal "plane" without interference from any other surfaces (such as windows) along the optical path. Focusing also has several disadvantages; the vibration amplitude is limited to the depth of field, re-focusing is required for surface scanning, and collimation is required. Fortunately, limiting the vibration amplitude to the depth

of field is rarely a problem; focusing is primarily an inconvenience, and collimation is a simple one-time procedure.

Collimation ensures that the reference beam is planar and that the object beam, as it converges to its waist at the lens' focal distance, is also planar. The interference of two planar co-linear beams yields the best signal at the detector. (Co-linearity of the reference and object beams is assisted by the fact that the lens collects the backscattered "spherical" wave and effectively re-collimates it.) The adaptor then returns the two planar beams to the photodetector along the same path.

In regard to focusing, the relationship between the frequency at the photodetector and the surface-normal velocity is altered by the lens angle  $\theta$  shown in Figure 2.1. When the object moves a distance  $d$  in the surface-normal direction the phase change is not simply  $\frac{2d}{\lambda}$  but  $\frac{2d}{\lambda} \cos \frac{\theta}{2}$  so that the equation relating frequency to velocity becomes:

$$f = \frac{2v}{\lambda} \cos \frac{\theta}{2} \quad (2.4)$$

Finally, if the velocity vector makes an angle of  $\beta$  with the optical axis the net shift is:

$$f = \frac{2v}{\lambda} \cdot \cos \frac{\theta}{2} \cdot \cos \beta \quad (2.5)$$

Also, as shown in Figure 2.1, the frequency shifting in the actual unit is accomplished by an acousto-optic modulator or Bragg cell. In the TCV system this shifts the reference beam frequency by 40MHz. This is accomplished by diffraction of the entering beam into several orders by passing it through a transparent medium experiencing acoustic waves

at 40 MHz. Only the first diffraction order is kept and becomes the "reference beam."

This is the least noisy way of shifting the reference beam. Other approaches such as passing the beam through a rotating diffraction grating or reflecting the beam off of a rotating wheel add a significant amount of frequency noise to the system due to rotational velocity variations and consequent shifting-frequency variations. These approaches are, however, much less expensive than the cost of a Bragg cell.

As a final difference between the Michelson setup (Figure 2.4) and the actual vibrometer setup (Figure 2.1), the vibrometer includes a polarization rotator. This enables one to rotate the (linear) polarization of the object beam and thus to maximize the signal by aligning the polarization of the reference and object beams for maximum interference.

### The Differential Doppler Technique

As noted previously, this technique allows for the detection of transverse motions. The setup is illustrated in Figure 2.3. There are several approaches to describing how transverse motions cause a frequency shift in this arrangement. Probably the two simplest approaches are the "fringe model" often used in explaining one component velocimetry (see Drain (1980) for example) and the other is a path length difference model as explained in Ennos (1978). Although these essentially are the same, the path length difference approach will be used here.

Referring to Figure 2.5, the target surface is illuminated by two plane waves coming in at equal angles to the surface normal. If the surface moves "down" (in the figure) some amount  $\delta$ , then every point on the surface experiences an increase in path length relative to the upper beam of:  $\Delta_u = \delta \sin \frac{\theta}{2}$ . Equally, every point on the surface experiences a decrease in path length of  $\Delta_L = \delta \sin \frac{\theta}{2}$  relative to the lower beam. The total change in path length experienced by every point on the surface is  $\Delta_T = 2\delta \sin \frac{\theta}{2}$ . The corresponding phase change (in cycles) is  $u = \frac{\Delta_T}{\lambda} = \frac{2}{\lambda} \delta \sin \frac{\theta}{2}$ . Taking the time derivative yields:

$$\frac{d\phi}{dt} = f = \frac{2}{\lambda} \frac{d\delta}{dt} \sin \frac{\theta}{2} = \frac{2v}{\lambda} \sin \frac{\theta}{2} \quad (2.6)$$

which relates the surface velocity to the fringe passing frequency at the photodetector for the differential Doppler technique.

Unfortunately, both this explanation for the presence of a Doppler signal as well as the fringe model explanation predict zero beat signal for solid surfaces; the various points within the illuminated area initially have a uniform phase distribution from 0 to  $2\pi$  and when the object moves there is a uniform phase shift at every point. This results in no net change in backscattered intensity to the detector and therefore no net beat signal. Drain (1980) refers to this situation and notes that "experiment and more detailed theory show that the signal does not completely disappear" as the number of particles in the probe volume (in the case of LDV) becomes very large.

The presence of a beat signal for the differential Doppler technique applied to solids lies in the fact that the intensity received by the photodetector consists of a speckle pattern which, as noted



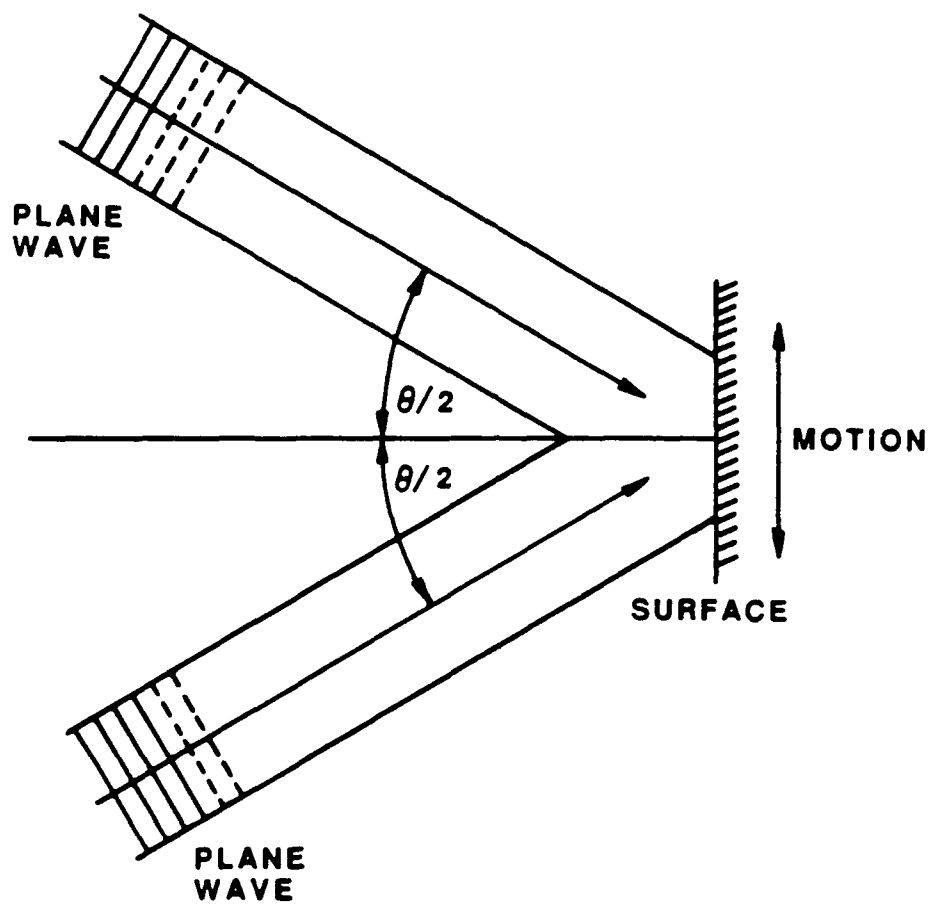


Figure 2.5 Illumination of Surface for In-Plane Sensitivity

previously, is characteristic of coherent light scattering from an optically rough surface. However, individual speckles have an intensity distribution which is not uniform but rather is skewed so that there is some resultant bias for the entire illuminated area. For a strong resultant intensity bias in the backscattered speckle pattern, the beat signal will be strong as the surface moves. For a weak resultant intensity bias in the backscattered signal, the beat signal will weaken with much more D.C. than A.C. optical return to the detector.

Skew in the intensity distribution of the speckle field is illustrated by Ennos (1978). The random phase distribution of the detected speckle field also accounts for some illuminated surface areas yielding high Doppler signals and others low Doppler signals (both in the differential Doppler technique as well as the reference beam technique). This is addressed by Rothberg, Baker, and Halliwell (1989).

One can see that the sensitivity ratio of the differential Doppler technique to the reference beam technique is:

$$\frac{\sin \frac{\theta}{2}}{\cos \frac{\theta}{2}} = \tan \frac{\theta}{2} . \quad (2.7)$$

For small lens angles (which are typical), the differential Doppler technique is considerably less sensitive.

Referring now to Figure 2.3 for the actual setup, collimation is again necessary to ensure that the converging beams are planar as they converge at the surface. This yields maximum interference. A Bragg cell is also used in this setup as it is in the reference beam setup for directionality. The backscattered light is collected through the center

of the lens and focused onto the face of a photodetector. Issuing from the detector is an FM signal which has a carrier frequency equal to the Bragg cell shifting frequency and which is frequency modulated due to the surface velocity in the relationship previously derived.

Similar to the other arrangement a downmixer reduces the carrier frequency to 50 kHz for processing by the phase-locked loops. The "dual" configuration for this technique is also as shown in Figure 2.2. The only changes required to move from the reference beam setup to the differential Doppler setup are to: remove the vibrometer adaptor, change the beamsplitters to a 50-50 ratio, rotate the beams depending on the direction of transverse motion desired, and check the focus on the object.

#### LASER VIBROMETER SIGNAL PROCESSING

As noted previously the current from the photodetector in the laser vibrometer is a frequency modulated (FM) signal. It has a carrier frequency which is modulated by the motion of the surface by an amount (for surface normal motions):

$$f_D = \frac{2}{\lambda} v \cos\left(\frac{\theta}{2}\right) \cdot \cos\beta \quad (2.8)$$

The signal processor for the vibrometer must extract these frequency deviations (Doppler shifts) and output a signal which is linearly proportional to the Doppler shift. Massey (1967) who constructed one of the first laser vibrometers used a phase-locked loop (PLL) to perform this task. Many of the commercial vibrometers now

entering the market use PLL processors (effectively FM receivers) to perform signal demodulation.

A phase locked loop yields a DC voltage which is directly proportional to the frequency difference between the input signal and an internal signal. This frequency difference is the Doppler shift. Consequently the output of the PLL is a DC voltage proportional to the surface velocity.

A PLL is a feedback system, with the basic block diagram as shown in Figure 2.6 (reproduced from Gardner (1979)).

The phase detector puts out a voltage,  $V_d$ , proportional to the phase difference between the input signal and oscillator signal. This voltage is filtered by the loop filter to suppress high frequency signal components and noise. (The filter design also controls the dynamic characteristics of the loop). Output from the loop filter is the control voltage. The voltage controlled oscillator (VCO) increases the control voltage by a gain of ( $K_0$ ) and changes its center frequency by  $\Delta\omega = K_0 V_0$ . The output of the VCO is a phase angle which is the integral of the VCO frequency. This phase angle is then fed back into the phase detector. The output of the PLL is taken after the loop filter and is the control voltage or filtered error signal.

As long as the changes of the input signal frequency are slow enough to remain within the bandwidth of the loop and as long as the signal remains sufficiently above the noise the PLL will remain "in lock." More rapid input frequency changes or lower amplitudes would cause the unit to lose tracking capability temporarily until it re-acquires lock.

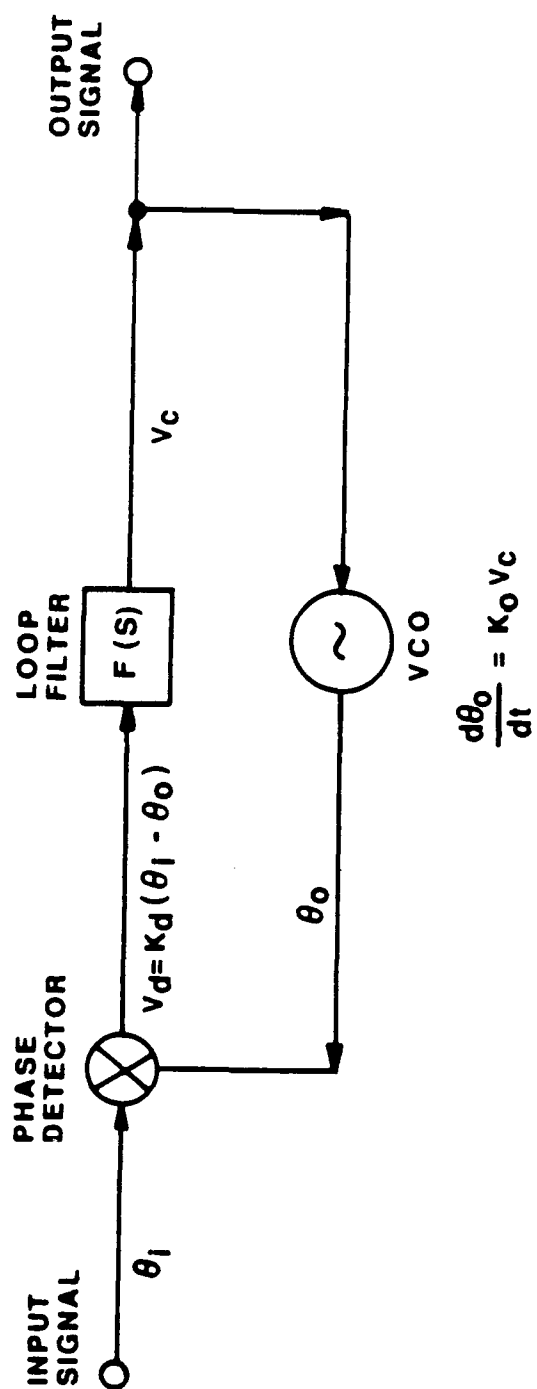


Figure 2.6 Block Diagram of a Phase-Locked Loop (Source: Gardner 1979)

The phase-locked loops used for this experiment have been designed so that the VCO has a center frequency of 50 kHz. This was considered high enough to be beyond the largest expected Doppler shift. The maximum frequency deviation (Doppler shift) for the PLL's is approximately  $\pm 30$  kHz. This corresponds to maximum velocities of  $\pm 0.78$  cm/s for out-of-plane motion and  $\pm 23.4$  cm/s for in-plane motion assuming 750 mm focal length lenses are used (i.e.  $\theta/2 = 1.91^\circ$ ). These values have been found to be sufficient for laboratory applications.

The maximum modulation rate is approximately 30 kHz. This corresponds to the maximum vibration frequency which the loop can track without losing lock.

The two PLL processors designed for this test have to be calibrated for amplitude and checked for phase mismatch. This is accomplished with the use of an FM signal generator and a spectrum analyzer.

PLL amplitude sensitivity, i.e. the amount of frequency deviation (Doppler shift) per volt of PLL output is determined by a well known Bessel zero technique as explained by Waters and Mottier (1986). A brief explanation follows.

The spectrum of an FM signal consists of a series of Bessel function sidebands. The heights of these sidebands are related to the peak frequency deviation in the FM signal. Using an FM signal generator, the amount of frequency deviation can be altered to reduce one of these sidebands to zero. Setting the corresponding Bessel function equal to zero will then yield the exact peak-to-peak frequency deviation in the FM signal. This is compared to the peak-to-peak

deviation in the voltage out of the PLL (subject to the same FM signal). The ratio of these gives the PLL sensitivity in Hz/volt at this modulation frequency. This can be performed at various modulation frequencies to find PLL sensitivity or gain factor as a function of modulation (or vibration) frequency. Alternatively a carrier frequency can be modulated by broadband noise to provide the PLL gain factor variation over a wide frequency range. This signal can be obtained by use of an FM signal generator and a random noise source.

Phase matching of the two PLL's has been checked by passing the same FM signal through both units and checking for the phase difference at their output by recording their output cross-spectrum using an FFT spectrum analyzer. The phase difference versus frequency up to 10 kHz is shown in Figure 2.7. Phase difference is large for low frequencies, levels off to 2.5 degrees from 600 Hz to approximately 4 kHz, is negligible from 4 kHz to 6.5 kHz, then slowly increases up to 10 kHz.

The amplitude and phase matching of the two PLL units can easily be improved. No strict tolerances were enforced on the design of these first two units. However, for the purpose of this work, the amplitude and phase data from these two PLL's are taken again at the specific frequencies of the test to provide the maximum accuracy of the PLL amplitude and phase data for each structural intensity test. This allows for accurate comparison of the test results to measured power inputs so that the feasibility of using the two-channel vibrometer for structural intensity measurements can be ascertained.

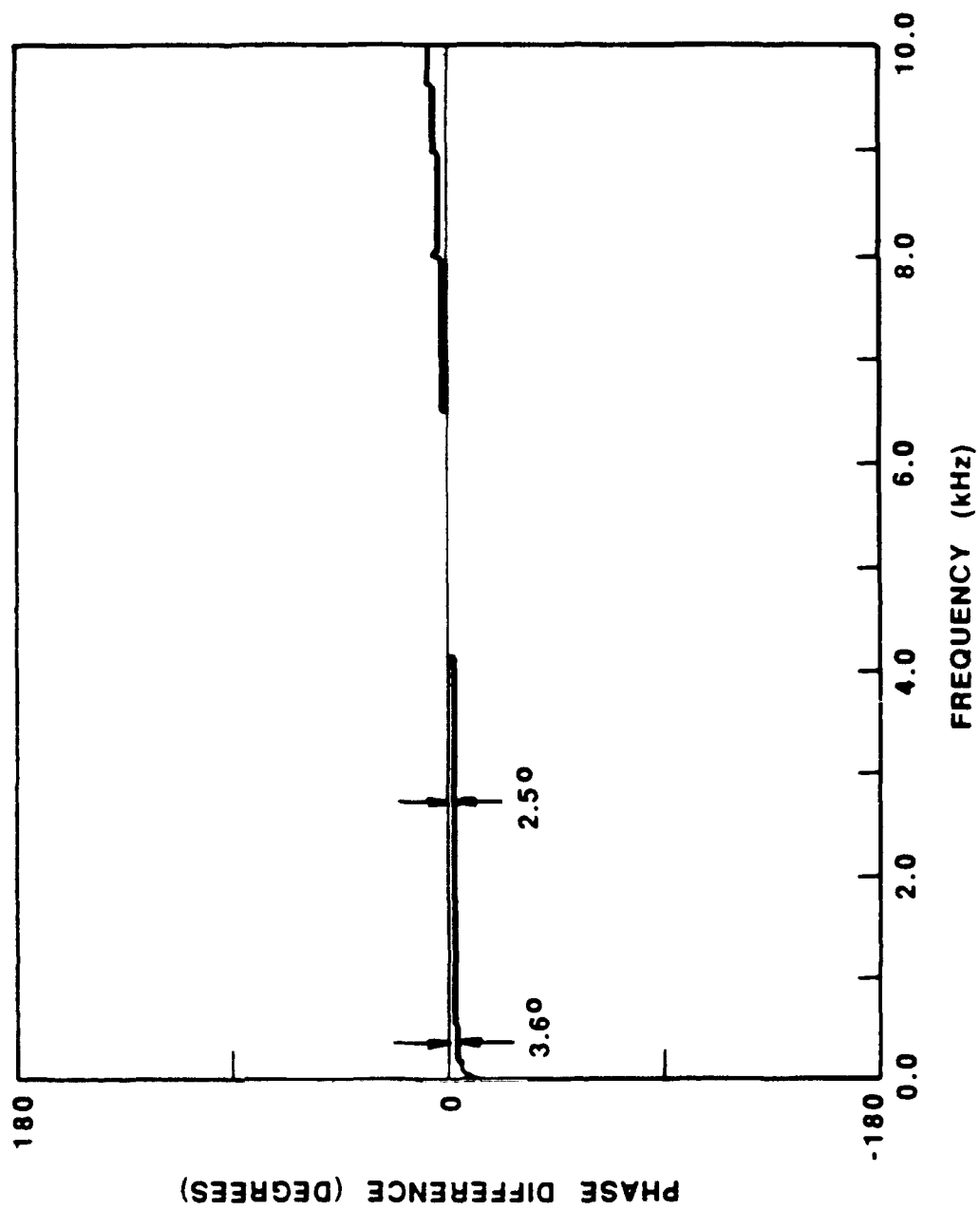


Figure 2.7 Phase Mismatch Between PLL Units



## LASER VIBROMETER NOISE SOURCES

### Characteristics of Laser Speckle

When coherent light is scattered by a rough surface a random intensity pattern is generated in space. This is caused by the random interference of the light due to each point on the surface acting as a "source" with its own random phase and scattering angle. The resultant complex amplitude of the scattered light at any point in space is the coherent addition of all the sources each with its own random amplitude and phase (a "random walk") relative to the point. This random interference presents a high contrast grainy appearance called laser speckle. Since laser vibrometry involves detection of the motion of surfaces which are typically "rough" (relative to the wavelength of laser light), speckle plays an important role in the quality of the signal.

If a surface which is illuminated by a spot of coherent light moves in a direction parallel to the illumination, so that the same spot on the surface is always illuminated, the backscattered light (observed on a screen for example) will contain a speckled intensity which will not change appreciably with the object motion. The speckle pattern is relatively insensitive to motion in this direction. However, if the same object is moved transverse to the illumination, the speckle pattern observed changes more significantly; an individual speckle will translate along with the object motion momentarily, but then, as a different population of scatters becomes illuminated on the surface, it disappears. This phenomenon is referred to in the literature as

"speckle boiling." The different behavior of the backscattered speckle for the two types of motions suggests separate evaluations of the effects of normal and transverse motions.

A final general speckle "characteristic" should be noted before considering the two separate motion effects mentioned above. This is that the mean speckle size can be controlled if the speckle is focussed. This requires a distinction between "objective speckle" and "subjective speckle."

Objective speckle is the light pattern observed when coherent light is backscattered from a rough surface and viewed directly on some observation surface such as a screen. The mean speckle size in this case is (Ennos 1978):

$$\langle \sigma_0 \rangle \approx 1.2 \lambda L/d \quad (2.9)$$

where:

$\lambda$  - laser wavelength

$L$  - distance from scatterer to observation screen

$d$  - diameter of the laser spot on the surface

Subjective speckle, on the other hand, is the light pattern observed when the speckle has been imaged by an optical system onto an observation screen. (This is the case in vibrometry since the speckle is imaged onto the surface of a photodetector). The mean speckle size in this situation is (Ennos 1978):

$$\langle \sigma_0 \rangle \approx 1.2 \lambda f.l./d \quad (2.10)$$

where  $\lambda$ , is the laser wavelength and, f.l. is the lens focal length, and d is the aperture. Consequently the size and, hence, number of speckles received by the photodetector can be controlled by the imaging system.

#### Speckle Noise Due to Normal Motion

For motion which is purely parallel to the optical axis there is one minor consideration. Large vibration amplitudes will cause some amplitude modulation of the FM signal. This is typically not a problem since the velocity information is in the frequency modulation of the signal.

The amplitude modulation in this case is caused by large excursions of the object which act to change the makeup of the received speckle field. However, the makeup of the speckle field does not change significantly when the identical scatters are illuminated on the surface since the contribution of each of the scatterers does not change appreciably. If a very poor FM signal is received initially at the surface (one reason for which will be explained in the next section) then a slight amplitude modulation caused by large normal vibration amplitude could cause a temporary loss of signal during the vibration cycle. This is referred to as signal dropout. The effect of temporary signal dropout depends on the dynamics of the processor. If a good FM signal is available at the measuring point it is unlikely that typical amplitude modulations would be enough to cause loss of the signal.

### Speckle Noise Due to Transverse Motion

Transverse object motion, which is the principal motion of interest in the laser Doppler mode, but which can also be present to some degree when observing normal motions, has two forms of speckle noise associated with it. The first is the possibility of signal dropout. The second is frequency noise or "Doppler broadening" due to the motion of the speckles across the face of the photodetector.

Signal dropout occurs in vibrometer systems when the amplitude of the FM or heterodyne signal falls below the background noise or at least below some threshold at which the processor can no longer track the signal. The amplitude fluctuations of the heterodyne signal from the photodetector are a manifestation of the statistics of laser speckle.

Meynart (1984) assessed the influence of transverse motion on a vibrometer setup for the reference beam mode in terms of the amplitude modulations caused by laser speckle. For interference between a single speckle and a uniphase reference beam he derives the probability density function for the amplitude of the FM signal to be:

$$p(A) = (A/2\langle I_L \rangle_x) \exp - A^2/4\langle I_L \rangle_x \quad (2.11)$$

where  $A$  is the amplitude of the FM signal and  $\langle I_L \rangle_x$  is the ensemble averaged light intensity over the scattering surface. The resulting spatially averaged FM signal amplitude is:

$$\langle A \rangle_x = \pi \langle I_L \rangle_x \quad (2.12)$$

and the ratio of the standard deviation to the mean is:

$$\sigma_A / \langle A \rangle_x = .523 \quad (2.13)$$

This means that due to the random amplitude and phase variation of the speckle as the laser spot moves across the surface, the amplitude of the FM signal will vary. According to the above results, it will vary by a fairly substantial amount so that appreciable dropout periods would be expected for sampling over the entire surface. This occurs when a single speckle is used at any given surface location.

Instead of using a single speckle, the aperture of the focussing system can be enlarged to allow a greater number of speckles to fall on the detector. In this case, however, Meynart shows by a similar analysis that the amplitude fluctuations are, however, not suppressed by the speckle averaging process.

Pickering, Halliwell and Wilmshurst (1986) have designed a vibrometer which uses a rotating disc to shift the frequency of the reference beam rather than a much more expensive but less noisy Bragg cell. In this instrument the reference beam is always subject to amplitude modulation due to the motion of the disk transverse to the beam so that signal dropout during disk rotation is very likely. Their processor, a gated rate meter, samples the frequency and holds the last value of the Doppler frequency received when the FM amplitude drops into the electronic noise. This results in "flats" in the output voltage which they have adjusted by thresholding the amplitude to have a mean duration of less than  $0.25 \times 10^{-4}$  seconds for a frequency response of 20 kHz.

However for the instrumentation used in this study, where frequency shifting is accomplished by a Bragg cell, signal dropout is not a problem. This is because the small amplitudes encountered in the

study of longitudinal vibrations (where the motion is transverse to the laser beam) do not appreciably change the speckle field received by the photodetector so that signal amplitude fluctuations should be minimal.

Large amplitude motions however, which might be caused by not securing the object would cause large signal amplitude modulations which may cause temporary signal dropout. The effects of this on the demodulated signal depend on the dynamics of the signal processor.

A final implication of these signal amplitude modulations is that surface scanning of the laser beam is restricted, but only to the extent that at some points on the surface the beam may have to be moved a small amount in order to obtain a good signal.

#### **Doppler Broadening**

Another general category of signal degradation which can be due to laser speckle is Doppler frequency broadening. Ideally an object moving at a constant velocity transverse to the laser illumination should provide a pure single Doppler frequency (for optics in the laser Doppler mode); its spectrum is a delta function. However, as noted in Pickering, Halliwell, and Wilmshurst (1986), the transverse object motion causes the backscattered speckles to sweep across the face of the detector possibly undergoing speckle boiling in the process. This creates noise in the photodetector output which shows up as a broadening of the Doppler frequency spectrum. This is referred to as finite transit time broadening.

Except for very small detector areas, the initial translation of the speckle across the detector can be ignored and the situation can be

viewed as purely a speckle "boiling" case where the speckle changes its phase as it moves across the photodetector. This is how Pickering, Halliwell, and Wilmshurst (1986) approach the problem in order to derive an expression for Doppler broadening due to finite transit time.

Through a straightforward analysis the authors calculate a standard deviation in the Doppler signal of approximately 720 Hz due to this effect for an object transverse velocity of 1 m/s and a laser spot size of 0.5 mm. This represents a fairly negligible noise floor of approximately  $1.5 \times 10^{-4}$  m/s. The effects of finite transit time broadening for the proposed studies are expected to be negligible since in this case the transverse motion will be due to small amplitude vibrations so that the photodetector always "sees" approximately the same speckle content.

Other sources of Doppler broadening exist in laser vibrometry beyond that due to laser speckle. Even with an ideal specular reflector these sources of noise exist. Velocity gradient broadening for example, is a result of the laser spot illuminating an area on the object which contains some variation in velocity so that more than a single Doppler frequency is received by the detector. For example, for a point on a standing wave where the displacement is:

$$u(x,t) = A \cos \omega t \cdot \sin kx \quad (2.14)$$

the velocity gradient is:

$$\frac{\partial^2 u(x,t)}{\partial t \partial x} = -Ak\omega \cos kx \cdot \sin \omega t \quad (2.15)$$

For some point  $X_0$  and a laser spot size  $d$ , a variation of velocity within  $d$  can be obtained. The maximum change in velocity within the spot is approximately  $Ak\omega d$ .

Doppler broadening can also occur due to the finite size of the receiving aperture. Ideally signals received at various points on the photodetector are perfectly in phase. However, for a finite detector aperture there is some finite difference in the phase of the received signal at different detector points due to the optical path length differences between the various receiver points and the source. Equivalently for a source moving with some constant velocity the different parts of the receiver will detect slightly different Doppler frequencies giving rise to a broadening of the Doppler spectrum. This source of broadening should be negligible in the proposed instrumentation since the object beam is effectively recollimated before it is focussed on to the photodetector.

Laser linewidth broadening refers to the fluctuations in frequency (or wavelength) of the emitted laser light. This can be caused internal to the laser cavity or more seriously by noise or ripple in the laser power supply or the electrical discharge (Pickering, Halliwell, and Wilmshurst 1986). Since the Doppler shift from the vibrating object is a function of wavelength, laser linewidth broadening will cause noise in the velocity signal. This is a fairly unavoidable source of broadening but it should not be a significant source of error, with the laser used in the proposed apparatus.

Vibration of any of the optical components after the beams have been split and before they interfere at the detector will induce an



artificial vibration signal showing up as noise on the measured signal which is considered a source of broadening. It is not difficult to isolate the optical components from the source vibration in the laboratory environment although this noise source can be particularly detrimental to intensity measurements (as will be discussed later) and must be checked with and without the source vibration. Additionally, any "ambient" motion of the source relative to the optics in the frequency range of interest will cause distortion of the measurements.

Two remaining sources of noise that can cause broadening of the Doppler signal are Bragg cell frequency drift and "third mirror feedback." Frequency drift in the Bragg cell can cause small drifts in the carrier frequency which can result in the PLL processor yielding small variations about the actual velocity. This type of noise can be checked by taking an RF spectrum of the input to the Bragg cell and checking the variation around the intended shift frequency. However, the output of the Bragg cell depends on the frequency response of the acoustic-optic element.

A more reliable approach to checking Bragg cell noise is to record the vibrometer output spectrum for zero object motion. The output will include several noise sources (including some discussed below) but an indication of the severity of these sources can be obtained by this method.

"Third mirror feedback" is a broadening source which occurs when frequency shifted light (from the object) is allowed to reenter the optical cavity of the laser. This can result in very large phase and amplitude fluctuations in the vibrometer output for sinusoidal surface

vibration (Cretin, Xie, Wang, Hauden 1988). When some means of optical isolation is used this is not a problem. For the vibrometer system in this test this problem should not occur due to the optical setup.

### Miscellaneous Noise Sources

The remaining noise sources are not considered as broadening sources since they typically extend over a wide frequency range.

However, they are no less important. These include the following:

- (i) Shot noise from the photodetector - this is normally considered a white noise source and is unavoidable. The electrical power of shot noise is (Willemin, Dandliker, and Khanna 1988):

$$P_{SN} = 2 \left( \frac{\Omega_0^2}{\Omega} \right) e b s \bar{P}_0 \quad (2.16)$$

where

- $\Omega_0$  - feedback resistance
- $\Omega$  - load resistance
- $e$  - electron charge
- $b$  - detector bandwidth
- $s$  - spectral sensitivity of the photodetector =  $\eta e / h\nu$
- $\eta$  - quantum efficiency of the detector
- $h\nu$  - photon energy
- $\bar{P}_0$  - average light power falling on the photodetector

- (ii) Thermal noise of the electronics ("Johnson noise"). This is independent of the detected optical power. Willemín, Dandliker, and Khanna note that for a reasonable reference beam (~1mW) this can be ignored relative to shot noise.
- (iii) Electro-magnetic pickup by the detector from the acoustic-optic modulators. This is an unavoidable source of noise with the setup in this experiment but it is expected to be minor.
- (iv) Laser intensity fluctuations. Depending on the amplitude and frequency of these fluctuations they can appear as noise in the Doppler signal. The fluctuation frequency can be over a large range. A number of heterodyne systems use a balanced detection scheme to remove this noise (see for example Stierlin, Battig, Henchoz, and Weber 1986). This is an effective noise reduction technique but is not used in these experiments.
- (v) Wavefront misalignment noise. When beating two wavefronts together the best signal is obtained when they have the same polarization, are aligned, planar, and normally incident on the detector. Aberrations in the imaging system can distort one or both of the wavefronts and produce a noisy signal. The result is a signal-to-noise ratio which is only a fraction of the ideal system (shot-noise limited system) signal-to-noise ratio. This fraction is the heterodyne efficiency (Takenaka, Takenaka, Fukumitsu 1978). This can be controlled by careful alignment of the optics and use of high quality lenses. Polarization upon backscatter is not

as easily controlled but application of a polarization preserving paint to the object is helpful.

- (vi) Laser mode noise. A high power laser with many longitudinal modes can distort the vibrometer signal. This can be avoided by using an etalon if a multi-mode laser is used. The etalon will suppress all but one longitudinal mode.

Three remaining sources of signal distortion yield bias errors rather than noise in the demodulated signal. The first is the frequency response of the photodetectors. This is important in balanced heterodyne systems and is equally important in a two-channel vibrometer for precise phase difference measurements. The gain factor of the photodetectors is effectively " $\eta$ " the quantum efficiency. These can vary slightly between detectors, but detector gain differences will not influence the output since amplitude differences in the Doppler signals are of no consequence. Detector phase differences, however, could play a role in altering demodulated signal phase differences.

The second bias error source is the frequency response of the phase lock loop detectors. This will influence the amplitude and phase of the demodulated signals. However, as noted previously, this is easily calibrated by use of an FM signal generator.

Finally a phase bias can be introduced by unequal optical and electrical paths in the two optical systems. However, for electrical or optical signals a pathlength difference of several meters would induce a phase difference approximating only one tenth of a degree. Therefore, for this application, reasonably matched pathlengths are sufficient.

# POSSIBLE EFFECTS OF LASER VIBROMETER NOISE SOURCES ON STRUCTURAL INTENSITY MEASUREMENTS

The severity of the various noise sources has to be viewed in light of their effect on the accuracy of the structural intensity measurements. The preceding noise sources can be considered as noise which is additive to the signal. For two measurement points we would have two stationary signals defined as:

$$x(t) = u(t) + m(t)$$

and

$$y(t) = v(t) + n(t)$$

where

$x(t)$ ,  $y(t)$  are the measured signals

$u(t)$ ,  $v(t)$  are the true signals

$m(t)$ ,  $n(t)$  are the additive noise signals.

It can easily be shown (Talbot 1975), that the measured cross-spectrum is:

$$G_{xy}(f) = G_{uv}(f) + G_{un}(f) + G_{mv}(f) + G_{mn}(f) \quad (2.17)$$

This can be viewed as a vector summation in the complex plane as shown in Figure 2.8.

Recall that the measured active structural intensity is proportional to the imaginary part of the measured cross-spectrum. It is easy to see the adverse effects of the noise related cross-spectra when one compares the imaginary part of the measured cross-spectrum with the imaginary part of the true cross-spectrum. For accuracy, the noise related cross-spectra ( $G_{un}$ ,  $G_{mv}$ ,  $G_{mn}$ ) must all be zero. Therefore the

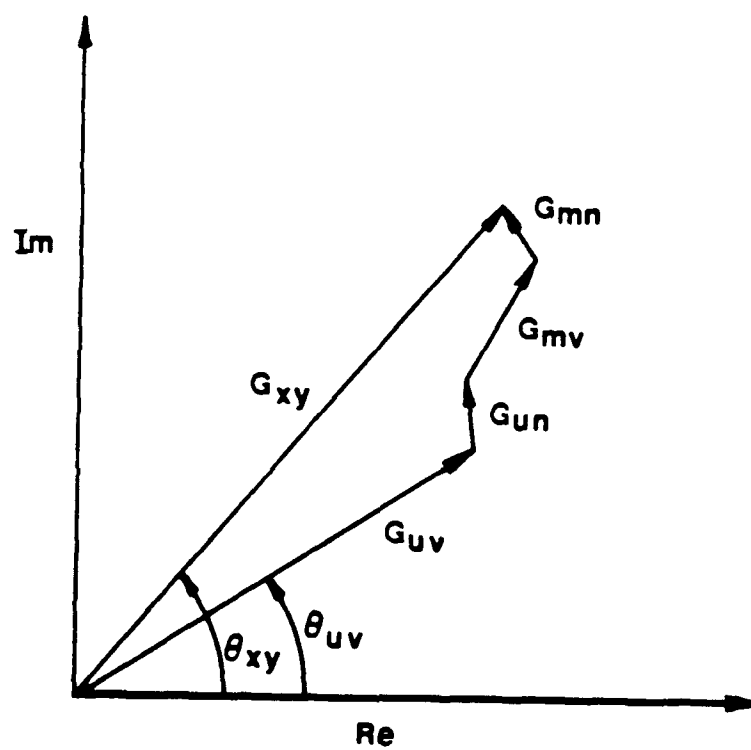


Figure 2.8 The Influence of Noise Correlation in the Measured Cross-Spectrum

type of noise which will most adversely effect the structural intensity measurements will be that which is correlated with itself (i.e.,  $m$  and  $n$ ) or with the true signals.

The most likely causes of significant correlated noise in the vibrometer setup used for this research are vibration of the optical components and possibly laser noise. Transit time broadening, velocity gradient broadening, and third mirror feedback can also be considered as possible sources of correlated noise since they are all velocity (signal) dependent. However for this application these sources are expected to be insignificant; transit time broadening will be negligible for detection of surface normal motions as well as for small amplitude zero mean transverse motions, velocity gradient broadening should be negligible for the small spot size compared to the surface wavelengths for this application, and "third-mirror" feedback as stated previously is not a problem for this optical setup.

Vibration of the optics, if caused by the source, will result in signals with noise components which correlate well with each other as well as the two true signals so that spurious cross-spectra will be nonzero and will distort the active intensity measurement.

Laser noise including intensity fluctuations, linewidth broadening, and noise in the power supply can result in a nonzero value of  $G_{mn}$  since the two laser Doppler channels use the same laser in this apparatus. Consequently, these noise sources can also act to alter the true value of the active intensity.

Noise sources which are uncorrelated can also act to degrade the quality of the measurements. These cause a random error in the measured value given by Elko (1984):

$$\epsilon_r = \frac{1}{\sqrt{n_d}} \left[ \frac{1 - \gamma_{12}^2 \cos 2\phi_{12}}{\gamma_{12}^2 (1 - \cos 2\phi_{12})} \right]^{1/2} \quad (2.18)$$

where

- $\epsilon_r$  - the normalized random error
- $n_d$  - the number of ensemble averages
- $\phi_{12}$  - phase difference between sensors
- $\gamma_{12}^2$  - the ordinary coherence measured between the sensors

For a fixed number of averages the random error increases sharply for phase differences of a few degrees when the coherence is less than one. Therefore if the noise causes coherence to drop below one, a large number of averages may be necessary in order to avoid appreciable random errors if small phase differences are to be measured.

In laser vibrometry the potential noise sources which are essentially uncorrelated and act only to induce this random error include: thermal noise, shot noise, electro-magnetic pickup noise, Bragg cell frequency drift noise (for independent Bragg cell drivers), photodiode resistance fluctuation noise, and the noise associated with less than unity heterodyne efficiency. Fortunately these sources are (except for heterodyne efficiency) fairly insignificant in the present apparatus. With proper alignment of the optics, heterodyne efficiency can be high enough to suppress appreciable noise due to possible wavefront misalignment.



The final category of sources of signal distortion includes those sources which alter the amplitude and/or phase of the demodulated signal. These sources include: differences in the phase-lock loop-frequency response functions, and differences in the electrical and optical paths comprising the two sensors.

The last source has negligible effects for reasonably matched path lengths but the different frequency responses of the PLL units and of the detectors represent bias errors in the demodulated signals which can distort the measured active intensity. However, the photodetector gain factor will not affect results since this only affects the amplitude of the Doppler signal which is not important (as long as it is above the threshold value for the PLL units).

## Chapter III

### FLEXURAL INTENSITY MEASUREMENTS USING THE TCV SYSTEM

The most difficult application for intensity measurements of any type occurs in a reverberant field. Intensity measurements demand an accurate measurement of phase difference. But in a reverberant field the phase angle between two points can be diminished below the value of  $k\Delta$  (the product of the wavenumber and the point spacing) due to the reflected waves. The prospects of accurately measuring this small phase difference can be dim unless the transducers are perfectly phase-matched or unless their phase bias can somehow be known with extremely high precision. Therefore it was decided to have the TCV system measure intensity on a reverberant beam as this would provide an excellent test of system capability.

Equally important was that the results should be verifiable by techniques which were not phase sensitive and hence were not subject to potentially large errors themselves. Such techniques exist for a reverberant beam which has damping predominantly at its ends and are explained, as is the cross-spectral method, in this chapter.

#### FORMULATION OF THE APPROACH

For a beam which is lossless compared to the energy dissipation at its ends, Carroll (1987) has shown that the vibrational power flowing from a point of excitation to the ends of the beam can be calculated at a resonance condition by measuring the farfield nodal and antinodal

displacements. Using this information the power flow is determined by two different approaches. The first is a standing wave technique analogous to the acoustic case for a standing wave tube. Advantage is taken of the fact that the expression for the power flow in the beam contains a term equivalent to the product of the nodal and antinodal displacements. Therefore once these displacements are found, the power flow is calculated using these values with geometric and material property constants.

The second approach is based on energetics. This approach involves calculating the total kinetic and potential energy in the resonant beam which is proportional to the sum of the squares of the nodal and antinodal displacements. Knowledge of the total energy, the in-situ beam loss factor (determined previously), and the frequency of vibration, then permits a determination of the power dissipation or equivalently the flow of power into the beam terminations from the point of excitation.

These two methods of calculating power flow are particularly useful for highly reverberant beams since they do not require phase measurements. The more versatile two-point cross-spectral method for determining power flow, on the other hand, does require phase measurements, and the required phase accuracy becomes greater as the beam becomes more reverberant (as the end losses decrease, in this case). Consequently the standing wave and the energetics methods can provide good checks on results of two-point cross-spectral determinations of the power flow in highly reverberant beams.

As detailed in Carroll (1987), the standing wave measurement procedure requires knowledge of  $Y$ , the material Young's modulus,  $I$  the flexural moment of inertia,  $f$  the excitation frequency,  $m'$ , the mass per unit length, and  $k$ , the flexural wavenumber (equal to  $(2\pi f)^{1/2}(m'/YI)^{1/2}$ ),  $\xi_N$ , the nodal rms displacement and,  $\xi_{AN}$  the antinodal rms displacement. The expression for energy flow by the standing wave method is:

$$\Pi_{SW} = 2YI(2\pi f)k^3\xi_N\xi_{AN} \quad (3.1)$$

The energetics measurement procedure requires knowledge of  $\eta$ , the system loss factor at frequency  $f$ ,  $L$  the beam length, as well as  $f$ ,  $m'$ ,  $\xi_N$  and  $\xi_{AN}$ . The expression for energy flow by the energetics approach is:

$$\Pi_E = \frac{\eta(2\pi f)^3}{2} m' L [\xi_N^2 + \xi_{AN}^2] \quad (3.2)$$

Finally, the two-point cross-spectral intensity measurement procedure requires  $Y$ ,  $I$ ,  $k$ ,  $f$ ,  $\Delta x$ , which is the separation distance between the measuring points, and  $\text{Im}[G_{12}(f)]$  which represents the imaginary part of the cross-spectrum between the two measured accelerations (or velocities in this case).

The expression for energy flow (adapted from Carroll (1987) for velocity measurements) is:

$$\Pi_{2P} = \frac{2k^2 Y I}{\Delta x (2\pi f)} \text{Im}[G_{12}(f)] \quad (3.3)$$

From Equation (1.38) this result has to be corrected for finite difference error by multiplying it by the quantity

$$\frac{k\Delta x}{\sin(k\Delta x)}$$

The three preceding power flow equations, when adapted to the laser vibrometer output, assume slightly different forms. The first two equations are recast in terms of the rms voltages at the node and antinode,  $V_N$  and  $V_{AN}$ , respectively, and the phase locked loop sensitivity,  $K$  as described in Chapter II. The two-point power flow equation, on the other hand, is recast in terms of either the imaginary part of the voltage output cross-spectrum or the rms voltages and phase angle for the two points. These different forms are discussed below.

In the standing wave and energetics expressions the rms displacements are related to the voltage output values from the vibrometer in the following manner. The Doppler shift associated with a velocity  $v$  is (from Equation 2.5):

$$f_D = \frac{2}{\lambda} v \cos\left(\frac{\theta}{2}\right) \cdot \cos\beta \quad (3.4)$$

For a velocity,  $v$ , in units of m/s and a laser wavelength of  $\lambda = 514.5$  nm (for the green line of the Argon Ion Laser) and for  $\cos(\theta/2) \sim 1$  and  $\cos\beta \sim 1$  the relationship becomes (in Hz):

$$f_D = 3.89 \cdot 10^6 v \quad (3.5)$$

(i.e. the Doppler shift is  $3.89 \cdot 10^6$  Hz per m/s of velocity.)

From Chapter II, the phase-locked loop (PLL) processor output voltage for a given sensitivity of  $K$  (in units of Hz/volt) then will be the Doppler shift for a velocity  $v$  divided by the sensitivity or:

$$v = \frac{3.89 \cdot 10^6 v \text{ Hz}}{K \text{ Hz/volt}} \quad (3.6)$$

The rms displacement in units of meters then becomes related to the rms voltage output in the following manner:

$$\xi = V \cdot \left( \frac{K}{(2\pi f) \cdot 3.89 \cdot 10^6} \right) \quad (3.7)$$

This result then yields the expression for the product of the displacements which is used in the standing wave equation:

$$(\xi_N)(\xi_{AN}) = \frac{V_N \cdot V_{AN} \cdot K^2}{[(2\pi f)(3.89 \cdot 10^6)]^2} \quad (3.8)$$

where  $\xi$  and  $V$  are rms displacement and voltage values respectively at the node (for subscript N) and the antinode (for subscript AN). (It is assumed that the same PLL is used to read both nodal and antinodal velocities).

Now the standing wave equation can be written, by substituting this result into equation (3.1), as:

$$\Pi_{SW} = 2YI(2\pi f)k^3 \left[ \frac{V_N \cdot V_{AN} \cdot K^2}{(2\pi f)^2 (3.89 \cdot 10^6)^2} \right] \quad (3.9)$$

$$\Pi_{SW} = 2YIk^3 \left[ \frac{V_N \cdot V_{AN} \cdot K^2}{(2\pi f) (3.89 \cdot 10^6)^2} \right] \quad (3.10)$$

where for  $Y$  in  $N/m^2$  (Pascals),  $I$  in  $m^4$  and  $k$  in radians/meter,  $\Pi$  acquires an energy flow in units of watts.

By a similar approach the equation for the energetics method becomes:

$$\Pi_E = \frac{\eta}{2} m' L (2\pi f) \frac{K^2}{(3.89 \cdot 10^6)^2} [V_N^2 + V_{AN}^2] \quad (3.11)$$

which has units of watts for  $m'$  in units of  $kg/m$  and  $L$  in meters.

Before deriving the appropriate expression for the two-point technique, some useful results can be obtained from the preceding

standing wave and energetics equations. For example, equating the power flow in the two approaches, and assuming that  $V_N^2 \ll V_{AN}^2$  in the energetics equation (true for low damping as in these tests) the two equations yield the following ratio for nodal and antinodal rms voltages (or displacements, etc.):

$$\frac{V_N}{V_{AN}} \approx \frac{\eta}{4} kL. \quad (3.12)$$

Furthermore, by using this approximation, the vibrometer rms voltage at the antinode becomes:

$$V_{AN} \approx \sqrt{\frac{2\pi(2\pi f) \cdot (3.89 \cdot 10^6)^2}{YIk^4\eta LK^2}}. \quad (3.13)$$

These equations assume the units are in the MKS system, that damping is low, and that the angle the laser beam makes with the surface normal,  $\theta$ , is such that  $\cos \theta \sim 1$ . The voltage distribution along the beam can then be expressed as:  $V(x) = \sqrt{V_{AN}^2 \cos^2 kx + V_N^2 \sin^2 kx}$  where  $V(x)$  is the rms voltage at any point  $x$  measured from an antinode.

Remaining to be addressed are the expressions for the two-point power flow method in terms of data obtained using the TCV system. From Equation 3.3 the expression for power flow obtained from the two-point method with the finite difference correction applied is

$$\Pi_{2P} = \frac{2k^2 YI}{\Delta(2\pi f)} \operatorname{Im}[G_{12}(f)] \frac{k\Delta}{\sin k\Delta} \quad (3.14)$$

At this point there are two approaches available which pertain to removing phase bias error. The first approach is to use an averaged value of  $\operatorname{Im}[G_{12}(f)]$  directly obtained by switching the photodetectors as

explained in Chapter V. The second approach is to break down  $\text{Im}[G_{12}(f)]$  into amplitudes and a phase difference between the two points so that a prerecorded phase bias error is removed from each reading before the power flow is calculated.

In the first case the averaged value of  $\text{Im}[G_{12}(f)]$  in units of volts squared can be converted to units of velocity squared by use of the relationship previously established between velocity and output voltage. The velocity in units of m/s for a PLL sensitivity of K Hz/volt becomes:

$$v = \frac{V \cdot K}{3.89 \cdot 10^6} \quad (3.15)$$

where V is the PLL output voltage. Therefore the output voltage cross-spectrum is converted to a velocity cross-spectrum by the relationship:

$$[G_{12}(f)]_{\text{VELOCITY}} = [G_{12}(f)]_{\text{VOLTAGE}} \cdot \frac{K_1 K_2}{(3.89 \cdot 10^6)^2} \quad (3.16)$$

where  $K_1$  and  $K_2$  are the two PLL sensitivities. The units of the velocity cross-spectrum will be in  $(\text{m/s})^2$  per Hz. This equation assumes that the laser wavelength is 514.5 nm and that the angles between the approaching laser beams and the surface normal is small. For any angles  $\beta_1$  and  $\beta_2$  between the two optical axes and the surface normal the following relationship is used:

$$[G_{12}(f)]_{\text{VELOCITY}} = [G_{12}(f)]_{\text{VOLTAGE}} \cdot \frac{K_1 K_2}{(3.89 \cdot 10^6)^2 (\cos \beta_1)(\cos \beta_2)} \quad (3.17)$$

Therefore, using the output from an FFT analyzer directly, the two-point power flow becomes:



$$\Pi_{2P} = \frac{2k^2 Y I}{\Delta(2\pi f)} \cdot \text{Im}[G_{12}(f)] \cdot \frac{K_1 K_2}{(3.89 \cdot 10^6)^2 (\cos \beta_1)(\cos \beta_2)} \cdot \frac{k\Delta}{\sin k\Delta} \quad (3.18)$$

(For  $Y$  in  $\text{N/m}^2$ ,  $I$  in  $\text{m}^4$  this equation yields  $\Pi$  in units of watts.) For correction of phase mismatch,  $\text{Im}[G_{12}(f)]$  is an averaged value obtained as explained in Chapter V.

If a calibrated phase mismatch is to be subtracted in the calculation of power flow, then  $\text{Im}[G_{12}]$  can be cast in terms of the rms voltages and the corrected phase angle between the points:

$$\text{Im}[G_{12}] = V_1 V_2 \sin(\psi - \phi) \quad (3.19)$$

where  $V_1$  and  $V_2$  are the rms voltages,  $\psi$  is the measured phase angle and  $\phi$  is the calibrated phase bias between the two vibrometer units. This expression is then substituted into the previous expression for power flow.

#### EXPERIMENTAL SETUP AND PROCEDURE

For flexural power flow measurements, a beam was clamped at one end leaving a 25.4 cm cantilevered length. At the free end the beam was vibrated by a shaker connected to the beam by a small sting to minimize twisting of the beam by the shaker. The mechanical setup and optical setup of the flexural test are illustrated in Figure 3.1. For two-point structural intensity readings, the two laser beams emanating from the TCV are arranged so as to approach the test object parallel to one another and be closely spaced.

The scanning mirror shown in the figure can move the laser beams in parallel along the object surface to allow for a reading of power flow by the two-point method anywhere along the beam length. Due to the

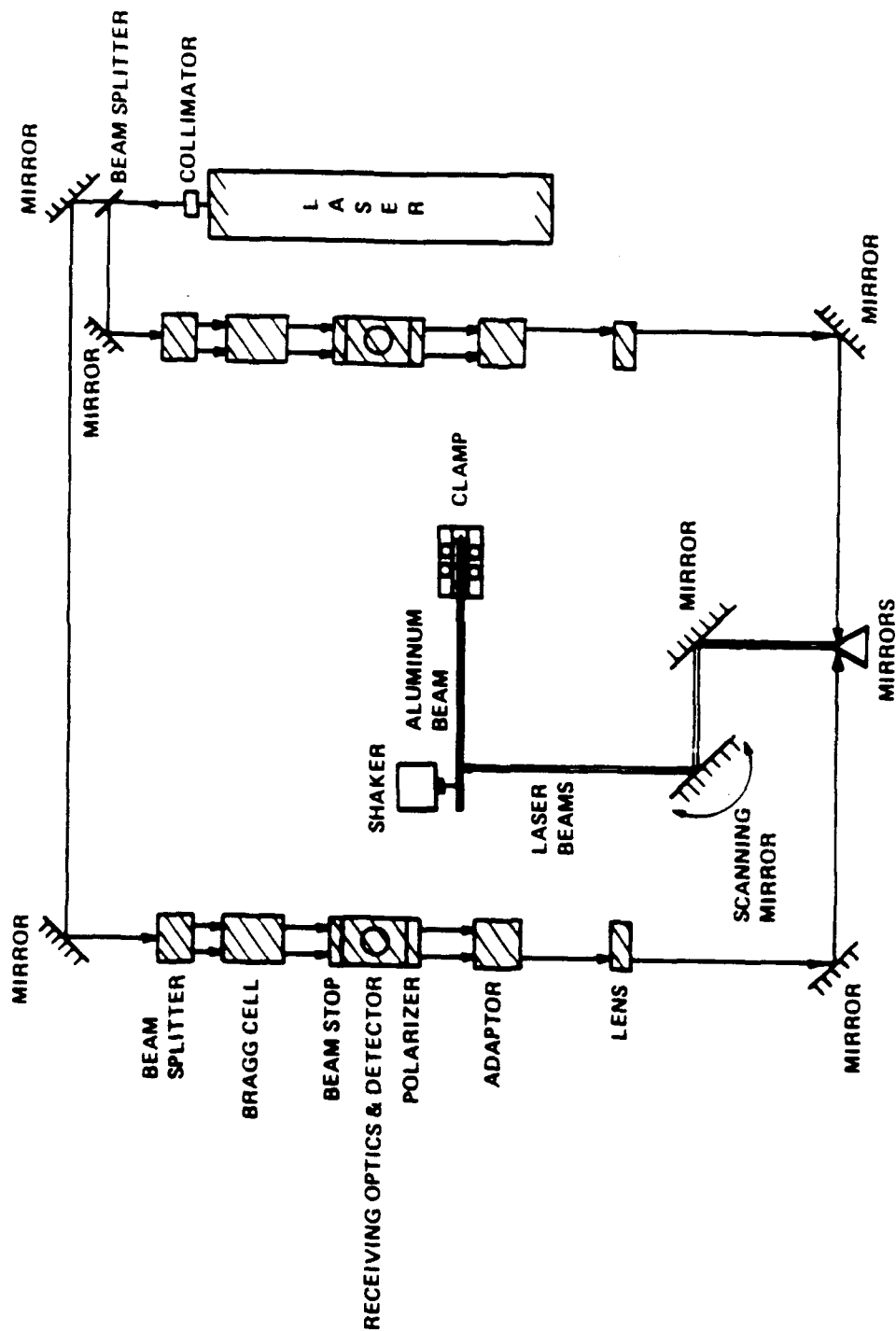


Figure 3.1 Mechanical and Optical Setup for Flexural Intensity Measurements

scanning radius in this setup, there is a very slight change in the laser beam separation distance as well as a slight sensitivity change due to the increased angle as the beams scan the surface. These are accounted for in the data. For measurements of the nodal and antinodal velocities, either laser beam can be used to scan the length of the object.

The overall measurement procedure consisted of the following. First the damping at the desired frequency was determined by using the output of a single laser beam focussed on the sample while the vibration frequency was swept by use of a programmable signal generator. The loss factor was then determined by a 3 dB down measurement at the antinode about one of the resonance frequencies. Following this, the excitation was fine-tuned to the resonance frequency, and the nodal and antinodal rms velocities of the sample were found by scanning the surface with one of the vibrometer beams. The distance between nodal points was also recorded for validation of the theoretical wavenumber at this frequency.

Finally, a series of two-point intensity measurements were taken by using both laser beams at a separation distance of approximately 0.2 times the bending wavelength (as suggested by Redman-White 1983) and scanning the surface at various stations axially (while avoiding the flexural nearfields at approximately one-half the bending wavelength from the ends of the sample). The rms velocities and phase angle at the two locations as well as the real and imaginary part of the cross-spectrum were determined at each location by use of a two-channel FFT spectrum analyzer. Coherence between the signals was also checked and 128 spectral averages were taken at each station. The angles the laser

beams made with the sample at each station were calculated for use in the two-point intensity equation.

The sample had been painted with retroreflective paint along its length so that the back scattered light would provide a consistently good Doppler signal over the surface. Unpainted metal proved to be too reflective; the back scattered light would be too directional so that large variations in signal strength occurred as the surface was scanned. Once the paint was applied, in most positions the peak-to-peak value of the Doppler signals was 0.1 volts or better (a good value for proper functioning of the PLL processors). However, in some cases the laser beam pair had to be moved very slightly from their intended axial station to obtain at least 0.1 volts in both channels. This position change was typically negligible.

Lenses used for this setup were 1500 mm focal length lenses. These provided a depth of field of approximately two centimeters; this is long enough to avoid the need for refocussing of the lenses when the object was scanned. The laser beam spot size at the  $1/e^2$  intensity points was calculated to be approximately 0.5 mm (where  $e = 2.7183$ ).

In initial tests, an aluminum sample which measured 30.48 cm long, 1.27 cm wide and 0.082 cm thick was clamped at one end leaving a cantilevered length of 25.4 cm. "High" loss factors were induced at the clamp by using several sheets of constrained damping layer between the sample and the faces of the clamp.

As the damping was gradually removed to allow for testing in the low loss factor range, it became increasingly apparent that the beam was twisting during testing; vertical scans at a given axial station on the beam yielded velocity amplitudes dependent on the vertical orientation.

To better avoid twisting problems, a different sample was used for the remaining low loss factor tests. This was a sample of key stock material constructed of stainless steel with a square cross section of 3.24 mm on a side and a total length of 30.5 cm.

Two approaches were used during testing to correct for the phase bias error in the PLL units. Initial tests used a correction to the measured phase angle based on the calibrated PLL phase bias found by using an FM signal generator. The intensity was found by using the two rms values of velocity at the points and the appropriately corrected phase angle.

A second approach, used during later testing, used a transducer switching technique as detailed in Chung (1978). In this approach the imaginary parts of the cross-spectrum were obtained with the two photodetectors both in the "normal" and "switched" positions for each axial station. The spectra were then effectively averaged. This approach was employed to prevent possible problems occurring due to inaccuracies in the determination of the actual PLL phase bias error and is outlined in more detail in Chapter III. The process of switching the detectors and obtaining a good signal in each system required only a few minute's time at each axial station along the beam.

In either case the resulting power flow measurement from the two-point approach was calculated by use of Equation 3.18. The value of  $\Delta x$ , the laser beam separation, was checked at each station by using a scale and a pair of green light filtering goggles which reduced the bright beams to two pinpoints of light.

## RESULTS OF FLEXURAL INTENSITY TESTS

The first test on the aluminum beam was run at the beam's tenth flexural mode at a frequency of 2520 Hz. Damping (predominantly induced at the clamp) was measured yielding a loss factor of  $\eta = 0.013$ . (A repeat of this measurement after the test yielded the same result). A check of the distance between the nodal points indicated a spacing of approximately 27 mm which results in a flexural wavelength of 54 mm. This compares very well with the value of 54.6 mm calculated by using the free-bending wavenumber equation. (The nodes present a much more precise indication of wavelength than do the antinodes due to the shape of the rms velocity distribution along the beam; the spatial velocity gradient at the nodes is sharp while at the antinodes it is relatively flat.)

The nodal and antinodal rms voltages were then recorded and the two-point intensity values were taken at stations starting at approximately a wavelength from the end of the beam with readings taken at five stations spaced 10 mm apart. The laser beam separation was set at 10 mm and checked at each station. Phase bias error in this case was removed by cross-spectrum averaging after switching the photodetectors at each station. The coherence at each station was recorded at 1.00, or at a few stations 0.998.

Figure 3.2 shows a comparison of the power flow calculated by the standing wave and energetics methods (at the bottom of the figure), as well as the power flow at each of the five stations calculated by the two-point method. There is a ten percent fluctuation in the two-point results due to the high value at station one. (Station one was located

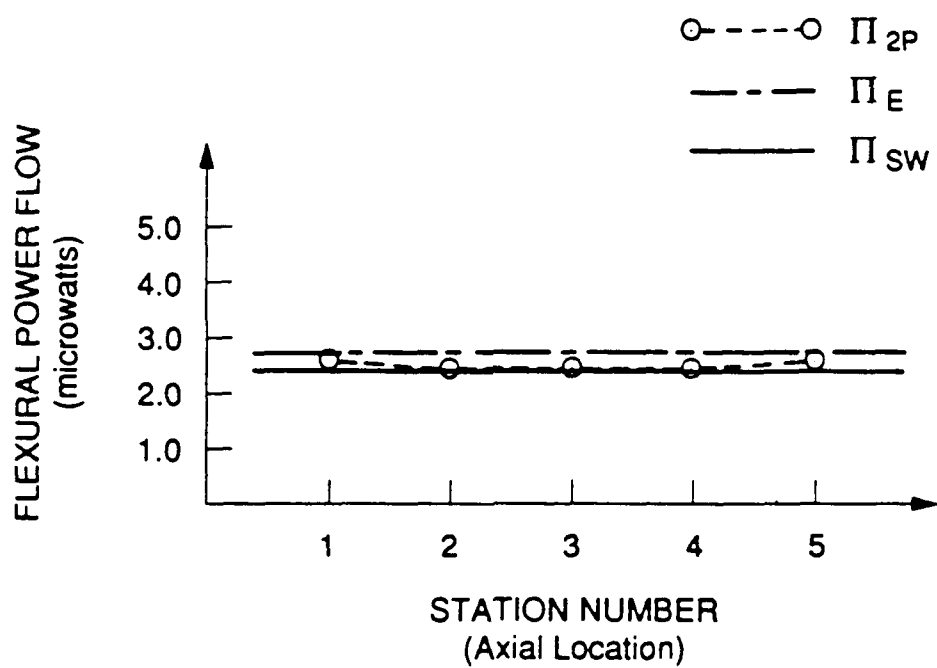


Figure 3.2 Comparison of Flexural Power Flow Results  
for  $n = 10$ ,  $\eta = 0.013$ ,  $f = 2520$  Hz

so that the laser beam closest to the shaker was at an antinode one wavelength from the excitation.) However, the two-point results agree very well overall with the standing wave and energetics values.

A second test was run on the aluminum sample for approximately the same damping but for the twelfth mode at a frequency of 3712 Hz. In this case the nodal spacing was recorded as 21 mm giving a flexural wavelength of 42 mm. This value compares fairly well with the calculated value of 44.9 mm. Damping for this test was measured to be  $\eta = 0.0126$  at the start of testing. (A check of the damping after testing indicated a value of  $\eta = 0.0118$ , a drop of 7 %). An average value of  $\eta = 0.0122$  was used for the energetics result. The results appear in Figure 3.3.

The fluctuations in the data may be due to a few minor problems occurring during the tests. First, the aluminum beam was twisting very slightly during testing as evidenced by slight variations (approximately a five percent amplitude increase at the upper and lower edges) in the vibrometer output for vertical scans at any station. This opened up the possibility of errors in the readings for laser beam positions off of the center of twist. Second, the signal generator used for these initial tests was an analog device which demonstrated very slight frequency drift during testing. For relatively low damping, such as in these tests, even a drift of one half of one percent will have an appreciable effect on the vibration amplitudes. Third, the slight variability in the damping (observed in these tests and similar preliminary tests) would also play a role in causing fluctuation of the calculated power flow values.



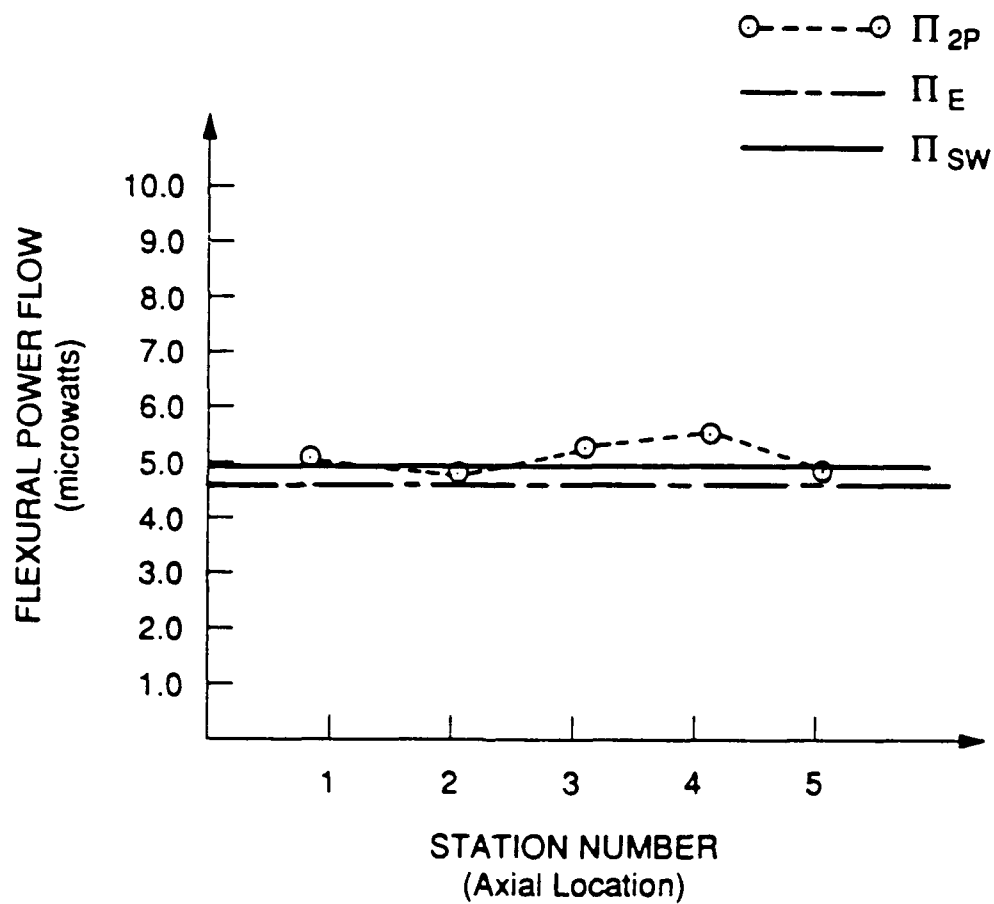


Figure 3.3 Comparison of Flexural Power Flow Results  
for  $n = 12$ ,  $\eta = 0.012$ ,  $f = 3712$  Hz

The relative success of these tests at "high" damping as well as the problems incurred during these tests suggested several changes. First, the thin, relatively wide aluminum sample was replaced by a stainless steel sample of a small square cross section with dimensions as noted previously. This was done to reduce the likelihood of torsion in the sample. Second, all damping at the site of the clamp was removed so that effectively only the significant frictional damping at the beam-to-clamp interface remained. Two thin flat plates of aluminum were placed between the beam and the vice grips to reduce this contact friction due to the grips. Since the signal generator was not yet replaced, it was decided to keep one laser beam fixed at the antinodal location and the second beam fixed at a spacing of  $0.2 \lambda$ . With this configuration a check of two-point results versus energetics results (which for low damping only require the antinodal value) as a function of time could then be made.

The steel beam was vibrated at 5650 Hz, its eighth mode. Nodal spacing was measured to be 34 mm corresponding to a wavelength of 68 mm. This compares well with the calculated value of 67.8 mm. Damping was very repeatable and was measured to be  $\eta = 0.003$ . Laser beam separation was set at 14 mm (approximately  $0.2 \lambda$ ). The two point and energetics results appear in Figure 3.4.

Typically the results compare well. It is apparent that the power flow is changing appreciably in time (the readings were taken every five minutes). This is most probably due to the oscillator frequency fluctuation which for this low damping case has very adverse effects. (For these readings none of the instrumentation settings were changed).

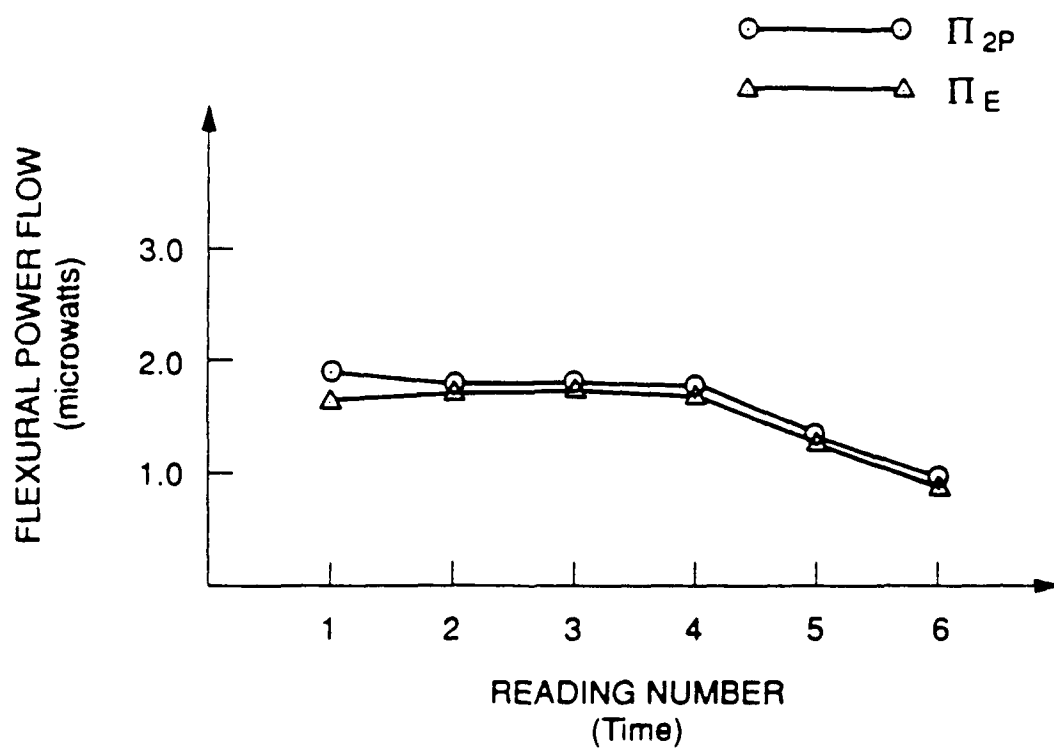


Figure 3.4 Comparison of Flexural Power Flow Results  
for  $n = 8$ ,  $\eta = 0.003$ ,  $f = 5650$  Hz

For the two-point results, photodetector switching was not used to remove the phase bias error in this case because of the possibility of phase angle changes occurring between the switched and "unswitched" readings at the point. Instead, the rms voltages and averaged phase angle were taken for each reading and the PLL calibrated phase bias, determined by using the FM signal generator, was subtracted from the measured phase angle to obtain the corrected power flow value.

## CONCLUSIONS

From this chapter it is evident that accurate flexural intensity measurements can be obtained from the TCV system in the reference beam mode. The argument could be made that the verification techniques used (i.e. the standing wave and energetics approaches) were not completely independent means of verification since they also depended on the vibrometer accuracy. However these depended only on the amplitude accuracy of the vibrometer which has been shown by this author and by numerous others in the open literature to be very reliable for the case of the reference beam mode and surface-normal vibration.

Despite the successful application outlined in this chapter, a detailed evaluation of the system in this application must address such considerations as the influence of the amount of optical backscatter on the phase-locked loop performance and the vibrometer noise floor, random error in flexural intensity using the TCV system, the possibility of coherent noise in the system, and the influence of laser speckle. These issues are addressed in the following chapters.

## **Chapter IV**

### **CHARACTERISTICS CONTROLLING THE SIGNAL-TO-NOISE RATIO IN THE REFERENCE BEAM METHOD**

#### **INTRODUCTION**

There are several parameters which control the velocity signal-to-noise ratio (SNR) in a vibrometer output when the instrument is in the reference beam mode. A true evaluation of the TCV system for flexural intensity measurements must consider the effects of these parameters since they ultimately control the quality of the intensity measurement obtained. The noise floor of each vibrometer channel is controlled by two major factors: the quality of the Doppler signal (FM signal) entering the FM demodulator and the response of the demodulator to this signal quality. These factors are reviewed in this chapter and experimental data illustrating these effects are presented. The signal level in each vibrometer channel, on the other hand, is also controlled by several parameters. These are presented in the latter part of the chapter. Knowledge of the noise floor parameters and the signal level parameters then provide predictions of signal-to-noise ratios as a function of optical and vibrational conditions. These, in turn, are used to evaluate the accuracy of the intensity measurement in cases where coherence is less than one (via random error analysis) in Chapter V.

# **CARRIER-TO-NOISE RATIO AND PLL PERFORMANCE AS APPLIED TO THE REFERENCE BEAM METHOD**

As is detailed in Chapter V, the accuracy of the TCV intensity measurement depends on the signal-to-noise ratio in each of the vibrometer channels. The signal-to-noise ratio (SNR) of the velocity signal in each channel is controlled by both the quality of the FM signal entering the FM demodulator from the photodetector and the PLL processor's sensitivity to this signal quality. The first consideration, FM signal quality, can be cast in terms of a carrier-to-noise ratio (CNR) where the carrier is the heterodyne or beat signal corresponding to zero object velocity (50 kHz for the TCV system used in this study). The CNR is then a ratio of the carrier electrical power to noise electrical power. The discussion below applies to the reference beam method where the reference beam and object beam are two separate entities.

The carrier or heterodyne signal electrical power exiting the photodetector (Willemin, Dandliker and Khanna 1988) is given by:

$$P_{AC} = 2 \left( \frac{\Omega_o^2}{\Omega} \right) m^2 s^2 P_{OB} P_{RB} \quad (4.1)$$

where  $\Omega_o$  is the feedback resistance and  $\Omega$  the load resistance of the detector amplifier,  $m$  is the heterodyne efficiency (equal to one for optimum alignment and coherence) and  $s = \eta e / h\nu$  is the spectral sensitivity of the photodetector determined by  $\eta$  the quantum efficiency,  $e$  the electron charge, and  $h\nu$  the photon energy. Additionally,  $P_{OB}$  and  $P_{RB}$  are the optical powers of the object and reference beams striking the photodetector.

Equation 4.1 establishes practical limits on the maximum beat signal obtainable due to the sensitivity and circuitry of the photodetector/ amplifier system, the optical alignment for maximum interference of the object and reference beams, and the intensity of the object and reference beams. Furthermore, for optically rough, diffusely scattering surfaces (which would ordinarily be the case in structural intensity measurements) the back scattered object beam is made up of laser speckle. This has the effect of reducing the backscattered object beam power,  $P_{OB}$ , used for interference at the photodetector. The effective value of  $P_{OB}$  for diffusely reflecting surfaces varies significantly over the surface; a very slight repositioning of the focused point (on the order of a millimeter) can cause as much as an order of magnitude difference in the amplitude of the heterodyne signal for the painted objects in these studies. This variability is a function of the surface roughness.

However, it is not simply the strength of the carrier signal but rather the CNR which governs the demodulated SNR. The broadband noise electrical power in the FM signal consists of shot noise and thermal noise from the detector. These sources extend evenly over the frequency spectrum. Shot noise is directly related to the amount of light incident on the photodetector whereas thermal noise (or Johnson noise) is a background noise existing independently of the optical power at the detector. The maximum CNR is obtained when shot noise is the dominant noise source (yielding "shot-noise limited detection") and when the reference beam intensity is much greater than the returning object beam intensity (Willemin, Dandliker, Khanna 1988). In this case

$$\text{CNR} = \frac{\left( \frac{\eta P_{\text{OB}}}{h\nu} \right)}{b} \quad (4.2)$$

In this equation,  $b$  is the detection bandwidth of the FM demodulator and the heterodyne efficiency is assumed to be unity. The value  $P_{\text{OB}}$  must be reduced for speckle considerations. For these studies the reference beam intensity at the photodetector was typically a couple orders of magnitude greater than the backscattered object intensity at the detector. In the apparatus used this could easily be discerned by viewing the two beams at the photodetector plane by use of an eyepiece in place of the detector. The condition of shot noise limited detection, on the other hand, was verified by ensuring that the FM noise floor was higher with the reference and object beams striking the photodetector (allowing both shot noise and thermal noise) than when the beams were prevented from impinging on the detector (allowing thermal noise only).

Figure 4.1 is an overlay of two spectra of the Doppler signals from one vibrometer focused on a stationary object. The upper spectrum shows the 50 kHz carrier signal and a noise floor which consists of the shot noise and thermal noise (plus some small spurious peaks). The lower spectrum is the result of blocking off the beams to the detector. The noise floor in this case drops at least 10 dB to the thermal noise level indicating that the detection is shot noise limited and that Equation 4.2 can legitimately be used. (The thermal noise level may be lower than the lower plot indicates since much of this spectrum consists of analyzer self-noise and noise from the downmixing circuitry.)



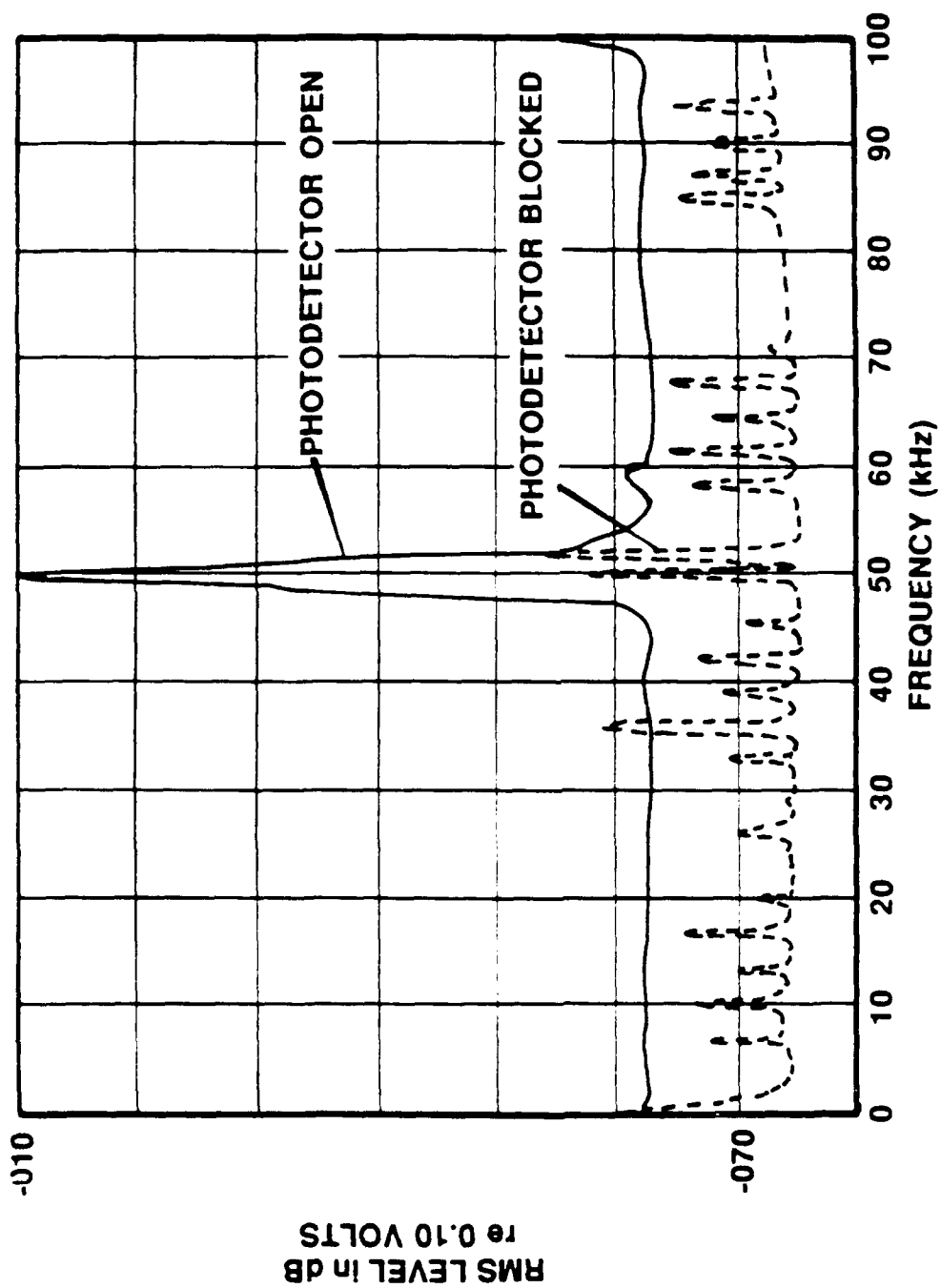


Figure 4.1 Comparison of Downmixed Photodetector Spectra With and Without Light to Photodetector

Equation 4.2 shows that the CNR is linearly related to the quantum efficiency of the photodiode,  $\eta$ . For the instrumentation used in this study the photodetectors were equipped with avalanche photodiodes type NEC NDL 1102. A curve of detector quantum efficiency versus wavelength for this photodiode shows a quantum efficiency of 65% at a wavelength of 633nm (helium neon laser light) but this falls off sharply to approximately 35% for a wavelength of 514.5nm (green light) used in this apparatus. For some vibrometer systems a quantum efficiency of 80% is not uncommon at the operating wavelength. According to Equation 4.2, there is approximately a 7 dB loss in the CNR due to the lower efficiency of the photodiodes in the TCV apparatus compared to the more efficient photodiodes.

The influence of laser power on the CNR of the FM signal appears in Equation 4.2 in the form of  $P_{OB}$ . For a fixed spot on the stationary object the CNR should vary linearly with the laser power assuming that the returning object beam power,  $P_{OB}$ , varies in the same fashion. Figure 4.2 is a spectral overlay of the Doppler signals from a stationary object. The upper part of the plot corresponds to a "total" laser power of 150 mW (of which approximately 50% is routed to the single vibrometer used in the test) and the lower portion corresponds to a reduction in total laser power down to 25 mW for otherwise identical conditions. The drop in CNR values is approximately 12 dB for a bandwidth of 250 Hz. Equation 4.2 predicts a reduction of 15.6 dB. The difference here is primarily due to bandwidth changes; some of the power exists in the nearby analyzer bins due to broadening of the Doppler signal. The Doppler broadening for this situation is due to the finite

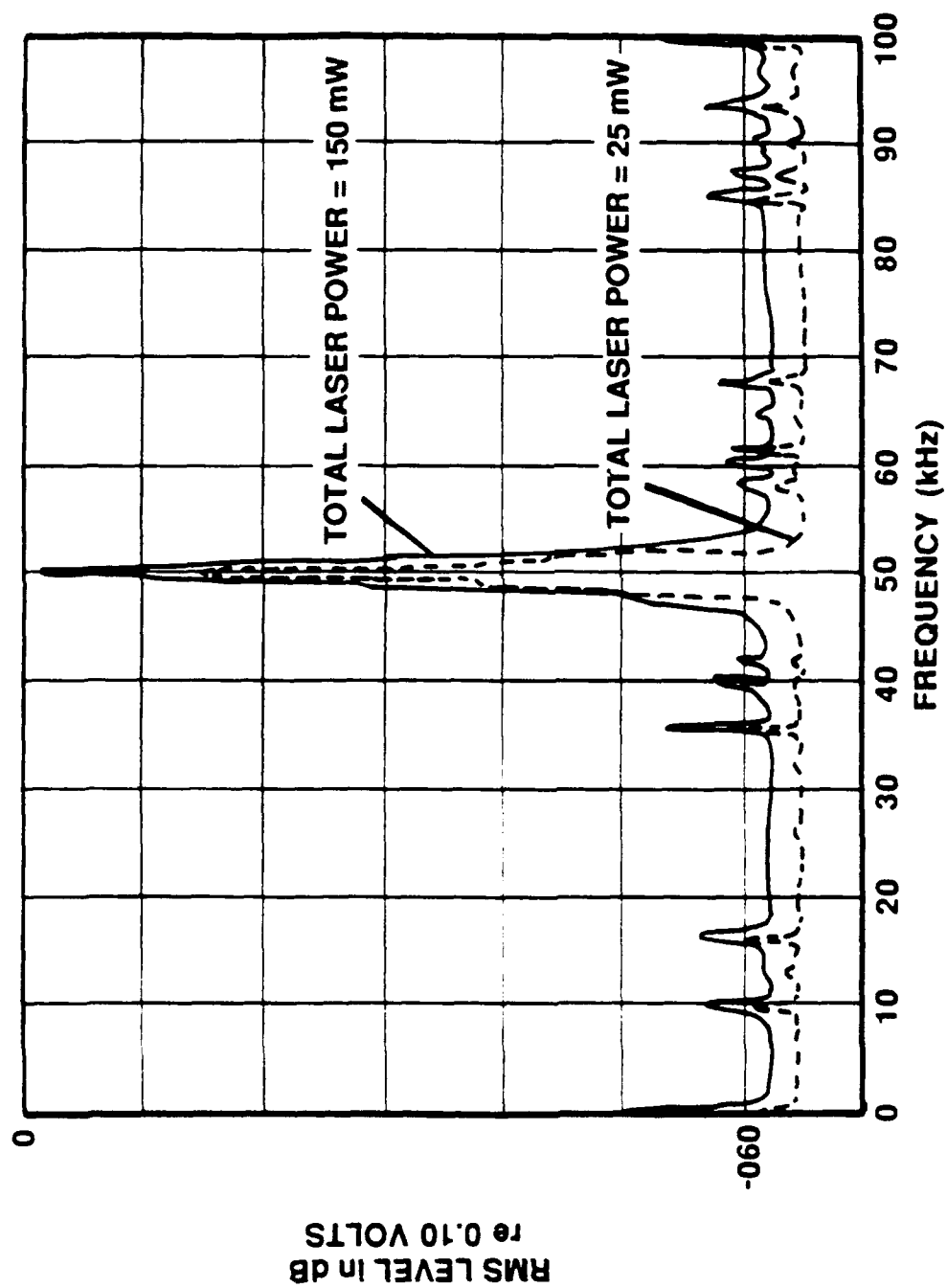


Figure 4.2 Comparison of Downmixed Photodetector Spectra  
at Two Different Levels of Total Laser Power

bandwidth of the 40 MHz signal used to activate the Bragg Cell. Ideally, if the 40 MHz carrier signal approximated a "pure" tone, then the downmixed carrier of 50 kHz (assuming perfect electronic downmixing) would have much narrower bandwidth. The values of the actual CNR values versus the "total" laser power based on the spectral height of the bin containing the 50 kHz carrier are shown in Table 4.1. A reduction in Doppler broadening (or an integration over the bandwidth) would provide higher values more compatible with Equation 4.2.

Table 4.1

Comparison of CNR Values for Various  
Amounts of Total Laser Power  
in the Reference Beam Mode

<u>Total Laser Power* (mW)</u>	<u>CNR (dB)</u>
150	61.2
100	57.1
50	54.8
25	49.3

\* Actual value for one vibrometer was approximately one-half this value.

Referring to Figure 4.2 again, it is worth noting that the shot noise increases as the laser intensity increases but not nearly to the extent that the carrier signal does. This is because the shot noise is proportional to the sum of the reference and object beam intensities falling on the detector whereas the carrier signal is proportional to their product. This is why "shot noise limited detection" yields the optimum CNR. This condition can be obtained by using a certain minimum reference beam power as outlined in Willemin, Dandliker and Khanna (1988).

In the time domain the broadbandedness of the carrier causes the demodulated signal (the velocity signal) to obtain a degree of uncertainty as detailed in Pickering, Halliwell and Wilmshurst (1986). However, if the velocity signal is Fourier analyzed, the signal due to the carrier jitter is decomposed into its constituent frequency components, and if the source of jitter is a stationary source, these components become a regular part of the instrumentation noise floor.

As discussed below, the CNR causes the demodulated noise floor to vary; a high CNR causes a low noise floor while a low CNR causes a high noise floor. However, the strength of the signal caused by carrier jitter would stay constant in the demodulated spectrum regardless of the CNR (although for low CNR values the noise floor may overcome these signals). An investigation of possible carrier jitter noise in the TCV system is discussed in Chapter V.

As stated previously, one of the parameters which govern the Doppler CNR is the power of the backscattered object beam which in turn is influenced strongly by laser speckle. Actually, the effect of laser speckle is to alter the power of the carrier; the broadband noise floor is effectively fixed by the much stronger reference beam. As an example, Figure 4.3 is an overlay of two Doppler spectra for a stationary object. The difference in the two signals is that the laser beam's position on the object was moved very slightly (approximately one mm). Due to laser speckle the change in carrier signal was fairly substantial but the noise floor stayed constant. The surface was rough due to an application of reflective paint. If the surface was to become more of a specular reflector with a much smoother finish, the carrier

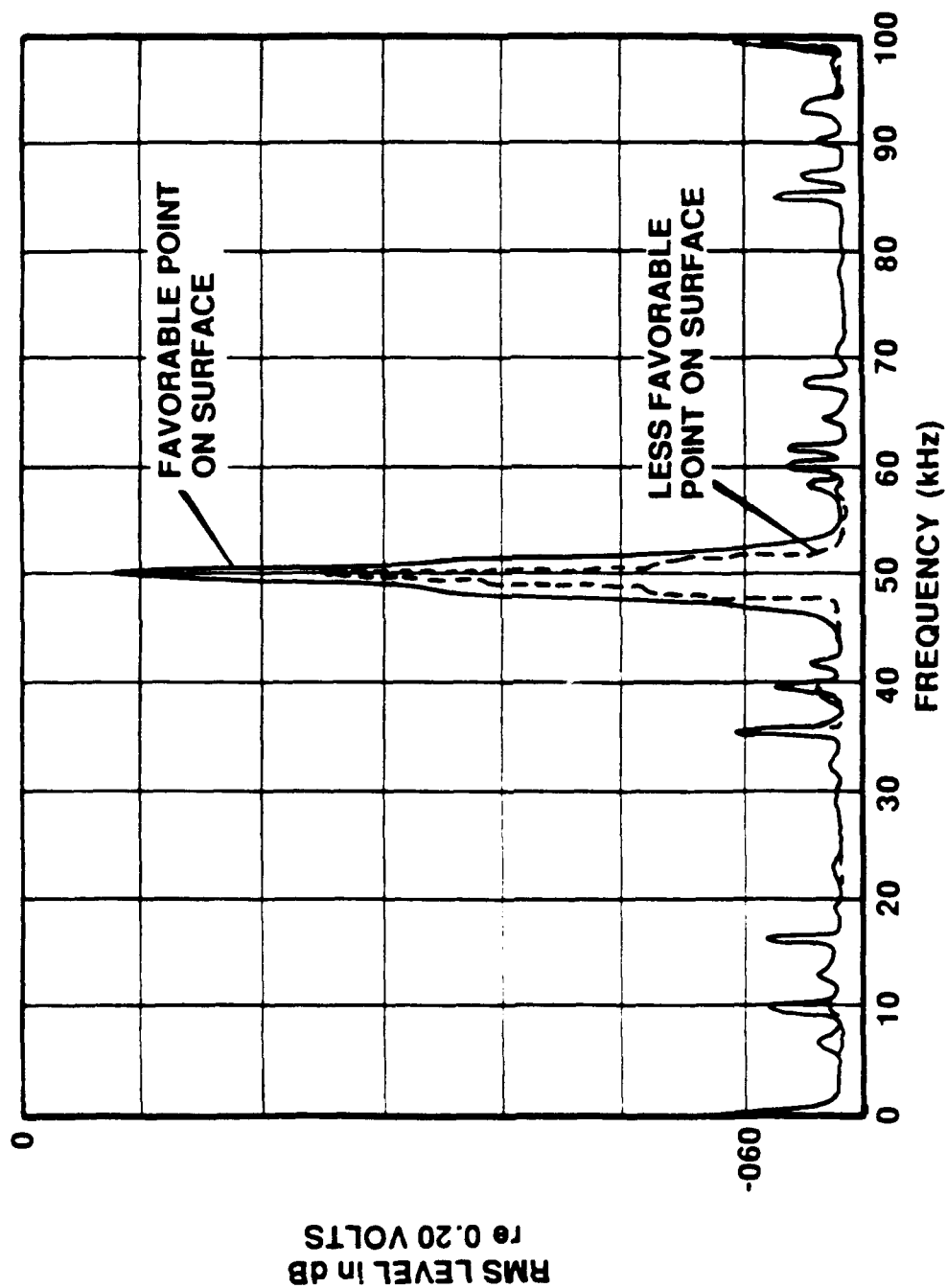


Figure 4.3 Comparison of Downmixed Photodetector Spectra  
at Two Nearby Points on a Stationary Object

signal would generally be higher and not have this degree of spatial variability. The limiting case is that of perfectly flat surface where no laser speckle would result.

In summary, there are a number of parameters influencing the heterodyne CNR in the reference beam method. Assuming shot noise limited detection conditions, the principal parameters include the proper alignment of the optics, the quantum efficiency of the detector, and the power of the backscattered object beam reaching the detector which can be strongly altered by the position of the focused spot on a diffusely scattering object or altered by the laser intensity.

However, it is not the CNR of the Doppler signal alone which determines the SNR of the velocity signal. Because demodulation of the FM signal is required to obtain the velocity signal, the way in which the particular demodulator responds to the CNR also influences the final SNR of the velocity signal and this response is a function of frequency. Actually, it is the noise floor of the demodulated signal which is influenced by the CNR of the FM signal entering the demodulator. This influence, for one of the PLLs, was tested by focusing one of the vibrometer beams at a point on the face of a shaker. The CNR of the heterodyne signal was recorded first by disconnecting the shaker to ensure a zero vibration condition and reading the 50 kHz signal and broadband noise spectral levels from an FFT analyzer. Then the shaker was actuated and the output signal from the PLL was recorded by the FFT. This was done for several closely spaced spots on the shaker face which yielded a varying CNR due to the speckle effect (this surface also had been painted with retro-reflective paint). An overlay of the resulting

spectra for a vibration signal at 4 kHz is shown in Figure 4.4 for five different CNR values.

Referring to Figure 4.4, the velocity signal at 4 kHz is constant for every case (all the curves reaching a value of -25 dB) but the demodulated noise floor rises quickly with decreasing CNR. (The large noise peaks below 2 kHz are constant in these plots. The source of these spurious peaks is discussed in Chapter V.) Despite the presence of the low frequency spurious peaks, one can see that for low frequencies (e.g., roughly 1 kHz) the noise floor does not rise nearly as rapidly with decreasing CNR as does the noise floor at 20 kHz. This is certainly true down to a CNR value of 42 dB. At 37 dB, however, the 1 kHz noise value jumps by roughly the same amount as was undergone by the 20 kHz noise. Willemin, Dandliker and Khanna (1988) illustrate this using a Revox 8760 FM tuner and show that for a high frequency (25 kHz) the noise level at the demodulated output increases linearly with decreasing CNR over most of the practical CNR range whereas at a lower frequency (500 Hz), the demodulated noise level is constant for CNR values down to 40 dB after which it increases rapidly.

A closer look at what happens for lower frequencies was obtained by operating the shaker at 400 Hz and using a total bandwidth of 2 kHz. The results are shown in Figure 4.5. Although the highest CNR starts at 56 dB (as opposed to 61 dB of the previous figure) and although the broadband noise floor is obscured somewhat by spurious noise peaks (60 Hz noise and multiples as well as spurious humps near 750 Hz and 1300 Hz), the trend is very evident; at 2 kHz the increase in the noise floor is slightly smaller than it is at higher frequencies but in the



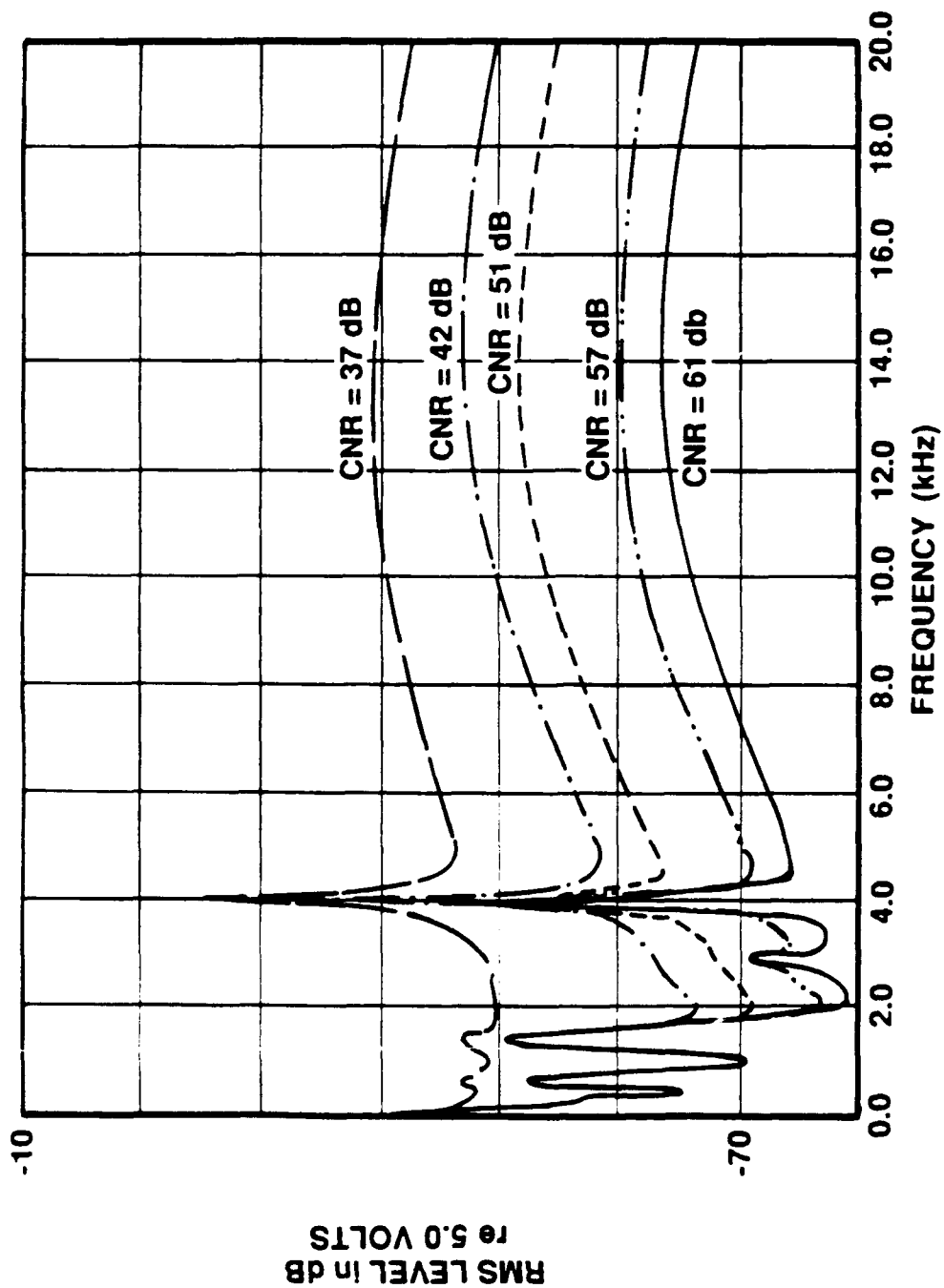


Figure 4.4 Comparison of Velocity Spectra for Different CNR Values With Signal at 4 kHz

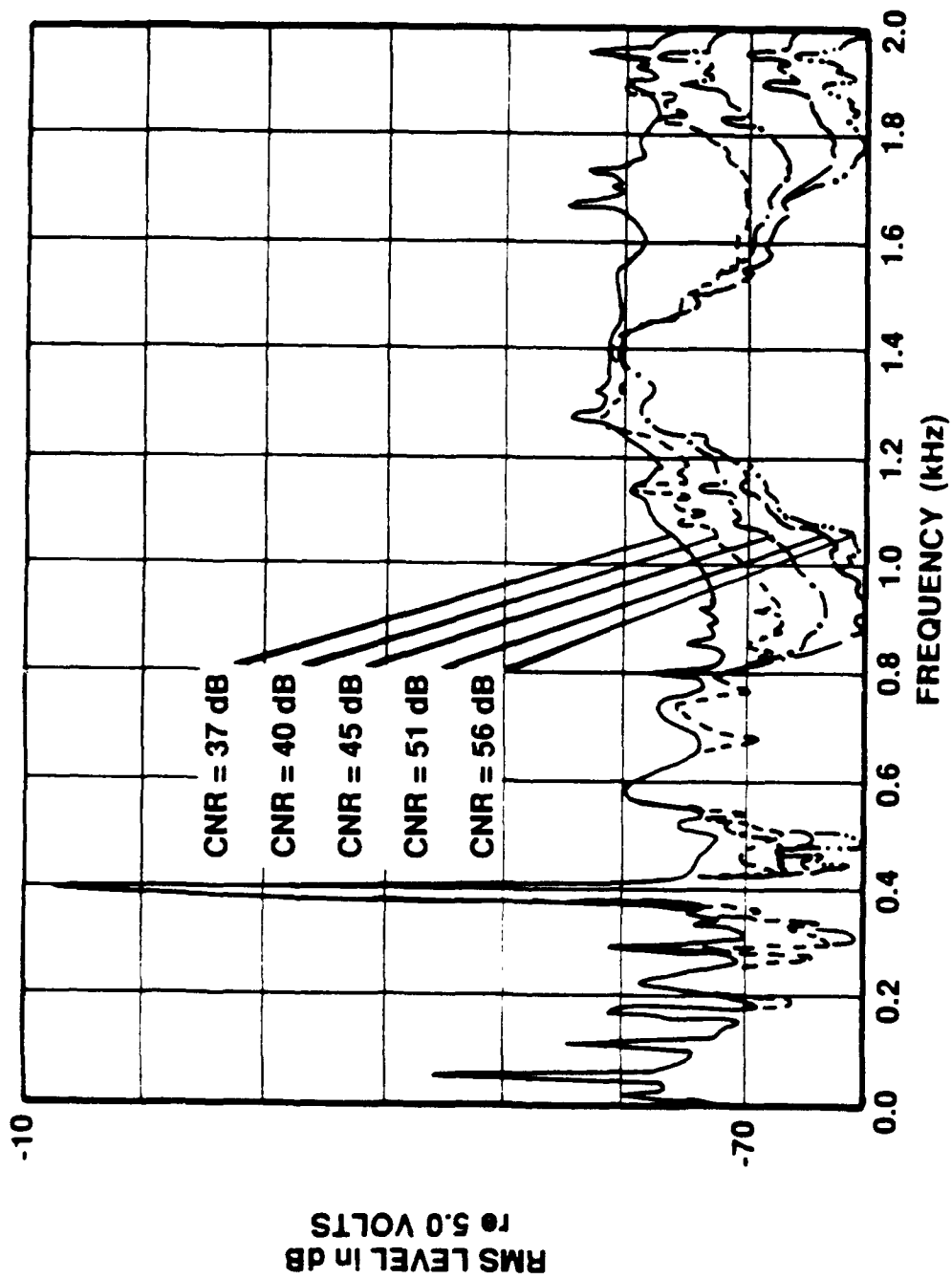


Figure 4.5 Comparison of Velocity Spectra for Different CNR Values With Signal at 400 Hz

vicinity of 1 kHz and below, the increase in noise floor is not nearly as severe.

For the instrumentation used in these tests typical values of CNR with a painted sample and a total laser power (split between the two vibrometer units) of 75 mW for 1500 mm focal length lenses (long standoff distances will decrease the received object beam power) ranged from roughly 61 dB to 42 dB which corresponds to roughly 0.30 to 0.05 peak-to-peak volts Doppler amplitude. With some searching on the sample, a CNR of 61 dB was obtainable, and a spot yielding 57 dB was easier to locate, but a conservative value of 51 dB for the CNR (corresponding to roughly 0.1 volts peak-to-peak) is realistic. For the painted surfaces in the structural intensity tests a value of at least 51 dB could be obtained for both units. Although in many cases one vibrometer beam would be higher or lower in the CNR value than the other, it takes very little displacement of the beam pair to find a location where one beam has at least 51 dB CNR and the other beam had the same or higher value. Therefore, for establishing the limits of the TCV system, it will be assumed that both channels have a CNR of 51 dB. This assumption results in a fairly high noise floor (10 dB above that for 61 dB CNR) but, as stated, this is a very practical (if not conservative) value for locating two beams on the specimen at a desired location without requiring a time-consuming search for optimum signals.

The noise floor for the PLL in vibrometer 1 is slightly different; the curve is roughly the same but PLL unit 1 was typically "noisier" by several dB. (This is due to the difference in sensitivity of the two units). The noise floors of the two PLL units for a CNR of 51 dB are

illustrated Figure 4.6. These were generated by focussing the vibrometer beams on a stationary object.

#### **SIGNAL-TO-NOISE RATIOS OF THE VELOCITY SIGNALS IN THE REFERENCE BEAM METHOD**

The noise floors of the two units have been established using typical values of the CNR which can be obtained easily on a surface treated with retro-reflective paint. (For untreated surfaces the surface plays an important role; smooth metallic surfaces can provide much better CNR values whereas rough dark surfaces will provide much smaller CNR values. In the case of smooth surfaces, it may be more difficult to assign a spatially averaged CNR value since the amount of backscattered light will depend greatly on the angle the laser beam makes with the normal to the object surface. For the metal objects used in these studies the paint on the surface provided a more consistent value of CNR as the laser beams were scanned over the object.) In cases where ease of scanning is important, the use of retro-reflective paint provides the optimum condition.

If one uses the noise floors shown in Figure 4.6, the SNR of the velocity signals can be determined if the velocity signal is known. The rms voltage signal obtained from a vibrating object is determined by using Equation 3.4 and converting the Doppler shift to a voltage by dividing by K, the PLL sensitivity:

$$V_{\text{rms}} = \frac{2\sqrt{2}\pi A f}{K\lambda} \cos\left(\frac{\theta}{2}\right) \quad (4.3)$$

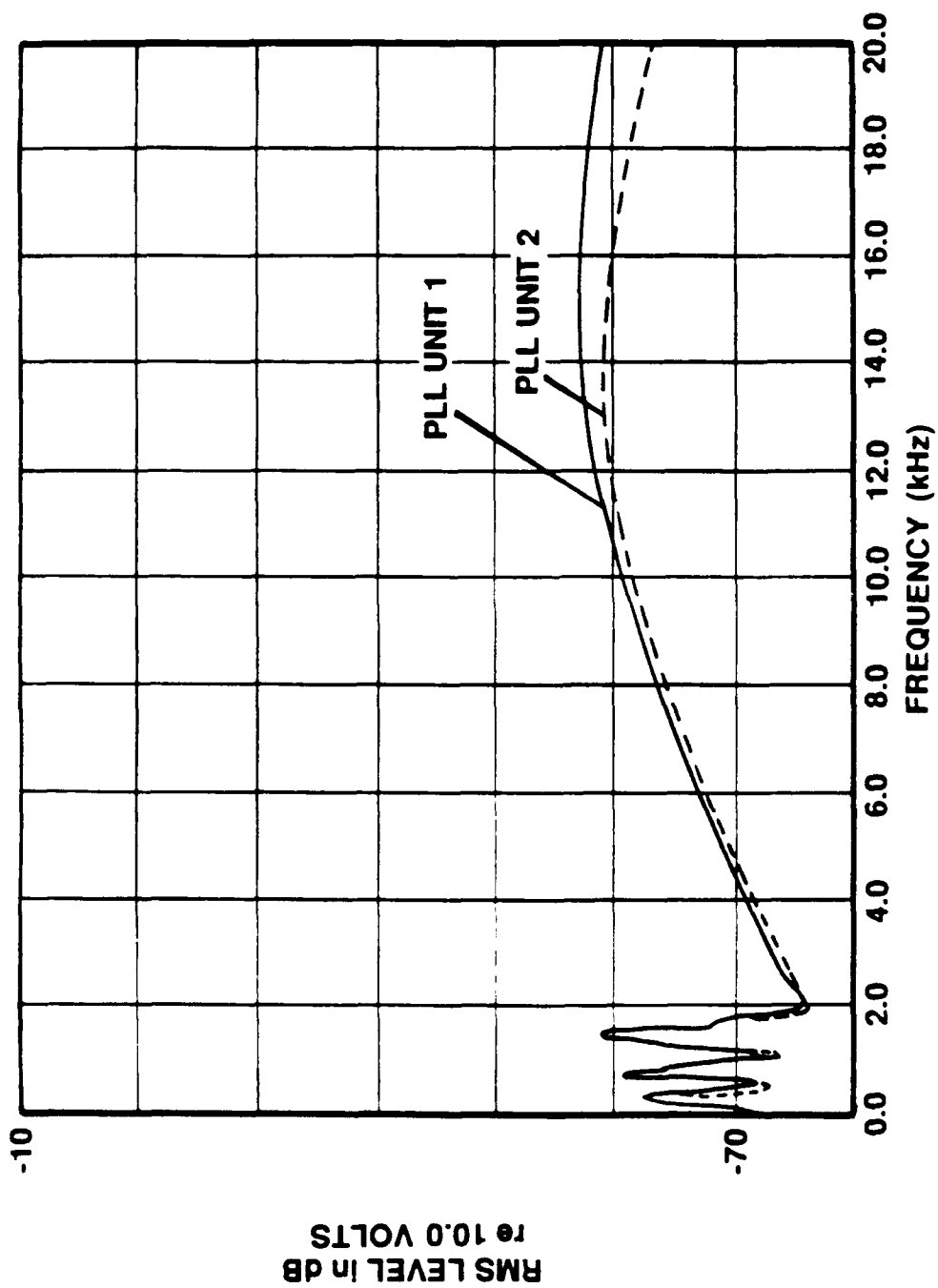


Figure 4.6 Noise Floors of the Two PLL Processors  
at Approximately 51 dB CNR

Here  $A$  is the displacement amplitude,  $f$  is the frequency in Hz,  $K$  is the PLL sensitivity in units of Hz/volt,  $\lambda$  is the laser wavelength (514.5 nm for green light), and  $\theta/2$  is the lens half-angle. This is the rms voltage obtained if the optical axis is normal to the object surface. The term  $\cos \theta/2$  arises in this situation due to the angle imparted to the beam by the focusing lens. In more general terms  $\theta/2$  is simply the angle the scanning beam makes with the normal to the object surface (assuming surface-normal deflections are being measured). For these studies two lenses with a focal length of 1500 mm were used. The value of  $\theta/2$  associated with such a long focal length would normally provide high sensitivity, although for the optical arrangement used in these studies,  $\theta/2$  was dictated by the second of the two scanning mirrors. (A more important advantage of the 1500 mm lenses is the large depth of field which allowed for scanning over the length of the object without refocusing.)

The PLL sensitivity, addressed in more detail in the next section of this chapter entitled "Signal Related PLL Characteristics," varies substantially with frequency. It ranges from approximately 3500 Hz per volt at a frequency of 2 kHz down to 2200 Hz per volt at a frequency of 12 kHz. As long as these values are obtained accurately, the variation with frequency does not present a problem as it becomes the calibration curve which can be applied automatically to the data obtained for the given vibrometer unit. It is in part the variation of  $K$  with frequency which accounts for the shape of the noise floor.

Using Equation 4.3 and converting it to a dB level with the appropriate reference voltage, signals for various vibration acceleration amplitudes can be superimposed on the noise floors of the

two PLLs to illustrate the SNR values which can be expected for a CNR of approximately 51 dB. This is done in Figures 4.7 and 4.8. A condition of normal incidence of the laser beam to the object is assumed ( $\theta/2 \sim 0^\circ$ ) and the values of the PLL sensitivity versus frequency are used from the PLL sensitivity results found in the section on signal related PLL characteristics.

Not appearing in the figures is the maximum signal which can be obtained before the PLLs begin to lose lock and output a distorted signal. This has an rms value of approximately minus 6.8 dB (re 10.0 volts). This was determined experimentally by using a signal from an FM signal generator as input to the PLLs. Another upper limit is the depth of field; the vibration amplitude must be such that the object remains within the depth of field for the lens being used. For 1500 mm lenses used in this setup, the depth of field was approximately two cm which is large enough not to put any practical restrictions on the ability to obtain a vibration signal.

The data in Figures 4.7 and 4.8 can be used to estimate the SNR values in the two vibrometer units as a function of the vibration amplitudes at two points on the object and the vibration frequency. The two SNR values can then be used to calculate the random error in the estimate of the imaginary part of the cross-spectrum used for the structural intensity measurement. This is done in Chapter V.

#### SIGNAL RELATED PLL CHARACTERISTICS

PLL sensitivity in this study is defined as the ratio of the amplitude of frequency deviation from the carrier frequency in the FM signal (input to the PLL) divided by the amplitude of PLL voltage

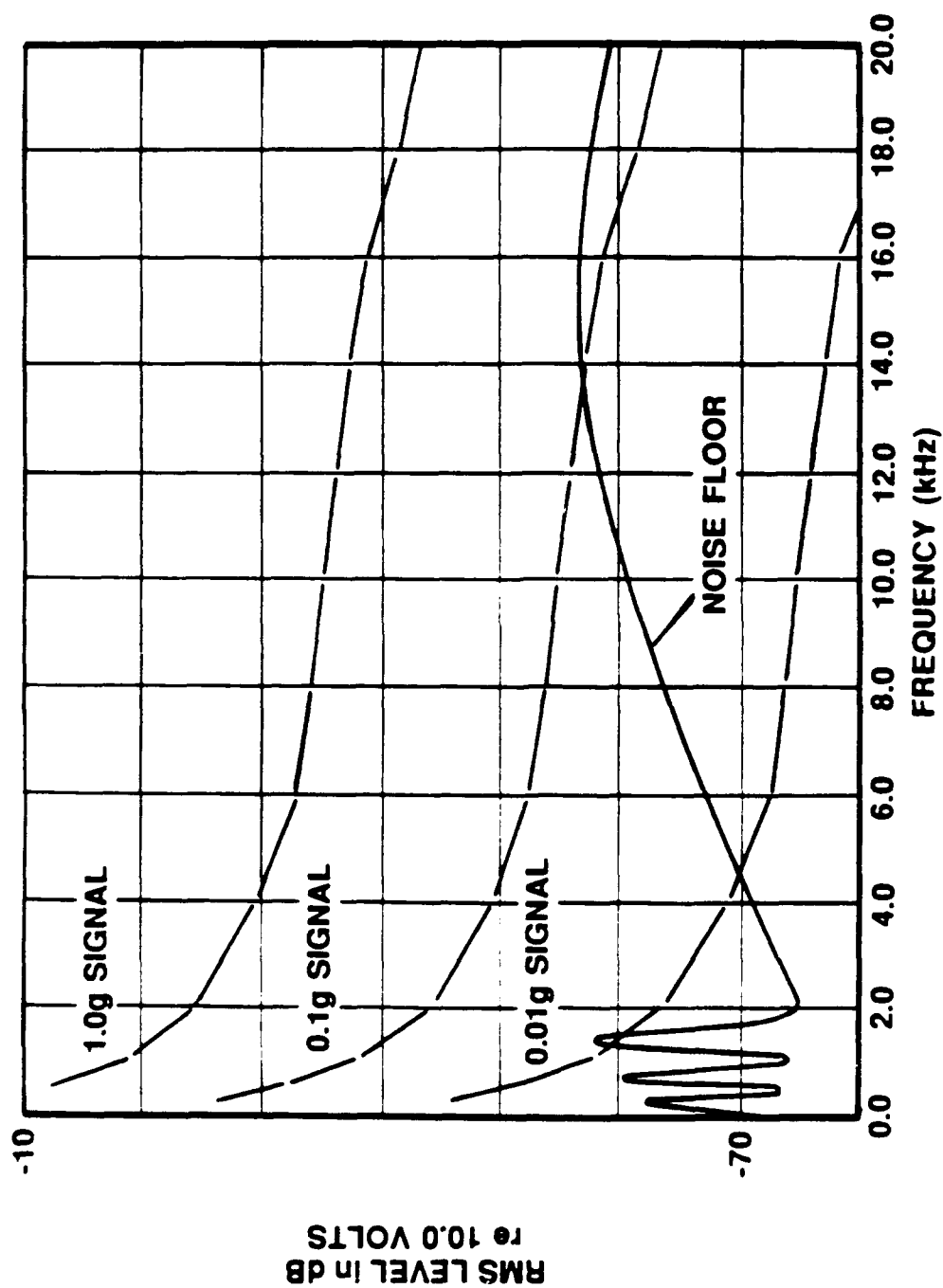


Figure 4.7 Noise Floor at Approximately 51 dB CNR for PLL Unit 1 (Signals Corresponding to Acceleration Amplitudes in g Are Also Shown)



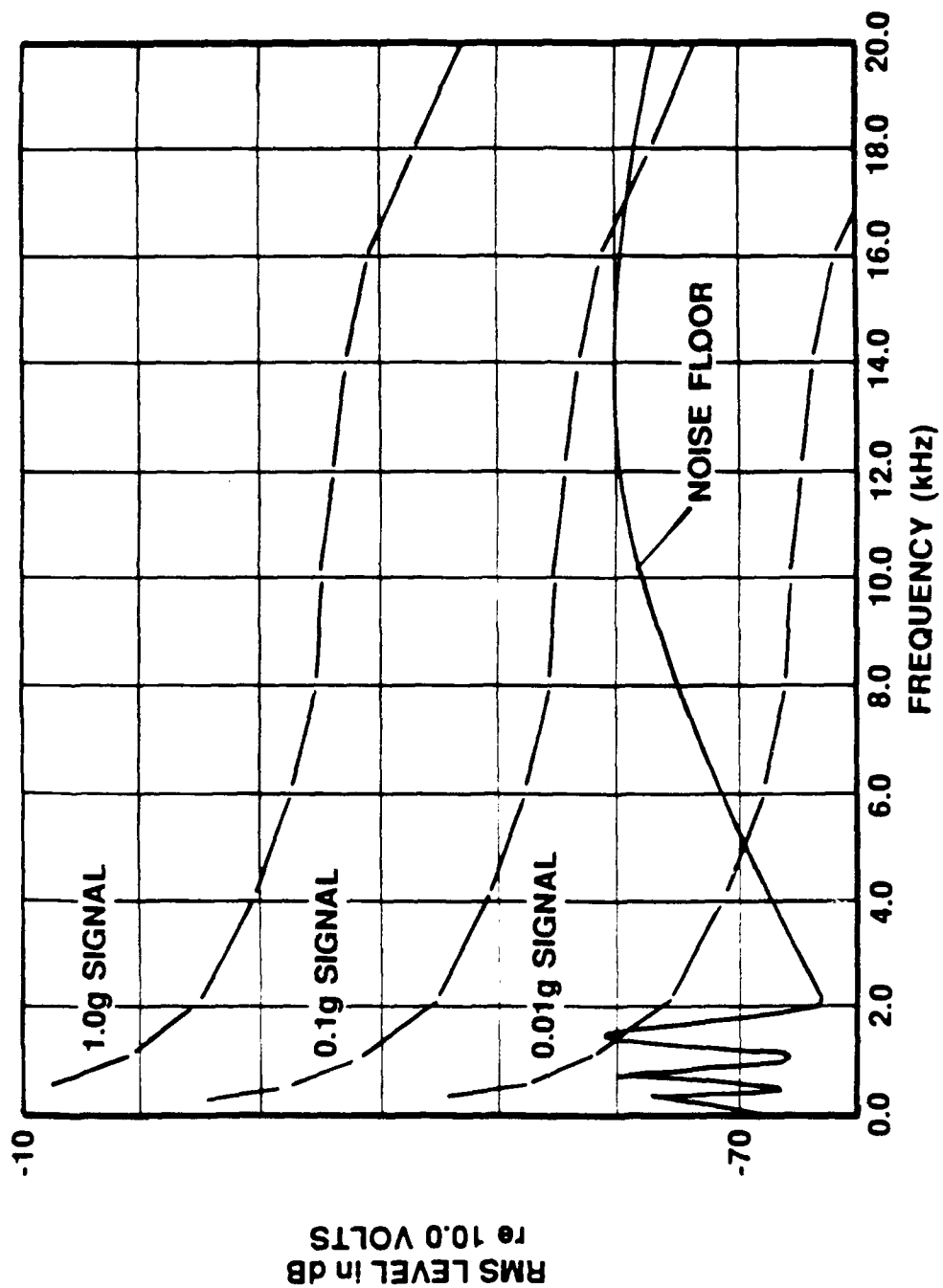


Figure 4.8 Noise Floor at Approximately 51 dB CNR for PLL Unit 2 (Signals Corresponding to Acceleration Amplitudes in g Are Also Shown)

output. This sensitivity is denoted as  $K$  and has units of Hz/Volt. A determination of the sensitivity of the two PLL processors was made by inputting an FM signal to the units (from an FM signal generator) and, for a prescribed amplitude of frequency deviation from the 50 kHz carrier, measuring the amplitude of PLL voltage output (as described previously). This procedure was followed in generating the PLL sensitivity curves in Figures 4.9 and 4.10 (for higher frequencies) and Figures 4.11 and 4.12 (for lower frequencies). The frequency on the horizontal axis is the modulation frequency at which the amplitude ratios were taken (this is equivalent to the vibration frequency of the object). Appearing in each of the figures are four curves: one which corresponds to a peak-to-peak frequency deviation of 3 kHz, and the others corresponding to deviations of 5 kHz, 10 kHz and 20 kHz. These are typical of the values occurring in the intensity studies.

In Figures 4.9 and 4.10 there is a large overall sensitivity to modulation frequency whereas in Figures 4.11 and 4.12 (less than 2 kHz modulation frequency), the overall sensitivity is fairly flat with approximately 5% variation over the frequency range. The most important point, however, is that the PLL sensitivity appears to show a slight dependency on the amplitude of frequency deviation (corresponding to the vibration amplitude of the object). These data would indicate a slight nonlinearity in the PLLs which could act to cause small amplitude errors in intensity readings or at least to make the calibration data more complicated. However, it is more probable that these small differences (of typically 3%) are at least in part, due to small errors in the data acquisition process because of, for example, the bin size in the analyzer used to determine the exact frequency deviation or the

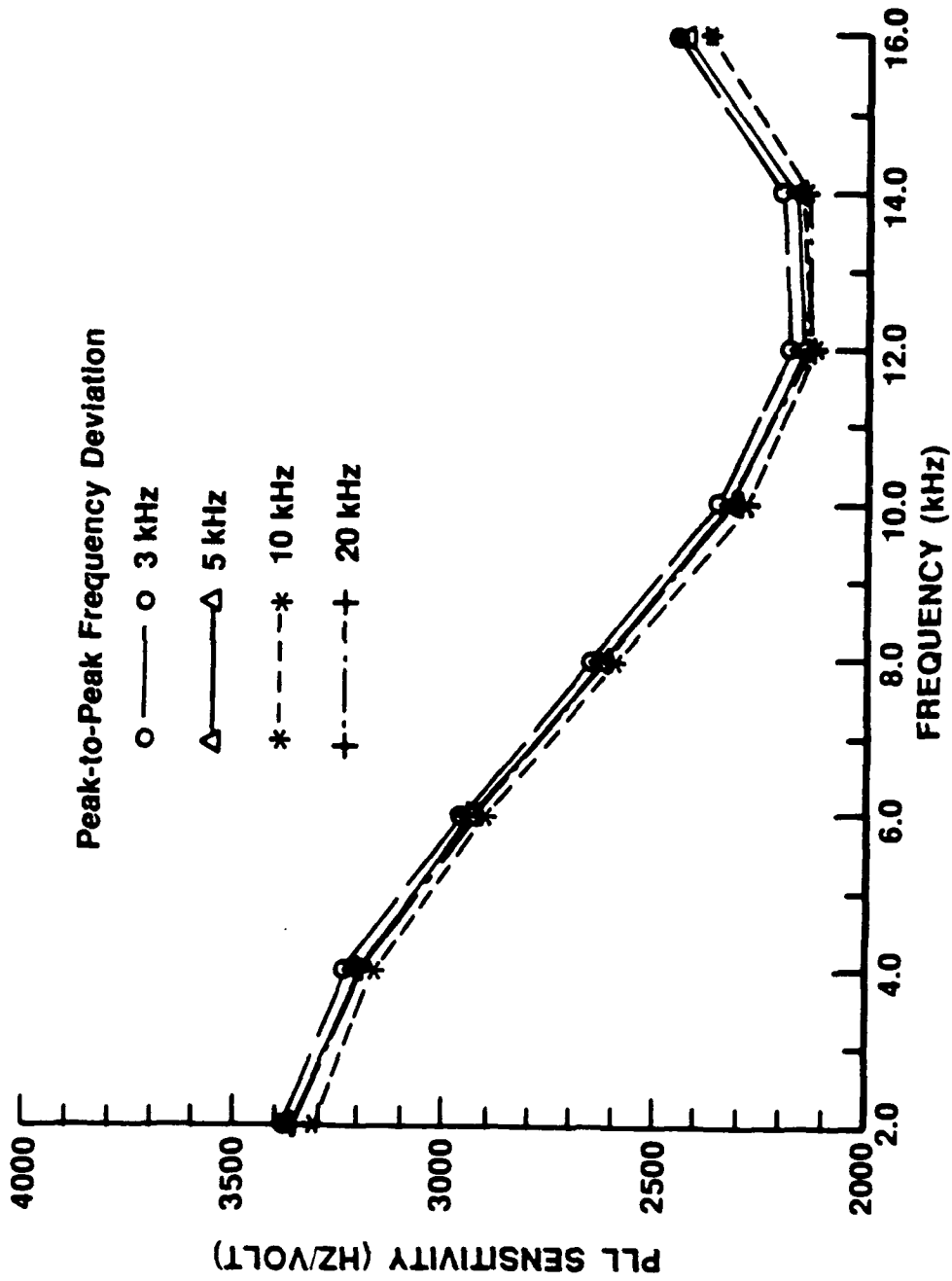


Figure 4.9 Sensitivity Curves for PLL Unit 1 at High Frequencies Versus Frequency Deviation

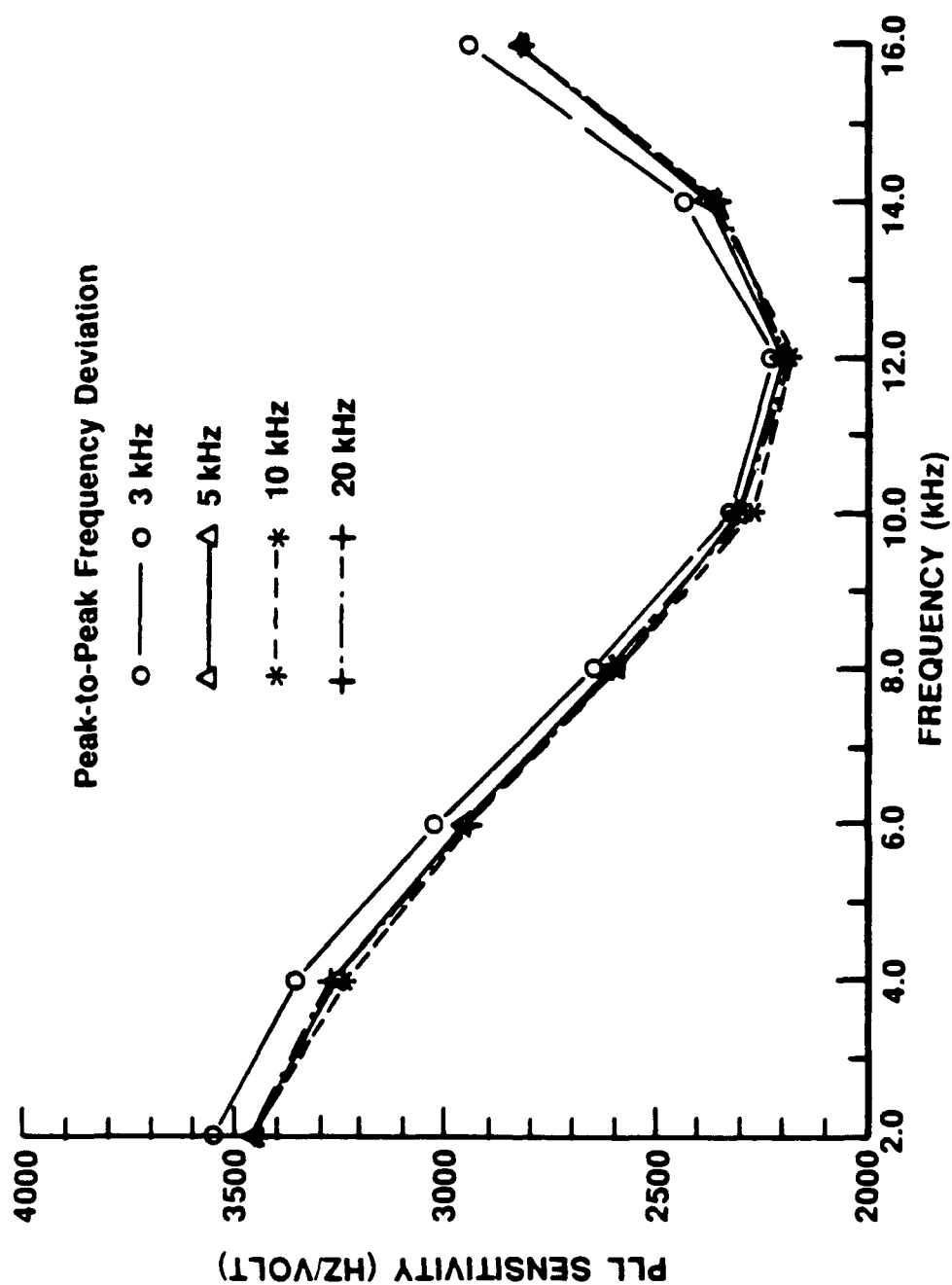


Figure 4.10 Sensitivity Curves for PLL Unit 2 at High Frequencies Versus Frequency Deviation

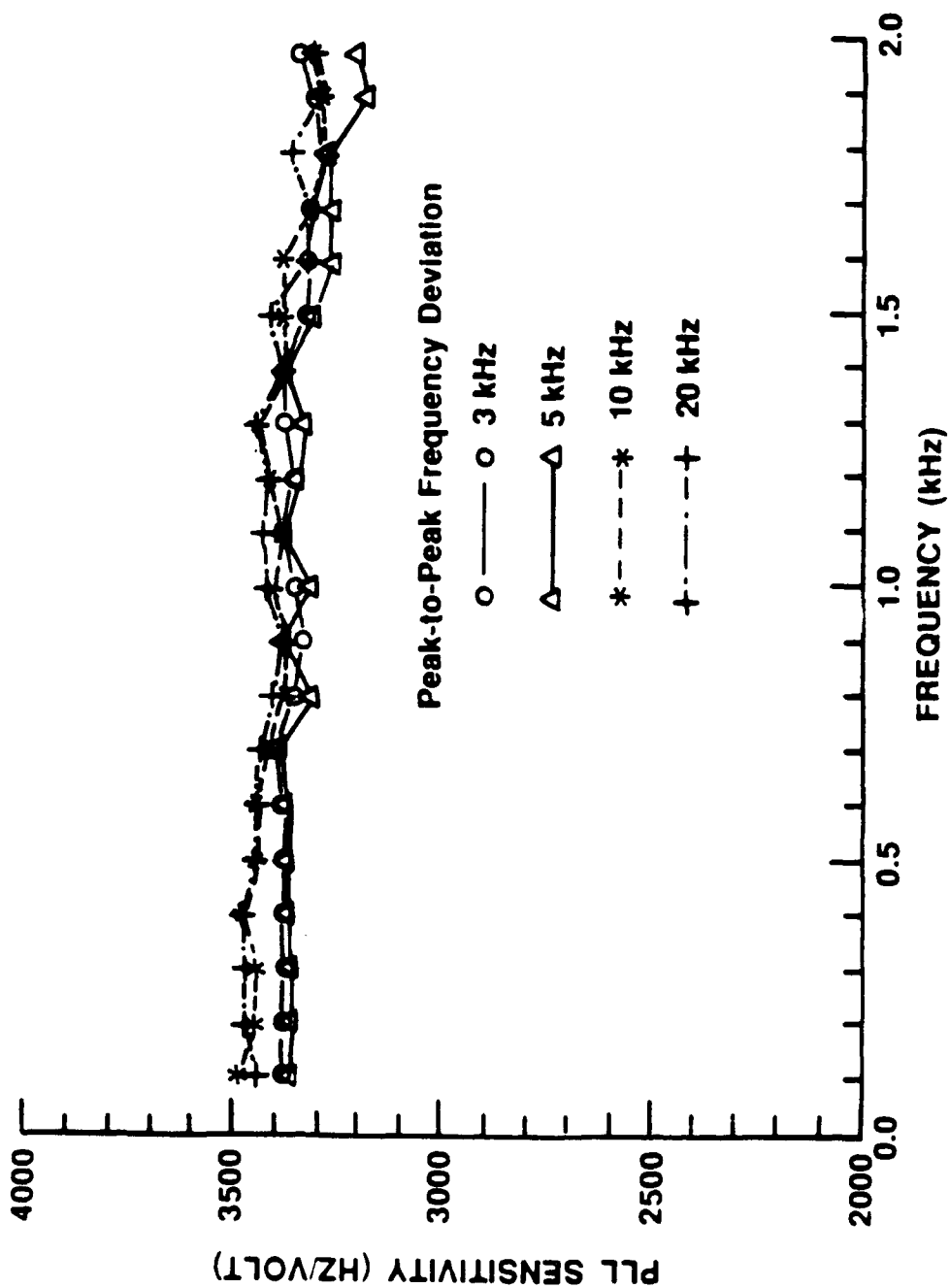


Figure 4.11 Sensitivity Curves for PLL Unit 1 at Low Frequencies Versus Frequency Deviation

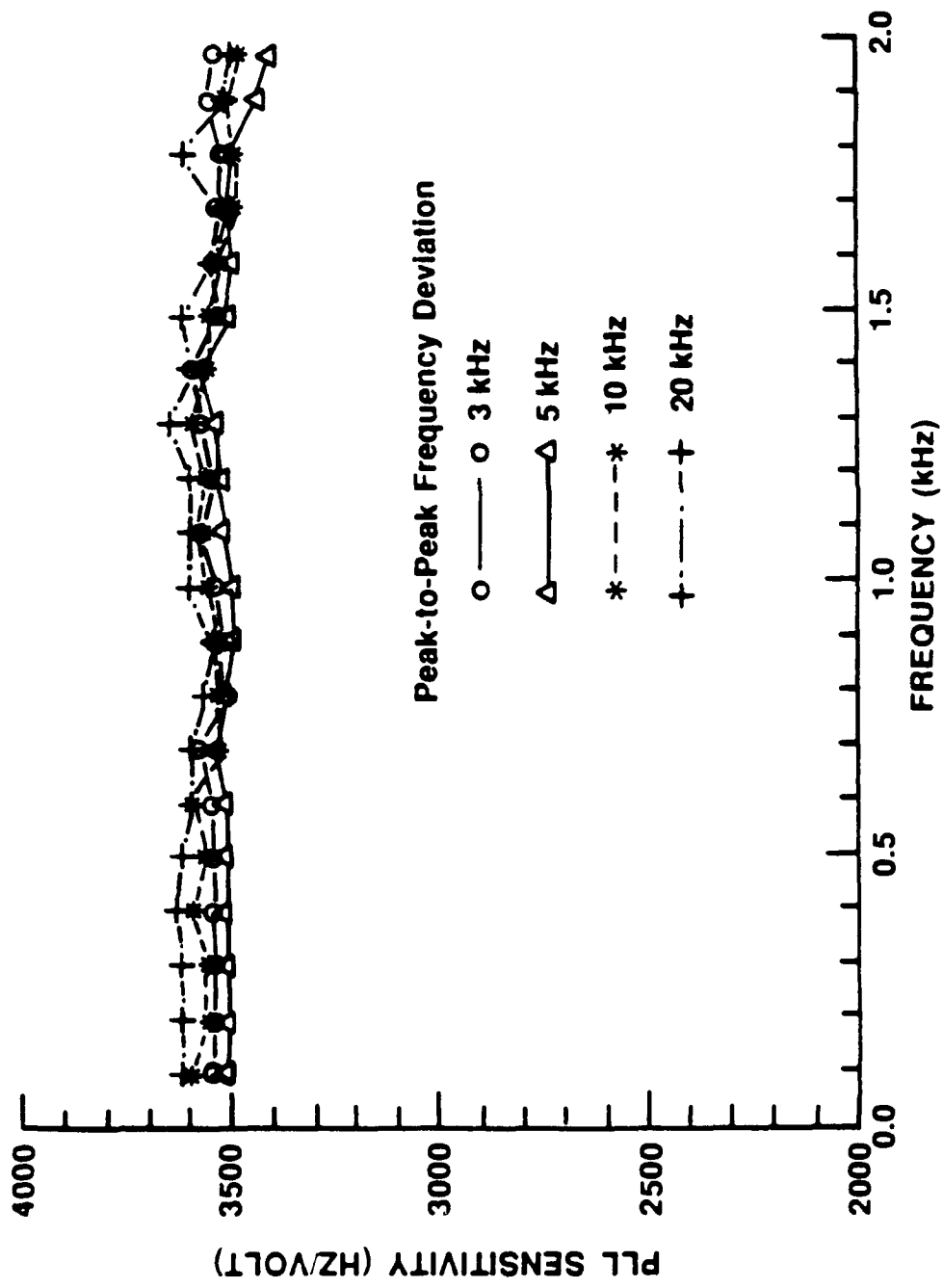


Figure 4.12 Sensitivity Curves for PLL Unit 2 at Low Frequencies Versus Frequency Deviation

influence of the demodulated noise floor on the voltage reading of the smaller amplitude signals.

Another parameter which can potentially influence PLL sensitivity values is the amplitude of the Doppler signal (i.e. the amplitude of the FM carrier signal) input to the PLL processors. PLL processors are ideally insensitive to amplitude modulation and only sensitive to frequency modulation. But in practice PLLs typically employ a means of increasing the amplitude of the signal and "clipping" it to some fixed value to prevent amplitude sensitivity. The PLL processors employed in this apparatus did not make use of this process and, therefore, were tested to investigate whether the Doppler amplitude might influence sensitivity.

Doppler amplitudes typical of the range of amplitudes occurring experimentally (0.4 volts and 0.05 volts peak-to-peak) were input to the PLLs from the FM signal generator and the PLL sensitivity was determined as previously described. Results showed negligible influence of the Doppler amplitude on sensitivity for Doppler amplitudes in this range. Examples are shown in Figures 4.13 and 4.14 for the two PLLs.

The phase bias in the two PLL processors is addressed in Chapter II. The data show the overall PLL phase differences up to 20 kHz and the section explains how these data was obtained.

A final but important consideration was the concern that the phase angle for signals output from the two PLLs might be subject to random fluctuations due to thermal changes in the analog filters of the PLLs. Equally, similar effects could occur due to the heating of the remaining electronics in each vibrometer system. This randomness in the measured

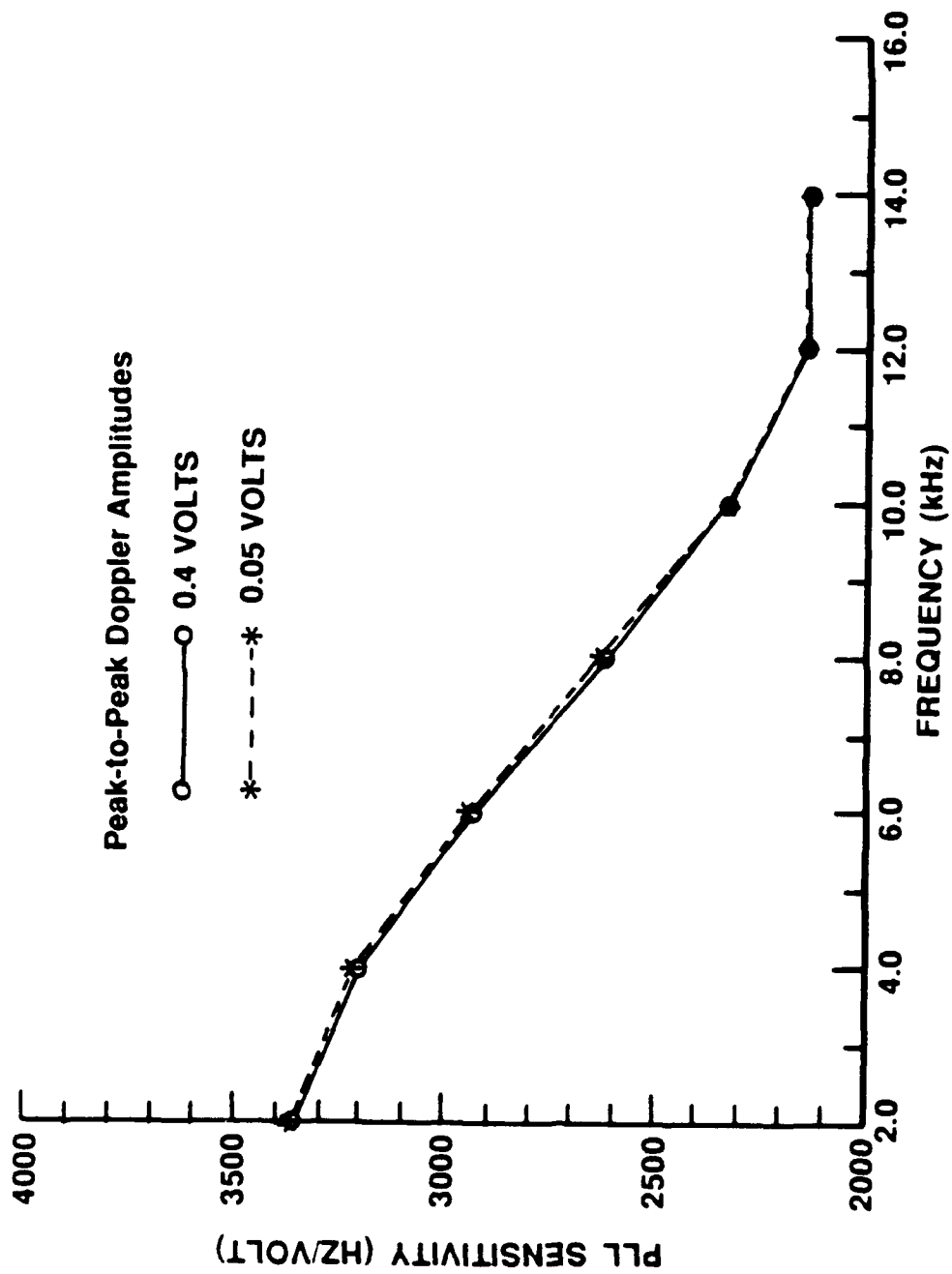


Figure 4.13 Sensitivity Versus Amplitude for PLL Unit 1



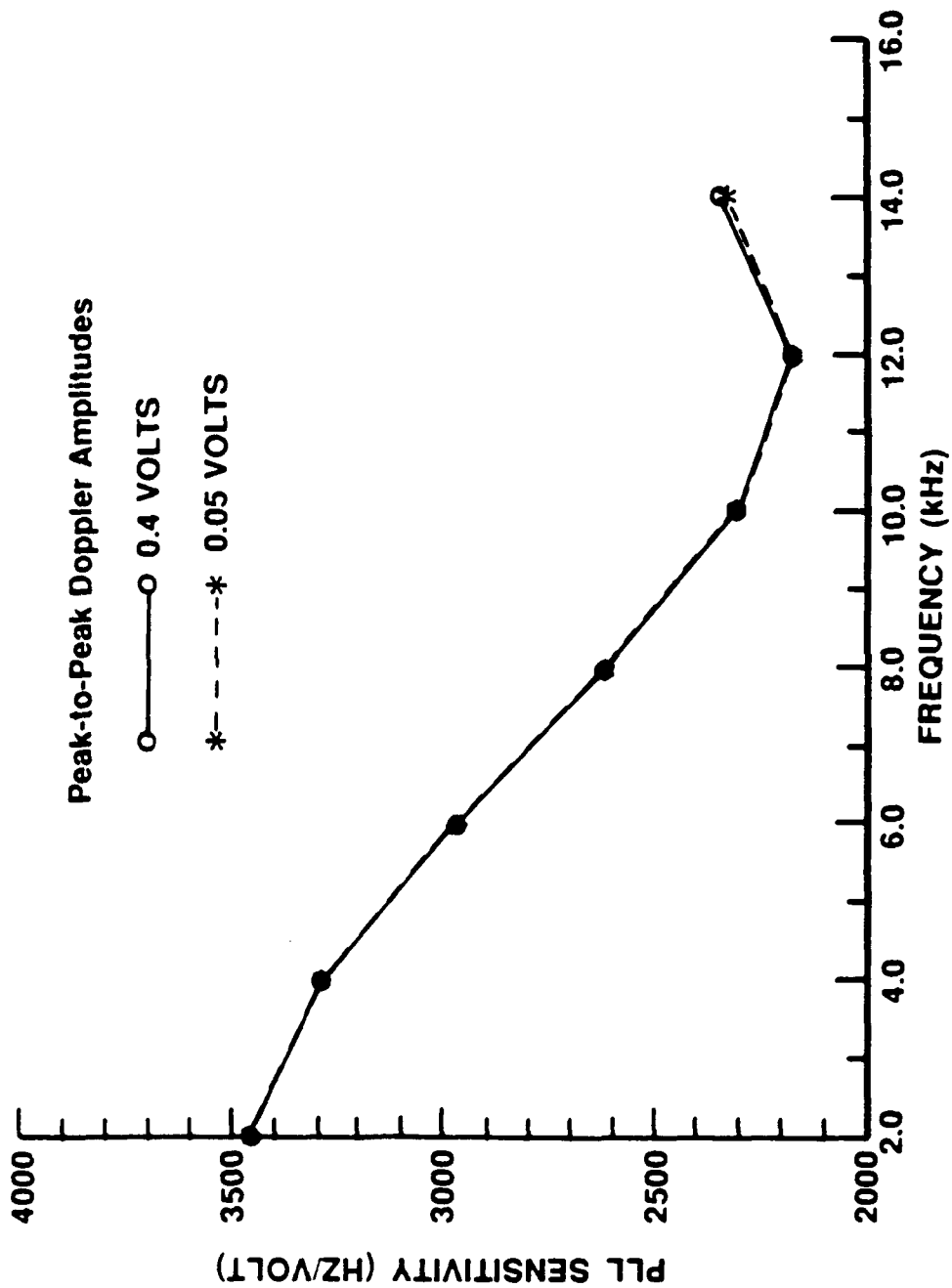


Figure 4.14 Sensitivity Versus Amplitude for PLL Unit 2

phase angle could have very adverse effects on the ability of the TCV system to accurately measure the structural intensity, especially in highly reverberant cases where phase angle measurements must be extremely accurate to provide reliable results.

A series of three tests was conducted to check for this possibility. For two tests the two vibrometer beams were focused on a small, thin, square piece of aluminum glued to a shaker face. The aluminum was painted with retro-reflective paint to insure a good "Doppler amplitude" (CNR). The shaker was operated at a single frequency and the phase angle between the two demodulated vibrometer signals was obtained at the excitation frequency. For the third test the FM signal was generated electronically and input directly to the two PLLs. The phase angle reading was taken frequently during each test. One test ran approximately ten hours, the other tests approximately two hours. In every case the demodulated SNR values and the number of spectral averages taken were such that SNR related random error was negligible.

Results showed no variation of phase angle to within 0.1 degrees beyond the first fifteen to twenty minutes of operation. Before this time the data showed fluctuations in the phase difference of 0.2 degrees. (This was true for both the "optical" as well as "electronic" tests.) Standard procedure then, for precise phase measurements, requires a warm-up time for the electronics (particularly the PLL processors) of twenty minutes. By that time the PLL phase bias error reaches a steady value.

## Chapter V

### SOURCES OF ERROR IN FLEXURAL INTENSITY MEASUREMENTS DUE TO TCV SYSTEM CHARACTERISTICS

#### INTRODUCTION

In the previous chapter, factors influencing signal-to-noise ratio of each vibrometer channel as well as several remaining details covering amplitude and phase integrity were addressed. The latter points were shown not to be a problem for the flexural intensity tests but the signal-to-noise ratio is always a consideration in intensity measurements since it is related to random error. A second source of error in intensity measurements is coherent noise. This is unusual in structural intensity probes which use accelerometers but it has been found to exist at certain frequencies in the TCV system. This chapter addresses these sources of error. It illustrates the influence of the FM signal carrier-to-noise ratio and the level of flexural intensity itself can have on the random error. In the latter half of the chapter a photodetector-switching technique is shown to remove the effects of coherent noise. This technique is also shown to remove a more familiar source of error in intensity measurements: namely phase bias error which exists when there is a phase difference in the two vibrometer signals caused by the vibrometer electronics. (A phase bias is known to exist in the TCV PLL processors as noted in Chapter II.)

# **RANDOM ERROR IN TCV FLEXURAL INTENSITY MEASUREMENTS**

In any intensity measurement system, background noise, which is significant relative to the signals in the two transducer channels, can cause a variability in the measured cross-spectrum. This causes the measured cross-spectrum to asymptotically approach its true value only as the number of ensemble averages increases. This is the case when the background noise is uncorrelated between the channels. For this situation Seybert (1981) has shown that the normalized random error in the imaginary component (for situations where the phase angle between the two points is very small and the coherence is less than unity) can be expressed as

$$\epsilon_r[\text{Im}(G_{12}(f))] = \frac{\cot \phi_{12}}{\sqrt{n_d}} \sqrt{\frac{1 - \gamma_{12}^2(f)}{2\gamma_{12}^2(f)}} \quad (5.1)$$

where  $\phi_{12}$  is the phase angle,  $n_d$  is the number of spectral averages, and  $\gamma_{12}^2$  is the ordinary coherence between the two channels.

On a reverberant beam where both travelling and standing waves can exist, the phase angle between points spaced  $\Delta x$  apart can be reduced below  $k\Delta x$ . If the two receivers straddle an antinode, for example, the phase difference,  $\phi_{12}$ , is such that the previous equation can be approximated as (Carroll 1987)

$$\epsilon_r[\text{Im}(G_{12}(f))] = \frac{2}{\sqrt{n_d}} \frac{\cot k\Delta x}{Lk\eta} \sqrt{\frac{1 - \gamma_{12}^2(f)}{2\gamma_{12}^2(f)}} \quad (5.2)$$

where  $L$  is the beam length and  $\eta$  is the loss factor.

Due to the extraneous background noise present in each channel, the coherence of each channel is reduced below unity by the relation (Bendat, Piersol 1980)

$$\gamma_{x1}^2 = 1 - \frac{G_{nn}(f)}{G_{11}(f)} \quad (5.3)$$

where  $G_{nn}(f)$  and  $G_{11}(f)$  are the noise and signal autospectra respectively. For two channels the coherence between the signals becomes

$$\gamma_{12}^2 = \left[ \frac{1}{\left(1 + \frac{G_{nn}}{G_{11}}\right) \left(1 + \frac{G_{mm}}{G_{22}}\right)} \right] \quad (5.4)$$

where  $G_{mm}$  and  $G_{22}$  are the noise and signal autospectra in channel two. The above equations assume that the system is a constant parameter linear system, that the channel noise is uncorrelated with itself (and with the signals), and that all unknown deviations from this ideal case can be considered as uncorrelated background noise at the input.

The previous equations, as well as the TCV background noise levels and equations predicting the vibrometer rms signal voltage distribution on the reverberant beam, can all be used to illustrate the influence of two parameters on the random error in the intensity measurements using the TCV system. The first parameter influencing random error is the CNR value. This is the "carrier to noise ratio" and pertains to the clarity of the Doppler signal available for detection. A low CNR will produce a high noise floor in the vibrometer output and conversely, a high CNR will produce a low noise floor in the vibrometer output. (The CNR is related linearly to the intensity of backscattered light, linearly to the quantum efficiency of the detector, and related to the square of

heterodyne efficiency). The second parameter influencing random error is the structural power flow itself.

In the following two examples an allowable random error of 10% will be assumed and the number of spectral averages,  $n_d$ , required to keep the maximum error at 10% will be calculated. From the previous equations the required number of spectral averages can be expressed as:

$$n_d = \frac{2}{e_r} \cdot \left[ \frac{\cot k\Delta x}{kL\eta} \right]^2 \left[ \frac{(1 - \gamma_{12}^2)}{2\gamma_{12}^2} \right] \quad (5.5)$$

The noise-to-signal ratios required for calculating the values of  $\gamma_{12}^2$  can be obtained from the experimentally determined noise floors as well as the vibrometer signal strength. Signal strength in this application is a function of the power flow (or power input)  $\Pi$ , the beam length,  $L$ , the position on the beam, the damping,  $\eta$ , the frequency,  $f$ , wavenumber,  $k$ , the modulus and moment of inertia of the beam,  $Y$  and  $I$ , the Doppler shift conversion equation, and finally the PLL sensitivity,  $K$  (see Equation 3.13 and subsequent paragraph).

For example, for the aluminum beam discussed in Chapter III, in the case where  $f = 2520$  Hz,  $\eta = .013$ , the influence of the CNR can be illustrated. Assume a laser beam separation of  $0.1 \lambda$  (which yields a low phase angle for illustration purposes), a value of phase locked loop (PLL) sensitivity of 3400 Hz/volt, and a laser beam angle such that  $\cos \theta \sim 1$ . Also note that the previous equations assume the center of the laser beams to be positioned at the antinode. Table 5.1 shows the resulting influence of the CNR (assuming it is the same in both channels) on the number of samples necessary to obtain a maximum normalized random error of 10% in the quadrature spectrum.

Table 5.1

Influence of CNR on the Number of Samples  
Required for 10% Random Error in Power Flow-  
Measurement With the Reference Beam Mode

<u>CNR(dB)</u>	<u><math>\gamma_{12}^2</math></u>	<u><math>n_d</math></u>
61	.98	52
57	.96	107
51	.83	524
42	.65	1378

The variations in the CNR can be viewed as variations in the intensity of backscattered light, variations in the photodetector quantum efficiency, or variations in the square of the heterodyne efficiency as in Equation 4.2.

For Table 5.1, it is also assumed that the power flow is  $2.5 \times 10^{-11}$  watts. Detecting this low power flow is possible because of the fact that the signals are from the vicinity of the antinode where maximum signal quality is obtainable. (The antinodal region was chosen for this example since it is the region of minimum phase gradient on the reverberant beam and consequently maximum random error). For higher power flows the coherence quickly becomes unity (due to the signal strength) and the CNR effects are much less influential.

If instead of varying the CNR it is kept fixed and the power flow is varied, the influence of power flow on the random error in the TCV system can be illustrated. For the same beam, damping and vibration frequency, Table 5.2 relates the power flow to the required number of averages for a maximum random error of 10% in the quadrature spectrum, if the laser beams are positioned over the antinodal area and both

channels are receiving a CNR value of 51 dB (which has been established experimentally as a typical value for the system when targeting surfaces coated with retro-reflective paint).

Table 5.2

Influence of Power Flow on the Number of Samples  
Required for 10% Random Error in Power Flow-  
Measurement With the Reference Beam Mode

$\Pi$ (Watts)	$\gamma_{12}^2$	$n_d$
$2.5 \cdot 10^{-10}$	.98	52
$1.0 \cdot 10^{-10}$	.95	135
$5.0 \cdot 10^{-11}$	.91	253
$2.5 \cdot 10^{-11}$	.83	524
$1.0 \cdot 10^{-11}$	.65	1378

(For  $\left(\frac{G_{nn}}{G_{11}}\right)^2 \ll 2 \left(\frac{G_{nn}}{G_{11}}\right)$  the relationship between the power flow and the required number of spectral averages is a simple inverse relationship.)

Random error in the measured flexural intensity using the TCV system, then, can be a problem if the CNR value is small (providing a high noise floor) and/or the power flow is small (providing a low signal in the two channels). The previous examples are intended to indicate the sensitivity of the random error to CNR and power flow. A rigorous mathematical model linking all the optical and mechanical parameters to random error could be established if the relationship between CNR and the demodulated noise floor could be quantified for the two PLL processors as a function of modulation frequency. This is most reliably done on an experimental basis as indicated in Figures 4.4 and 4.5. Some



experimental curves for a Revox B760 FM Tuner are illustrated in Willemin, Dandliker, and Khanna (1988).

#### COHERENT NOISE

The source of the two spectral peaks consistently showing up in the two vibrometer noise floors in the reference beam mode at approximately 750 and 1300 Hz was investigated. This noise can be due to a number of possible sources including: vibration of the optics due to some common source such as the laser head or laser power unit, FM noise in the Bragg cell drivers or downmixers, noise in the PLL units, laser "intermode beating" noise, laser intensity fluctuation noise, and possibly photodetector noise. Before these possibilities were investigated, a check on the coherence of these common spectral peaks was conducted.

The two laser beams were focused on a stationary object while the coherence of the velocity signals was calculated and averaged with an FFT analyzer. Results indicated zero coherence up to 20 kHz except at the two spectral peaks where the coherence approached 0.95. (The coherence between one of the vibrometers and an accelerometer on the stationary object was zero at these frequencies indicating that the "stationary" object was not the source of these signals.) The fact that the noise in the two vibrometer systems is coherent can have a potentially harmful effect on intensity measurements at these frequencies.

The possible sources of these coherent noise peaks were then investigated. Vibration of the optics due to airborne and structureborne paths from the laser head as well as airborne paths from

the laser power supply was excluded when accelerometer measurements of these components provided zero coherence with the noise in the vibrometer units. FM noise in the Bragg cell drivers could also give an apparent vibration signal. However, the 40 MHz signal used to drive the Bragg cells, when heterodyned directly down to 50 kHz and demodulated by one of the PLLs, provided a noise floor with no peaks at these frequencies. Considering this same result, noise in the PLLs which might provide erroneous vibration peaks also was discarded as the cause.

Further evidence that the noise source was not in the electronics was found when the Bragg Cell driver/downmixing box and one of the PLLs were replaced by a commercial "vibrometer controller." This is a new processor adaptable to this instrumentation. The spectrum of the controller output also showed the identical spectral peaks in its noise floor.

The most likely source of these noise peaks is the laser. Unstabilized multi-frequency lasers can cause Doppler signals due to heterodyning of the reference beam and unwanted light of a slightly different frequency (Buchave 1975). However, an etalon was used in the laser and a test for the presence of a single longitudinal mode, using an optical spectrum analyzer, showed that all longitudinal modes but one were successfully suppressed. This fact, combined with the fact that the optical heterodyning referred to above would most likely cause a D.C. vibration signal rather than peaks at certain frequencies (i.e. it would not be a source of FM noise in the modulated signal) indicates that optical beating from the laser was not the source of the two spectral peaks. It should be noted that during those tests the laser

tube was replaced. The spectral peaks were still present indicating that the problem was not a characteristic of the particular tube.

Another possible source of the common noise peaks is laser intensity fluctuations. These would appear as Doppler signals to the electronics. However, the fluctuations would again have to be FM in nature; a steady fluctuation, regardless of its frequency would cause only a DC component in the demodulated signal. Consequently, FM noise in the laser intensity remains the most probable cause of these peaks in the modulated noise floor.

A very effective means of eliminating intensity noise is to use a "balanced detection" arrangement (see, for example, Stierlin, Battig, Henchoz, and Weber 1986). This effectively cancels out any noise present in the reference beam. This technique would reduce both intensity noise as well as optical beating noise described previously.

Later studies showed, however, that these coherent noise peaks do not exist in the differential Doppler mode. This indicates that laser intensity fluctuations are not the source of the coherent noise in the reference beam setup nor in anything related to the electronics. The noise is most likely optical in origin (i.e. it may be FM noise in the laser). It may be that the path length difference between the object and reference beams accounts for this noise in the reference beam setup as opposed to the differential Doppler setup. (It should be noted that this problem was not a manifestation of light re-entering the laser since use of an optical isolator did not influence these noise peaks).

## REMOVAL OF COHERENT NOISE AND PHASE BIAS EFFECTS

It has been shown that the two-channel vibrometer (TCV) system, when set up in the reference beam mode (as used for flexural intensity readings), contains fairly broad peaks in the noise floor in the vicinity of 750 and 1300 Hz. This noise is random but stationary. The coherence between these noise peaks, as computed on an FFT analyzer, is nearly unity at these frequencies as shown in Figure 5.1. At these frequencies and adjacent frequencies the measurement of the intensity will be altered by this coherent noise and provide erroneous results if left uncorrected.

The error stems from the addition of the noise cross-spectrum to the true cross-spectrum as illustrated in the Argand diagram in Figure 5.2. If the noise cross-spectrum,  $G_{nm}$ , has some non-zero phase angle,  $\phi_n$ , the imaginary part of the resultant (measured) cross-spectrum,  $G_{xy}$ , will not equal the imaginary part of the true cross-spectrum,  $G_{uv}$ , and a measurement error in the active intensity will result. Both the relative magnitude as well as the phase of  $G_{nm}$  will influence the severity of this error. Fortunately, photodetector switching, normally employed to remove bias error due to phase mismatch in intensity measurements will also serve to remove coherent noise for the TCV system.

Regardless of the origin of these peaks and regardless of their mutual phase angle, their effect can be removed by photodetector switching. Removing the error entails the following: computing the imaginary part of the measured cross-spectrum, switching the

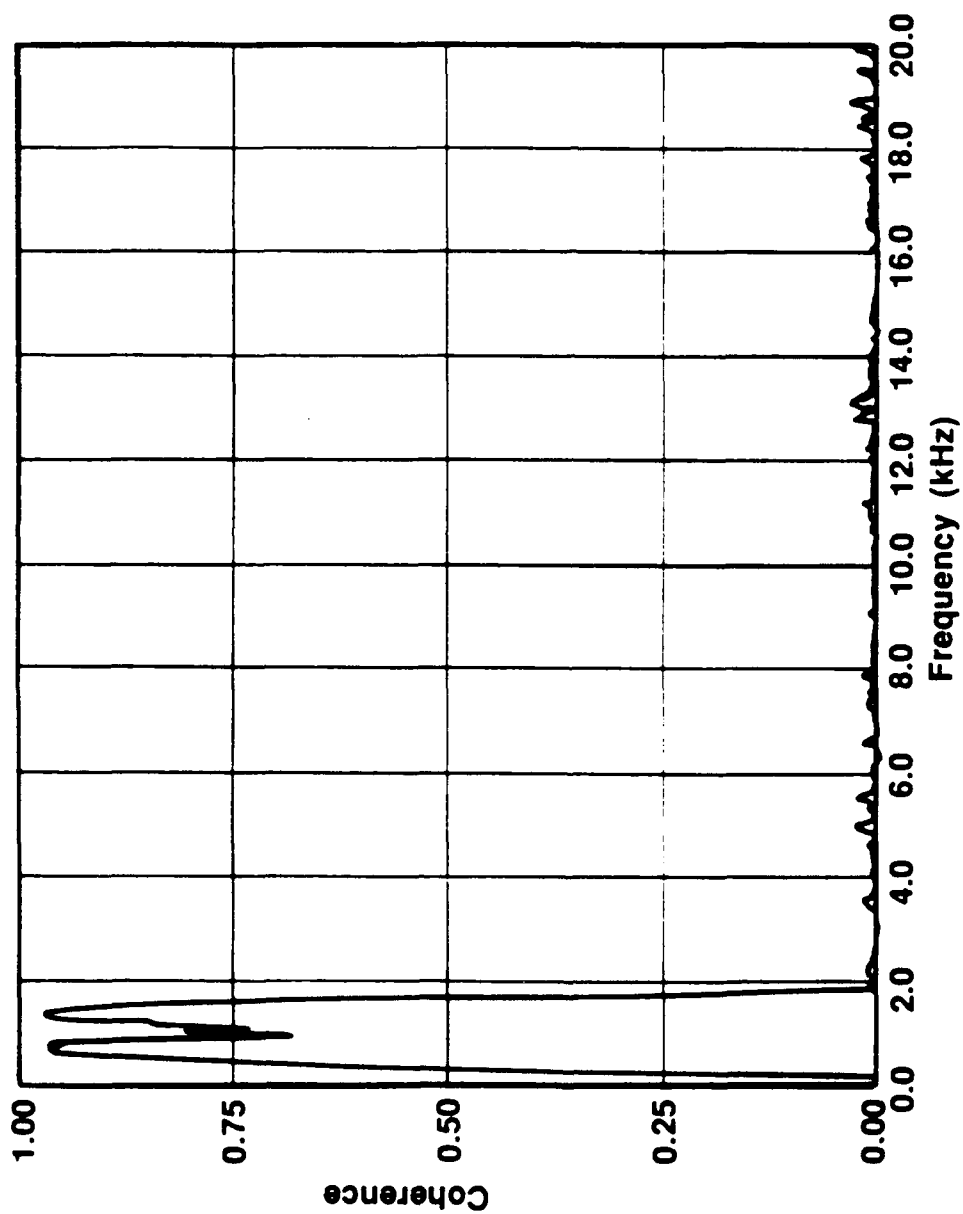


Figure 5.1 Coherence of Noise Between TCV Channels  
in the Reference Beam Mode

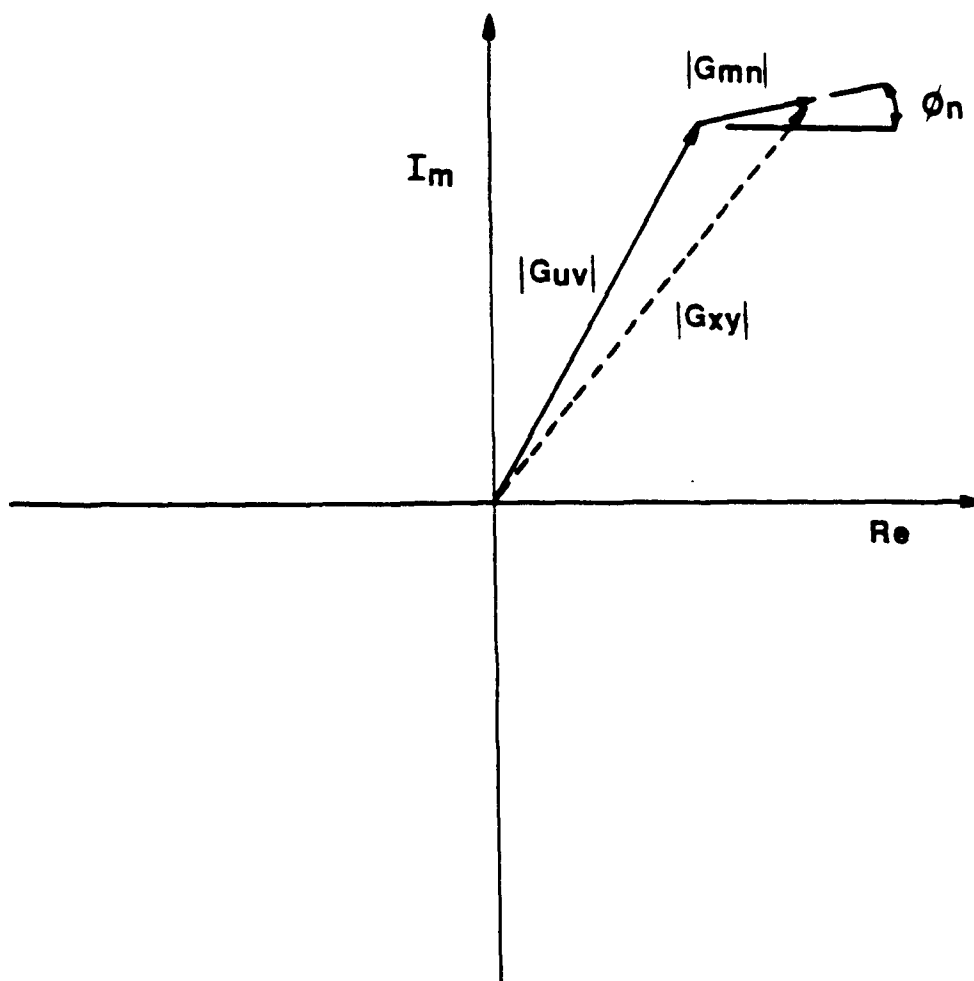


Figure 5.2 Illustration of the Effects of Coherent Noise on the Measured Cross-Spectrum

photodetectors and computing the imaginary part of the cross-spectrum again. The corrected value is then the difference between the two computed values divided by two. This approach is simple, and it is valid to the extent that the cosine of the phase bias between the two channels approximates unity. This result is illustrated below.

The process of instrument switching used in intensity measurements is a vector averaging process; the vector average of the "unswitched" cross-spectrum and the switched cross-spectrum, is equivalent to the true cross-spectrum unbiased by phase mismatch.

For the case of propagating intensity (as opposed to reverberant intensity) it is only necessary that the imaginary parts of the corrected cross-spectrum and the true cross-spectrum are the same. The influence of the phase bias angle, the noise phase angle, and the result of photodetector switching on the cross-spectra are illustrated in the Argand diagram of Figure 5.3.

In the first quadrant is vector  $\vec{OP}$  with a magnitude of  $|G_{uv}|$  and phase angle of  $\phi_A$ . This is the true cross-spectrum with an imaginary part equal to  $|G_{uv}| \sin \phi_A$ . Also in the first quadrant is vector  $\vec{OE}$ . This is the original cross-spectrum with a magnitude of  $|G_{uv}|$  but it has been shifted by the phase bias angle,  $\phi_B$ . Added to this is the noise vector  $\vec{EA}$  with a magnitude of  $|G_{nn}|$  and a phase angle of  $\phi_n$ . At frequencies where the coherence is close to unity (i.e. at 750 Hz and 1300 Hz)  $|G_{nn}|$ , the magnitude of the noise cross-spectrum, will approximate the square root of the product of the noise autospectra,  $\sqrt{G_{nn}G_{nn}}$ . This is the maximum magnitude of  $\vec{EA}$ . At nearby frequencies, where the coherence is smaller than unity, the magnitude of the vector

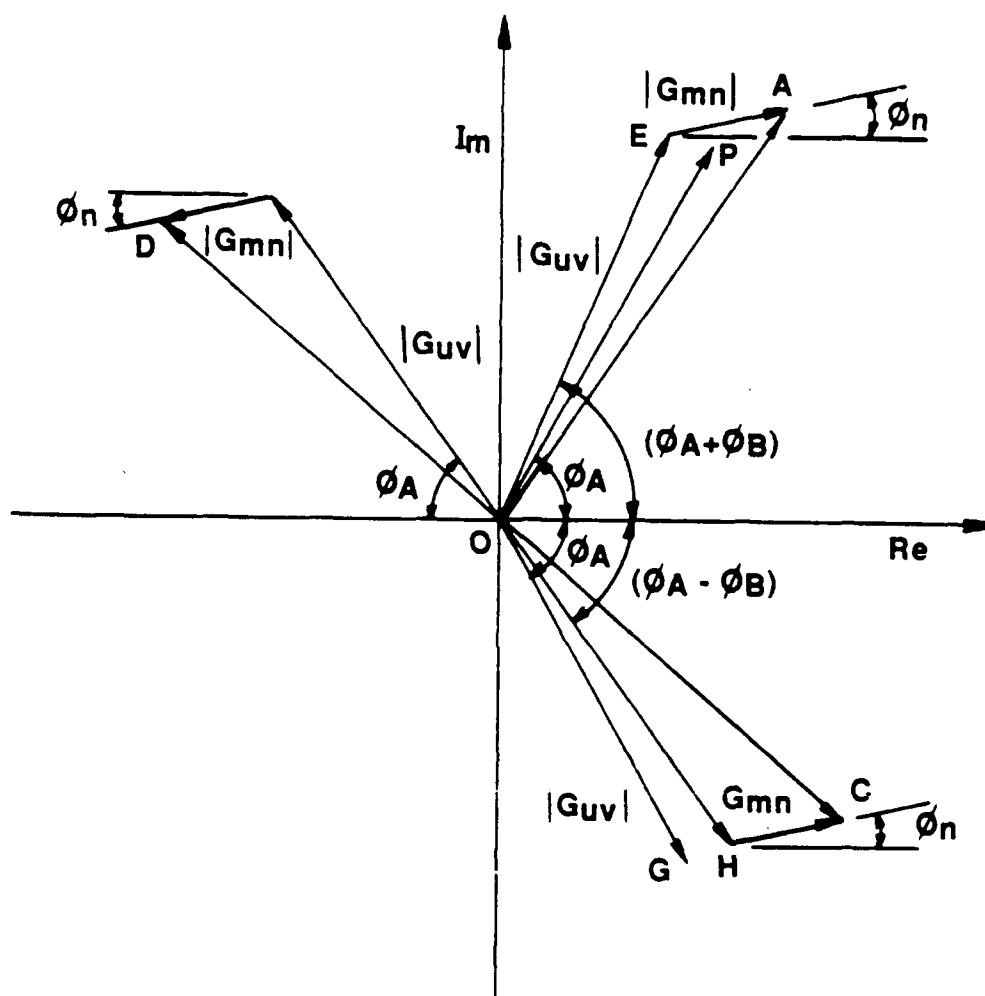


Figure 5.3 Illustration of the Effects of Coherent Noise, Phase Bias, and Photodetector Switching on the Measured Cross-Spectrum



will drop below this value. In any event the resultant,  $\vec{OA}$ , is the measured cross-spectrum in the "unswitched" position.

Switching the photodetectors (but not the inputs to the FFT analyzer) causes the measured cross-spectrum to be composed of vectors in the fourth quadrant: vector  $\vec{OH}$  which is the phase-biased version of  $\vec{OG}$ , the true cross-spectrum for the switched position, and vector  $\vec{HC}$  the noise cross-spectrum. The resultant,  $\vec{OC}$  is the measured cross-spectrum in the switched position.

If vector  $\vec{OC}$  is negated to form  $\vec{OD}$ , as illustrated in the second quadrant, it can easily be shown that the algebraic average of the imaginary part of  $\vec{OA}$  and the imaginary part of  $\vec{OD}$  is equal to the imaginary part of the true ("unswitched") cross-spectral vector  $\vec{OP}$  if the cosine of  $\phi_B \sim 1$ . Therefore, for "small" phase bias angles (8 degrees or less for one percent error or less) the active intensity without phase error or coherent noise error can be obtained by dividing by two the sum of the "unswitched" quadrature spectrum and the negative of the switched quadrature spectrum where "switching" in this case refers only to the interchanging of the photodetectors.

As a final point, coherent noise, like incoherent noise, will also act to reduce the measured coherence but to a slightly greater extent. If the noise is assumed to be completely coherent with itself (nearly the case for the noise peaks in the TCV system) and if the signals are completely coherent then the overall coherence for the combined signals becomes (Talbot 1975):

$$\gamma^2 = \frac{1 - \left( \frac{G_{mm}}{G_{uu}} \right) \left( \frac{G_{nn}}{G_{vv}} \right)}{\left( 1 + \frac{G_{mm}}{G_{uu}} \right) \left( 1 + \frac{G_{nn}}{G_{vv}} \right)} \quad (5.6)$$

where  $G_{mm}$  and  $G_{nn}$  are the noise autospectra and  $G_{uu}$  and  $G_{vv}$  are the corresponding signal autospectra. This contrasts with the case of incoherent noise when the second term in the numerator is absent. Figure 4.4, for curves corresponding to a CNR of greater than 37 dB, illustrates the typical values of the noise autospectrum (the two peaks below 2 kHz). These values are the same in both channels.

#### EFFECTS OF VIBRATION OF THE OPTICS

Another potential source of error in using TCV instrumentation for intensity measurements is the vibration of the optics. If the optics are excited by the same source as the object then the optical vibration "noise" will be fully coherent with the true signals. The problem will not be indicated by the measured signal coherence since this value, due to the coherence between the optics vibration and the object vibration, will show no reduction. The measured intensity will be in error due to this signal contamination and the error will not be removable by photodetector switching as it is in the case where the noise and signal are incoherent.

However, if the optics can be properly isolated, or if the response of the optics is negligible compared to the signals, then this potential source of error is greatly reduced. With a long focal distance in the reference beam mode and "high impedance" optical

components (as opposed to using light weight optical elements) this potential problem is made insignificant.

#### OPTIMIZATION OF TCV SYSTEM DESIGN FOR MAXIMUM ACCURACY

The previous sections have addressed the influence which various TCV system characteristics have on intensity measurements. It is appropriate here to prioritize these characteristics in relation to their importance in measurement accuracy and make recommendations, based on these priorities, for effective design and operation of TCV systems intended for intensity measurements.

Assuming the vibrometer channels themselves have been adequately designed using basic vibrometer principles, the most important design component from an intensity point of view is the provision for adequate vibration isolation. As noted previously, if the source excites the optics, the results will be erroneous and not correctable. Therefore, the system should include lenses with focal lengths long enough to preclude potential vibration of the components from the source. Optical components themselves should not be highly resonant and should be clamped to an isolation table. The admittance of the components should be minimized.

For measurement situations where the coherence between the two channels may be less than one (due to low surface velocities, for example) the optical parameters which can influence random error by way of their influence on the channel CNR should be addressed in the system design. However, the more important subject is not the parameters which

govern the CNR, but rather how the CNR influences the resultant vibrometer noise floor. This is determined by the design of the demodulators. For example, Willemin and Dandliker (1988) show that for a Revox B760 tuner at 500 Hz, a CNR of 40 dB yields a demodulated noise floor approximately 30 dB lower than the same CNR at 25 kHz. They suggest, for system improvement, the design of a new demodulator or the use of a phase tracking system to avoid this frequency dependent deterioration in FM demodulators. In intensity measurements a better demodulator design would translate to less random error for a fixed optical system in cases where coherence between the channels is less than unity.

Once the signal processing has been optimized, the parameters influencing the CNR should then be addressed. These include optical power, quantum efficiency of the photodetectors, and the heterodyne efficiency. Since the CNR varies as the square of the heterodyne efficiency, the susceptibility to random error (for low coherence) can be best reduced by optimizing the alignment of the reference beam and object beam wavefronts (by use of precision optics and careful collimation of the laser beam) and by optimizing the alignment of reference beam and object beam polarizations. Polarization alignment per se is easily accommodated by a "polarization rotator" (quarter wave plate) along one of the two beam paths. More difficult is the task of maintaining polarization of the object beam upon backscattering; backscattering from a shiny metal surface will maintain the initial polarization whereas backscattering from a diffuse non-metallic surface will distribute it. In the latter case the use of a reflective,

polarization preserving paint on the object surface will aid in increasing the heterodyne efficiency.

Use of a photodetector which has optimum quantum efficiency at the wavelength in use will also aid in increasing the CNR (and decreasing the potential for random error in intensity measurements) since the detector quantum efficiency is linearly related to the CNR. Similarly, since the power of the object beam incident on the detector is linearly related to the CNR, increased laser power will generally assist in reducing the demodulated noise floor and decrease the random error. However, this is not to say that a high powered laser is necessary. High powered lasers present a greater safety hazard than lower powered Helium Neon lasers for example. Nearly all current commercial vibrometer systems are Helium Neon based and provide adequate signal-to-noise ratios. For use of these systems at long distances (100 meters, for example) collection optics have been used to substantially increase the power of the backscattered beam on the detector (Corti, Marazzini, Martinelli, and DeAgostini 1986).

Finally it should be noted that this discussion addresses only the optical aspects which relate to measurement accuracy. There are additional errors which can occur with cross-spectral power flow measurements such as nearfield errors, finite difference errors, and bandwidth limitation errors (see for example Redman-White 1983).

## Chapter VI

### LONGITUDINAL INTENSITY MEASUREMENTS USING THE TCV SYSTEM

#### INTRODUCTION

Measurement of in-plane vibrations by the differential Doppler mode of laser vibrometry is considerably less practiced than is the measurement of surface-normal motions in the reference beam mode. There is a sparsity of literature available on this measurement technique. One of the few known by the author is Dandliker and Willemin (1981) who addressed the measurement of microvibrations and illustrated how both surface-normal and in-plane vibrations could be monitored with the two different optical setups. McDevitt and Stuart (1989) were successful in using the technique for longitudinal vibrations at frequencies where appreciable bending was not present in the object. The phase agreement obtained between the TCV results and an accelerometer pair for the phase difference at the ends of the sample, was not of the accuracy required for intensity measurements in reverberant fields (it varied from zero to 2.2 degrees). This difference may have been due to the degree of phase-matching in the accelerometers, small errors in the calculated value of vibrometer channel phase bias, or mounting-related phase errors in the accelerometers as noted in Chapter I. It was felt that this problem (if it were due to inaccuracies in the vibrometer channel phase bias) could be solved this time by photodetector switching.

This chapter forms the theoretical basis for longitudinal intensity measurements and presents the experimental setup, procedure, and results. Included is development of the expressions for the two verification techniques (the longitudinal standing wave and energetics techniques) and the expression for the cross-spectral longitudinal intensity measurement technique. The equations are derived in a fashion analogous to the derivations for flexural intensity by Carroll (1987). As with the flexural intensity equations, the equations are written in variables attributable to the laser vibrometer.

#### FORMULATION OF THE APPROACH

The expressions for longitudinal power flow in a reverberant rod can be derived by using the derivations of flexural power flow used by Carroll (1987). For example, the standing wave expression for longitudinal power flow is derived as follows.

Power flow due to longitudinal waves in terms of the spatial and temporal derivatives of the axial displacement can be written as:

$$\Pi = SY \left\langle \frac{\partial \xi(x, t)}{\partial x} \cdot \frac{\partial \xi(x, t)}{\partial t} \right\rangle_t \quad (6.1)$$

where  $\xi$  is the axial displacement,  $S$  is the cross-sectional area,  $Y$  is Young's modulus and the brackets denote a time averaged value. If the motion is harmonic, the displacement can be expressed as a complex quantity,  $\tilde{\xi}(x, t)$ . In this case the power flow can be written:

$$\Pi = SY \frac{\text{Re}}{2} \left[ \left[ \frac{\partial \tilde{\xi}(x, t)}{\partial x} \right]^* \cdot \left[ \frac{\partial \tilde{\xi}(x, t)}{\partial t} \right] \right] \quad (6.2)$$

where the asterisk denotes the complex conjugate. The expression for

the complex longitudinal displacement can be written as:

$$\tilde{\xi}(x,t) = \tilde{A}(e^{-ikx} + \tilde{R}e^{ikx})e^{i2\pi ft} \quad (6.3)$$

This is the same expression as for the flexural displacement. If this expression is substituted into the previous power flow equation and if the equation relating the nodal and antinodal displacement amplitudes to the original wave amplitude and reflection coefficient is utilized, i.e.:

$$2(\xi_N) \cdot (\xi_{AN}) = |A|^2(1 - |R|^2) \quad (6.4)$$

where  $\xi_N$  and  $\xi_{AN}$  are nodal and antinodal rms displacements,  $|A|$  is the magnitude of the incident wave and  $|R|$  is the magnitude of the complex reflection coefficient, the following equation for longitudinal power flow by the standing wave formulation results:

$$\Pi_{SW} = SY(2\pi f)k(\xi_N \cdot \xi_{AN}) \quad (6.5)$$

In this equation  $k$  is the longitudinal wavenumber:

$$k = \frac{\omega}{\sqrt{\frac{Y}{\rho}}} = \frac{\omega}{\sqrt{\frac{Y}{m'/S}}} \quad (6.6)$$

The equation for the power flow via the energetics method can also be derived by comparison with the flexural derivation. In this case the same expression holds for the longitudinal power as for the flexural power. This is:

$$\Pi_E = \frac{\eta(2\pi f)^3 m' L}{2} [\xi_N^2 + \xi_{AN}^2] \quad (6.7)$$

Finally, the longitudinal two-point power flow expression, can be shown to be (refer to Appendix A):



$$\Pi_{2P} = \frac{YS}{2\pi\Delta} \int_0^{\infty} \frac{\text{Im}[G_{12}(f)]}{f} df \quad (6.8)$$

where  $G_{12}(f)$  is the velocity cross-spectrum between the two measuring points spaced at a distance of  $\Delta$ . However this has to be corrected for finite difference error so that the corrected expression becomes:

$$\Pi_{2P} = \frac{YS}{2\pi\Delta} \int_0^{\infty} \frac{\text{Im}[G_{12}(f)]}{f} df \cdot \left( \frac{k\Delta}{\sin k\Delta} \right) \quad (6.9)$$

where  $k$  is the longitudinal wavenumber. For a single frequency,  $f_0$ , the expression for power flow using the two-point cross-spectral method becomes:

$$\Pi_{2P} = \frac{YS}{2\pi\Delta} \cdot \frac{\text{Im}[G_{12}(f_0)]}{f_0} \cdot \frac{k\Delta}{\sin k\Delta} \quad (6.10)$$

where  $f_0$  is the frequency.

The three expressions for longitudinal power, when adapted to the laser vibrometer output, will assume slightly different forms as in the flexural case. However, the conversion to a vibrometer output format will not be the same as it was in the flexural case since for longitudinal tests the differential Doppler technique rather than the reference beam technique is used. As derived in Chapter II, this situation requires that the expression for the Doppler shift associated with a velocity,  $v$  becomes:

$$f_D = \frac{2}{\lambda} v \sin\left(\frac{\theta}{2}\right) \quad (6.11)$$

For a velocity in units of m/s and a laser wavelength of  $\lambda = 514.5$  nm (for the green line of the Argon Ion laser) the relationship becomes:

$$f_D = \left[ 3.89 \cdot 10^6 v \cdot \sin\left(\frac{\theta}{2}\right) \right] \text{ Hz} \quad (6.12)$$

where  $\theta/2$  is the lens half-angle. Note that use of the term  $\sin \theta/2$  is required if the transverse motion is in the same plane as the two incident laser beams and is perpendicular to the bisector of the beams. Because the differential Doppler technique is only sensitive to motion which is in the same plane as the two incident laser beams and is perpendicular to the beam bisector, an adjustment to the equation has to be made for general motions or beam inclinations. Specifically, if the surface velocity vector is denoted as  $\tilde{v}$  and the unit sensitivity vector is denoted as  $\tilde{j}$  (i.e. the unit vector which falls in the same plane as the beams and is perpendicular to their bisector) then the Doppler shift becomes:

$$f_D = \left[ 3.89 \cdot 10^6 \cdot \sin\left(\frac{\theta}{2}\right) \cdot \{\tilde{v} \cdot \tilde{j}\} \right] \text{ Hz} \quad (6.13)$$

(The sign of vector  $\tilde{j}$  will actually be determined by which of the two incident laser beams is frequency shifted. For measuring intensity this will not matter as long as corresponding beams in the two vibrometer units are both shifted in the same way so that there is no confusion regarding the phase difference between the units). The previous equation can be written as:

$$f_D = \left[ 3.89 \cdot 10^6 \cdot \sin\left(\frac{\theta}{2}\right) \cdot v \cos \beta \right] \quad (6.14)$$

where  $\beta$  is the angle between the velocity vector and the unit sensitivity vector and  $\theta/2$  is the lens half-angle. This equation illustrates the loss in sensitivity that the differential Doppler

technique can suffer when lenses with small half-angles (i.e. long focal length lenses) and beam inclinations at a glancing angle with the velocity vector are used.

The PLL voltage output for a sensitivity of  $K$  (in units of Hz/volt) then will be:

$$V = \frac{3.89 \cdot 10^6 \cdot \sin\left(\frac{\theta}{2}\right) \cdot v \cos \beta}{K} \quad (6.15)$$

The rms longitudinal displacement (in units of meters) is then related to the rms voltage output in the following manner:

$$\xi = V \cdot \left[ \frac{K}{(2\pi f) \cdot 3.89 \cdot 10^6 \cdot \sin\left(\frac{\theta}{2}\right) \cdot \cos \beta} \right] \quad (6.16)$$

This equation then yields the expression for the product of the nodal and antinodal rms displacements used in the standing wave equation:

$$(\xi_N)(\xi_{AN}) = \frac{V_N \cdot V_{AN} \cdot K^2}{[(2\pi f) \cdot 3.89 \cdot 10^6 \cdot \sin\left(\frac{\theta}{2}\right) \cdot \cos \beta]^2} \quad (6.17)$$

where  $\xi$  and  $V$  are the rms displacement and voltage values respectively at the node (subscript  $N$ ) and the antinode (subscript  $AN$ ). Here it has been assumed that the same PLL is used to read both the nodal and antinodal velocities.

The standing wave equation for the longitudinal case can now be written, substituting the previous equation, as:

or

$$\Pi_{sw} = SY(2\pi f)k \left[ \frac{V_N \cdot V_{AN} \cdot K^2}{[(2\pi f) \cdot 3.89 \cdot 10^6 \cdot \sin\left(\frac{\theta}{2}\right) \cdot \cos \beta]^2} \right] \quad (6.18)$$

$$\Pi_{sw} = \frac{SYk}{2\pi f} \left[ \frac{V_N \cdot V_{AN} \cdot K^2}{[3.89 \cdot 10^6 \cdot \sin\left(\frac{\theta}{2}\right) \cdot \cos \beta]^2} \right] \quad (6.19)$$

where for  $Y$  in  $N/m^2$ ,  $S$  in  $m^2$ , and  $k$  in radians/m,  $\Pi$  acquires an energy flow in units of watts.

By a similar approach, the equation predicting the longitudinal power flow via the energetics method and laser vibrometer output at a node and antinode becomes:

$$\Pi_E = \frac{\eta}{2} m' L (2\pi f) \frac{K^2}{[3.89 \cdot 10^6 \cdot \sin\left(\frac{\theta}{2}\right) \cdot \cos \beta]^2} [V_N^2 + V_{AN}^2] \quad (6.20)$$

which has units of watts for  $m'$  in  $kg/m$  and  $L$  in units of  $m$ .

In a manner similar to that for the flexural case, some useful equations for the vibrometer output on the rod can be developed at this point. For example, equating the power flow in the standing wave and energetics approaches, and assuming that  $V_N^2 \ll V_{AN}^2$  in the energetics equation (true for low damping) the two equations yield the following ratio for the longitudinal nodal and antinodal rms voltages (or displacements, etc.):

$$\frac{V_N}{V_{AN}} \approx \frac{\eta}{2} kL \quad (6.21)$$

This contrasts with the equivalent expression in the flexural case (Equation 3.12); for that case the ratio is one half of this value.

By using Equation 6.21, the vibrometer rms voltage at the antinode becomes:

$$V_{AN} \approx \sqrt{\frac{2\Pi(2\pi f) [(3.89 \cdot 10^6) \sin\left(\frac{\theta}{2}\right) \cos \beta]^2}{SYk^2\eta LK^2}} \quad (6.22)$$

(Note that this approximation assumes  $\eta$ , due to end losses, is appreciably greater than the material loss factor. If  $\eta$  assumes a value of zero, the antinodal value is undefined). The form of the voltage (or velocity, displacement, etc.) distribution is the same as it is in the flexural case since the motion is sinusoidal. This distribution is:

$$V(x) = \sqrt{V_{AN}^2 \cos^2 kx + V_N^2 \sin^2 kx} \quad (6.23)$$

where  $V(x)$  is the rms voltage at any point  $x$  measured from an antinode.

Finally, to be considered is the expression for the two-point longitudinal power flow in terms of the data obtained using the TCV system. As in the flexural case, the value of  $\text{Im}[G_{12}]$  can be averaged by photodetector switching or can be calculated by using a corrected phase angle in order to remove any phase bias error due to the PLL processors. If one uses the same approach used for the flexural case, in Chapter III, the power flow predicted by the two-point cross-spectral method (Equation 6.10) becomes:

$$\Pi_{2P} = \frac{YS}{2\pi\Delta} \cdot \frac{\text{Im}[G_{12}(f)]}{f} \cdot \frac{k\Delta}{\sin k\Delta} \cdot \frac{K_1 K_2}{[3.89 \cdot 10^6 \sin\left(\frac{\theta}{2}\right) \cos \beta]^2} \quad (6.24)$$

## EXPERIMENTAL SETUP AND PROCEDURE

Initially the experimental setup for longitudinal intensity measurements was similar to the setup for flexural intensity measurements; a shaker was used to excite longitudinally the free end of

a long thin rod which was clamped at the other end as shown in Figure 6.1. Damping was predominantly due to frictional losses in the clamping fixture. However, this setup brought about bending motion which was greater than the longitudinal motion of interest. Under the combined conditions of high bending motion and appreciable transverse (longitudinal) motion the vibrometer output in the differential Doppler mode was typically unstable. A study of this phenomenon was conducted and is discussed in Chapter IX.

In order to reduce the flexural motion to some extent the original longitudinal setup was changed; the rod was positioned inside a hollow circular pipe and held in place at its ends by two very thin plastic diaphragms which were fixed at the ends of the pipe. The pipe was slotted to allow for readings along the rod using the laser vibrometer. A shaker was again placed at one end to drive the rod longitudinally. With this arrangement the ends of the rod were relatively free in the longitudinal direction but practically fixed in the other two directions due to the in-plane stiffness of the diaphragms. This decreased the flexural motion of the rod but of course the pinned-pinned flexural modes were still capable of existing. An aluminum rod with a length of 52.1 cm was chosen in order to provide a longitudinal resonance that did not match a flexural resonance too closely. The rod cross-sectional dimensions were 0.635 cm on each side.

The lenses used in this experiment had a focal length of 243 mm. Lenses of a fairly short focal length were preferred in order to maximize the longitudinal signal. However, as a result of using these short focal length lenses there was little optical path available for

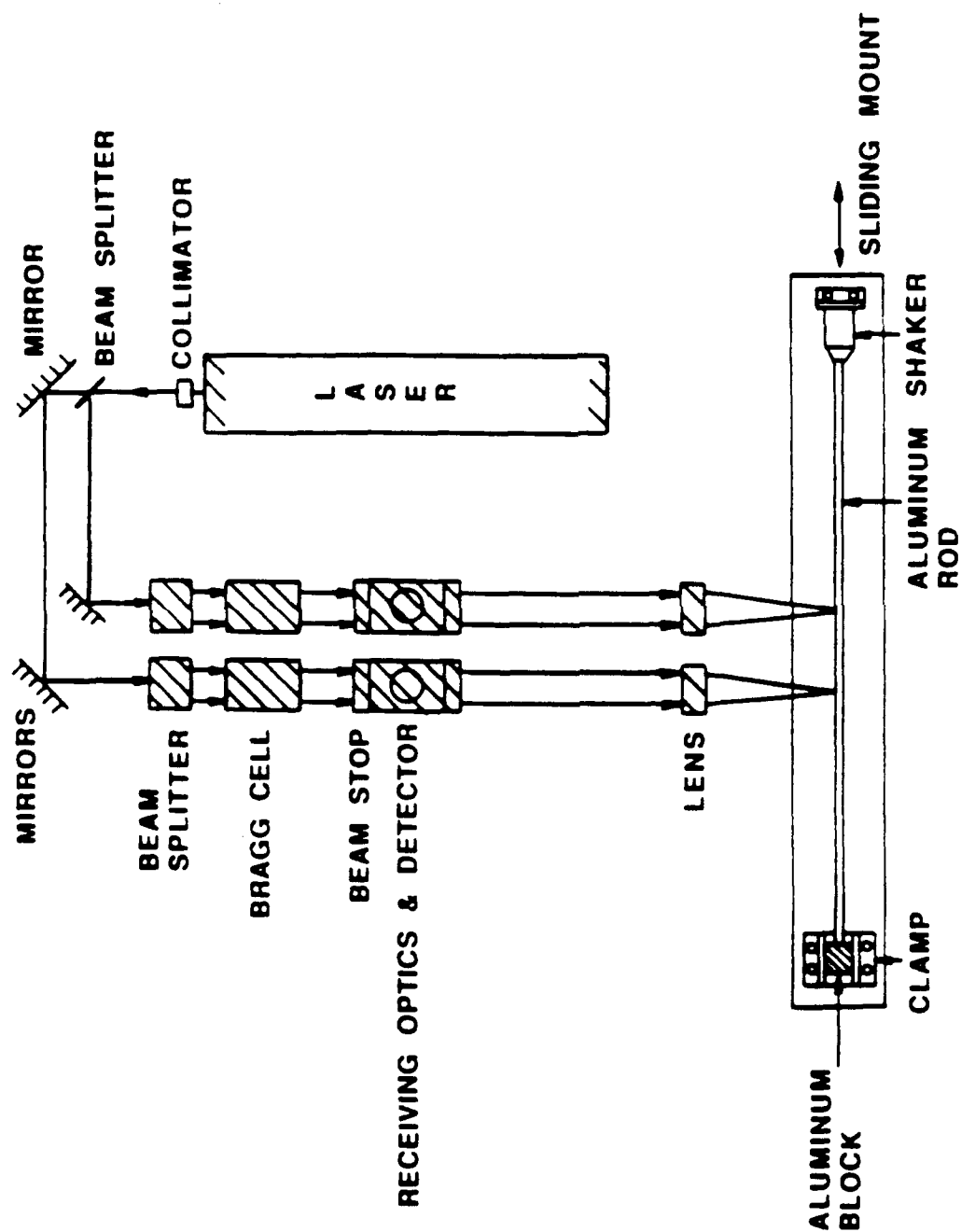


Figure 6.1 Mechanical and Optical Setup for Longitudinal Intensity Measurements

use of scanning mirrors. Consequently it was decided to do without scanning mirrors for this test and scan the object by moving the entire assembly on a moveable track as portrayed in Figure 6.1. The two vibrometers were spaced at 15.24 cm to provide a fixed laser beam spacing on the object of less than half of the expected longitudinal wavelength. The physical dimensions of the optical components prevented a closer spacing of the two vibrometer beams.

The experimental procedure was identical to the procedure for flexural intensity measurements: identify a resonance, find the damping by a 3 dB down approach (i.e. by a half power point measurement using a longitudinal antinode), find the nodal and antinodal rms voltages at resonance, then find the intensity by the cross-spectral technique at five stations along the rod. These stations were spaced 10 mm apart for these tests.

## RESULTS OF LONGITUDINAL INTENSITY TESTS

The third longitudinal resonance was better separated from bending resonances than the first two longitudinal resonances and so was chosen as the test resonance. The frequency was 13.8 kHz which provided a theoretical longitudinal wavelength of 36.6 cm. The three nodal positions located on the rod indicated a longitudinal wavelength of 36.3 cm. System damping, found by a 3 dB down approach, indicated a loss factor of 0.014. The relatively low sensitivity provided by the differential Doppler technique made reading the nodal values a difficult procedure but a value much lower than that predicted by Equation 6.21 for this  $\eta$  was found. Values of antinodal voltages were very



consistent. Results of  $\Pi_{2P}$  at the five stations scanned showed that there was very good agreement with  $\Pi_E$  (within 10%) for the first three stations but very poor agreement for stations four and five. For these stations the two-point intensity results fell off dramatically.  $\Pi_{SW}$  was also of course low due to the low value of the nodal voltage.

Additional tests, with an expanded object scan of fifteen axial stations, showed that  $\Pi_E$  and  $\Pi_{2P}$  agreed well but only at several stations and that  $\Pi_{SW}$  was always relatively low. The value of the cross-spectral intensity was repeatable at the various stations; a "good" station always provided favorable results and a "bad" station always provided poor results (in comparison with the energetics result).

It was decided to increase the phase difference between the two points at the various stations to cover the possibility that the problem at some of the stations might be due to too low a phase angle for accurate measurement by the FFT analyzer. This was done by applying a thin sealant compound on the diaphragm at the end opposite the shaker. Application of the sealant increased the system loss factor to 0.04. The resonance frequency changed slightly to 13.3 kHz. Ten stations were scanned.

Again the energetics intensity compared well with the cross-spectral intensity only at a few stations, the remainder falling below the energetics prediction. The amplitude distribution of the longitudinal voltages (velocities) versus axial position appeared to be accurate; both curves (one for each vibrometer at each station) were smooth up through the longitudinal antinode positions and back down. However the longitudinal intensity results, not as consistent, are shown in Figure 6.2

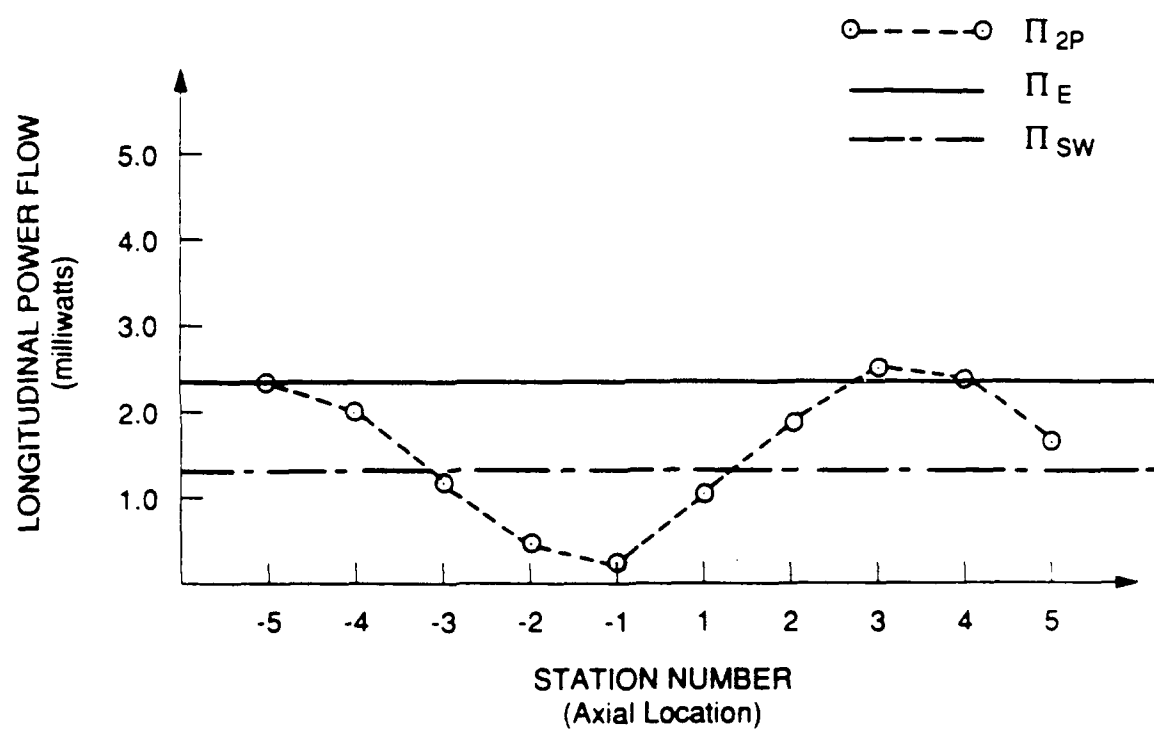


Figure 6.2 Comparison of Longitudinal Power Flow Results  
for  $n = 3$ ,  $\eta = 0.04$ ,  $f = 13.3$  kHz

Most apparent in the figure is the sinusoidal fashion in which the cross-spectral intensity results vary with position. The distance between stations -5 and +4, an approximate wavelength for the sinusoid in the figure, is 80 mm. As illustrated in the next section, the out-of-plane flexure of the rod was influencing the longitudinal results with a severity that depended on the position of the two laser beams relative to the position of the standing flexural wave. The presence of a longitudinal velocity component induced by bending is well known and should be accounted for (as by Kendig 1988) when taking longitudinal intensity measurements. It was thought that the bending resonance close to 13.3 kHz (a strong flexural resonance existing at 13.9 kHz) was not playing a significant role in the results until this time.

An investigation into why the  $\Pi_{2p}$  curve varies in this fashion is conducted in the next section but a brief explanation follows. Recall the two vibrometer beams are separated a distance of 152.4 mm. This represents approximately 2.25 bending wavelengths at this frequency and the two channels as they scan the specimen alternately are in and out-of-phase with each other. This pertains to the bending component of longitudinal motion. The longitudinal motion due the longitudinal wave, however, is always out-of-phase between the two channels for the entire scan, since the two stations are spaced at approximately 42% of the longitudinal wave length. Figure 6.3 aids in visualizing the role the bending component of longitudinal motion plays in the resultant longitudinal amplitudes and phase angles at a given station.

The condition at the first vibrometer beam location (subscripted "A") is represented in the first quadrant while the condition at the

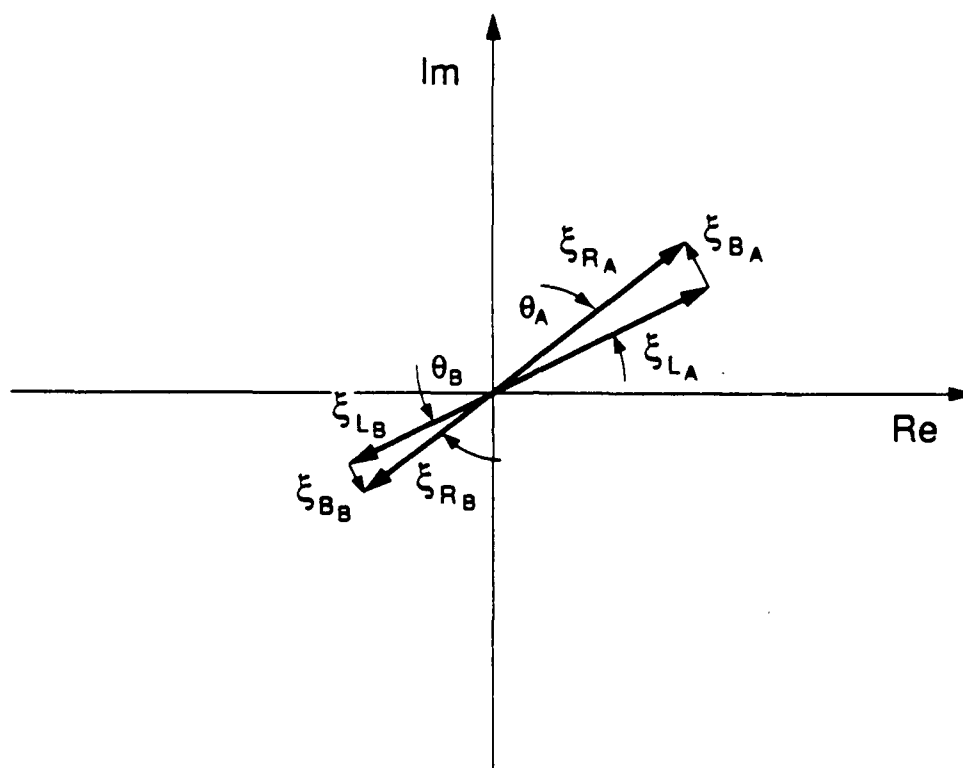


Figure 6.3 Illustration of the Effects of the Bending-Induced Longitudinal Motion

second vibrometer beam location (subscripted "B") is represented in the third quadrant. The component of longitudinal motion caused by the bending waves is  $\xi_B$ , that caused by the longitudinal waves is  $\xi_L$ , and their resultant longitudinal motion is  $\xi_R$ . If the bending resonance is out-of-phase with the longitudinal resonance by some phase angle as shown in the figure, then the phase angles of the resultants at the two laser beam locations will be affected. Furthermore, if the bending components are completely out-of-phase with each other, as shown in the figure, the phase difference between the two locations may remain relatively unaltered. However, if the bending components are in phase with each other (so that one of the bending vectors in the figure is negated) then the phase difference between the two locations becomes altered to a significant extent especially if small phase differences are important (as they are in intensity measurements in resonant structures).

It is the relative station-to-station constancy of longitudinal wave results, modified in a sinusoidal fashion by the bending-induced component which causes the sinusoidal degradation of the cross-spectral longitudinal intensity results.

The degree to which the amplitude and phase results are modified depends on the amplitude of the bending-induced longitudinal motion. This can be appreciable. Figure 6.4 shows the undeflected beam and the deflected beam (exaggerated). Normal displacement of the neutral axis for the flexural standing wave can be expressed as:

$$\xi = A \cos kx \cdot \sin \omega t \quad (6.25)$$

where  $A$  is the amplitude and  $k$  is the flexural wavenumber. The slope of the neutral axis,  $\theta$  is:

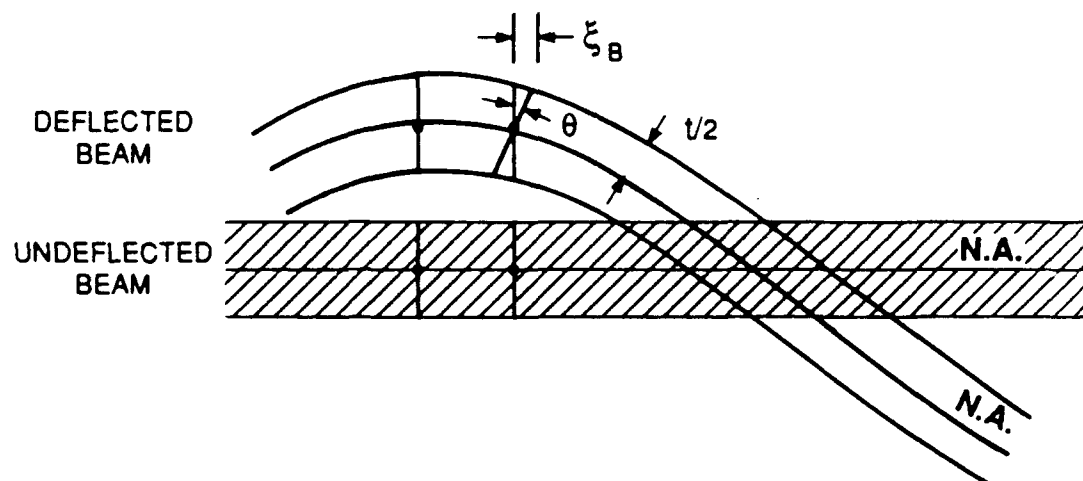


Figure 6.4 Bending-Induced Longitudinal Component of Motion

$$\theta = \frac{d\xi}{dx} = -Ak \sin kx \cdot \sin \omega t \quad (6.26)$$

Then  $\xi_B$  is found (for small  $\theta$ ) by:

$$\xi_B = \frac{t}{2} \cdot \sin(\theta) \approx \frac{t}{2} \cdot \theta \quad (6.27)$$

$$\xi_B \approx \frac{t}{2} (-Ak \sin kx \cdot \sin \omega t) \quad (6.28)$$

(This same result is achieved if the strain distribution at the outer fiber is integrated to find transverse displacement).

Therefore the longitudinal displacement due to a standing flexural wave is zero at the bending antinodes ( $kx = 0, \pi, 2\pi, \dots$ ) and maximum at the bending nodes ( $kx = \pi/2, 3\pi/2, 5\pi/2, \dots$ ). For the aluminum rod in this study the actual bending wavenumber at 13.3 kHz was 0.98 radians/cm and the beam thickness was 0.635 cm. The ratio of the bending-induced longitudinal amplitude at the flexural node to the bending surface-normal amplitude at the flexural antinode becomes:

$$\text{amplitude ratio} \approx \frac{kt}{2} = 0.31 \quad (6.29)$$

Therefore, if there is a flexural resonance present with an amplitude comparable to the longitudinal wave motion, the results can be altered significantly. Whether the longitudinal results are influenced more in amplitude or phase depends on the phase difference between the bending motion at the two points, as well as the phase difference between the flexural and longitudinal resonances in the structure.

If there is power flow due to the flexural waves then the component of longitudinal motion due to the flexural travelling waves

can also alter longitudinal results. As is illustrated in the next section, the amplitude ratio in Equation 6.29 is also true for travelling waves; the ratio of the amplitude of the travelling flexural wave longitudinal component to the amplitude of the travelling flexural wave is the same (although it is constant spatially). An investigation of the aluminum rod at 13.3 kHz showed a damped flexural resonance at this frequency with a loss factor of 0.05, a wavelength of approximately 64 mm and a nodal to antinodal velocity ratio of 0.40. This indicates that a fairly strong flexural travelling wave is present and that therefore the longitudinal amplitudes may be altered even at the flexural antinodes. However, it was recognized that if bending antinodes spaced one bending wavelength apart were used for the determination of longitudinal power flow, the bending components would be in-phase and the bending-induced longitudinal motion should not interfere with the two-point measurement.

In order to investigate the possibility of obtaining reasonably accurate longitudinal power flow results by using the flexural antinodes, in a similar test the flexural antinodes were first located on the beam by a scan of one vibrometer in the reference beam mode. Since the flexural antinodal spacing at this frequency was much shorter than the distance at which the two vibrometers could be spaced for this setup, it was decided to scan the sample with only one unit in the differential Doppler mode and use the shaker signal as a reference phase. (This approach is more convenient than using two systems but it does require phase information from artificial excitation. This would not be practical for locating unknown energy sources or sinks in a structure).



The beam was scanned at its flexural antinodes and the longitudinal amplitude and phase with respect to the excitation were recorded. Additionally the longitudinal antinode was located and its amplitude was recorded for purposes of calculating the longitudinal energy flow by way of the energetics method. The longitudinal nodal value was not recorded, but from previous tests it was known to be low enough not to significantly add to the energetics result.

For this test, the power flow by the energetics method was calculated to be 1.68 mW. However, the power flow measured by the cross-spectral approach using antinodes spaced one bending wavelength apart provided much lower but very consistent values; for four different flexural antinode pairs at a spacing of one bending wavelength the readings were: 0.70 mW, 0.73 mW, 0.72 mW, 0.71 mW. For two different flexural antinode pairs at a spacing of two bending wavelengths the readings were 0.74 mW, and 0.77 mW. These tests indicated that the flexural antinodes provided consistent predictions of the longitudinal power flow. But these were only 42% of the power flow predicted by the energetics method. (Nodal data were not taken for this test for standing wave results.)

The next section investigates the influence of bending waves on longitudinal power flow results and attempts to explain the discrepancies in the previous longitudinal data.

## ANALYSIS OF LONGITUDINAL POWER FLOW RESULTS

It has been noted that the probable cause of the sinusoidal nature of the longitudinal power flow results plotted in Figure 6.2 is the longitudinal component of motion due to bending waves present in the sample. A study was conducted to verify whether the bending present in the sample could have caused this variation in results. First, a numerical model was constructed of the various longitudinal motions possible in the sample (due to travelling and reflected longitudinal and bending waves). Second, the imaginary part of the resultant cross-spectrum was derived in terms of the separation between the two stations,  $\Delta x$  and the midpoint between the two stations,  $x_0$ . The equation was then programmed on a personal computer, and using inputs obtained from the experimental data, the results were then plotted as a function of  $\Delta x$  and  $x_0$ . The following describes the procedure in detail.

The numerical model includes the effects of the longitudinal waves and also the effects of the bending waves on the longitudinal power flow reading. Bending waves yield a component of motion in the longitudinal direction with a value of half the thickness times the instantaneous slope. For a right travelling wave, for example, with an amplitude of  $A$  the bending induced longitudinal motion is:

$$\begin{aligned} \frac{t}{2} \left[ \frac{\partial \xi}{\partial x} \right] &= \frac{t}{2} \cdot \frac{\partial}{\partial x} [Ae^{i(\omega t - k_B x)}] \\ &= \frac{tk_B}{2} [-iAe^{i(\omega t - k_B x)}] \end{aligned} \quad (6.30)$$

Therefore the component of bending-induced longitudinal motion has an amplitude of  $\frac{tk_b}{2}$  times the bending amplitude and a phase which lags the

bending wave by  $\pi/2$ . For a left travelling wave the amplitude ratio is the same but the phase of the longitudinal motion leads the phase of the bending motion by  $\pi/2$ .

With this as background, the longitudinal motion at stations one and two due to the incident and reflected longitudinal waves and the incident and reflected bending waves can be represented by the following equations.

$$u = \bar{A}(e^{-ik_L x_1} + \bar{R}_L e^{ik_L x_1}) e^{i\omega t} \text{ (Longitudinal Signal At } x_1) \quad (6.31)$$

$$v = \bar{A}(e^{-ik_L x_2} + \bar{R}_L e^{ik_L x_2}) e^{i\omega t} \text{ (Longitudinal Signal At } x_2) \quad (6.32)$$

$$m = \frac{tk_B}{2} \bar{B}(e^{-i(k_B x_1 + \pi/2)} + \bar{R}_B e^{i(k_B x_1 + \pi/2)}) e^{i\omega t} \text{ (Bending Induced Motion At } x_1) \quad (6.33)$$

$$n = \frac{tk_B}{2} \bar{B}(e^{-i(k_B x_2 + \pi/2)} + \bar{R}_B e^{i(k_B x_2 + \pi/2)}) e^{i\omega t} \text{ (Bending Induced Motion At } x_2). \quad (6.34)$$

where  $\bar{A}$  - complex longitudinal amplitude  
 $\bar{R}_L$  - complex longitudinal reflection coefficient  
 $k_L$  - longitudinal wavenumber  
 $t$  - thickness of rod (in measurement plane)  
 $\bar{B}$  - complex bending amplitude  
 $\bar{R}_B$  - complex bending reflection coefficient  
 $k_B$  - bending wavenumber  
 $x_1$  - station one location  
 $x_2$  - station two location  
 $(x_1 - x_2) = \Delta$ , the station spacing  
 $(x_1 + x_2) = 2x_0$ , where  $x_0$  is the midpoint between stations

The resultant signal at station one is  $x = u + m$  and the resultant signal at station two is  $y = v + n$ . The cross-spectrum between the fully coherent signals, is:

$$G_{xy}(f) = G_{uv}(f) + G_{un}(f) + G_{mv}(f) + G_{mn}(f) \quad (6.35)$$

Each term on the right hand side must be evaluated. This is done by forming each of the cross-spectra using the complex expressions previously listed and noting the following general relationship (derived in Appendix C):

$$G_{AB}(f) = A^*(t) \cdot B(t) \quad (6.36)$$

Here  $A^*(t)$  is the complex conjugate of the complex form of the rms signal at A and  $B(t)$  is the complex form of the rms signal at B. (Note: to abbreviate the notation at this point, the dependency on frequency will be understood so that  $G_{un}$ , for example, represents  $G_{un}(f)$ , etc.)

Evaluation of  $G_{uv}$ :

$$G_{uv} = \bar{A}\bar{A}^* \left( e^{ik_L x_1} + \bar{R}_L^* e^{-ik_L x_1} \right) \left( e^{-ik_L x_2} + \bar{R}_L e^{ik_L x_2} \right) e^{i\omega t} \cdot e^{-i\omega t} \quad (6.37)$$

$$G_{uv} = |\bar{A}|^2 \left( e^{ik_L(x_1 - x_2)} + \bar{R}_L e^{ik_L x_2} e^{ik_L x_1} + \bar{R}_L^* e^{-ik_L x_1} e^{-ik_L x_2} + \bar{R}_L^* e^{-ik_L x_1} \cdot \bar{R}_L e^{ik_L x_2} \right) \quad (6.38)$$

$$G_{uv} = |\bar{A}|^2 \left( e^{ik_L(x_1 - x_2)} + 2R_E (\bar{R}_L e^{ik_L(x_2 + x_1)}) + |\bar{R}_L|^2 e^{-ik_L(x_1 - x_2)} \right) \quad (6.39)$$

Since  $x_1 - x_2 = \Delta x$  and since  $x_2 + x_1 = 2x_0$ :

$$G_{uv} = |\bar{A}|^2 \left( e^{ik_L \Delta x} + 2R_E \left\{ \bar{R}_L e^{ik_L(2x_0)} \right\} + |\bar{R}_L|^2 e^{-ik_L \Delta x} \right) \quad (6.40)$$

If one just focuses on the imaginary part (for active power flow):

$$\text{Im}[G_{uv}] = |\tilde{A}|^2 \text{Im}\{e^{ik_L \Delta x} + |\tilde{R}_L|^2 e^{-ik_L \Delta x}\} \quad (6.41)$$

$$\text{Im}[G_{uv}] = |\tilde{A}|^2 (\sin k_L \Delta x - |\tilde{R}_L|^2 \sin k_L \Delta x) \quad (6.42)$$

$$\text{Im}[G_{uv}] = |\tilde{A}|^2 (\sin k_L \Delta x) (1 - |\tilde{R}_L|^2) \quad (6.43)$$

Note that  $|\tilde{R}_L| \leq 1$ . This expression is proportional to the true longitudinal power flow. This is not a function of  $x_0$  for the loss free beam. (Note that the quantity has to be multiplied by the appropriate constants and finite difference correction terms in Equation 6.10 to be an absolute power flow.)

Evaluation of  $G_{mn}$ :

$$\begin{aligned} G_{mn} &= M^*(t) \cdot N(t) \\ &= \frac{\tau k_B}{2} \tilde{B}^* \left( e^{i(k_B x_1 + \pi/2)} + \tilde{R}_B^* e^{-i(k_B x_1 + \pi/2)} \right) \\ &\quad \cdot \frac{\tau k_B}{2} \tilde{B} \left( e^{-i(k_B x_2 + \pi/2)} + \tilde{R}_B e^{i(k_B x_2 + \pi/2)} \right) e^{i\omega t} \cdot e^{-i\omega t} \end{aligned} \quad (6.44)$$

$$\begin{aligned} G_{mn} &= \left( \frac{\tau k_B}{2} \right)^2 |\tilde{B}|^2 \left( e^{ik_B(x_1 - x_2)} - \tilde{R}_B e^{ik_B(x_1 + x_2)} \right. \\ &\quad \left. - \tilde{R}_B^* e^{-ik_B(x_1 + x_2)} + \tilde{R}_B^* \tilde{R}_B e^{-i(x_1 - x_2)k_B} \right) \end{aligned} \quad (6.45)$$

$$\begin{aligned} G_{mn} &= \left( \frac{\tau k_B}{2} \right)^2 |\tilde{B}|^2 \left( e^{ik_B(x_1 - x_2)} - 2\tilde{R}_B \tilde{R}_B^* e^{ik_B(x_1 + x_2)} + |\tilde{R}_B|^2 e^{-ik_B(x_1 - x_2)} \right) \\ &\quad \text{Since } x_1 - x_2 = \Delta x \text{ and } x_1 + x_2 = 2x_0: \end{aligned} \quad (6.46)$$

$$G_{mn} = \left( \frac{\tau k_B}{2} \right)^2 |\tilde{B}|^2 \left( e^{ik_B \Delta x} - 2\tilde{R}_B \tilde{R}_B^* e^{ik_B 2x_0} + |\tilde{R}_B|^2 e^{-ik_B \Delta x} \right) \quad (6.47)$$

Using just the imaginary part:

$$\text{Im}[G_{mn}] = \left( \frac{\tau k_B}{2} \right)^2 |\tilde{B}|^2 \text{Im}\{e^{ik_B \Delta x} + |\tilde{R}_B|^2 e^{-ik_B \Delta x}\} \quad (6.48)$$

$$\text{Im}[G_{mn}] = \left( \frac{\tau k_B}{2} \right)^2 |\tilde{B}|^2 (\sin k_B \Delta x) (1 - |\tilde{R}_B|^2) \quad (6.49)$$

Evaluation of Gun:

$$\text{Gun} = U^*(t) \cdot N(t) \quad (6.50)$$

$$\begin{aligned} \text{Gun} = \bar{A}^* \left( e^{ik_L x_1} + \bar{R}_L^* e^{-ik_L x_1} \right) e^{-i\omega t} \cdot \frac{tk_B}{2} \bar{B} \left( e^{-i(k_B x_2 + \pi/2)} \right. \\ \left. + \bar{R}_B e^{i(k_B x_2 + \pi/2)} \right) e^{i\omega t} \end{aligned} \quad (6.51)$$

$$\begin{aligned} \text{Gun} = \bar{A}^* \bar{B} \frac{tk_B}{2} \left\{ e^{i(k_L x_1 - k_B x_2 - \pi/2)} + \bar{R}_B e^{i(k_L x_1 + k_B x_2 + \pi/2)} \right. \\ \left. + \bar{R}_L^* e^{i(-k_L x_1 - k_B x_2 - \pi/2)} + \bar{R}_L^* \bar{R}_B e^{i(-k_L x_1 + k_B x_2 + \pi/2)} \right\} \end{aligned} \quad (6.52)$$

No simplification appears possible here but using

$e^{+i\pi/2} = i$  and  $e^{-i\pi/2} = -i$  to reduce the exponential terms:

$$\begin{aligned} \text{Gun} = \bar{A}^* \bar{B} \frac{tk_B}{2} \left\{ -ie^{i(k_L x_1 - k_B x_2)} + i\bar{R}_B e^{i(k_L x_1 + k_B x_2)} \right. \\ \left. - i\bar{R}_L^* e^{i(-k_L x_1 - k_B x_2)} + i\bar{R}_L^* \bar{R}_B e^{i(-k_L x_1 + k_B x_2)} \right\} \end{aligned}$$

$$\begin{aligned} \text{Gun} = \bar{A}^* \bar{B} i \frac{tk_B}{2} \left\{ -e^{i(k_L x_1 - k_B x_2)} + \bar{R}_B e^{i(k_L x_1 + k_B x_2)} \right. \\ \left. - \bar{R}_L^* e^{-i(k_L x_1 + k_B x_2)} + \bar{R}_L^* \bar{R}_B e^{-i(k_L x_1 - k_B x_2)} \right\} \end{aligned}$$

Evaluation of Gmv:

$$\text{Gmv} = M^*(t) \cdot V(t) \quad (6.55)$$

$$\begin{aligned} \text{Gmv} = \frac{tk_B}{2} \bar{B}^* \left( e^{+i(k_B x_1 + \pi/2)} + \bar{R}_B^* e^{-i(k_B x_1 + \pi/2)} \right) e^{-i\omega t} \\ \cdot \bar{A} \left( e^{-ik_L x_2} + \bar{R}_L e^{ik_L x_2} \right) e^{i\omega t} \end{aligned} \quad (6.56)$$

$$\begin{aligned} \text{Gmv} = \frac{tk_B}{2} \bar{A} \bar{B}^* \left\{ e^{i(k_B x_1 + \pi/2 - k_L x_2)} + \bar{R}_B^* e^{-i(k_B x_1 + \pi/2 + k_L x_2)} \right. \\ \left. + \bar{R}_L e^{i(k_B x_1 + \pi/2 + k_L x_2)} + \bar{R}_L \bar{R}_B^* e^{-i(k_B x_1 + \pi/2 - k_L x_2)} \right\} \end{aligned} \quad (6.57)$$

Using  $e^{i\pi/2} = i$  and  $e^{-i\pi/2} = -i$  obtain:

$$\begin{aligned} \text{Gmv} = \bar{A} \bar{B}^* \frac{tk_B}{2} \left\{ ie^{i(k_B x_1 - k_L x_2)} - i\bar{R}_B^* e^{-i(k_B x_1 + k_L x_2)} \right. \\ \left. + i\bar{R}_L e^{i(k_B x_1 + k_L x_2)} - i\bar{R}_L \bar{R}_B^* e^{-i(k_B x_1 - k_L x_2)} \right\} \end{aligned} \quad (6.58)$$

$$\begin{aligned} \text{Gmv} = \bar{A} \bar{B}^* i \frac{tk_B}{2} \left\{ e^{i(k_B x_1 - k_L x_2)} - \bar{R}_B^* e^{-i(k_B x_1 + k_L x_2)} \right. \\ \left. + \bar{R}_L e^{i(k_B x_1 + k_L x_2)} - \bar{R}_L \bar{R}_B^* e^{-i(k_B x_1 - k_L x_2)} \right\} \end{aligned} \quad (6.59)$$

The exponents of  $\text{Gun}(f)$  and  $\text{Gmv}(f)$  can be related to  $x_0$  and  $\Delta x$  if one uses the following forms:

$$x_1 = \left[ \frac{2x_0 + \Delta x}{2} \right] \quad (6.60)$$

$$x_2 = \left[ \frac{2x_0 - \Delta x}{2} \right] \quad (6.61)$$

Substitution of these equations into the exponents with some simplification yields expressions for  $\text{Gun}$  and  $\text{Gmv}$  such that their sum becomes:

$$\begin{aligned} \text{Gun} + \text{Gmv} = & \tilde{A}^* \tilde{B} \frac{i\tau k_B}{2} \left\{ e^{i\left\{\frac{\Delta x}{2}(k_L + k_B)\right\}} e^{-ix_0(k_B - k_L)} \right. \\ & + \tilde{R}_B e^{-i\left\{\frac{\Delta x}{2}(k_B - k_L)\right\}} e^{ix_0(k_B + k_L)} \\ & - \tilde{R}_L^* e^{i\left\{\frac{\Delta x}{2}(k_B - k_L)\right\}} e^{-ix_0(k_B + k_L)} \\ & \left. + \tilde{R}_L^* \tilde{R}_B e^{-i\left\{\frac{\Delta x}{2}(k_B + k_L)\right\}} e^{ix_0(k_B - k_L)} \right\} \\ & + \tilde{A} \tilde{B}^* \frac{i\tau k_B}{2} \left\{ e^{i\left\{\frac{\Delta x}{2}(k_L + k_B)\right\}} e^{ix_0(k_B - k_L)} \right. \\ & - \tilde{R}_B^* e^{-i\left\{\frac{\Delta x}{2}(k_B - k_L)\right\}} e^{-ix_0(k_B + k_L)} \\ & + \tilde{R}_L e^{i\left\{\frac{\Delta x}{2}(k_B - k_L)\right\}} e^{ix_0(k_B + k_L)} \\ & \left. - \tilde{R}_L \tilde{R}_B^* e^{-i\left\{\frac{\Delta x}{2}(k_B + k_L)\right\}} e^{-ix_0(k_B - k_L)} \right\} \end{aligned} \quad (6.62)$$

An inspection of this equation shows that the comparable terms of  $\text{Gun}$  and  $\text{Gmv}$  are complex conjugates except for the following points; they are both multiplied by "i", one is negated (i.e., multiplied by  $e^{i\pi}$ ), and then both vectors are rotated through multiplication by some  $e^{i\psi}$ . If one considers the corresponding terms initially as complex conjugates (so that the two vectors reflect about the real axis), and steps through

these operations, it can be shown that the imaginary part of the sum of any pair of the corresponding terms is equal to the resultant (after the one vector is negated) times the sine of the rotation angle  $\psi$ . This leads to the following simplification for the imaginary part of  $G_{un}$  and  $G_{mv}$ :

$$\begin{aligned} \text{Im}[G_{un} + G_{mv}] = & 2R_E \left\{ \bar{A}\bar{B}^* i \frac{tk_B}{2} e^{ix_0(k_B - k_L)} \right\} \cdot \sin\left\{\frac{\Delta x}{2}(k_B + k_L)\right\} \\ & + 2R_E \left\{ \bar{A}^* \bar{B} i \frac{tk_B}{2} \bar{R}_B e^{ix_0(k_B + k_L)} \right\} \cdot \sin\left\{\frac{-\Delta x}{2}(k_B - k_L)\right\} \\ & + 2R_E \left\{ \bar{A}\bar{B}^* i \frac{tk_B}{2} \bar{R}_L e^{ix_0(k_B + k_L)} \right\} \cdot \sin\left\{\frac{\Delta x}{2}(k_B - k_L)\right\} \\ & + 2R_E \left\{ \bar{A}^* \bar{B} i \frac{tk_B}{2} \bar{R}_L \bar{R}_B e^{ix_0(k_B - k_L)} \right\} \cdot \sin\left\{\frac{-\Delta x}{2}(k_B + k_L)\right\} \quad (6.63) \end{aligned}$$

The total measured longitudinal power flow is then proportional to:

$$\text{Im}[G_{xy}] = \text{Im}[G_{uv} + G_{un} + G_{mv} + G_{mn}] \quad (6.64)$$

which represents the sum of Equations 6.43, 6.63, and 6.49.

The next task is to evaluate all of the coefficients in the previous equations, namely  $\bar{A}$ ,  $\bar{B}$ ,  $\bar{R}_L$ , and  $\bar{R}_B$ . These values can be obtained from the experimental data, and from the boundary conditions. First to be noted is that since the initial longitudinal travelling wave and bending travelling wave have their origin at the shaker they must both be in phase at this point. Therefore the complex constants  $\bar{A}$  and  $\bar{B}$  both have the same phase value and consequently the product  $\bar{A}^* \bar{B}$  or  $\bar{A}\bar{B}^*$  must be a real quantity.



Examination of the longitudinal data relating to Figure 6.2 yields an antinodal value of 0.924 volts (rms) and a nodal value of approximately 0.085 volts (rms). This provides an incident wave amplitude of 0.505 volts and a reflected wave amplitude of 0.420 volts. The magnitude of the reflection coefficient is then the ratio of the previous values or approximately 0.83. Finally the node closest to the termination diaphragm was located 37 mm away from it. Using Equation 6.22 of Kinsler and Frey (1962) the phase angle of the reflection coefficient is:

$$\theta_L = -\pi - 2k_L x \quad (6.65)$$

$$\theta_L = -\pi - 2 \left[ .173 \frac{\text{rad}}{\text{cm}} \right] (-3.7 \text{ cm}) \quad (6.66)$$

$$\theta_L = -1.86 \text{ radians} \quad (6.67)$$

Examination of the bending data yields a recorded value of the nodal to antinodal voltage equal to 0.40. This is the inverse of the standing wave ratio in Kinsler and Frey so that Equation 6.21a of this reference yields a magnitude of the bending reflection coefficient of 0.43. The bending antinodal voltage was 2.11 volts rms. However, this has to be reduced to an equivalent value considering the difference in sensitivities of the reference beam and differential Doppler techniques. The lens was a 243 mm lens with a half-angle of approximately 5.9 degrees so that the above value should be multiplied by the tangent of this angle or 0.103. Therefore the bending antinodal voltage, corrected for sensitivity, is 0.22 volts rms. Consequently, the nodal voltage is (0.40 • 0.22 volts) or 0.088 volts rms. Knowledge of the bending nodal

and antinodal voltages provides a bending incident wave amplitude of 0.154 volts rms.

Finally to be determined is the phase angle of the bending reflection coefficient. A bending node was recorded to be at approximately 318 mm from the diaphragm. If one uses the recorded bending wavelength of 64 mm there are approximately five wavelengths (4.97) between this node and the diaphragm. This indicates that a bending node occurs at the diaphragm. This agrees with the fact that the diaphragms should be preventing transverse motion. For a bending node at the diaphragm, the phase angle of the bending reflection coefficient is  $\theta_B = -\pi$  radians.

In summary, the coefficients which should be entered into the program are for longitudinal data:

$$A = 0.505 \text{ volts rms (incident wave amplitude)}$$

$$\tilde{R}_L = 0.83 e^{i(-1.86)}$$

and for bending data:

$$B = 0.154 \text{ volts rms}$$

$$\tilde{R}_B = 0.43 e^{i(-\pi)}$$

Additionally, other relevant input includes:

$$\Delta x = 15.24 \text{ cm (laser beam separation)}$$

$$k_L = 0.173 \text{ radians/cm (longitudinal wavenumber)}$$

$$k_B = 0.98 \text{ radians/cm (bending wavenumber)}$$

$$t = 0.635 \text{ cm (beam thickness)}$$

Results from the theoretical model are then multiplied by the constants in Equation 6.10 to convert to a power flow. These results

have been superimposed on experimental results in Figure 6.5 through Figure 6.9. Figure 6.5 illustrates the theoretical data for the input previously cited. The data from the model shows the same sinusoidal nature and nearly the same wavenumber as the experimental data although the amplitudes and phase are mismatched somewhat. Nevertheless the most important point here is that the bending-induced longitudinal motion can indeed induce a high amplitude periodicity in the measured power flow data. The theoretical "true" value of the longitudinal power flow (i.e., the value obtained from the model when the bending amplitude is zero) is 1.21 mW which compares very well with the experimental standing wave result of 1.23 mW shown in Figure 6.5. The energetics result (2.30 mW) is also shown.

A brief investigation into the influence of the angle of the reflection coefficient on the results was also conducted. Figure 6.6 illustrates an example of what occurs to the predictions from the model if this reflection angle is zero. In this case the theoretical and experimental two-point data begin to compare quite well in amplitude and phase.

In the previous section it was speculated that using a laser beam separation equal to the bending wavelength and positioning the two laser beams on the bending antinodes might provide a reasonably unaffected longitudinal power flow measurement. To investigate this possibility the program was run with this laser beam separation (with a corresponding adjustment in the finite difference correction factor). Figure 6.7 illustrates the result for a reflection angle of zero radians. The theoretical two-point data is considerably less periodic

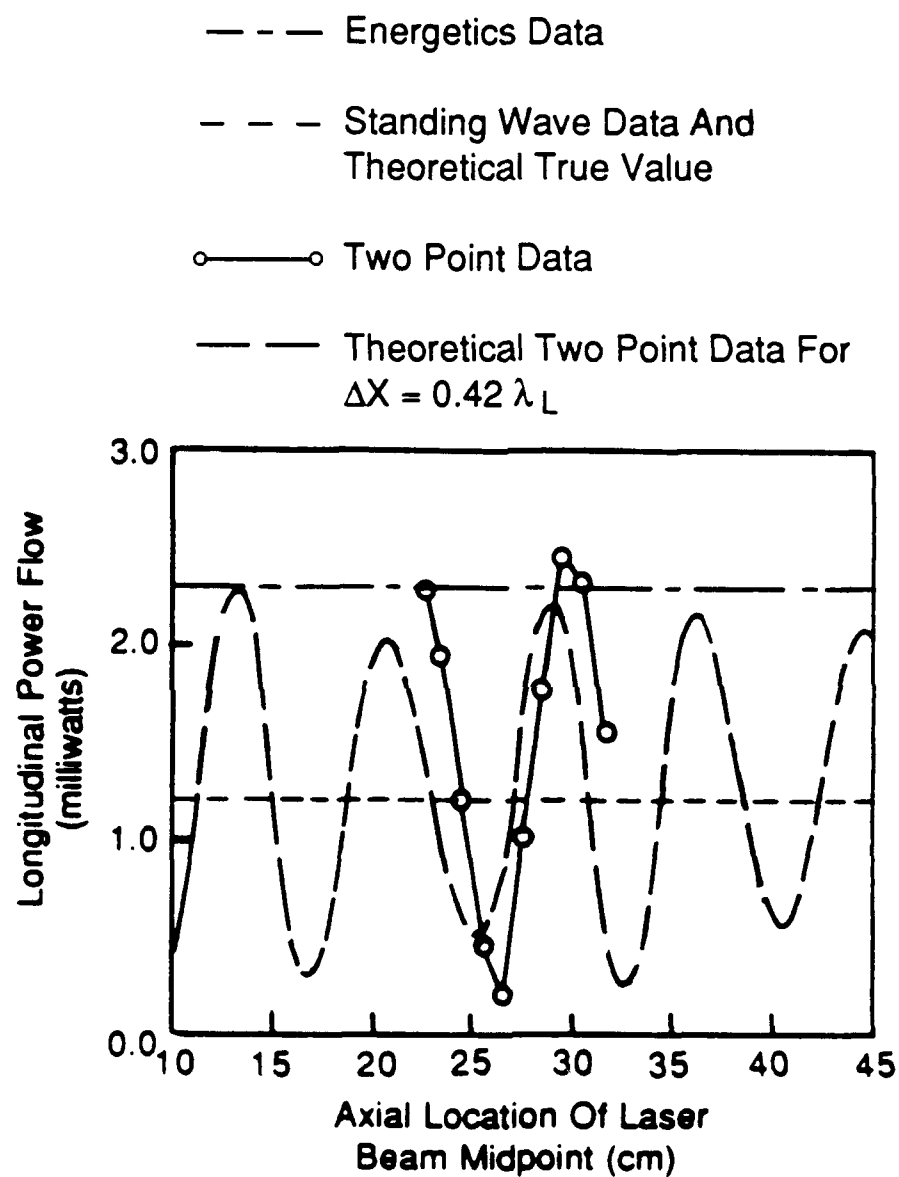


Figure 6.5 Comparison of Longitudinal Power Flow Experimental Results and Theoretical Results ( $\Delta x = 15.24$  cm,  $\theta_L = -1.86$  radians)

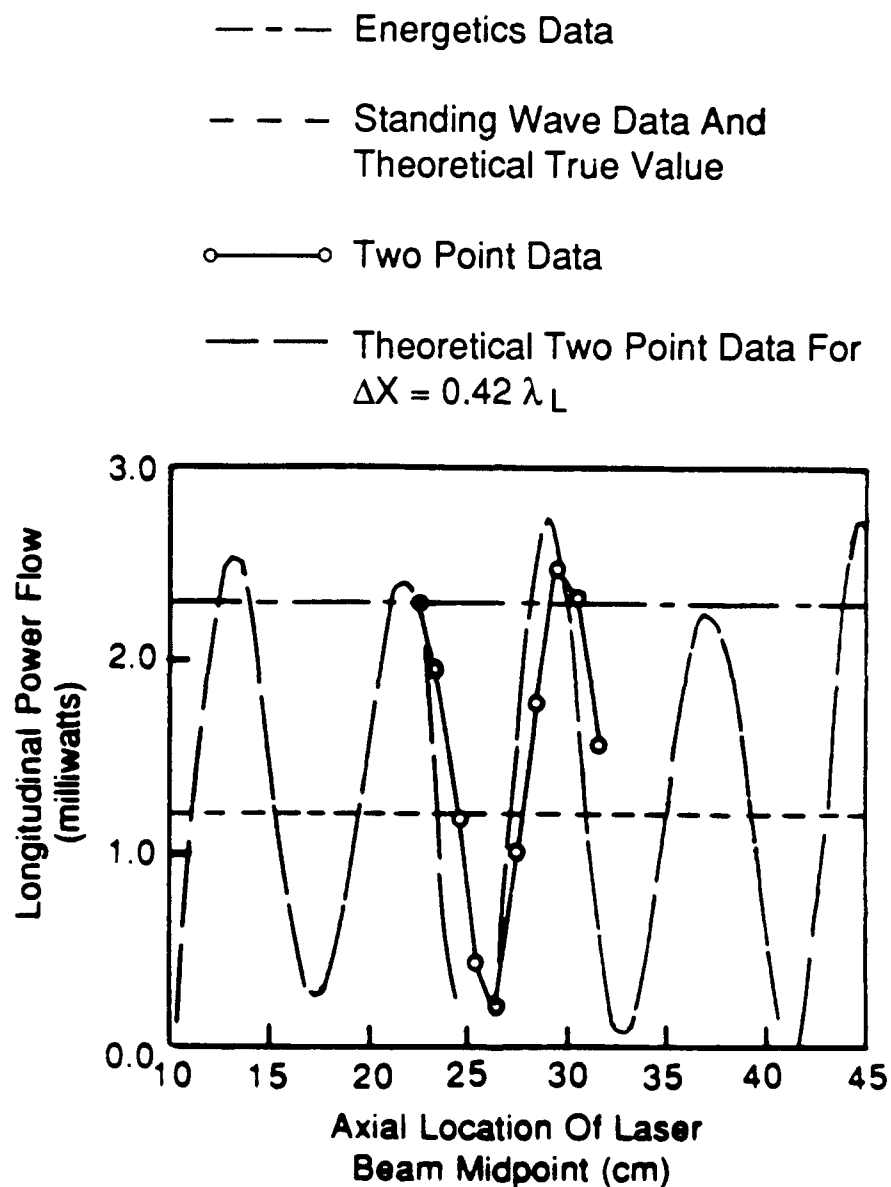


Figure 6.6 Comparison of Longitudinal Power Flow  
 Experimental and Theoretical Results  
 ( $\Delta x = 15.24$  cm,  $\theta_L = 0.0$  radians)

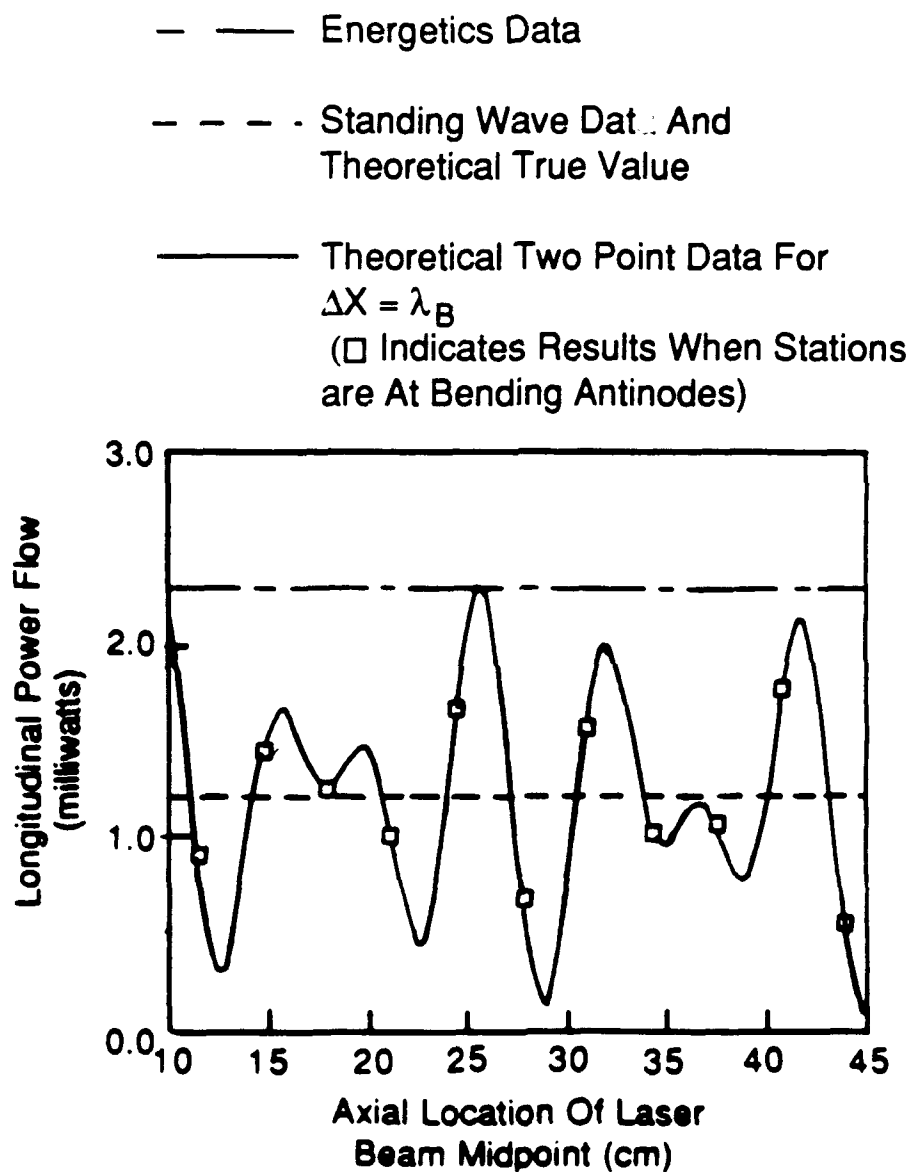


Figure 6.7 Comparison of Longitudinal Power Flow  
 Experimental and Theoretical Results  
 ( $\Delta x = \lambda_B$ ,  $\theta_L = 0.0$  radians)

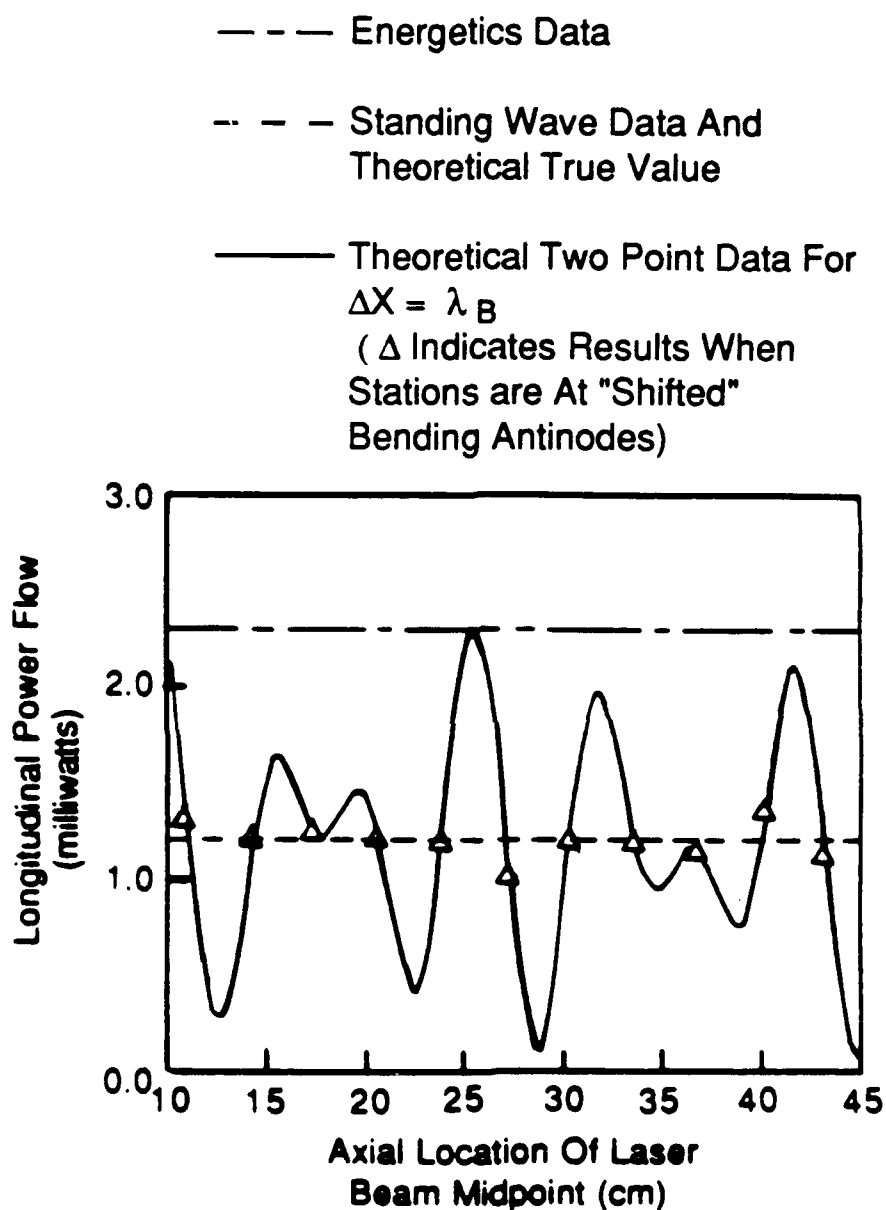


Figure 6.8 Comparison of Longitudinal Power Flow Experimental and Theoretical Results (Shifted Antinodes)  
 ( $\Delta x = \lambda_B$ ,  $\theta_L = 0.0$  radians)

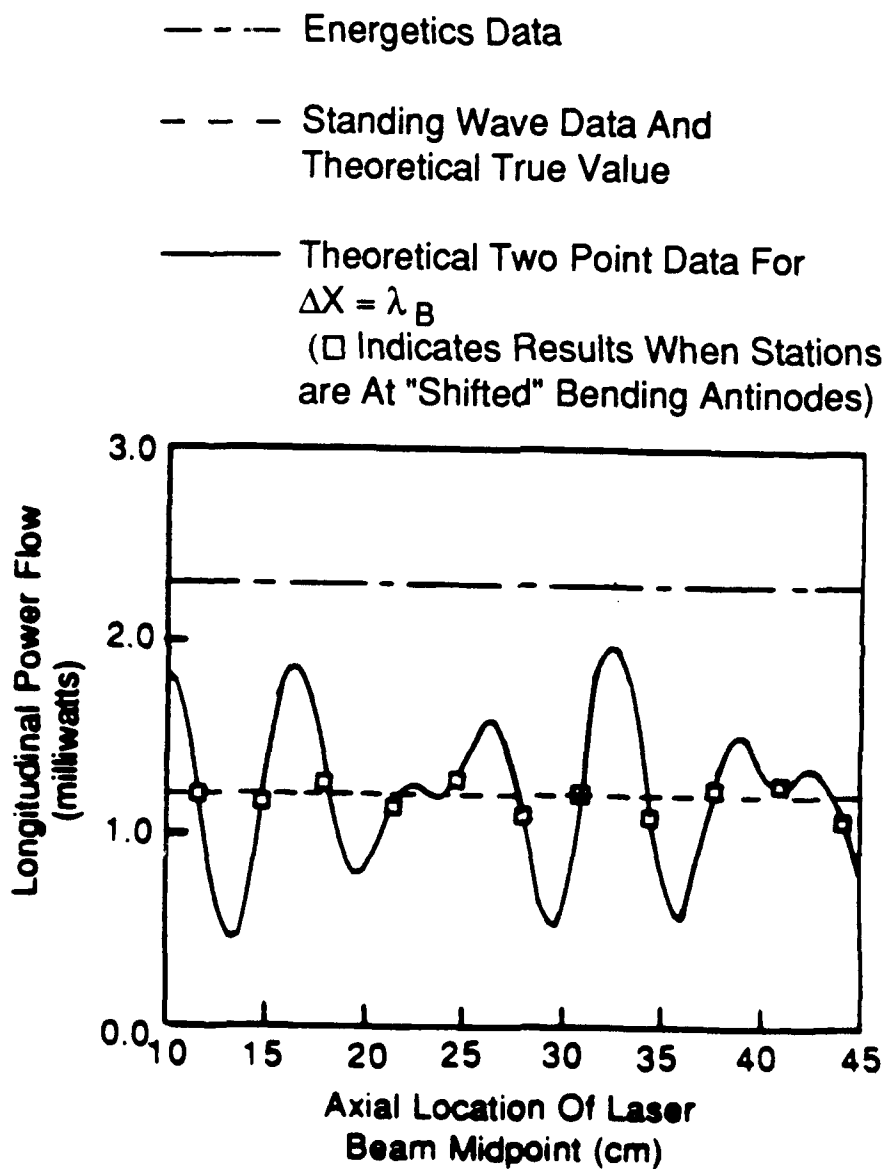


Figure 6.9 Comparison of Longitudinal Power Flow Experimental and Theoretical Results ( $\Delta x = \lambda_B$ ,  $\theta_L = 1.86$  radians)



than it was for the previous separation distance. Markers on the theoretical data represent axial locations of the laser beam midpoint such that both laser beams would be positioned on bending antinodes. These are the bending antinodal locations as estimated from the experimental data. The figure indicates that using the antinodes would not provide results consistent with the theoretical true value. However if one allows for the possibility that the experimental antinodal locations may be slightly in error, and allows for a shift of approximately 0.67 cm, one obtains the results illustrated in Figure 6.8. These marked positions indicate that the antinodal technique provides data consistently very close to the theoretical true value.

For the reflection angle of -1.86 radians, as obtained experimentally, Figure 6.9 again shows a general grouping at these points toward the "true" value of the longitudinal power flow. The majority of the points are within approximately ten percent of the true value.

Due to the relatively high value of power flow predicted by the energetics equation, an investigation was also conducted into its applicability in this low longitudinal mode number test. Equation 6.7 actually incorporates an integration of the square of the velocity over the beam length which is found to be equal to:

$$\int_0^L [v(x)]^2 dx = \frac{|v_N|^2 + |v_{AN}|^2}{2} L \quad (6.68)$$

(Here  $v_N$  is the nodal velocity and  $v_{AN}$  is the antinodal velocity). This is an approximation in the flexural case since it ignores the nearfields

although for all but the lowest modes it is sufficient. In the longitudinal case, no nearfields are present but for very low order modes the integral will depend on the boundary conditions. For the third longitudinal mode as in this test, the integral will provide the result in Equation 6.68 if the ends are true antinodes. However, if the reflection coefficient is not real but complex (as indicated by the data) then the mode shape is altered and the integration may not be exact. The data indicates a first longitudinal node at approximately 9.8 cm from the shaker, the second spaced an additional 19.0 cm and the third spaced an additional 19.5 cm leaving 3.7 cm to the end diaphragm. This implies that the end diaphragm may not be a true antinode. This would result in an overprediction of the longitudinal power flow by use of Equation 6.7 but the difference would only be on the order of ten to fifteen percent.

Other potential errors which may account for the high value of  $\Pi_E$  include measurements of the loss factor, the mass per unit length, the Young's modulus, the beam length, and the longitudinal antinodal value itself. Of these, the loss factor and antinodal voltage measurements have the most potential for error. It is well known that in constrained beams (such as in the termination of the beam in these tests), the loss factors for bending waves are higher than the loss factors for longitudinal waves. Therefore, the bending waves induced in the beam may have produced a loss factor measured for longitudinal waves that was higher than the true loss factor for longitudinal waves. This would result in an erroneously higher value of  $\Pi_E$  as indicated in Equation 6.7. Since the determination of the standing wave power flow

does not depend on the loss factor for longitudinal waves, it is expected to be more accurate. Agreement between the two-point power flow measurements, corrected for bending-induced longitudinal motion, and the standing wave power flow measurements indicates that corrections can be made for the bending-induced longitudinal motion to obtain accurate measurements for the pure longitudinal wave power flow.

## CONCLUSIONS

Results from this chapter indicate that an important optical problem has to be solved before the differential Doppler technique can reliably be used for general longitudinal power flow measurements. This problem is the instability of the technique in the presence of high bending amplitudes. One solution, as will be demonstrated in Chapter IX, lies in using an "appropriately sized" aperture but this technique requires considerable study and quantification.

If this speckle-related problem can in general be solved then the effects of bending-induced longitudinal motion must somehow be addressed so that true longitudinal power flows can be measured. The modelling of the effects of the bending induced longitudinal motion on the power flow was successful for this simple case but for two-dimensional motion this modelling may be extremely difficult. For the cancellation of such bending effects one may be forced to use one vibrometer beam on opposite sides of the structure. This may be difficult for plates and cylinders.

The computer model of the influence of bending on longitudinal power flow readings illustrates how even a moderate degree of bending (approximately thirty percent of the longitudinal motion in this case)

can produce high fluctuations in the measured longitudinal power flow if both laser beams illuminate the object on the same surface. Also shown by the model is that the procedure of spacing the laser beams one bending wavelength apart and positioning the beams on bending antinodes may provide accurate (to within approximately 10%) longitudinal power flow measurements.

Finally, although the longitudinal power flow results are generally acceptable considering the agreement between the computer model results and the experimental standing wave and two-point results, the disparity in the energetics result (which is approximately twice the standing wave result) can not be quantitatively reconciled. It is suspected that the influence of nearby damped bending modes on the longitudinal loss factor result may have been the problem. One also has to keep in mind that the experimental longitudinal values input to the computer model are also "tainted" in that they too contain some degree of bending-induced longitudinal motion in them. Considering these points, the longitudinal technique, although it appears to be promising, should undergo further verification before general use. The verification technique must be one in which the speckle instability problem can be suppressed if it is present, and one in which the presence of bending does not interfere with verification.

## Chapter VII

### CHARACTERISTICS CONTROLLING THE SIGNAL-TO-NOISE RATIO IN THE DIFFERENTIAL DOPPLER METHOD

#### INTRODUCTION

This chapter is analogous to Chapter V for flexural intensity (for the reference beam method). The objective of the chapter is ultimately to establish the noise floor in each channel as a function of optical parameters such as the carrier-to-noise ratio. This chapter does not have the detail that Chapter II has, principally because there is no known documentation of the influence of optical parameters on the CNR in differential Doppler vibrometry. However, the noise floors of the vibrometers are established experimentally as a function of the CNR. The establishment of these noise floors assumes that the presence of the longitudinal motion does not alter the noise floors. This has been found to be true for moderate longitudinal motion in the differential Doppler technique. The introduction of large amplitude longitudinal motion or motion other than longitudinal motion may, in some cases, alter both the signal and the noise floor due to speckle effects. This phenomenon is addressed in the Chapter IX.

The latter part of this chapter addresses the signal associated with longitudinal motion so that vibrometer signal-to-noise ratios can be presented as a function of the CNR and the amount of longitudinal motion. Phase-locked loop characteristics are not addressed in this

chapter since these remain the same (as in Chapter V) despite the difference in the optical mode being used.

#### **CARRIER-TO-NOISE RATIO AND PLL PERFORMANCE AS APPLIED TO THE DIFFERENTIAL DOPPLER METHOD**

As with the reference beam method, the signal-to-noise ratio of the velocity signal in the differential Doppler method is also influenced by both the quality of the FM signal and the sensitivity of the PLL processor to the quality of the FM signal. Recall from Chapter II that the quality of the FM signal is characterized by the carrier-to-noise ratio (CNR). Unfortunately there is little available in the literature regarding the theoretical prediction of the CNR for the differential Doppler technique as applied to vibrations of solids. Consequently this section considers the experimentally determined influence of such parameters as laser power, and laser spot position on the object in order to establish practical limits of a two-channel differential Doppler technique in the study of longitudinal power flow.

For experimental studies of the carrier-to-noise ratio and the signal-to-noise ratio, both channels of the TCV system were setup in the differential Doppler mode; the vibrometer adaptor was removed from both channels and the beam splitter in each channel was switched to allow for a 50-50 intensity split in the two beams (rather than the 99.5 - 0.5 split in the reference beam method). This resulted in an interferometric sensitivity in the horizontal direction as the two equal intensity beams in each channel were focussed in a horizontal plane when they emerged from the respective lenses. The beams from each channel

were focussed on two spots on a stationary object located on the optical (vibration isolated) table. Only one vibrometer was needed for studies concerning the FM signal quality. Both vibrometers were used only in the test for coherent noise. The results are reviewed below.

The noise floor in the FM signal is associated with the detector shot noise and is above the thermal or "Johnson noise" of the detector. This is illustrated by the spectral overlay shown in Figure 7.1. The upper spectrum is, for the vibrometer, in regular operation with the beams focussed onto the stationary object; the 50 kHz carrier in this case is more than 50 dB above the noise. The lower spectrum is for the beams blocked off to the photodetector. One can see that the broadband noise drops off when the detector is receiving no input. A test on the makeup of this lower spectrum revealed that it consists only of the self-noise of the analyzer combined with some noise spikes generated by the electronic downmixer; the thermal noise is below these levels. Nevertheless the detection can be said to be "shot noise limited" in the differential Doppler technique as it was for the reference beam technique.

The influence of laser power on the FM signal for a fixed point on the object was tested next. Laser power (total power into both channels) was set at 25 mW, and advanced to 50, 100, 150 mW while the FM spectrum in each case was recorded after 128 linear averages. As the laser power increased, the FM noise floor continually decreased (while the 50 kHz signal increased) with a cumulative drop of 7 dB from the 25 mW laser power case to the 150 mW power case. At 150 mW the FM noise floor was at a level of minus 72 dB relative to an rms voltage of

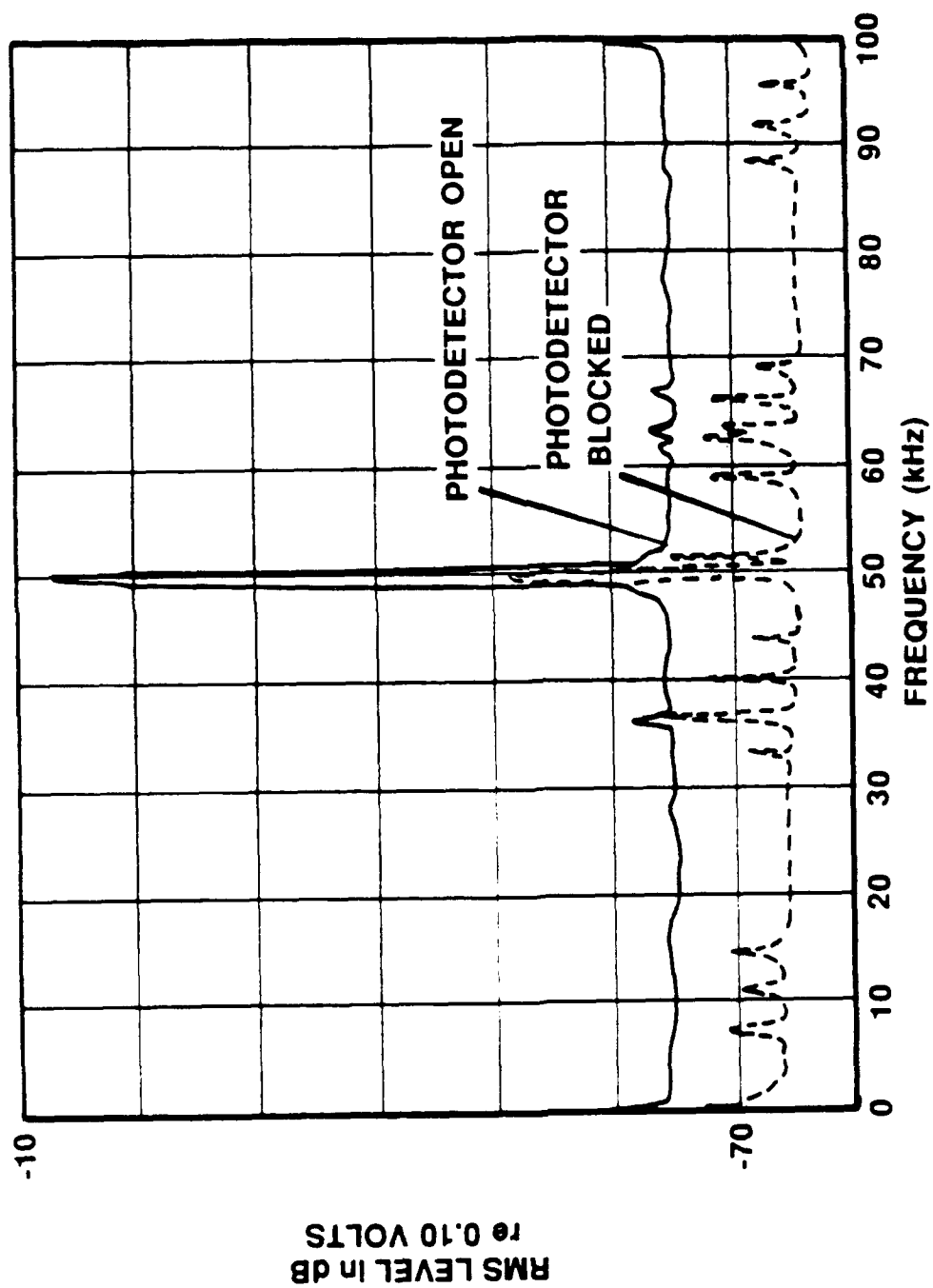


Figure 7.1 Comparison of Downmixed Photodetector Spectra With and Without Light to Photodetector for the Differential Doppler Mode



0.1 volts which is approximately the noise floor of the analyzer itself. This drop in the FM noise floor with laser power was repeatable. But why the noise floor should decrease rather than increase somewhat with laser power (as in the reference beam case) at first was not fully understood. (Later it was found that the beam moved slightly with laser power inducing a speckle related effect.) Table 7.1 shows a listing of laser power (total laser power in both channels) versus the carrier-to-noise ratio obtained from these differential Doppler tests. (Note that these results are for an arbitrary point on the object surface; the absolute values are not as important as the trends.)

Table 7.1

Comparison of CNR Values for Various Amounts of  
Total Laser Power in the Differential Doppler Mode

<u>Total Laser Power (mW)*</u>	<u>CNR (dB)</u>
150	65.5
100	59.6
50	55.7
25	52.6

\* Actual value for one vibrometer was approximately one-half this value.

As was done in the case of the reference beam approach, a test was run to determine the influence of the focussed spot location on the FM signal quality (a result of laser speckle). A comparison of the spectra resulting from an optimum spot versus a "less optimum" spot for a fixed laser power shows that only the FM signal amplitude is altered while the noise floor remains constant. Figure 7.2 illustrates these results.

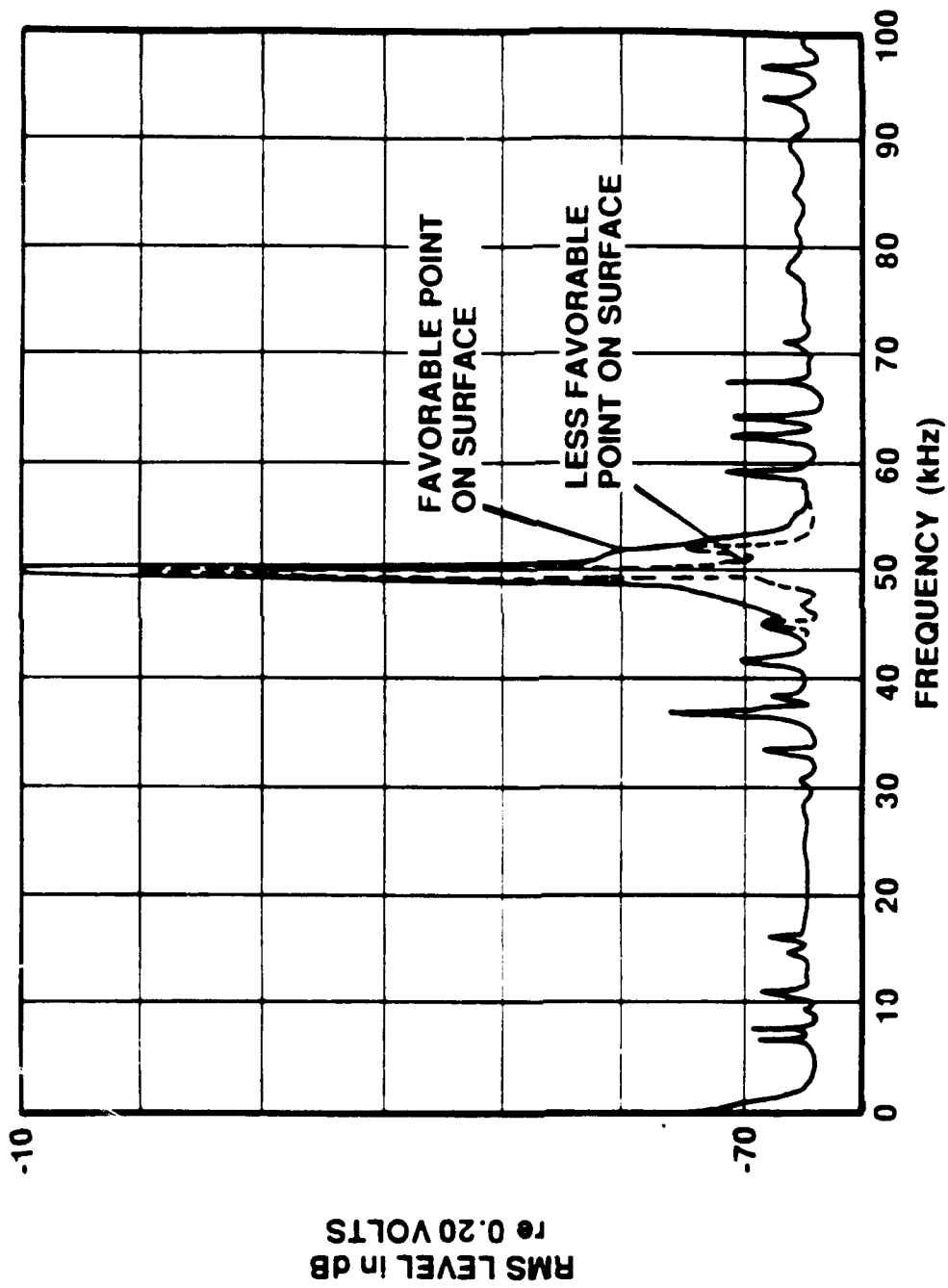


Figure 7.2 Comparison of Downmixed Photodetector Spectra at Two Nearby Points on a Stationary Object for the Differential Doppler Mode

(The actual amplitude of the signal in the upper spectrum was minus 5.6 dB but the vertical scale had to be chosen so as to illustrate the noise.) This figure upon comparison with Figure 4.3 (a comparison of optimum and "non-optimum" points using the reference beam technique), shows an interesting characteristic of the FM noise floor for the differential Doppler technique; it is at least 7 dB lower than the noise floor in the FM spectrum for the reference beam technique.

The noise floor in Figure 7.2 is approximately the value of the analyzer noise floor (which occurs for a total laser power of 150 mW as noted previously) so that the true FM noise floor for the differential Doppler case at 150 mW may be more than 7 dB below that of the reference beam technique.

The next tests examined the effects of different CNR values on the demodulated noise floor. For these tests the laser spot was moved slightly on the object in each case to provide a varying amplitude of the Doppler (FM carrier) signal while the total laser power was constant at 150 mW. Figure 7.3 is an overlay of the noise spectra at five different values of CNR. These values span the realistic range of obtainable Doppler signals for a differential Doppler setup.

Most notable in Figure 7.3 is the absence of the spurious spectral peaks at approximately 750 Hz and 1300 Hz which were always present in the demodulated noise floors for the reference beam technique. Their absence in this technique indicates several things; the spurious peaks in the reference beam technique are not caused by instability in the Bragg cell shifting frequency nor are they caused by laser intensity fluctuations (since those problems would be expected to show up in the differential

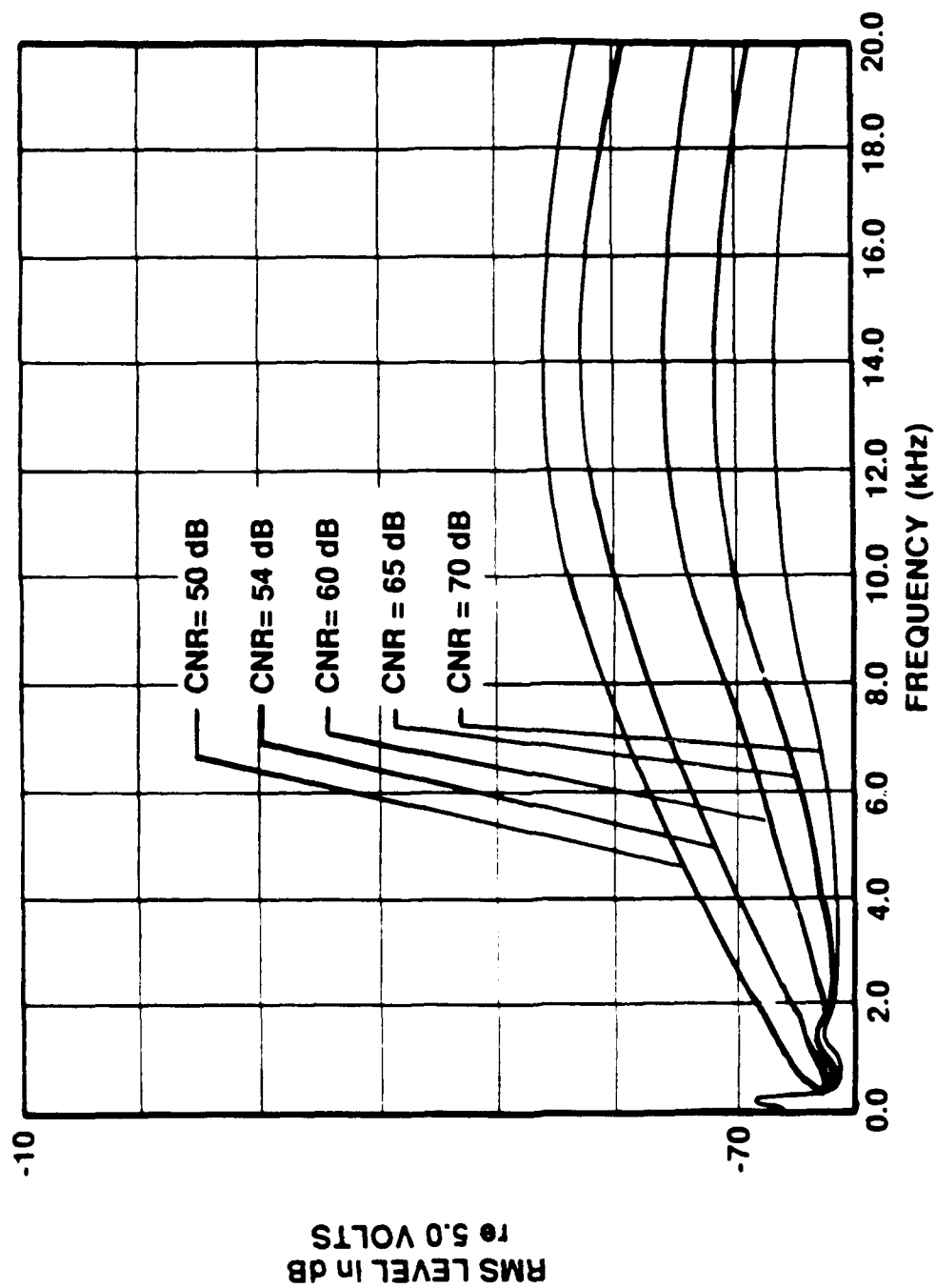


Figure 7.3 Comparison of Velocity Noise Floors for Different CNR Values for the Differential Doppler Mode

Doppler technique), and they are not caused by any of the electronics (since the electronics are the same for both techniques).

The remaining potential sources of the spectral peaks are vibration of the optics (which has not been detected using an accelerometer) and possibly a pathlength difference related problem. Neither of these two problems would yield spurious peaks in the differential Doppler mode. The pathlength difference in the reference beam mode was set to an integer multiple of the laser cavity length even though an etalon was used. But the pathlength matching in the differential Doppler mode is inherently exact due to the setup. It should also be noted that the replacement of the laser tube did not resolve this problem nor did the exchanging of the etalon card which actively controls the heating of the etalon to ensure single line operation. Consequently the origin of spurious peaks in the reference beam technique is suspected to be due to laser FM noise which is not canceled out by perfect pathlength matching as in the differential Doppler technique.

The absence of the spurious spectral peaks in the differential Doppler mode indicates that there is no coherent noise between the channels for this technique. A test of the coherence between the two systems for both channels focussed on a stationary object verified that there is zero coherence across the whole spectrum extending up to 20 kHz for this method.

As can be noted from Figure 7.3, the noise floor is reduced at the same rate at which the CNR is increased. The CNR values in Figure 7.3 are lower than those plotted for the comparable reference beam case

because of the lower FM noise floor in the differential Doppler technique. An examination of typical signals obtained from a surface treated with retro-reflective paint indicated that a CNR of approximately 60 dB was a conservative value of the average CNR to be expected in the differential Doppler technique for such a surface. This value corresponds to a peak-to-peak Doppler voltage of 0.1 volt for this system. The CNR in this technique is approximately 9 dB higher than the corresponding typical CNR in the reference beam technique which results in a noise floor nearly 10 dB lower than for the typical signal in the reference beam technique.

The lower sensitivity of the PLL processor to CNR at low frequencies is also illustrated by Figure 7.3. Below approximately 2 kHz the drop in noise floor due to an increase in the CNR is less appreciable than it is above 2 kHz. This same property of the PLL processors was addressed in the reference beam section. Figure 7.4 illustrates the decreasing influence of the CNR on the noise floor below 2 kHz; except for spurious low frequency peaks (60 Hz and multiples), the two spectra at CNR values of 55 dB and 70 dB show a larger difference in noise starting from approximately 200 Hz and increasing to 2 kHz.

Figure 7.5 is a comparison of the two PLL processor noise floors for the "typical" CNR of 60 dB in the differential Doppler mode. As was noted in Chapter IV, one processor in the TCV system is from 2 to 4 dB quieter than the other for the same input signal (although this is at least in part due to the difference in their sensitivities).

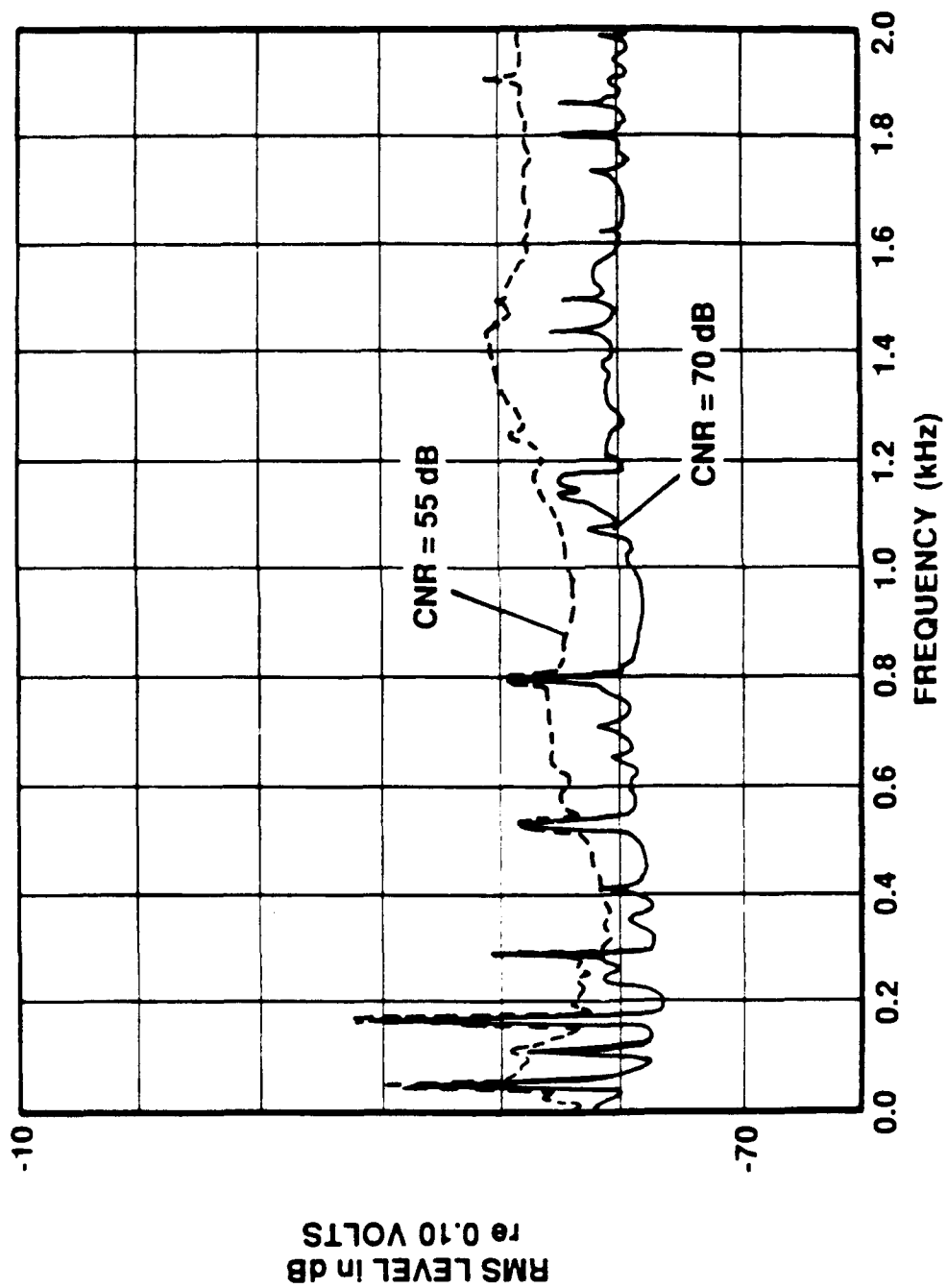


Figure 7.4 Comparison of Velocity Noise Floors for Two Different CNR Values for the Differential Doppler Mode at Low Frequencies

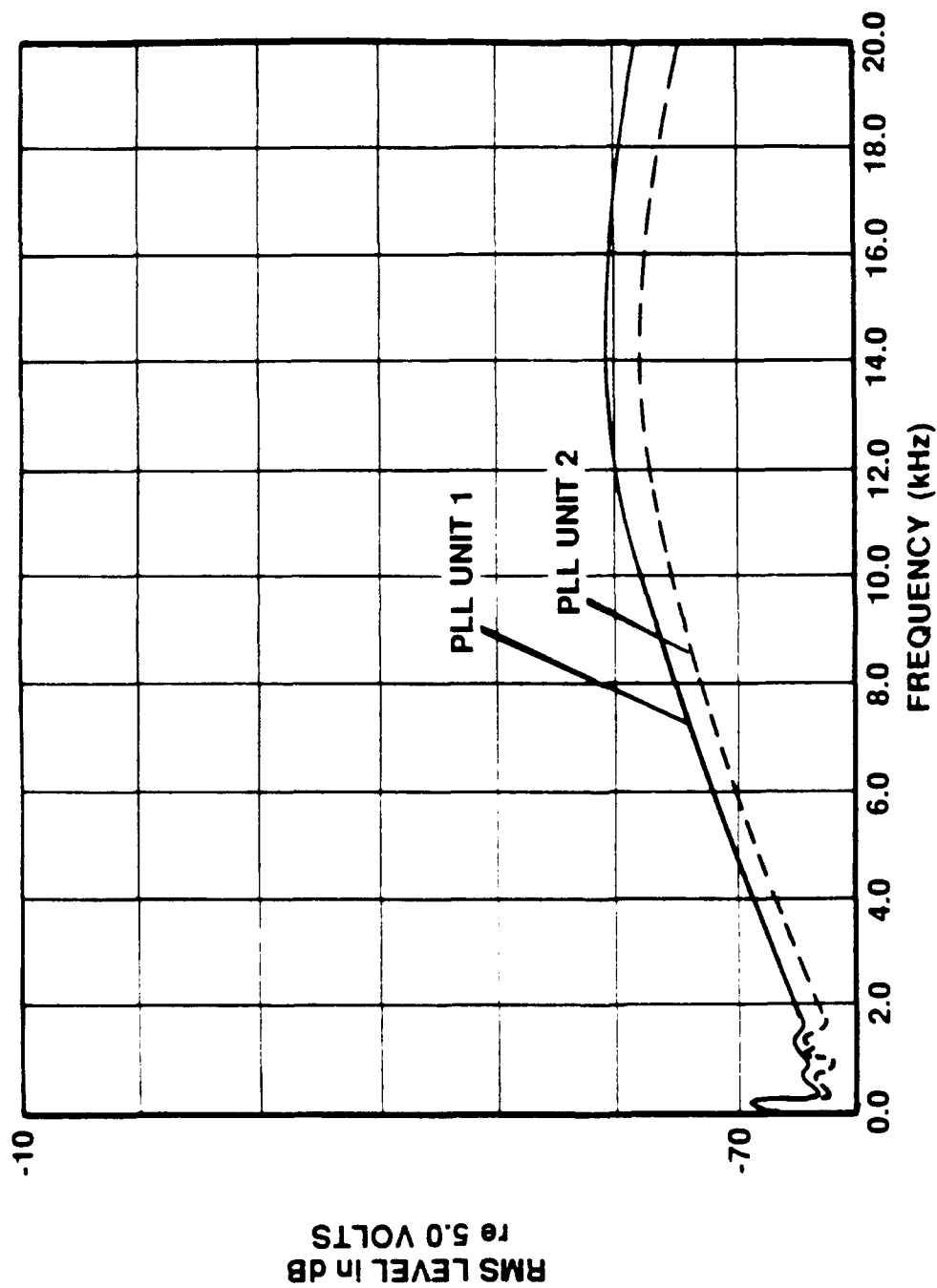


Figure 7.5 Comparison of Velocity Noise Floors for the Two PLL Units at a CNR of 60 dB in the Differential Doppler Mode



# SIGNAL-TO-NOISE RATIOS OF THE VELOCITY SIGNALS IN THE DIFFERENTIAL DOPPLER METHOD

If the noise floors in Figure 7.5 are used, the SNR of the velocity signals for a characteristic case can be determined if the velocity signal is known. The rms voltage signal obtained from an object vibrating transverse to the beams is determined by:

$$V_{\text{rms}} = \frac{2\sqrt{2}\pi Af}{K\lambda} \sin\left(\frac{\theta}{2}\right) \quad (7.1)$$

where A is the displacement amplitude, f is the frequency in Hz, K is the PLL sensitivity in units of Hz/volt,  $\lambda$  is the laser wavelength (514.5 nm for green light), and  $\theta/2$  is the lens half angle. This equation assumes that the vibration is in a direction perpendicular to the bisector of the two beams. For other cases the right hand side is multiplied by the factor  $\sin \psi$  where  $\psi$  is the angle between the beam bisector and the vibration velocity vector.

If the rms voltage obtained for a given acceleration amplitude of the surface is calculated by this equation and (assuming  $\psi = 0$ ) converted to a dB level relative to 5.0 volts, the signal level compatible with the noise floor plots can then be calculated by using the PLL sensitivity at any desired frequency. Figures 7.6 and 7.7 are plots of the signal and noise levels for the two PLL processors for different acceleration amplitudes. The noise floor in these plots are those corresponding to the average CNR of 60 dB and the signals are those for a value of  $(\theta/2)$  of 5.9 degrees (for 243 mm focal length lenses). From these figures the SNR for various acceleration amplitudes can be estimated.

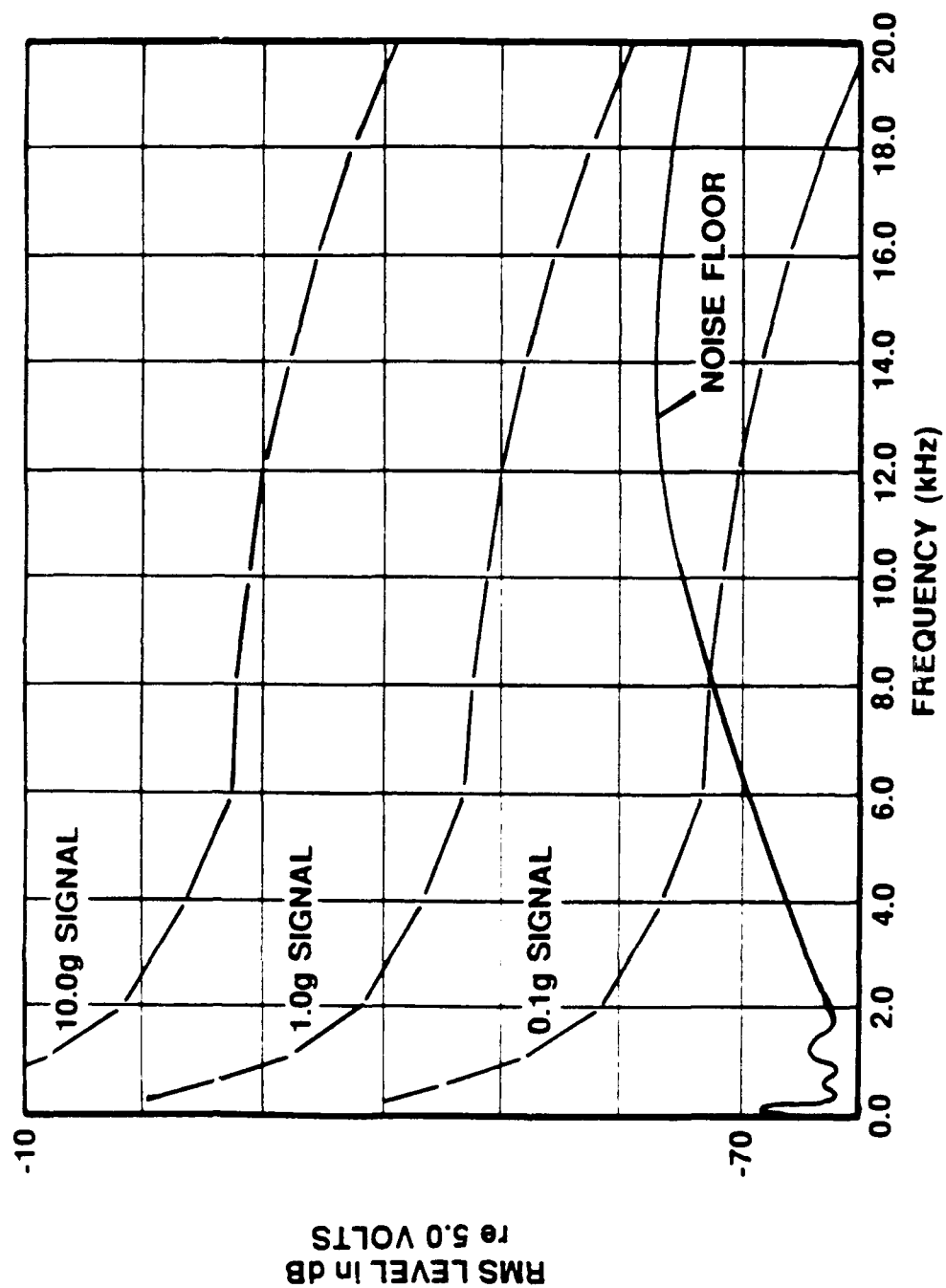


Figure 7.6 Noise Floor at a CNR of 60 dB for PLL Unit 1 and Signals Corresponding to Acceleration Amplitudes in g for  $\theta/2$  of  $5.9^\circ$  in the Differential Doppler Mode

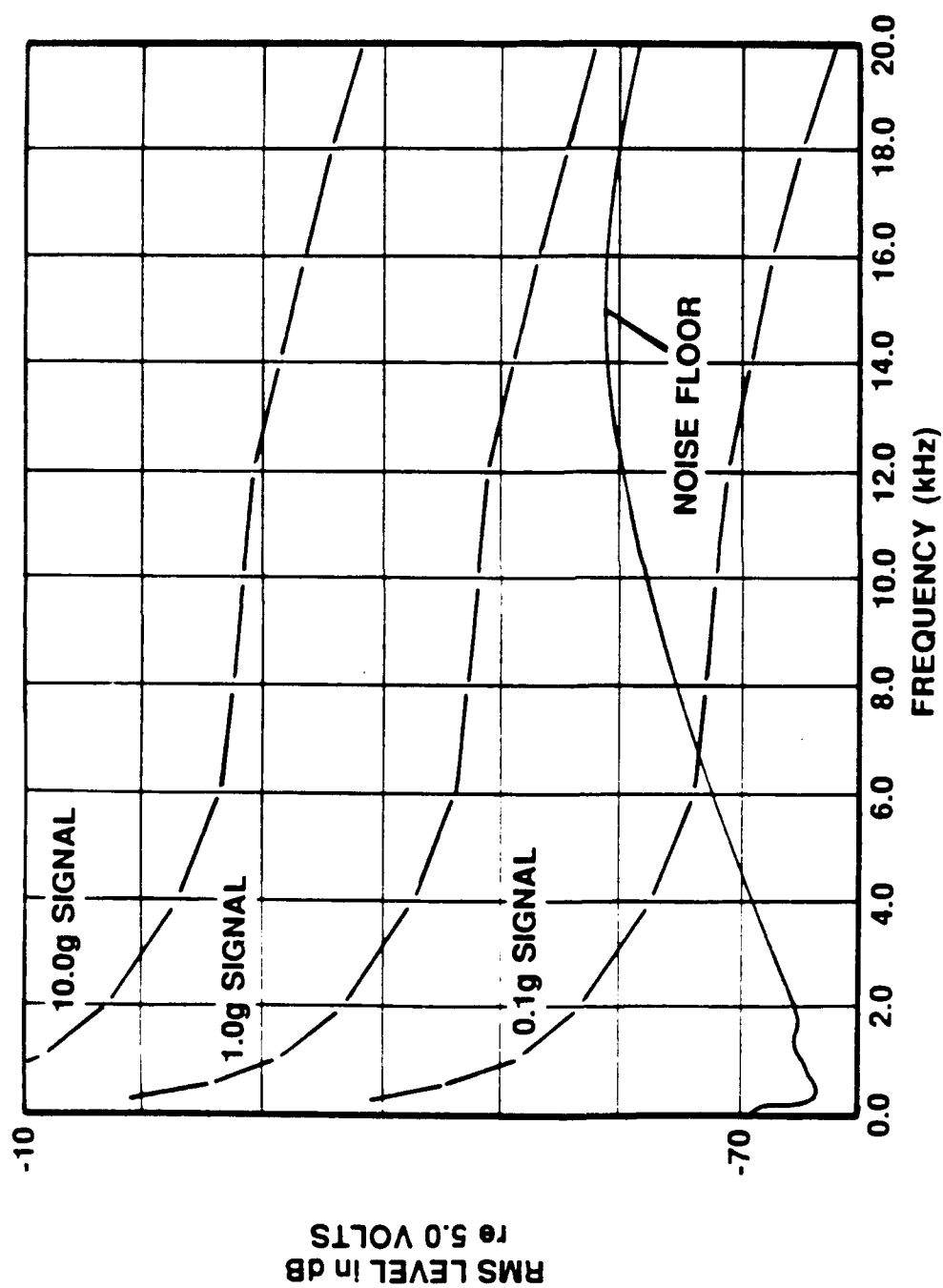


Figure 7.7 Noise Floor at a CNR of 60 dB for PLL Unit 2 and Signals Corresponding to Acceleration Amplitudes in g for  $\theta/2$  of 5.9° in the Differential Doppler Mode

## **Chapter VIII**

### **SOURCES OF ERROR IN LONGITUDINAL INTENSITY MEASUREMENTS DUE TO TCV SYSTEM CHARACTERISTICS**

#### **INTRODUCTION**

This chapter, the longitudinal counterpart to Chapter V, addresses random error in the longitudinal intensity measurements for a coherence less than one based on the vibrometer signal-to-noise ratios developed in Chapter VII. Examples covering the effects of the CNR, the longitudinal intensity level itself, and the lens focal length on the random error in longitudinal intensity measurements are illustrated.

Coherent noise phase bias errors are not discussed in this chapter since the photodetector switching technique detailed in Chapter V would also eliminate these errors in the differential Doppler technique. Coherent noise error was found not to exist in the differential Doppler mode as has been noted in Chapter VII.

#### **RANDOM ERROR IN TCV LONGITUDINAL INTENSITY MEASUREMENTS**

Longitudinal intensity measurements, like flexural intensity measurements, can also be tainted by random error due to the presence of extraneous background noise in each channel. The lower sensitivity which the differential Doppler technique typically exhibits compared to the reference beam technique can result in lower signal-to-noise ratios and, consequently, can make random error a greater problem in longitudinal intensity than in flexural intensity measurements when the

TCV instrumentation is used. In the case of a reverberant beam, where the energy loss is predominantly at the end, the phase angle difference,  $\phi$ , across an antinode can be approximated such that (refer to Appendix B)

$$\cot \phi \approx \frac{2 \cot k\Delta x}{Lk\eta} \quad (8.1)$$

This approximation, good for  $k\Delta x \leq 0.2\pi$ , was used previously in the expression for an example of random error in flexural intensity measurements. In the longitudinal case, however, the phase angle approximation at the antinode becomes (refer to Appendix A)

$$\cot \phi \approx \frac{\cot k\Delta x}{Lk\eta} \quad (8.2)$$

The expression for coherence between the two channels and the general expression for random error as a function of phase angle are the same as in the flexural case so that the final expression for the required number of spectral averages, allowing a maximum random error of 10%, is

$$n_d = \left[ \frac{1}{\epsilon_r} \cdot \frac{\cot k\Delta x}{kL\eta} \right]^2 \left[ \frac{(1 - \gamma_{12}^2)}{2\gamma_{12}^2} \right] \quad (8.3)$$

Noise-to-signal ratios required for calculating the coherence can be obtained from the experimentally determined noise floors at the various CNR levels and from the vibrometer signal strength in the differential Doppler mode. The signal strengths are a function of the power flow (or power input)  $\Pi$ , the beam length  $L$ , the position on the beam, the loss factor  $\eta$ , frequency  $f$ , wavenumber  $k$ , the modulus and cross-sectional area of the beam  $Y$  and  $S$ , the Doppler shift conversion,

PLL sensitivity  $K$ , and finally the lens half-angle as noted in Equations 6.22 and 6.23.

For example, for an aluminum rod 6.35 millimeters in diameter, 0.525 meters long, assuming  $\eta = .01$  and a resonance at 7.5 kHz and also using  $K = 2700$  Hz/volt (the value at 7.5 kHz) and a lens half-angle of 5.88 degrees with a laser beam separation of  $0.1\lambda$  with the beams centered over the antinode, the influence of the CNR (in the differential Doppler mode) on random error can be illustrated. Table 8.1 shows the influence of the CNR (assuming it is the same in both channels) on the number of spectral averages,  $n_d$ , necessary to obtain a maximum normalized random error of 10% in the quadrature spectrum.

Table 8.1

Influence of CNR on Number of Samples Required  
for 10% Random Error in Power-Flow Measurement  
With the Differential Doppler Mode

<u>CNR (dB)</u>	<u><math>\gamma_{12}^2</math></u>	<u><math>n_d</math></u>
70	.993	30
65	.986	60
60	.966	153
54	.851	751
50	.728	1603

Here, the power flow has been assumed to be  $1 * 10^{-6}$  watts for illustration purposes. For much higher power flows, the coherence quickly becomes unity and CNR effects are much less influential. Assuming the same relationship as in the reference beam mode, variations in the CNR can be viewed as variations in the backscattered

intensity, variations in the photodetector quantum efficiency, or variations in the square of the heterodyne efficiency.

If instead of varying the CNR, it is kept fixed and the power flow is varied, the influence of power flow on the random error in the differential Doppler mode can be illustrated. For the same conditions, if a CNR value of 60 dB is chosen (which has been established experimentally as a typical value for this mode when targeting surfaces coated with retro-reflective paint) the results shown in Table 8.2 are obtained.

Table 8.2

Influence of CNR on Number of Samples Required  
for 10% Random Error in Power Flow Measurement  
With the Differential Doppler Mode

$\Pi$ (watts)	$\gamma_{12}^2$	$n_d$
$1.0 \cdot 10^{-6}$	.996	153
$0.5 \cdot 10^{-6}$	.993	301
$0.25 \cdot 10^{-6}$	.986	611
$0.1 \cdot 10^{-6}$	.966	1530

(For cases where the square of the noise-to-signal autospectrum ratio is much less than twice the ratio, as is the case above, the relationship between power flow and the required number of spectral averages is a simple inverse relationship).

It should be noted here that these examples are for the case (used in the experiments) of a "lossless" rod at resonance with power input at one end; a portion of this power is absorbed at the termination and the remainder is reflected back. The magnitude of the reflection coefficient at the "receiving end" is fixed by the values of loss

factor, resonance wavenumber, and rod length (as noted in Appendix B). Consequently, for each value of active power flow listed in the table (due to propagating waves) there exists a certain corresponding value of reactive power flow (due to reflected waves) and a fixed value of coherence (for a given CNR). The coherence and random error for active power flows with greater or less reactive power (i.e: different values of reflection coefficients) will vary from the values in the tables. For example, comparable tables can be established for a semi-infinite rod by setting  $|R|$  equal to zero in the equation for  $\Pi$  in Appendix B, finding the displacement amplitude, using the vibrometer conversions, and setting  $\cot \phi = \cot k\Delta x$  in the expression for random error.

The influence of the focussing lens power on random error is also of interest. In this example a power flow of  $1.0 \times 10^{-6}$  watts and a CNR of 60 dB are assumed with all other conditions the same as in the previous examples. Table 8.3 illustrates the number of spectral averages required when various focal length lenses are used and a maximum random error of 10% is to be maintained.

TABLE 8.3

Influence of Lens Focal Length on the Number of  
Samples Required for 10% Random Error in Power  
Flow Measurement With the Differential Doppler Mode

<u>Lens Focal Length (mm)</u>	<u><math>\gamma_{12}^2</math></u>	<u><math>n_d</math></u>
243	.996	153
500	.986	620
750	.967	1485
1500	.879	5991



## Chapter IX

### **SPECKLE DYNAMICS AND SIGNAL DETECTION IN THE REFERENCE BEAM AND DIFFERENTIAL DOPPLER MODES**

#### INTRODUCTION

As noted in Chapter II, laser speckle can play an important role in vibrometry signal detection. In the reference beam mode, when the surface is vibrating predominantly in the direction of the illuminating object beam, there is negligible change in the backscattered speckle pattern during the vibration cycle. Consequently the reference beam interferes with a well behaved backscattered object beam and a clean interferometric signal results. This situation is what accounts for the success of the reference beam technique in measuring structural intensity for flexural motion.

However, in the reference beam mode, if significant motion which is perpendicular to the object beam is present, then the speckle in the backscattered object beam may undergo translation and possibly speckle boiling during the vibration cycle. For periodic excitation this situation can cause the output of the vibrometer to contain spurious spectral peaks at harmonics of the excitation frequency. This has been reported recently and is reviewed in this chapter.

The differential Doppler mode on the other hand has somewhat different characteristics in regard to speckle dynamics. These characteristics are unreported in the literature since there has been so little activity to date in differential Doppler laser vibrometry.

However, they are addressed in this chapter due to the importance of signal quality in longitudinal intensity measurements.

This chapter has the ultimate objective of addressing whether the reference beam mode can provide reliable flexural intensity measurements and whether the differential Doppler mode can provide reliable longitudinal intensity measurements in a vibration field which is composed of both surface-normal and in-plane motion. This question has to be approached from the aspect of speckle dynamics. The chapter attempts to answer these issues primarily from an experimental standpoint since a full statistical treatment of the makeup of the backscattered speckle at the photodetector as a function of the surface motion, the imaging lenses, the apertures, and the surface roughness are beyond the scope of the thesis.

The chapter includes discussion on the effects of speckle dynamics in the reference beam mode, and to a larger degree the effects of speckle dynamics in the differential Doppler mode, as well as the response of the phase-locked loop processors to simulated speckle effects.

#### **SPECKLE DYNAMICS IN THE REFERENCE BEAM MODE**

For motions which change the backscattered speckle makeup, Rothberg, Baker, and Halliwell (1989) report that periodic excitation can result in spurious peaks which are harmonics of the excitation frequency. This motion can be either tilt, rotation, or in-plane motion. The argument for these effects begins on a mathematical basis (with the influence of the changing speckle population on the net

amplitude and phase at the photodetector), but the authors revert to an empirical argument and actual data. According to the authors, spurious harmonics of the excitation frequency appear in the output spectrum and additionally some (unspecified) spurious component exists in the "true" (excitation frequency) signal as well.

An investigation into this effect was conducted by using one unit of the TCV in the reference beam mode and using as a target a rod which was excited longitudinally at one end and clamped at the other end. The reference beam signal showed that appreciable bending was induced in the rod as well as the longitudinal motion. In this case harmonics of the excitation frequency (which was 9 kHz) did appear in the reference beam signal. The ratio of surface-normal to in-plane motion (determined by the differential Doppler mode) was approximately 1.3 to 1.0. (The value for the differential Doppler mode was somewhat unsteady but was averaged for this result). The reference beam signal harmonics were low; the highest was the second harmonic at 18.0 kHz which was 30 dB below the true signal. Decreasing the shaker input reduced these spurious harmonics to a value below the noise floor.

A "worst case" test was run by targeting the side of a small aluminum disk excited by a shaker. Motion was predominantly transverse to the illuminating laser beam but the shaker did output some motion in the direction of the illuminating beam. Use of a low frequency (100 Hz) and large shaker input provided enough vibration amplitude to cause appreciable harmonics in the reference beam signal spectrum; the value at 300 Hz was only 6 dB lower than the signal at the excitation frequency. At this time the ratio of surface-normal to in-plane motion

was approximately 0.40. As the shaker input was reduced, the output harmonics (as well as the severity of the speckle-induced amplitude modulations of the Doppler signal) were also reduced.

These tests, and other similar tests, indicated that the amplitude of transverse motion in the reference beam mode had to be very significant before the spurious harmonics became significant. In the reference beam mode tests, these spurious harmonics were few in number, and transverse motion never destabilized the signal. A small aperture can be used to increase the speckle size at the photodetector to eliminate these harmonics. This was done for the differential Doppler mode (as is discussed below).

#### **SPECKLE DYNAMICS IN THE DIFFERENTIAL DOPPLER MODE**

More susceptible to signal deterioration by speckle dynamics is the differential Doppler mode. In this case in-plane motion (with its associated speckle motion and possible speckle boiling) is what comprises the desired signal. Initial tests in attempting to use the differential Doppler mode on a free-fixed rod excited longitudinally showed that at certain frequencies and at certain points of focus the demodulated signal was highly unstable and erratic for steady sinusoidal excitation. This was found to be due to the presence of high out-of-plane (flexural) motion combined with the in-plane (longitudinal) motion. Additionally it was found that the instability could be reduced in many cases by slightly refocussing the lens, by using an aperture in

front of the receiving optics, or by letting the "fixed" end free to slide (thus reducing the induced bending in the rod).

The instability appears to be due to combined speckle translation and speckle "boiling" at the photodetector. Refocussing of the lens would change the speckle makeup at the detector in some cases so that the problem was not as severe. Additionally, a smaller aperture would increase the speckle size at the detector which may decrease the sensitivity to transverse speckle motion. (Evidence of this is shown later). Why the instability is erratic under steady state conditions is not entirely understood but the phase-locked loop processor dynamics will have a significant influence on the demodulated output when the input FM signal has phase ramps and phase jumps caused by speckle transverse motion and speckle "boiling." PLL response may be very nonlinear in such cases.

As noted in Chapter VI, the flexural motion of the sample was reduced by revising the original setup design (a fixed-free rod driven longitudinally at the free end) to a design which would prevent out-of-plane motion at the rod ends. This design involved a rod which was held in place by screws at its ends which screwed through thin plastic diaphragms. The diaphragms were then fixed at the ends of a cylinder so that the rod ends were flexible in the direction of longitudinal motion but were very stiff in the out-of-plane direction. A shaker then excited the rod longitudinally at one end of the cylinder.

This arrangement reduced the high amplitude bending motion (at least at the sample ends) which was caused by the shaker in the previous setup. However, the pinned-pinned bending modes in the rod were still

very capable of being excited as was evident from reference beam tests on this setup. Nevertheless the bending motion, even when at the frequency of the first (and strongest) bending mode, was reduced to the point where the instability present in the differential Doppler signal was no longer present. However, there was enough bending to alter the output spectrum.

For example, the sample was excited longitudinally at 350 Hz which was its first bending resonance. The differential Doppler signal contained a very steady value at 350 Hz but also many spurious harmonics and a noise hump at approximately 10 kHz as shown in Figure 9.1. The signal was greatly improved however, by use of a small (5 mm) aperture in front of the collection optics. This is also illustrated in Figure 9.1. For this situation the noise floor shows its characteristic curve and the harmonics are gone. Consequently, when the bending motion is not severe the proper choice of aperture (used to increase the speckle size at the detector) can provide a much cleaner output.

It should be noted that the center of the noise hump found at approximately 10 kHz increased in frequency as the amplitude of motion increased and decreased for decreased motion. Later tests showed that pure bending causes these noise floor humps in the differential Doppler method and that their location in the spectrum is a function of the bending amplitude (and probably also a function of the wavenumber makeup of the speckled intensity pattern as it impinges on the detector). However, for bending at a single frequency, negligible signal was present at that frequency in the differential Doppler spectrum.

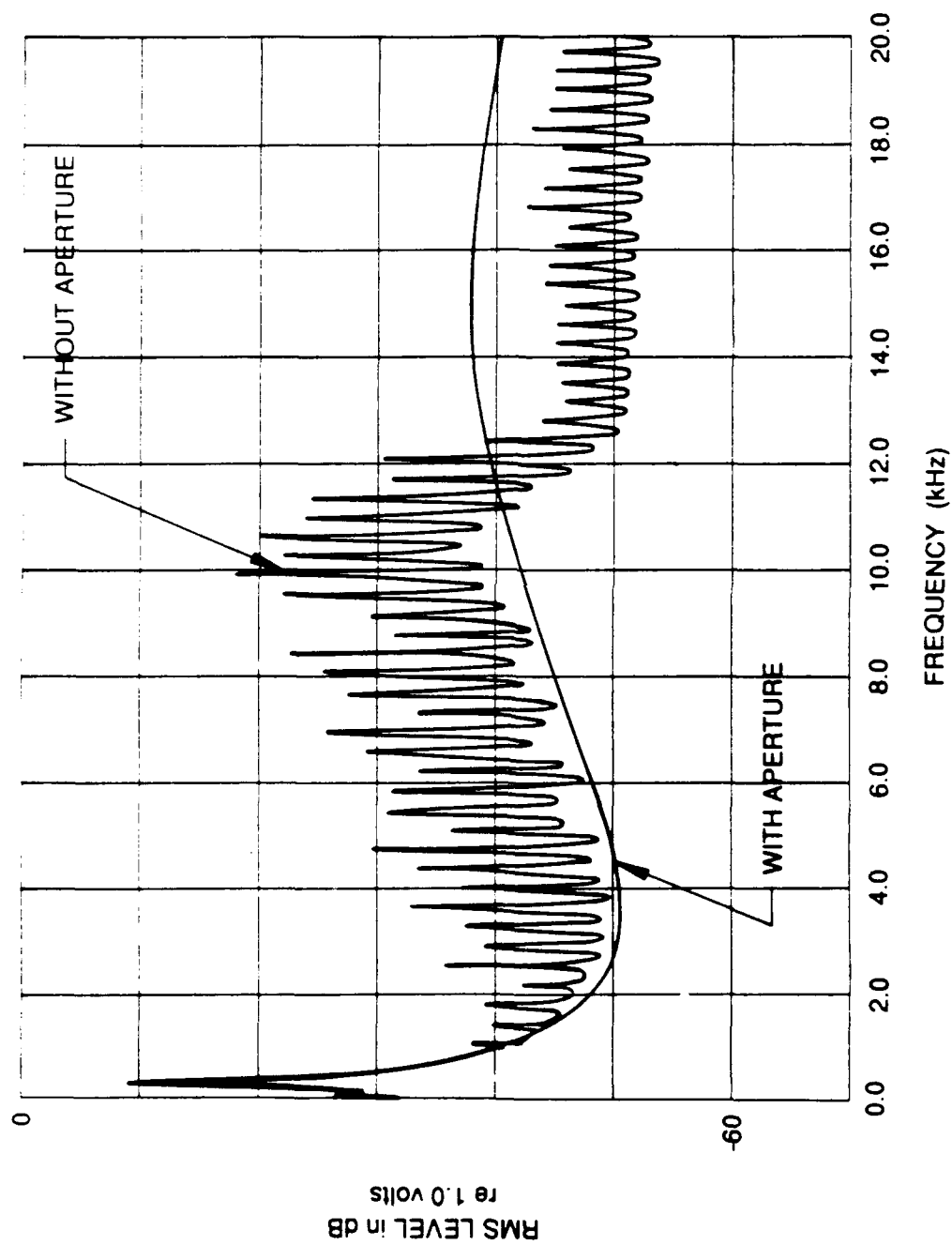


Figure 9.1 Effect of an Aperture on the Noise Floor in the Differential Doppler Mode in the Presence of Appreciable Bending

In order to minimize out-of-plane motion, a test was conducted on a small mass attached to a shaker. An accelerometer was placed at the front face of the mass and a vibrometer in the differential Doppler mode was focussed on the side of the mass. Test results showed very consistent agreement between the accelerometer and vibrometer results. For extremely high motion the differential Doppler output did contain very low amplitude harmonics but the true signal was unaffected by their presence.

The harmonics in the spectrum are caused by severe amplitude modulation of the FM signal due to speckle translation. This amplitude modulation can be reduced (and the harmonics eliminated) by repositioning the photodetector on its mount (which changes the speckle makeup) or by using an aperture (which changes the speckle size).

Tests using an FM signal generator with the PLL processors also showed that appreciable amplitude modulation in the FM signal can cause low level harmonics of the modulation frequency to appear in the demodulated spectrum.

## CONCLUSIONS

Transverse motions in the reference beam mode can cause harmonics of the vibration frequency to show up in the output spectrum but the transverse motion must be very significant before the amplitude of the harmonics is appreciable. Except in rare cases flexural intensity results should not be adversely affected.



The differential Doppler mode is subject to instability in the presence of combined out-of-plane and in-plane motions of high amplitude. For slightly less out-of-plane motion the differential Doppler mode provides high amplitude harmonics but these can be eliminated by choosing a proper aperture. For moderate out-of-plane motion the output spectrum is unaltered and a good signal is obtained.

## Chapter X

### CONCLUSIONS AND RECOMMENDATIONS FOR FURTHER STUDY

An optical system has been developed which can accurately measure flexural power flow by the cross-spectral method. This is the first reliable optical vibrational power flow measurement system which is inherently amenable to random vibration measurements. The importance of developing optical techniques for vibrational power flow has been stressed very recently by numerous authors including F. J. Fahy and R. G. White (1990). The accuracy of the two-channel laser Doppler system for intensity measurements has been shown to be increased by a novel optical technique - photodetector switching.

Investigations into the electro-optical characteristics of the system show that the signal-to-noise ratio (and ultimately the random error in the measured intensity) is a function of the carrier-to-noise ratio as well as the PLL response. A characteristic of the PLLs is that the noise in their output is less sensitive to the CNR at low frequencies so that for a given Doppler signal strength the noise floor is lower at lower frequencies.

In the differential Doppler mode, the optical system provides longitudinal intensity results which can be influenced appreciably by the presence of bending. (This problem will occur with accelerometers if used in the same fashion.) A computer model of the influence of bending on the measured longitudinal intensity illustrated that the longitudinal data obtained from the laser system may be correct.

Standing wave longitudinal data also align well with the computer predictions but the energetics power flow data is approximately twice the standing wave data. This difference cannot be fully reconciled, although the longitudinal loss factor measurement is suspect due to the interference of nearby bending resonances. Therefore the longitudinal measurement capability of the system should be subject to verification in the absence of bending. This should be done with a non-resonant technique such as at a very low frequency with verification by a force gage and accelerometer.

The differential Doppler mode is subject to signal instability in the presence of longitudinal and "high" bending motion. This must be investigated and a solution obtained if the technique is ever going to be applicable to general use. Chapter IX demonstrated one solution to this problem (using an "appropriately sized" aperture), but this solution needs to be studied and quantified. The previous problems should not be approached without addressing this signal instability problem. The reference beam mode does not suffer from signal instability but in cases of high amplitude transverse motion it does provide spurious harmonics. However, these are typically at an insignificant amplitude. These harmonics can arise due to amplitude modulation of the carrier signal at a frequency equal to the modulation frequency.

Recommendations for further study, beyond those previously mentioned, include:

- Determining the absolute phase accuracy of the system (these studies have indicated a phase accuracy of at least 0.2 degrees).
- Applying the technique to flat plates.
- Investigating the accuracy of the technique in situations where the object is illuminated at an appreciable angle so that flexural and longitudinal cross-talk exists.
- Applying the technique to broadband excitation.
- Investigating an improved processor that would provide minimum "tuner noise" and allow the CNR to be less at higher frequencies.
- Expanding the technique to nearfield measurements and ultimately to measurement of "surface intensity" as developed by Pavic (1987).
- Applying the techniques for measuring bending and longitudinal wave power flow to measuring power flow through junctions of beams or plates where coupling between bending and longitudinal waves occur.
- Applying the techniques for measuring bending and longitudinal wave power flow to measuring power flow in curved structures, such as cylindrical shells, where the curvature couples bending and in-plane waves.

## BIBLIOGRAPHY

- Bendat, J. S. and Piersol, A. G., "Engineering Applications of Correlation and Spectral Analysis," Wiley, New York, 1980.
- Bernhard, R. J., Bolton, J. S., Gardner, B., Mickol, J., Mollo, C., and Bruer, C., "A Study of Methods to Predict and Measure the Transmission of Sound Through the Walls of Light Aircraft," Semiannual Status Report to NASA, Purdue University, Report No. 0353-3, May 1986.
- Bouchard, G. and Bogy, D. B., "Experimental Measurement of Scattered Surface Waves Using a Laser-Doppler Probe," *Journal of the Acoustical Society of America*, Vol. 77, No. 3, March 1985.
- Buchave, P., "Laser Doppler Vibration Measurements Using Variable Frequency Shift," *DISA Information*, No. 18, September 1975.
- Buunen, T. J. F. and Vlaming, M. S. M. G., "Laser Doppler Velocity Meter Applied to Tympanic Membrane Vibrations in Cat," *Journal of the Acoustical Society of America*, Vol. 69, No. 3, pp. 774-750, March 1981.
- Carroll, G. P., "Structural Response and Power Flow Measurements Utilizing Cross Spectra," PhD Dissertation, Catholic University of America, Washington, DC, 1987.
- Chung, J. H., "Cross Spectral Method of Measuring Acoustic Intensity Without Error caused by Instrument Phase Mismatch," *Journal of the Acoustical Society of America*, Vol. 64, No. 6, pp. 1613-1616, December 1978.
- Clark, J. A. and Tucker, A. J., "Optical Measurements of Structural Intensity Distributions," Proceedings from the Second International Congress on Acoustic Intensity, pp. 171-176, 1985.
- Cockson, R. A. and Bandyopadhyay, P., "Mechanical Vibration Measurements Using a Fiber Optic Laser-Doppler Probe," *Optics and Laser Technology*, pp. 33-36, February 1978.
- Corti, M., Marazzini, S., Martinelli, A., and DeAgostini, A., "Cross-Spectrum Technique for High Sensitivity Remote Vibration Analysis by Optical Interferometry," *SPIE Vol. 672*, pp. 64-72, 1986.
- Cremer, L., Heckl, M., and Ungar, E. E., "Structure-Borne Sound," Springer-Verlag, Berlin, 1973.
- Cretin, B., Xie, W. X., Wang, S., and Hauden, D., "Heterodyne Interferometers: Practical Limitations and Improvements," *Optics Communications*, Vol. 65, No. 3, pp. 157-162, February 1, 1988.

- Dandliker, R. and Willemin, J. F., "Measuring Microvibrations by Heterodyne Speckle Interferometry," *Optics Letters*, Vol. 6, No. 4, pp. 165-167, April 1981.
- Downing, J. M. and Shepherd, K. F., "Power Flow in a Beam Using a 5-Accelerometer Probe," NOISE-CON 88 Proceedings, Purdue University, pp. 335-340, June 20-22 1988.
- Dragsten, P. R., Webb, W. W., Paton, J. A., and Capranica, R. R., "Light Scattering Heterodyne Interferometer for Vibration Measurements in Auditory Organs," *Journal of the Acoustical Society of America*, Vol. 60, No. 3, pp. 665-671, September 1976.
- Drain, L. E., *The Laser Doppler Technique*, Wiley, New York, 1980.
- Drain, L. E. and Moss, B. C. "Optical Techniques in Process Control," Proceedings of the International Conference on Optical Techniques in Process Control, The Hague, The Netherlands, Paper J1, June 14-16, 1983.
- Eastwood, P. G., Halliwell, N. A., and Gilbert, P., "Laser Tools for Diesel Engine Diagnosis," *Proceedings of the Institution of Mechanical Engineers, Part D*, Vol. 199, No. D4, pp. 295-300, 1985.
- Elko, G. W., "Frequency Domain Estimation of the Complex Acoustic Intensity and Acoustic Energy Density," PhD Thesis, The Pennsylvania State University, 1984.
- Ennos, A. E., "Speckle Interferometry," *Progress in Optics*, Vol. 16, pp. 235-288, 1978.
- Fahy, F. J. and White, R. G., "Statistical Energy Analysis and Vibrational Power Flow," *Proceedings of the Third International Congress on Intensity Techniques*, pp. 29-34, August, 1990.
- Gardner, F. M., *Phaselock Techniques*, Wiley, New York, 1979.
- Goyder, H. G. D. and White, R. G., "Vibrational Power Flow from Machines Into Built-Up Structures, Part I: Introduction and Approximate Analysis of Beam and Platelike Foundations," *Journal of Sound and Vibration*, Vol. 68, No. 1, pp. 59-75, 1980.
- Goyder, H. G. D. and White, R. G., "Wave Propagation and Power Flow in Beam-Stiffened Plates, Part II," *Journal of Sound and Vibration*, Vol. 68, No. 1, pp. 77-96, 1980.
- Goyder, H. G. D. and White, R. G., "Wave Propagation and Power Flow Through Isolation Systems, Part III," *Journal of Sound and Vibration*, Vol. 68, No. 1, pp. 97-117, 1980.
- Halliwell, N. A., "Laser Doppler Measurement of Vibrating Surfaces: A Portable Instrument," *Journal of Sound and Vibration*, Vol. 62, No. 2, pp. 312-315, 1979.

- Halliwel, N. A. and Eastwood, P. G., "The Laser Torsional Vibrometer: A New Instrument," *Journal of Sound and Vibration*, Vol. 93, No. 4, pp. 588-592, 1984.
- Halliwel, N. A., Pullen, L., and Baker, J., "Laser Tools for Diesel Engine Development," *Automotive Engineer*, pp. 44-46, April-May 1983.
- Joyeux, D. and Lowenthal, S., "Real Time Measurement of Angstrom Order Transverse Displacement or Vibrations by Use of Laser Speckle," *Optics Communications*, Vol. 4, No. 2, October 1971.
- Kendig, P., "Measuring Vibration Transmission in Structures," NOISE-CON 88 Proceedings, Purdue University, pp. 341-346, June 20-22, 1988.
- Kinsler, L. E., and Frey, A. R., "Fundamentals of Acoustics," Wiley, New York, 1962.
- Lewin, A. C., Kersey, A. D., and Jackson, D. A., "Non-Contact Surface Vibration Analysis Using a Monomode Fiber Optic Vibrometer Incorporating an Open Air-Path," *Journal of Physics E: Scientific Instruments*, Vol. 18, pp. 604-608, 1985.
- Madigosky, G. F. and Lee, G. F., "Improved Resonance Technique for Materials Characterization", *Journal of the Acoustical Society of America*, Vol. 73, pp. 1374-1377, 1983.
- Massey, G. A., "Study of Vibration Measurements by Laser Methods," NASA Report under NASA CR-985, 1967.
- Massey, G. A. and Carter, R. R., "Portable Laser Instrument for Vibration Analysis and Transducer Calibration," Report to NASA Ames Research Center under Contracts NAS2-3137, NAS2-3643, NAS2-4176, pp. 1-6, 1967.
- McDevitt, T. E. and Vikram, C. S., "Optical Determination of the Effects of a Microminiature Accelerometer on Resonance of a Small Airfoil," *Optics and Lasers in Engineering*, Vol. 9, pp. 77-83, 1988.
- McDevitt, T. E. and Stuart, A. D., "A Two Channel Laser Doppler Vibrometer for Characterizing the Doppler Vibrometer for Characterizing the Dynamic Properties of Elastomeric Materials," *Journal of the Acoustical Society of America*, Vol. 85, No. 1, pp. 450-453, January 1989.
- Meyer, B., "Comparative Techniques for Structural Intensity in Cylinders," NOISE-CON 88 Proceedings, Purdue University, pp. 347-352, June 20-22, 1988.

- Meynart, R., "A Simple Interferometric Vibrometer Based on a Laser Doppler Velocimeter," *Journal of Physics E: Scientific Instruments*, Vol. 17, pp. 984-987, 1984.
- Mickol, J. D., "An Investigation of Energy Transmission Due to Flexural Wave Propagation in Lightweight Build-up Structures" M.S. Thesis, Purdue University, 1986.
- Noiseux, D. U., "Measurement of Power Flow in Uniform Beams and Plates," *Journal of the Acoustical Society of America*, Vol. 47, No. 1, Part 2, pp. 238-247, 1970.
- Pavic, G., "Measurement of Structure Borne Wave Intensity, Part I: Formulation of the Methods," *Journal of Sound and Vibration*, Vol. 49, No. 2, pp. 221-230, 1976.
- Pavic, G., "Measurement of Vibrations by Strain Gages, Part I: Theoretical Basis," *Journal of Sound and Vibration*, Vol. 102, No. 2, pp. 153-163, 1985A.
- Pavic, G., "Measurement of Vibrations by Strain Gages, Part II: Selection of Measurement Parameters," *Journal and Sound Vibration*, Vol. 102, No. 2, pp. 165-188, 1985B.
- Pavic, G., "Structural Surface Intensity: An Alternate Approach in Vibration Analysis and Diagnosis," *Journal of Sound and Vibration*, Vol. 115, No. 3, pp. 405-422, 1987.
- Pickering, C. J., Halliwell, N. A., and Wilmshurst, T. H., "The Laser Vibrometer: A Portable Instrument," *Journal of Sound and Vibration*, Vol. 107, No. 3, pp. 471-485, 1986.
- Quinlan, D., "Measurement of Complex Intensity and Potential Energy Density on Structural Bending Waves," M.S. Thesis, The Pennsylvania State University, 1985.
- Rasmussen, P., "Measurement of Vibration Intensity," B & K Technical Report 30/5 C1-C12, 1983.
- Redman-White, W., "The Experimental Measurement of Flexural Wave Power Flow in Structures," Institute of Sound and Vibration Research, University of Southampton, pp. 467-474, 1983.
- Rothberg, S. J., Baker, J. R., Halliwell, N. A., "Laser Vibrometry: Pseudo-Vibrations," *Journal of Sound and Vibration*, Vol. 135, No. 3, pp. 516-522, 1989.
- Seybert, A. F., "Statistical Errors in Acoustic Intensity Measurements," *Journal of Sound and Vibration*, Vol. 75, No. 4, pp. 519-526, 1981.



- Stierlin, R., Battig, R., Henchoz, P. T., and Weber, H. P., "Excess Noise Suppression in a Fiber Optic Balanced Heterodyne Detection System," *Optical and Quantum Electronics*, Vol. 18, pp. 445-454, 1986.
- Stoffregen, B., "Scanning Laser Doppler Vibration Analysis System," (German) *Techniques Messen* 51, Jahrgang 1984 Heft 11 V436-12.
- Su, R. T. K., "Surface Wave Measurement Using a Laser Doppler Technique," M.S. Thesis, University of California, Berkely, 1980.
- Takenaka, T., Takenaka, K., and Fukumitsu, O., "Signal-to-Noise Ratio in Optical Heterodyne Detection for Gaussian Fields," *Applied Optics*, Vol. 17, No. 21, pp. 3466-3471, November 1, 1978.
- Talbot, C. R. S., "Coherence Function Effect on Phase Difference Determination," *Journal of Sound and Vibration*, Vol. 39, No. 3, pp. 345-358, 1975.
- Thierry, G. Y. S., "A Simple Multimode Fiberoptic Vibrometer," *Optics Communications*, Vol. 56, No. 2, pp. 79-82, November 1985.
- Verheij, J. W., "Cross Spectral Density Methods for Measuring Power Flow on Beams and Pipes," *Journal of Sound and Vibration*, Vol. 70, No. 1, pp. 133-139, 1980.
- Waters, J. P. and Mottier, F. M., "Fiber Optic Laser Vibration Sensor" *ISA Transactions*, Vol. 25, No. 1, pp. 63-70, 1986.
- White, P. H. and Wilby, J. F., "Diagnostic Technique to Identify Airborne and Structureborne Noise Components," ASTRON Research and Engineering Report 7111, under NASA Contract NAS1-18407, November 8, 1987.
- Willemin, J. F. and Dandliker, R., "Measuring Amplitude and Phase of Microvibrations by Heterodyne Speckle Interferometry," *Optics Letters*, Vol. 8, No. 2, pp. 102-103, February 1983.
- Willemin, J. F., Khanna, S. M., and Dandliker, R., "Heterodyne Interferometer for Submicroscopic Vibration Measurements in the Inner Ear," *Proceedings of the SPIE* 746, pp. 104-112, 1987.
- Willemin, J. F., Dandliker, R., and Khanna, S. M., "Heterodyne Interferometer for Submicroscopic Vibration Measurements in the Inner Ear," *Journal of the Acoustical Society of America*, Vol. 83, No. 2, pp. 787-795, 1988.

Williams, E. G., Dardy, H. D., and Fink, R. G., "A Technique for Measurement of Structure-Borne Intensity in Plates," *Journal of the Acoustical Society of America*, Vol. 78, No. 6, pp. 2061-2068, December 1985.

Wlezien, F. W., Miu, D. K., and Kibens, V., "Characterization of Rotating Flexible Disks Using a Laser Doppler Vibrometer," *Optical Engineering*, Vol. 23, No. 4, pp. 436-442, July-August 1984.

## Appendix A

### DERIVATION OF CROSS-SPECTRAL EXPRESSIONS FOR POWER FLOW

#### LONGITUDINAL POWER FLOW

If  $\xi_0$  and  $\xi_\Delta$  are the displacements at two points along the rod and  $\Delta$  is their separation distance, then the longitudinal strain at the midpoint can be approximated as:

$$\epsilon \approx \frac{\xi_0 - \xi_\Delta}{\Delta} \quad (\text{A.1})$$

Additionally, if the velocities at the two points are  $v_0$  and  $v_\Delta$ , the velocity at the midpoint can be approximated as:

$$v \approx \frac{v_0 + v_\Delta}{2} \quad (\text{A.2})$$

The power flow is:

$$\Pi = \langle f \cdot v \rangle \quad (\text{A.3})$$

where  $\langle \rangle$  represents time average and  $f$  is the force existing at the midpoint. For a rod with a modulus of  $Y$  and a cross-sectional area of  $S$  this can be written as:

$$\Pi = \langle YS\epsilon \cdot v \rangle \quad (\text{A.4})$$

or

$$\Pi \approx \left\langle YS \left[ \frac{\xi_0 - \xi_\Delta}{\Delta} \right] \left[ \frac{v_0 + v_\Delta}{2} \right] \right\rangle \quad (\text{A.5})$$

or

$$\Pi \approx \frac{YS}{2\Delta} \langle \xi_0 v_0 - \xi_\Delta v_0 + \xi_0 v_\Delta - \xi_\Delta v_\Delta \rangle \quad (\text{A.6})$$

The terms in the bracket represent the zero time-delay cross-correlation function between the respective quantities so that the equation can be written as:

$$\Pi \approx \frac{YS}{2\Delta} [R_{\xi_0 v_0}(0) - R_{\xi_\Delta v_0}(0) + R_{\xi_0 v_\Delta}(0) - R_{\xi_\Delta v_\Delta}(0)] \quad (A.7)$$

However, since velocity is the time derivative of displacement and since  $R_{xx}(0) = 0$  then only the cross terms remain. (If the "self" terms are left intact, they become the reactive, non-propagating intensity). Continuing:

$$\Pi \approx \frac{YS}{2\Delta} [-R_{\xi_\Delta v_0}(0) + R_{\xi_0 v_\Delta}(0)] \quad (A.8)$$

But  $R_{xy}(0) = \int_{-\infty}^{+\infty} S_{xy}(\omega) d\omega$ , therefore:

$$\Pi \approx \frac{YS}{2\Delta} [- \int_{-\infty}^{+\infty} S_{\xi_\Delta v_0}(\omega) d\omega + \int_{-\infty}^{+\infty} S_{\xi_0 v_\Delta}(\omega) d\omega] \quad (A.9)$$

Also since:

$$S_{\xi_\Delta v_0}(\omega) = \frac{S_{v_\Delta v_0}(\omega)}{i\omega} \quad (A.10)$$

and since:

$$S_{\xi_0 v_\Delta}(\omega) = \frac{S_{v_0 v_\Delta}(\omega)}{i\omega} \quad (A.11)$$

then:

$$\Pi \approx - \frac{YS}{2\Delta} \left[ \int_{-\infty}^{+\infty} \frac{S_{v_\Delta v_0}(\omega) d\omega}{i\omega} - \int_{-\infty}^{+\infty} \frac{S_{v_0 v_\Delta}(\omega) d\omega}{i\omega} \right] \quad (A.12)$$

But  $S_{v_0 v_\Delta}^*(\omega) = S_{v_\Delta v_0}(\omega)$  (where \* denotes the complex conjugate) so that:

$$\Pi \approx -\frac{YS}{2\Delta} \left[ \int_{-\infty}^{+\infty} -1 \left[ \frac{S_{v_0 v_\Delta}^*(\omega)}{\omega} - \frac{S_{v_0 v_\Delta}(\omega)}{\omega} \right] d\omega \right] \quad (A.13)$$

In terms of the one sided cross-spectrum:

$$\Pi \approx \frac{YS}{2\Delta} \left[ \int_0^{+\infty} i \left[ \frac{G_{v_0 v_\Delta}^*(\omega)}{\omega} - \frac{G_{v_0 v_\Delta}(\omega)}{\omega} \right] d\omega \right] \quad (A.14)$$

$$\Pi \approx \frac{YS}{2\Delta} \left[ \int_0^{+\infty} i \left[ \frac{2i \operatorname{Im}[G_{v_0 v_\Delta}(\omega)]}{\omega} \right] d\omega \right] \quad (A.15)$$

$$\Pi \approx \frac{-YS}{\Delta} \int_0^{+\infty} \frac{\operatorname{Im}[G_{v_0 v_\Delta}(\omega)]}{\omega} d\omega \quad (A.16)$$

$$\Pi \approx \frac{-YS}{\Delta} \int_0^{+\infty} \frac{\operatorname{Im}[G_{12}(\omega)]}{\omega} d\omega \quad (A.17)$$

(since  $G_{v_0 v_\Delta}(\omega)$  is the same as  $G_{12}(\omega)$ ). Since  $G_{12}(\omega) = G_{12}(f)/2\pi$  then

$$\Pi \approx \frac{-YS}{\Delta} \int_0^{+\infty} \frac{\operatorname{Im}[G_{12}(f)]}{2\pi(2\pi f)} \cdot 2\pi df \quad (A.18)$$

$$\Pi \approx \frac{-YS}{2\pi\Delta} \int_0^{+\infty} \frac{\operatorname{Im}[G_{12}(f)]}{f} df = \frac{YS}{2\pi\Delta} \int_0^{+\infty} \frac{\operatorname{Im}[G_{21}(f)]}{f} df \quad (A.19)$$

This is then corrected for finite difference error by multiplying by

$$\left( \frac{k\Delta}{\sin k\Delta} \right)$$

#### FLEXURAL POWER FLOW

$$\Pi_x = \underbrace{\langle F_x \dot{\xi} \rangle_t}_{\Pi_{F_x}} + \underbrace{\langle M_x \dot{\theta}_x \rangle_t + \langle M_{xy} \dot{\theta}_y \rangle_t}_{\Pi_{M_x}} \quad (A.20)$$

where:

$$M_x = -B \left( \frac{\partial^2 \xi}{\partial x^2} + \nu \frac{\partial^2 \xi}{\partial y^2} \right) \quad (A.21)$$

$$\theta_y = \frac{\partial \xi}{\partial y} ; \quad \theta_x = \frac{\partial \xi}{\partial x} \quad (\text{A.22})$$

$$M_{xy} = B(1 - \nu) \frac{\partial^2 \xi}{\partial x \partial y} \quad (\text{A.23})$$

$$F_x = -B \frac{\partial}{\partial x} \left( \frac{\partial^2 \xi}{\partial x^2} + \frac{\partial^2 \xi}{\partial y^2} \right) \quad (\text{A.24})$$

Substituting into the last two terms of A.20:

$$\Pi_{M_x} = \left\langle -B \left( \frac{\partial^2 \xi}{\partial x^2} + \nu \frac{\partial^2 \xi}{\partial y^2} \right) \frac{\partial^2 \xi}{\partial x \partial t} \right\rangle_t + \left\langle B(1 - \nu) \frac{\partial^2 \xi}{\partial x \partial t} \frac{\partial^2 \xi}{\partial y \partial t} \right\rangle_t \quad (\text{A.25})$$

From Noiseux:

$$\Pi'_{M_x} = \left\langle \left[ \frac{M_x + M_y}{1 + \nu} \right] \dot{\theta}_x \right\rangle_t \quad (\text{A.26})$$

$$= \left\langle \left[ B \left( \frac{\partial^2 \xi}{\partial x^2} + \frac{\partial^2 \xi}{\partial y^2} \right) \left( \frac{\partial^2 \xi}{\partial x \partial t} \right) \right] \right\rangle_t \quad (\text{A.27})$$

and

$$\Pi'_{M_x} \approx \Pi_{M_x} \quad (\text{A.28})$$

In the vibration farfield:

$$\frac{\partial^2 \xi}{\partial x^2} + \frac{\partial^2 \xi}{\partial y^2} = k^2 \xi \quad (\text{A.29})$$

where

$$k^4 = \frac{\omega^2 m}{B} \quad (\text{A.30})$$

Substituting into Equation A.27:

$$\Pi'_{M_x} = \left\langle \left[ B k^2 \xi \left( \frac{\partial^2 \xi}{\partial x \partial t} \right) \right] \right\rangle_t \quad (\text{A.31})$$

In the farfield:

$$\Pi_{F_x} = \Pi_{M_x} \quad (\text{A.32})$$

Since:

$$\Pi_x = \Pi_{F_x} + \Pi_{M_x} \quad (A.33)$$

then from Equation A.28:

$$\Pi_x \approx \Pi_{F_x} + \Pi'_{M_x} \quad (A.34)$$

$$\Pi_x \approx 2\Pi'_{M_x} \quad (A.35)$$

$$\Pi_x \approx \left\langle 2\sqrt{Bm} \omega \xi \frac{\partial^2 \xi}{\partial x \partial t} \right\rangle_t \quad (A.36)$$

#### FINITE DIFFERENCE APPROXIMATION

$$\frac{\partial^2 \xi}{\partial x \partial t} = \frac{\partial}{\partial x} \frac{\partial \xi}{\partial t} = \frac{\partial}{\partial x} (v) \approx \frac{v_2 - v_1}{\Delta} \quad (A.37)$$

where  $\Delta$  is the separation distance between points one and two. And

$$\xi \approx \frac{\xi_1 + \xi_2}{2} \quad (A.38)$$

$$\Pi_x \approx 2\sqrt{Bm} \omega \left\langle \left[ \frac{v_2 - v_1}{\Delta} \cdot \frac{\xi_1 + \xi_2}{2} \right] \right\rangle_t \quad (A.39)$$

$$\Pi_x \approx \frac{\sqrt{Bm} \omega}{\Delta} \langle v_2 \xi_1 + v_2 \xi_2 - v_1 \xi_1 - v_1 \xi_2 \rangle_t \quad (A.40)$$

$$\Pi_x \approx \frac{\sqrt{Bm} \omega}{\Delta} [R_{v_2 \xi_1}(0) + R_{v_2 \xi_2}(0) - R_{v_1 \xi_1}(0) - R_{v_1 \xi_2}(0)] \quad (A.41)$$

Since  $R_{xx}(0) = 0$  then  $R_{v_2 \xi_2}(0) = 0$  and  $R_{v_1 \xi_1}(0) = 0$ . This leaves:

$$\Pi_x \approx \frac{\sqrt{Bm} \omega}{\Delta} [R_{v_2 \xi_1}(0) - R_{v_1 \xi_2}(0)] \quad (A.42)$$

Since  $R_{xy}(0) = \int_{-\infty}^{+\infty} S_{xy}(\omega) d\omega$ ; then:

$$\Pi_x \approx \frac{\sqrt{Bm} \omega}{\Delta} [\int_{-\infty}^{+\infty} S_{v_2 \xi_1}(\omega) d\omega - \int_{-\infty}^{+\infty} S_{v_1 \xi_2}(\omega) d\omega] \quad (A.43)$$

In order to use velocity cross-spectra it is noted that:

$$S_{v_2 \xi_1}(\omega) = \frac{S_{v_2 v_1}(\omega)}{i\omega} \quad \text{and} \quad S_{v_1 \xi_2}(\omega) = \frac{S_{v_1 v_2}(\omega)}{i\omega}$$

Therefore

$$\Pi_x \approx \frac{\sqrt{Bm}\omega}{\Delta} \left[ \int_{-\infty}^{+\infty} \frac{1}{i\omega} [S_{v_2 v_1}(\omega) S_{v_1 v_2}(\omega)] d\omega \right] \quad (\text{A.44})$$

But  $S_{v_2 v_1}(\omega) = S_{v_1 v_2}^*(\omega)$ , therefore:

$$\Pi_x \approx \frac{\sqrt{Bm}\omega}{\Delta} \left[ \int_{-\infty}^{+\infty} \frac{1}{i\omega} [S_{v_1 v_2}^*(\omega) - S_{v_1 v_2}(\omega)] d\omega \right] \quad (\text{A.45})$$

If the two-sided spectrum is replaced with the one-sided spectrum:

$$\Pi_x \approx \frac{\sqrt{Bm}\omega}{\Delta} \left[ \int_0^{+\infty} \frac{1}{i\omega} [G_{v_1 v_2}(\omega) - G_{v_1 v_2}(\omega)] d\omega \right] \quad (\text{A.46})$$

$$\Pi_x \approx \frac{\sqrt{Bm}\omega}{\Delta} \left[ \int_0^{+\infty} \frac{1}{i\omega} [-2i \operatorname{Im}[G_{v_1 v_2}(\omega)]] d\omega \right] \quad (\text{A.47})$$

$$\Pi_x \approx \frac{-2\sqrt{Bm}\omega}{\Delta} \int_0^{+\infty} \frac{\operatorname{Im}[G_{v_1 v_2}(\omega)]}{\omega} d\omega \quad (\text{A.48})$$

For single frequency excitation at  $\omega_1$ :

$$G_{v_1 v_2}(\omega) = \delta(\omega - \omega_1) G_{v_1 v_2}(\omega)$$

and

$$\int_0^{+\infty} \frac{\operatorname{Im}[G_{v_1 v_2}(\omega)] \delta(\omega - \omega_1) d\omega}{\omega} = \frac{\operatorname{Im}[G_{v_1 v_2}(\omega_1)]}{\omega_1} \quad (\text{A.49})$$

Therefore at frequency  $\omega_1$ :

$$\Pi_x \approx \frac{-2\sqrt{Bm}\omega_1}{\Delta} \cdot \frac{\operatorname{Im}[G_{v_1 v_2}(\omega_1)]}{\omega_1} \quad (\text{A.50})$$



$$\Pi_x \approx \frac{-2\sqrt{Bm}}{\Delta} \cdot \text{Im}[G_{v_1 v_2}(\omega)] \quad (\text{A.51})$$

This has to be corrected for finite difference error so that:

$$\Pi_x \approx \frac{-2\sqrt{Bm}}{\Delta} \text{Im}[G_{v_1 v_2}(\omega)] * \frac{k\Delta}{\sin k\Delta} = \frac{2\sqrt{Bm}}{\Delta} \text{Im}[G_{v_2 v_1}(\omega)] * \frac{k\Delta}{\sin k\Delta} \quad (\text{A.52})$$

## Appendix B

### PHASE ANGLE BETWEEN TWO POINTS SEPARATED BY $\Delta x$ ON A RESONANT BEAM (AND ROD) WITH WAVENUMBER $k$ AND MIDPOINT OVER THE ANTINODE

For a reverberant one-dimensional structure vibrating with wavenumber  $k$ , the cross-spectrum between two transducers spaced  $\Delta x$  apart with a midpoint of  $x_0$  is (from Carroll 1987):

$$G_{21} = (2\pi f)^4 |A|^2 [e^{ik\Delta x} + 2|R|\cos 2kx_0 + |R|^2 e^{-ik\Delta x}] \quad (B.1)$$

This, if expanded and separated into its real and imaginary parts provides:

$$\text{Im}[G_{21}] = (2\pi f)^4 |A|^2 \sin k\Delta x (1 - |R|^2) \quad (B.2)$$

and

$$\text{Re}[G_{21}] = (2\pi f)^4 |A|^2 (\cos k\Delta x + 2|R|\cos 2kx_0 + |R|^2 \cos k\Delta x) \quad (B.3)$$

Therefore, the phase angle,  $\phi$  is such that:

$$\tan \phi = \frac{\text{Im}[G_{12}]}{\text{Re}[G_{12}]} = \left[ \frac{\sin k\Delta x (1 - |R|^2)}{(\cos k\Delta x + 2|R|\cos 2kx_0 + |R|^2 \cos k\Delta x)} \right] \quad (B.4)$$

This is the general expression for a reflection coefficient of  $|R|$ . For the examples associated with random error it is desired to situate the transducers where the phase difference,  $\phi$ , is the smallest i.e.: where their midpoint is at an antinode. Yet it is desired to maintain a simple relationship between the phase difference and parameters such as  $\eta$ ,  $k$ , and  $L$ . This is done by approximating the phase difference at the antinode as one half the phase difference at the midpoint between a node and antinode (where the expression is a simple one). This is performed below.

At a point half-way between the node and antinode  $\cos 2kx_0 = 0$   
(since at the antinodes  $kx_0 = 0, \pi, 2\pi \dots$  etc.) so that:

$$\tan \phi = \left[ \frac{\sin k\Delta x (1 - |R|^2)}{\cos k\Delta x (1 + |R|^2)} \right] \quad (\text{B.5})$$

Therefore at the antinode the phase difference is approximated as:

$$\tan \phi \approx \frac{1}{2} \left[ \tan k\Delta x \cdot \frac{(1 - |R|^2)}{(1 + |R|^2)} \right] \quad (\text{B.6})$$

The approximation is a good one for  $k\Delta x \leq .2\pi$  and  $0.7 \leq |R| \leq 1$ .  
However, since the measurement of  $\eta$  is typically simpler than the  
measurement of  $|R|$ , the equation is cast in terms of  $\eta$ . The process of  
relating  $|R|$  to  $\eta$  depends on whether flexural waves or longitudinal  
waves are being addressed.

#### FLEXURAL CASE

For flexural power flow (from Carroll 1987):

$$\Pi = YI(2\pi f)k^3|A|^2(1 - |R|^2) \quad (\text{B.7})$$

so that

$$(1 - |R|^2) = \frac{\Pi}{YI(2\pi f)k^3|A|^2} \quad (\text{B.8})$$

Also for the total energy (which is twice the kinetic energy):

$$\langle E \rangle = m'(2\pi f)^2|A|^2(1 + |R|^2)L \quad (\text{B.9})$$

(This is obtained by integrating the kinetic energy over the  
reverberating beam length and multiplying by two).

So that:

$$(1 + |R|^2) = \frac{\langle E \rangle}{m'(2\pi f)^2|A|^2L} \quad (\text{B.10})$$

Then:

$$\frac{(1 - |R|^2)}{(1 + |R|^2)} = \frac{\Pi/YI(2\pi f)k^3|A|^2}{\langle E \rangle / m' (2\pi f)^2 |A|^2 L} = \frac{\Pi}{\langle E \rangle} \frac{m' (2\pi f) L}{YIk^3} \quad (B.11)$$

but

$$\frac{\Pi}{\langle E \rangle} = \eta \cdot 2\pi f \quad (B.12)$$

Therefore:

$$\frac{(1 - |R|^2)}{(1 + |R|^2)} = \eta \cdot 2\pi f \cdot \frac{m' (2\pi f) L}{YIk^3} \quad (B.13)$$

and, since for flexural waves:

$$k^4 = (2\pi f)^2 \frac{m'}{YI} \quad (B.14)$$

then:

$$\frac{(1 - |R|^2)}{(1 + |R|^2)} = \eta k L \quad (B.15)$$

This relates the loss factor to reflection coefficient for the flexural waves, where the losses all occur at the end of the beam. Now the phase difference at the antinode for this case becomes:

$$\tan \phi \approx \frac{\eta k L}{2} \cdot \tan k \Delta x \quad (B.16)$$

(Note: This derivation is composed from Carroll (1987), but is included here in a more succinct form. It also closely parallels the longitudinal case, illustrated next, which is not included in Carroll.)

#### LONGITUDINAL CASE

For longitudinal power flow the power flow expression, analogous to the flexural case, is:

$$\Pi = SY(2\pi f)k \frac{|A|^2(1 - |R|^2)}{2} \quad (B.17)$$

so that:

$$(1 - |R|^2) = \frac{2\Pi}{SY(2\pi f)k|A|^2} \quad (B.18)$$

From the energy equation (which is the same as in the flexural case):

$$(1 + |R|^2) = \frac{\langle E \rangle}{m'(2\pi f)^2|A|^2L} \quad (B.19)$$

Therefore:

$$\frac{(1 - |R|^2)}{(1 + |R|^2)} = \frac{2\Pi/SY(2\pi f)k|A|^2}{\langle E \rangle/m'(2\pi f)^2|A|^2L} \quad (B.20)$$

or

$$\frac{(1 - |R|^2)}{(1 + |R|^2)} = \frac{2\Pi}{\langle E \rangle} \cdot \frac{m'(2\pi f)L}{SYk} \quad (B.21)$$

For longitudinal waves

$$k^2 = (2\pi f)^2 \frac{m'}{YS} \quad (B.22)$$

and since

$$\frac{\Pi}{\langle E \rangle} = \eta \cdot 2\pi f \quad (B.23)$$

obtained for the longitudinal case is:

$$\frac{(1 - |R|^2)}{(1 + |R|^2)} = 2 \eta kL \quad (B.24)$$

Therefore in the longitudinal case the phase angle difference at the antinode is:

$$\tan \phi \approx \eta kL \cdot \tan k\Delta x \quad (B.25)$$

This is twice the phase angle found in the flexural case for transducers centered over the antinode at a spacing of  $\Delta x$ . The previous phase

difference expressions at the antinode were used in the examples for random error where it was assumed that  $\Delta x = 0.1 \lambda$  which satisfies  $k\Delta x \leq .2\pi$  for approximation purposes.

## Appendix C

### RELATIONSHIP BETWEEN THE CROSS-SPECTRUM AND THE COMPLEX FORMS OF TWO SINUSOIDAL SIGNALS

To show that  $G_{xy}(f) = [X^*(t) \cdot Y(t)/2] \delta(f - f_0)$  where  $X(t)$  and  $Y(t)$  are complex forms of the single frequency signals at  $x$  and  $y$ , and the asterisk represents the complex conjugate, first define:

$$x(t) = A \cos \omega t = \text{Re} \{Ae^{i\omega t}\} = \text{Re} \{X(t)\} \quad (\text{C.1})$$

$$y(t) = B \cos (\omega t + \phi) = \text{Re} \{Be^{i(\omega t + \phi)}\} = \text{Re} \{Y(t)\} \quad (\text{C.2})$$

Therefore:

$$\left[ \frac{X^*(t)Y(t)}{2} \right] = \frac{ABe^{i\phi}}{2} \quad (\text{C.3})$$

The value  $G_{xy}(f)$  can be obtained by finding  $R_{xy}(\tau)$ , the cross-correlation function between the signals, and then Fourier transforming to find the cross-spectrum:

$$R_{xy}(\tau) = \lim_{T \rightarrow \infty} \frac{1}{T} \int_0^T AB \cos(2\pi f_0 t) \cos(2\pi f_0 (t + \tau) + \phi) dt \quad (\text{C.4})$$

Using trigonometric identities for the cosine products this can be integrated to obtain:

$$R_{xy}(\tau) = \frac{AB}{2} \cos(2\pi f_0 \tau + \phi) \quad (\text{C.5})$$

$$S_{xy}(f) = \int_{-\infty}^{\infty} R_{xy}(\tau) e^{-i2\pi f \tau} d\tau \quad (\text{C.6})$$

But

$$\cos(2\pi f_o t + \phi) = \frac{1}{2} [e^{i\phi} e^{i2\pi f_o t} + e^{-i\phi} e^{-i2\pi f_o t}] \quad (C.7)$$

Therefore Equation (C.6) yields:

$$S_{xy}(f) = \frac{AB}{2} \int_{-\infty}^{\infty} \frac{1}{2} [e^{i\phi} e^{i2\pi(f_o - f)\tau} + e^{-i\phi} e^{-i2\pi(f_o + f)\tau}] d\tau \quad (C.8)$$

$$S_{xy}(f) = \frac{AB}{4} [e^{i\phi} \delta(f_o - f) + e^{-i\phi} \delta(f_o + f)] \quad (C.9)$$

However;

$$G_{xy}(f) = \begin{cases} 2 S_{xy}(f); & f \geq 0 \\ 0; & f < 0 \end{cases} \quad (C.10)$$

Therefore

$$G_{xy}(f) = \frac{AB}{2} e^{i\phi} \delta(f_o - f) = \frac{AB}{2} e^{i\phi} \delta(f - f_o) = \left[ \frac{X^*(t)Y(t)}{2} \right] \delta(f - f_o) \quad (C.11)$$

Rather than use the complex "amplitudes" the division by two can be removed if  $X(t)$  and  $Y(t)$  represent complex root mean square values. Also, the text drops the use of the delta function. In practice, when single frequency excitation is used, the output from the FFT analyzer will be the integrated result within the resolution binwidth. This will yield the total vibrational energy flux occurring at  $f_o$ , the excitation frequency. Some FFT analyzers, however, will divide this result by the bin width in which case the value must be multiplied by this binwidth for the total energy flux at  $f_o$ .